MEASUREMENT OF $\tau^+\tau^-$ PAIRS FROM Z^0 DECAYS

Jose Pedro Miragaia Trancoso Vaz

À memória do meu avô Jaime

MEASUREMENT OF $\tau^+\tau^-$ PAIRS FROM Z^0 DECAYS

Abstract

The analysis of $\tau^+\tau^-$ pairs, produced at seventeen centre of mass energies from 88 to 95 GeV in the Z^0 resonance range, allowed the study of the process $Z^0 \to \tau^+\tau^-$ and its properties.

The measurements have been performed in the DELPHI experiment at LEP. The number of tau pairs measured at each energy point and the corresponding cross-section are presented. With the information on the number of hadronic decays of the Z^0 measured at each point, the ratio between the partial decay widths of the Z^0 into tau pairs and into hadrons is measured.

The partial width $\Gamma_{\tau\tau}$ is extracted from a fit to the measured cross-section values.

The forward-backward asymmetry A^{τ}_{FB} at seven centre of mass energy values is obtained measuring the angular distribution of the charged tracks produced in τ decays.

Identification of the final states produced in τ decays allows the measurement of the τ polarization, A^{τ}_{POL}. Two independent measurements using the decay channels $\tau \to \mu\bar{\nu}_\mu\nu_\tau$ and $\tau \to \pi X \nu_\tau$ (inclusive pion detection) are used to extract the polarization and a third measurement corresponding to the channel $\tau \to \pi\nu_\tau$ is performed.

Combining the measurements of the last three "observables", the determination of the vector and axial couplings of the Z^0 to $\tau^+\tau^-$ pairs is obtained and the Standard Model parameter $\sin^2\theta_w$ is extracted with an accuracy of 0.0046.

Intermediate results are obtained combining the Z^0 resonance parameters measured in DELPHI and some of the above measurements: the branching ratio for Z^0 decays into $\tau^+\tau^-$ and a determination of the number of neutrino families with an accuracy of half a family.

No inconsistencies are found between the Standard Model expectations and the measurements above. Our measurements using $\tau^+\tau^-$ data, compared with similar measurements performed for the other leptonic decay channels of the Z^0 agree well with the lepton universality hypothesis.

Contents

8   TRIGGER & DAS

Chapter 1

INTRODUCTION

The τ particle was first detected in 1975[1] at the SPEAR e^+e^- storage ring, following the formulation of the theory of the sequential heavy leptons[2,3] and the heavy lepton searches at ADONE[4,5]. Up to 1980, further and more accurate measurements at SPEAR and also at DORIS improved the determination of some of its properties (mass,spin, point-like structure, decay modes and branching ratios)[6,8,9,10,11].

During the eighties, additional studies of the τ lepton concerning universality, V-A Lorentz structure, the lifetime, the decay modes, the pointlike structure and the asymmetries were carried on at higher energies, at the PEP (29 GeV), PETRA (energies up to 46 GeV) and TRISTAN (up to 56 GeV) e^+e^- colliders.

In the energy range of the e^+e^- colliders in the pre-LEP era, $\tau^+\tau^-$ pair production is dominated by QED annihilation. However, the effects due to the Z^0 small contribution are already visible on the PETRA and TRISTAN cross-sections and asymmetries measurements. The main diagram responsible for the production cross-section is the pure-QED (γ exchange) annihilation diagram of figure 1.1, the Z^0 contribution coming from the interference between the diagrams sketched in figure 1.2.
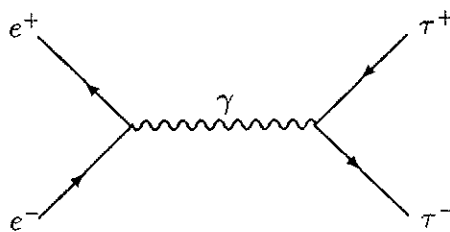
Figure 1.1: $e^+e^- \rightarrow \gamma \rightarrow \tau^+\tau^-$ process
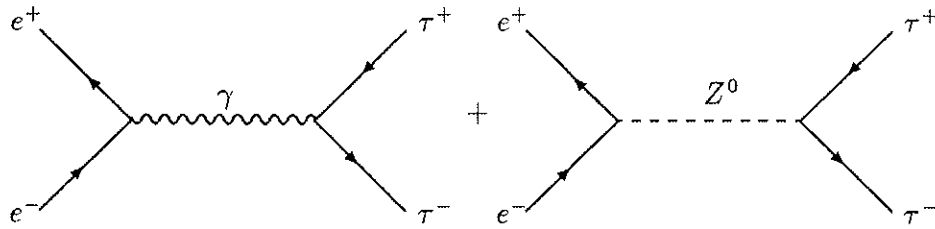
Figure 1.2: γZ^0 interference, product of the 2 diagrams

At PETRA energies, due to the small sensitivity to the Z^0 exchange contribution (only the $\gamma - Z$ interference term is sizeable), the experimental determination of the vector couplings v_e and v_τ is poor and only the product of the axial couplings $a_e a_\tau$ is measured with accuracy (from A_{FB}, the forward-backward asymmetry and $R_{\tau\tau} = \frac{\sigma_{\tau\tau}}{\sigma_{point}}$).

On the Z^0 resonance, τ pair production is dictated mainly by the creation and subsequent decay of the neutral boson Z^0 (see figure 1.3). New tests of the electroweak theory are possible, through all quantities depending on the vector and axial vector couplings of the Z^0 to the leptonic current. Measurements of the cross-section for tau pair production or of the Z^0 decay width into $\tau^+\tau^-$, exhibit high sensitivity to terms containing $(v_\tau^2 + a_\tau^2)$, the sum of the squares of the vector and axial couplings, while the measurement of the τ polarization asymmetry or of the τ forward-backward asymmetry allow the determination of v_τ/a_τ, the ratio between the vector and axial vector couplings. Precise measurements of the "observables" above translate in a highly accurate determination of the $\sin^2\theta_w$ parameter, constraining the level of uncertainties still remaining in the Model or opening frontiers for New Physics by deviations relative to the expectations.

Radiative corrections accquire, on-resonance, where a high level of accuracy is expected, a different dimension and importance, and must be carefully treated and understood in order to allow the correct interpretation of the measured parameters.

Event topology changes considerably at LEP with respect to previous e^+e^- colliders, given the higher centre of mass energy and higher boost factor of the decay products into the laboratory system. This can represent an advantage in event tagging and selection as well as a disavantage due to detector limitation in the resolution of collimated tracks and acompanying photons.
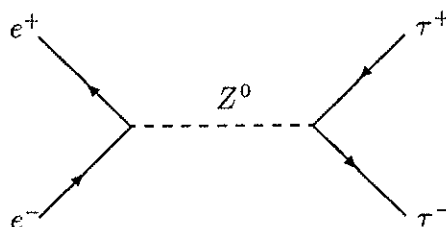
Figure 1.3: $e^+e^- \rightarrow Z^0 \rightarrow \tau^+\tau^-$ processes.

At LEP energies, the physics involved in the production and decay of the τ lepton is an example of the interplay between all the sub-domains of the underlying theory, the Standard Model of the Electroweak Interactions: the weak neutral currents coupling to the heavy neutral boson in the decays $Z^0 \rightarrow f\bar{f}$; the pure weak process at the decay $\tau \rightarrow W\nu_\tau$; the QCD processes of the semi-leptonic τ decays, with the weak charged bosons ($W^\pm$) coupling to quarks and subsequent hadronization.

The large variety of possible final states in τ decays provides an interesting field of investigation, allowing checks on the leptonic universality, V-A structure of weak interactions, lepton number or flavour violation, verification of PCAC and CVC, the existence of second class currents etc., and allows the establishment of limits on New Physics or extensions to the Standard Model.

Nowadays, the τ properties are well studied and understood: it is a spin 1/2 object, grouping with the corresponding neutrino in the doublet scheme of the Standard Model, has pointlike structure and decays weakly via W emission. The world averaged measurement of mass, spin, lifetime, bounds on the tau neutrino mass and deviations from pointlike structure are[12]:

- *Mass*: $M_\tau = 1784.1^{+2.7}_{-3.6}$ MeV

- *Spin*: $s_\tau = 1/2$

- *Lifetime*: $\tau_\tau = (0.304 \pm 0.009) \cdot 10^{-12}$ s

- *Tau Neutrino Mass*: $M_{\nu_\tau} < 35$ MeV

- *Pointlike Structure*: no deviations up to 10^{-18} m

The resonance parameters of the Z^0 boson (mass M_Z and total width Γ_Z) were first determined by the UA1 and UA2 experiments at the CERN $p\bar{p}$ collider in 1983 based on a few dozens of recorded events. During the first year of operation of LEP, the scan of the Z^0 resonance was made, with beams colliding at seventeen different centre of mass energies from 88 to 95 GeV. In DELPHI, a total sample of 68000 hadronic events ($Z^0 \to q\bar{q}$) allowed with much higher statistics and smaller systematic errors a more accurate measurement of the resonance parameters.

In the sequence, the measurement of $\tau^+\tau^-$ pairs from Z^0 decays at the DELPHI detector is described. The data was collected during the same period mentioned above, at the seventeen energy points from 88 to 95 GeV. A brief description of the contents of this work is as follows:

In Part I the physics motivations for studying $Z^0 \to \tau^+\tau^-$ decays at centre of mass energies in the range of the Z^0 resonance are discussed in detail. In Chapter 2 the lowest order differential and integrated cross-section for fermion pair production near the Z^0 resonance are discussed and the role of the axial and vector couplings of the neutral boson to the fermionic current in the physics measurements is exhibited. The definition of the observables, Forward-Backward Asymmetry A_{FB} and Helicity Asymmetry A_{POL}, is made in Chapter 3 where a detailed discussion of the τ polarization is presented and the details of the spin effects in τ decays are shown. In Chapter 4, the importance of the radiative corrections, distorting the measurements relative to the lowest order predictions and the need for parametrizations taking into account such corrections, is quantitatively shown. Finally, in Chapter 5, the large and rich variety of topics and subjects involved in the τ decays are discussed in the framework of the coupling of the intermediate charged W boson to the fermionic doublets of leptons or quarks. The theoretical predictions for the branching ratios of τ decays are summarized and compared with the world averaged measurements of the τ branching fractions. Checks on the consistency of SM assumptions (V-A Lorentz structure, universality, etc.) and PCAC,CVC theorems are also discussed.

In Part II an attempt is made to describe the apparatus that makes possible this and other studies of the Z^0 production in e^+e^- annihilation, hopefully giving the right idea of the techonogical and scientific dimension of a LEP experiment. In Chapter 6 the description of LEP, the acelerator and the machine parameters, is presented. It is pointed out the importance for the LEP experiments performance of a correct understanding of the beam backgrounds. Chapter 7 contains the description of the DELPHI detector. The description of the sub-detector components, their geometry, resolutions and performances is made. Chapter 8 makes the bridge between the detectors and the complex task of selecting in real time, based on detector signals, the "interesting" events and collecting the detector information into the storage medium.

Part III deals with the detection and analysis of the $\tau^+\tau^-$ pairs. Chapter 9 describes the software tools used to reconstruct the information from each detector and combine them to reconstruct the overall particle characteristics (momentum, direction, charge,

energy, mass), and to simulate physics events in the DELPHI detector. From Chapter 10 onwards, all the chapters are τ-oriented. In Chapter 10 the ways of triggering the $\tau^+\tau^-$ events and the efficiency of such online procedures are discussed. The typical signatures of e^+e^- and $\mu^+\mu^-$ events are discussed and compared to the expected signature from $\tau^+\tau^-$ events. In Chapter 11, the offline event selection criteria based on the reconstructed global quantities (topology,number of tracks,total energy, total momentum, etc.) or on individual particle quantities (signature in individual detectors, origin of the particle from the interaction point, isolation, etc.) lead to the sample of $\tau^+\tau^-$ events. The sources of background to such event sample are also discussed. Chapter 12 explains the luminosity determination by counting the number of Bhabha events in the low angle region and how it allows to normalize the number of detected events of a given physics channel.

In *Part IV*, the measurements of the $\tau^+\tau^-$ cross-section at 17 energy points in the Z^0 resonance are presented. After a short review in Chapter 13 of the Z^0 resonance parameters determined in DELPHI and used as inputs for the $\tau^+\tau^-$ analysis, Chapter 14 describes the measurement of the partial decay width of the Z^0 into $\tau^+\tau^-$ and the determination of the forward-backward asymmetry in the $\tau^+\tau^-$ differential cross section. In Chapter 15, two measurements of the τ polarization are presented, obtained from the measured energy spectra of identified muons and pions from τ decays. Finally, in Chapter 16, the physical properties of $\tau^+\tau^-$ pairs from Z^0 decays are analysed in the framework of the Standard Model, in order to extract some of its parameters and to check its consistency and agreement with the data.

Part I

$Z^0 \rightarrow \tau^+\tau^-$ Physics

Chapter 2

CROSS-SECTION FOR $e^+e^- \to f\bar{f}$ PRODUCTION

In the framework of the Standard Model of the Electroweak Interactions the most general way of writing the fermionic current $\mathcal{J}_\mu$ coupling to the Z^0 is

$$\mathcal{J}_\mu = \sum_f \bar{f} \, \gamma_\mu \left[g_{f_L} \left(\frac{1 + \gamma_5}{2} \right) + g_{f_R} \left(\frac{1 - \gamma_5}{2} \right) \right] f \tag{2.1}$$

which exhibits the mixing between the left and right components of the fermionic spinor coupling to the Z^0 with "weights" g_L, g_R. Defining the vector coupling as

$$v_f = \frac{1}{2} \left[g_{f_L} + g_{f_R} \right] \tag{2.2}$$

and the axial-vector coupling as

$$a_f = \frac{1}{2} \left[g_{f_L} - g_{f_R} \right] \tag{2.3}$$

the lagrangian term describing the interaction of the neutral boson Z^0 with a fermionic pair is then

$$\mathcal{L}_{Zff} \sim \frac{e}{\sin\theta_w \, \cos\theta_w} \, \bar{f} \, \gamma_\mu \, (\, v_f - a_f\gamma_5 \,) \, f \, Z^\mu \tag{2.4}$$

The vector and axial-vector couplings are functions of the model parameters $e, \sin\theta_w$, and of the quantum numbers of the underlying symmetry groups SU(2) (I-weak isospin) and U(1) (Q-charge) through the expressions

$$v_f = 2I_{3f} - 4Q_f \sin^2 \theta_w \qquad (2.5)$$

$$a_f = 2I_{3f} \qquad (2.6)$$

with Q_f the fermion charge and I_{3f} the third component of the fermion weak isospin.

2.1 Fermion Pair Production Near The Z^0 Resonance

In the neighbourhood of the Z^0 resonance, the lowest order Feynman graphs describing the electron-positron annihilation process $e^+e^- \rightarrow f\bar{f}$ with production of fermionic (f=quark,lepton) pair in the final state, are shown in figure 2.1:
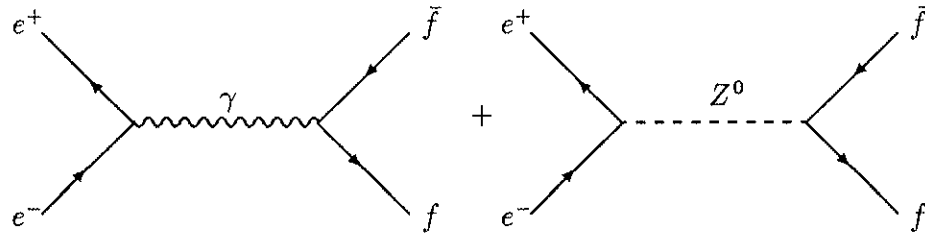
Figure 2.1: The basic $e^+e^- \rightarrow \gamma, Z \rightarrow f\bar{f}$ processes.

The differential cross-section has 3 components due, respectively, to the contribution from the γ exchange graph, the Z^0 exchange graph and the interference term coming from the product of one of the graphs times the complex conjugate of the other, and can be written as

$$\frac{d\sigma}{d\Omega} = \left(\frac{d\sigma}{d\Omega}\right)^\gamma + \left(\frac{d\sigma}{d\Omega}\right)^Z + \left(\frac{d\sigma}{d\Omega}\right)^{\gamma Z} \qquad (2.7)$$

The pure photon exchange contribution exhibits the $1 + \cos^2 \theta$ symmetric distribution and the $1/s$ typical dependence of the QED annihilation, while the neutral boson (Z^0) contribution can be written as the combination of a symmetric (F_S) and anti-symmetric (F_A) functions of $\cos\theta$[13]:

$$\left(\frac{d\sigma}{d\Omega}\right)^{\gamma Z} \sim (g_{e_L}^2 + g_{e_R}^2)(g_{f_L}^2 + g_{f_R}^2) \, F_S(\cos\theta) \; + \; (g_{e_L}^2 - g_{e_R}^2)(g_{f_L}^2 - g_{f_R}^2) \, F_A(\cos\theta) \quad (2.8)$$

showing that the odd $\cos\theta$ contribution is weighted by the asymmetry between left and right handed fermion couplings. One of the usual ways of writing the differential cross-section is[14]

$$\frac{d\sigma}{d\Omega} = \frac{\alpha^2}{4s} \, N_c \, [\, a(1 + \cos^2\theta) + 2b\cos\theta \,] \quad (2.9)$$

where

$$a = \underbrace{Q_e^2 Q_f^2}_{\gamma} + \underbrace{2Q_e Q_f v_e v_f \mathcal{R}(\chi)}_{\gamma \cdot Z^0} + \underbrace{(v_e^2 + a_e^2)(v_f^2 + a_f^2)|\chi|^2}_{Z^0} \quad (2.10)$$

$$b = \underbrace{2Q_e Q_f a_e a_f \mathcal{R}(\chi)}_{\gamma \cdot Z^0} + \underbrace{4v_e v_f a_e a_f |\chi|^2}_{Z^0} \quad (2.11)$$

with

$$\chi = \frac{1}{16\sin^2\theta_w \cos^2\theta_w} \frac{s}{(s - M_Z^2 + iM_Z\Gamma_Z)} \quad (2.12)$$

$$v_f = -1 + 4\,\sin^2\theta_w \quad , \quad a_f = -1 \quad (f = e, \mu, \tau \ \ leptons) \quad (2.13)$$

$$v_f = -1 + 4/3\,\sin^2\theta_w \quad , \quad a_f = -1 \quad (f = d, s, b \ \ quarks) \quad (2.14)$$

$$v_f = +1 - 8/3\,\sin^2\theta_w \quad , \quad a_f = +1 \quad (f = u, c \ \ quarks) \quad (2.15)$$

where N_c is the fermion colour factor (3 for quarks, 1 for leptons), Q_e and Q_f the charge of the electron and of the final state fermion, and v_e, a_e, v_f, a_f respectively the axial and vector couplings of the electron and final state fermion. $\mathcal{R}(\chi)$ is the real part of the χ factor which contains the Z^0 propagator contribution and determines the resonance shape together with M_Z and Γ_Z, respectively, the mass and width of the Z^0 boson. Finally, $\sin^2\theta_w$ is the basic parameter of the Standard Model of Electroweak Interactions.

2.2 On-Resonance Measurements

In the neighbourhood of the Z^0 resonance the total cross-section for the process $e^+e^- \to f\bar{f}$ can be written in lowest order as

$$\sigma_f^0(s) = 12\pi \underbrace{\frac{\Gamma_{ee}\Gamma_{ff}}{(s - M_Z^2) + \frac{s^2}{M_Z^2}\Gamma_Z^2}}_{\sigma_Z} + \underbrace{\frac{4\pi\alpha}{3s}Q_f^2}_{\sigma_\gamma} \qquad (2.16)$$

where the second term represents the "continuum" cross-section (γ exchange), much smaller than the Z^0 contribution in the energy range of the resonance and Γ_{ee}, Γ_{ff} are the partial widths for the processes $Z^0 \to e^+e^-$ and $Z^0 \to f^+f^-$, defined as

$$\Gamma_{ff} = \frac{G_\mu M_Z^3}{6\sqrt{2}\pi}\left(v_f^2 + a_f^2\right) \qquad (2.17)$$

Expressions 2.16 and 2.17 summarize the resonance parameters that can be extracted from the measurement of the cross-section for Z^0 production and subsequente decay into fermion pairs $f\bar{f}$:

- *Mass*, M_Z
- *Width*, Γ_Z
- *Pole Cross Section*, σ_Z
- *The partial widths*, Γ_{ff} .

From the measurement of the partial width Γ_{ff} follows the determination of $v_f^2 + a_f^2$. Additional information is obtained by measuring the asymmetries exhibited in the angular or energy distributions of the final state fermions, that allow the determination of the products $a_f v_f$. Combining the measurements of the partial widths and asymmetries the individual values of v_f and a_f can be determined.

Chapter 3

ON-RESONANCE ASYMMETRIES

The quantity describing the asymmetry between the left(L) and right(R) coupling intensities (respectively g_{f_L} and g_{f_R}) of the fermionic current to the Z^0 is

$$A^f = \frac{L - R}{L + R} = \frac{g_{f_L}^2 - g_{f_R}^2}{g_{f_L}^2 + g_{f_R}^2} = \frac{2 v_f a_f}{v_f^2 + a_f^2} \tag{3.1}$$

This quantity can also be defined as function of the theory parameter $\sin^2 \theta_w$, as follows:

$$A^f = \frac{2 \left(2 I_{3f} - 4 Q_f \sin^2 \theta_w \right) \left(2 I_{3f} \right)}{\left(2 I_{3f} - 4 Q_f \sin^2 \theta_w \right)^2 + 4 I_{3f}^2} \tag{3.2}$$

On the Z^0 resonance, the main types of asymmetries that can be experimentally measured by the study and detection of fermion pairs produced in Z^0 decays are:

- A_{FB}, Forward-Backward Asymmetry.

- A_{POL}^τ, Left-Right Helicity Asymmetry of the τ (τ polarization).

- A_{LR}, A_{FB}^{Pol}, "Polarized" Asymmetries (requiring polarized beams).

As seen in the sequence ($f = \tau$), the value of these asymmetries at the Z^0 resonance peak can be expressed as a function of A^f and A^e. Their measurement allows the determination of v_f, a_f and $\sin^2 \theta_w$.

3.1 $\tau^+\tau^-$ Differential Cross-Section

The differential cross-section for $\tau^+\tau^-$ production, corresponding to the Born term of the diagrams in e^+e^- annihilation in the energy range of the Z^0 resonance, can be written (with the τ^- longitudinal polarization p left free) as [17]

$$\frac{d\sigma}{d\cos\theta}(s,\cos\theta,p) \simeq (1+\cos^2\theta)F_0(s) + 2\cos\theta F_1(s) + \tag{3.3}$$

$$p\left[(1+\cos^2\theta)F_2(s) + 2\cos\theta F_3(s)\right] \tag{3.4}$$

with

$$F_0(s) = \frac{\pi\alpha^2}{2s}\left[Q_e^2 Q_\tau^2 + 2\mathcal{R}(\chi)Q_e Q_\tau v_e v_\tau + |\chi|^2(v_e^2 + a_e^2)(v_\tau^2 + a_\tau^2)\right] \tag{3.5}$$

$$F_1(s) = \frac{\pi\alpha^2}{2s}\left[2\mathcal{R}(\chi)Q_e Q_\tau a_e a_\tau + |\chi|^2 4v_e a_e v_\tau a_\tau\right] \tag{3.6}$$

$$F_2(s) = \frac{\pi\alpha^2}{2s}\left[2\mathcal{R}(\chi)Q_e Q_\tau v_e a_\tau + |\chi|^2 2v_\tau a_\tau(v_e^2 + a_e^2)\right] \tag{3.7}$$

$$F_3(s) = \frac{\pi\alpha^2}{2s}\left[2\mathcal{R}(\chi)Q_e Q_\tau a_e v_\tau + |\chi|^2 2v_e a_e(v_\tau^2 + a_\tau^2)\right] \tag{3.8}$$

$$\chi(s) = \frac{s}{(s - M_Z^2) + is\frac{\Gamma_Z}{M_Z}} \tag{3.9}$$

with Q_e, v_e, a_e and Q_τ, v_τ, a_τ respectively, the charge, the vector and the axial vector couplings of the electron and tau, α the QED coupling constant and s the square of the centre of mass energy. The odd terms in $\cos\theta$ come from the $\gamma - Z$ interference (product of the 2 diagrams) and the even terms in $\cos\theta$ are due to the pure γ or pure Z^0 exchange. The term $\chi(s)$ clearly exhibits the Z^0 resonance behaviour with the centre of mass energy s.

3.2 A^τ_{FB}, Forward-Backward Asymmetry

Due to the odd $\cos\theta$ terms in the differential cross-section, the number of produced τ^- at a given angular interval around the direction θ is different from the number of τ^- produced in the same angular interval around the opposite direction $\pi - \theta$. The angular asymmetry is evaluated from the expression

$$A^\tau_{FB}(\theta) = \frac{\frac{d\sigma}{d\Omega}(\theta) - \frac{d\sigma}{d\Omega}(\pi - \theta)}{\frac{d\sigma}{d\Omega}(\theta) + \frac{d\sigma}{d\Omega}(\pi - \theta)} \qquad (3.10)$$

Near the peak of the resonance $\mathcal{R}(\chi) \simeq 0$, the last expression can be written as

$$A^\tau_{FB}(\theta) \simeq 2A^e A^\tau \frac{2\cos\theta}{1 + \cos^2\theta} \qquad (3.11)$$

with

$$A^e = \frac{2 v_e a_e}{v_e^2 + a_e^2} \qquad , \qquad A^\tau = \frac{2 v_\tau a_\tau}{v_\tau^2 + a_\tau^2} \qquad (3.12)$$

Integrated over the forward and backward θ hemispheres, the last expression leads to the forward-backward asymmetry defined at the peak of the resonance ($\sqrt{s} = M_Z$):

$$A^\tau_{FB} = \frac{\sigma_\tau(\cos\theta > 0) - \sigma_\tau(\cos\theta < 0)}{\sigma_\tau(\cos\theta > 0) + \sigma_\tau(\cos\theta < 0)} = \frac{N_\tau(\cos\theta > 0) - N_\tau(\cos\theta < 0)}{N_\tau(\cos\theta > 0) - N_\tau(\cos\theta < 0)} \simeq \frac{3}{4} A^e A^\tau \qquad (3.13)$$

More generally, its dependence on the centre of mass energy (s) is given by

$$A^\tau_{FB}(s) = \frac{3}{4} \frac{F_1(s)}{F_0(s)} \qquad (3.14)$$

The sign of the asymmetry changes with the centre of mass energy due to the terms in $\mathcal{R}(\chi)$: it is negative for $\sqrt{s} < M_Z$ and positive when $\sqrt{s} > M_Z$. The energy at which $A_{FB}(s) = 0$, predicted by the lowest order expressions (above) to occur close to $\sqrt{s} = M_Z$ is shifted by a few dozens MeV towards higher values of $\sqrt{s}$ due to the radiative corrections.

3.3 A^τ_{POL}, Helicity Asymmetry

3.3.1 τ Polarization

The fermions produced in $e^+ e^-$ annihilation through Z^0 creation and decay are polarized due to the different intensities of the g_L, g_R (left,right) couplings of the neutral boson to the fermionic currents. As such, the helicity asymmetry reflects the difference in the cross-section for producing left handed fermions relative to the cross-section for producing right handed fermions. At high energies, in the limit $s \gg m_\tau^2$, left-handed produced τ's have helicity -1/2, right handed produced τ's have helicity +1/2 and helicity is conserved in the production and subsequent decay of the Z^0 and the τ. The measured angular and energy distributions of the final state particles reflect the spin polarization of the decaying τ. The τ helicity asymmetry is defined as

$$A^\tau_{POL} = -\frac{\sigma(\tau_L) - \sigma(\tau_R)}{\sigma(\tau_L) + \sigma(\tau_R)} \tag{3.15}$$

where $\sigma(\tau_{L,R})$ are the cross-sections for the production of left,right τ's in Z^0 decays. The last expression can be equivalently written as

$$A^\tau_{POL} = -\frac{\left(g_{\tau_R}\right)^2 - \left(g_{\tau_L}\right)^2}{\left(g_{\tau_R}\right)^2 + \left(g_{\tau_L}\right)^2} = -A^f \quad (f = \tau) \tag{3.16}$$

or, recalling the relation between the left and right handed couplings and the vector and axial couplings,

$$A^\tau_{POL} = -\frac{2v_\tau a_\tau}{v_\tau^2 + a_\tau^2} = -\frac{\frac{2v_\tau}{a_\tau}}{1 + \frac{v_\tau^2}{a_\tau^2}} \tag{3.17}$$

The variation of the helicity asymmetry with the centre of mass energy (s) and direction (θ) at which the τ's are produced is obtained from expression 3.3

$$A^\tau_{POL}(s, \cos\theta) = -\frac{d\sigma(\cos\theta, p = +1) - d\sigma(\cos\theta, p = -1)}{d\sigma(\cos\theta, p = +1) + d\sigma(\cos\theta, p = -1)} \tag{3.18}$$

$$= -\frac{(1 + \cos^2\theta)F_2(s) + 2\cos\theta F_3(s)}{(1 + \cos^2\theta)F_0(s) + 2\cos\theta F_1(s)} \tag{3.19}$$

3.3.1.1 $s^{1/2}$ Dependence

The centre of mass energy (s) dependence of the helicity asymmetry can be written as:

$$A^\tau_{POL}(s) = -\frac{\sigma(p = +1) - \sigma(p = -1)}{\sigma(p = +1) + \sigma(p = -1)} = -\frac{F_2(s)}{F_0(s)} \qquad (3.20)$$

In figure 3.1, the s-dependence of A^τ_{POL} is plotted for various values of $\sin^2 \theta_w$ exhibiting the high sensitivity to this parameter in the resonance region.
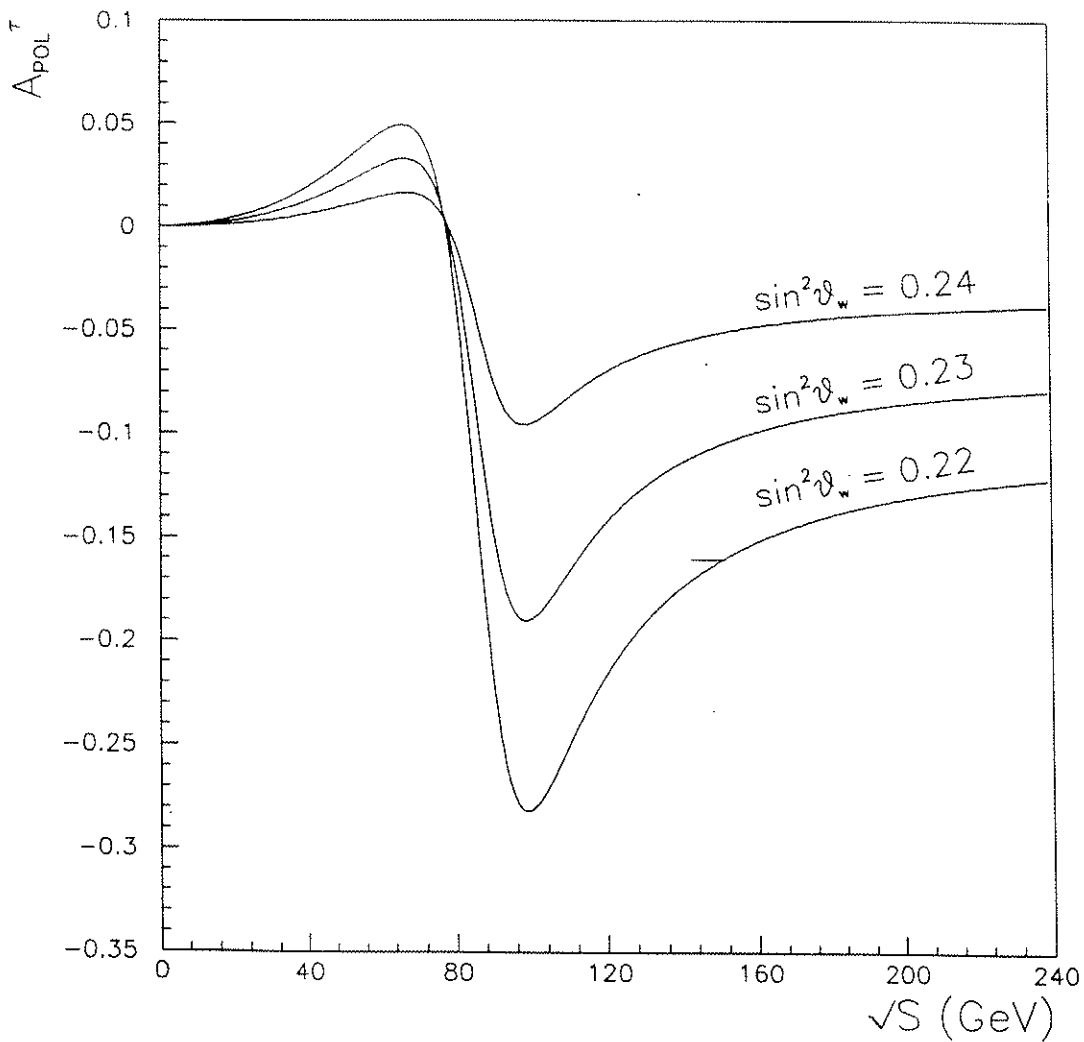
Figure 3.1: Centre of mass energy $(s^{1/2})$ dependence of A^τ_{POL}. Different curves correspond to different values of $\sin^2\theta_w$.

3.3.1.2 $\cos\theta$ Dependence

Near the top of the Z^0 resonance, $\mathcal{R}(\chi) \simeq 0$, expression 3.19 can be simplified to yield the angular dependence of the helicity asymmetry:

$$A^\tau_{POL}(\cos\theta) = \frac{A^\tau + \frac{2\cos\theta}{1+\cos^2\theta}\,A^e}{1 + \frac{2\cos\theta}{1+\cos^2\theta}\,A^e A^\tau} \qquad (3.21)$$

In figure 3.2 the θ dependence of the τ polarization and its sensitivity to $\sin^2\theta_w$ are plotted, showing that the τ is weakly polarized in the backward hemisphere ($cos\theta < 0$).
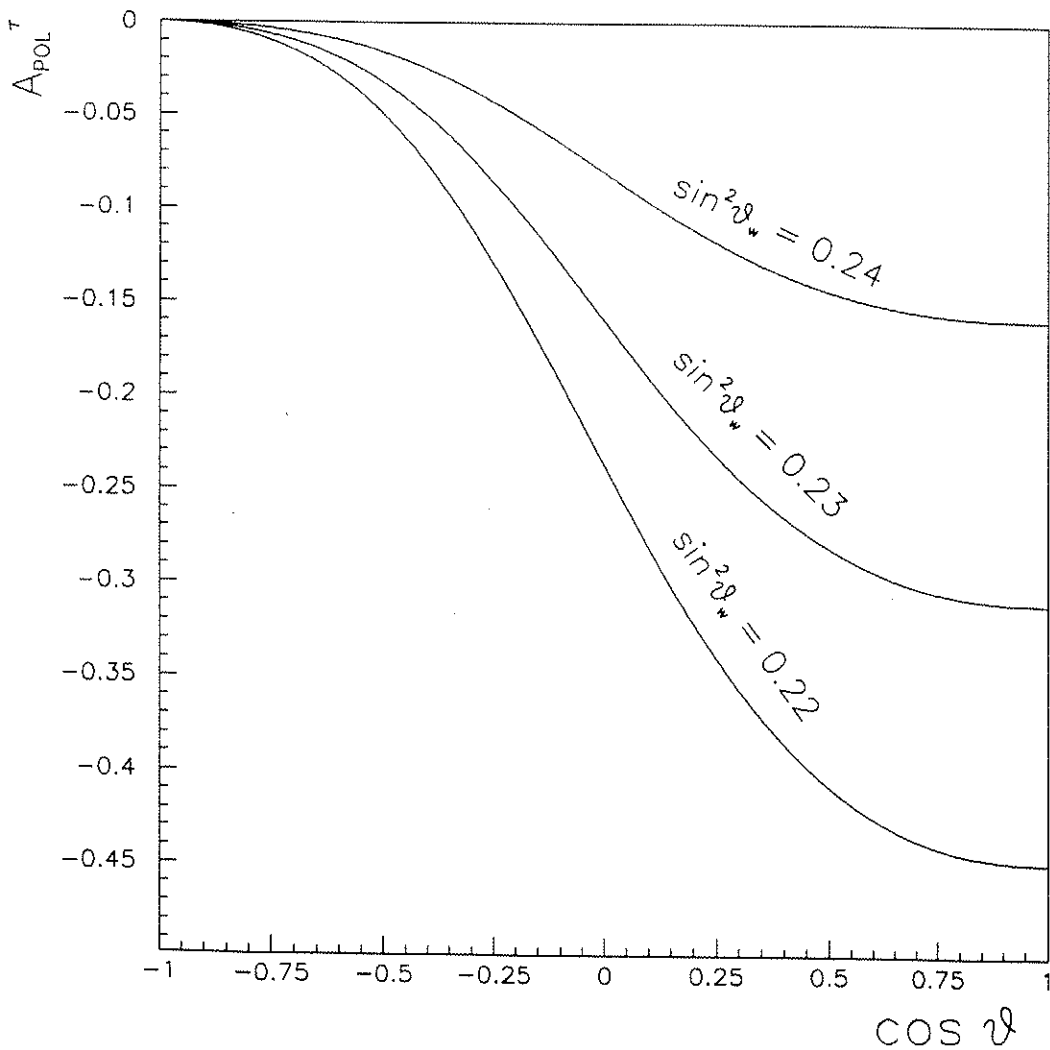
Figure 3.2: $\cos\theta$ dependence of A^τ_{POL} parametrized for different values of $\sin^2\theta_w$.

The study of the τ decays allows the measurement of the fermion spin polarization (helicity asymmetry). Due to helicity conservation, the energy spectrum in the laboratory, of each type of particles produced in the decays, exhibits a distribution that allows the measurement of the average polarization of the decaying τ's.

3.3.2 $\tau \rightarrow \pi\nu_\tau$ Polarimeter

The decay $\tau^- \longrightarrow \pi^-\nu_\tau$ proceeds in the τ rest frame as shown schematically in the next figure:

$$ALLOWED \qquad\qquad\qquad\qquad FORBIDDEN$$
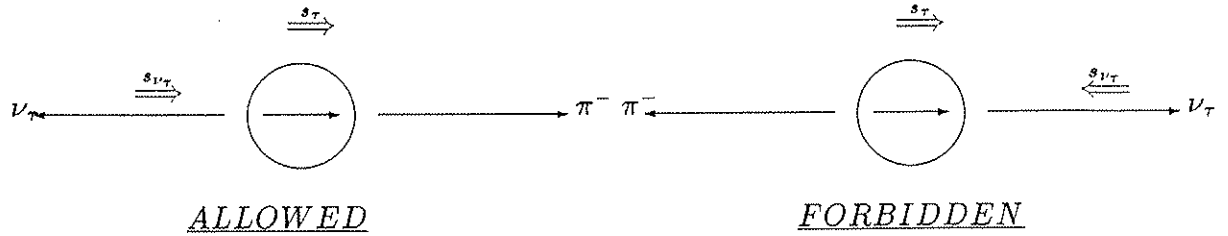
The average polarization reflects the asymmetry between the number of τ's with spin projection oriented along the (conventioned) positive direction and the number of τ's with spin projection oriented opposite to the same direction. Defining P_τ the momentum of the produced τ in the lab frame and s_τ the τ spin, the polarization asymmetry can be written as

$$A^\tau_{POL} \approx \frac{N_{s_\tau \cdot p_\tau > 0} - N_{s_\tau \cdot p_\tau < 0}}{N_{s_\tau \cdot p_\tau > 0} + N_{s_\tau \cdot p_\tau < 0}} \tag{3.22}$$

In the general case, if θ^* is the angle between the π^- and the τ^- spin in the τ rest frame, the angular distribution of the emitted π^- is

$$\frac{dN}{d\cos\theta^*} \simeq \frac{1}{2}\left(1 + \alpha \, \cos\theta^*\right) \quad , \quad \alpha = \frac{m_\tau^2 - 2m_\pi^2}{m_\tau^2 + 2m_\pi^2} \tag{3.23}$$

and P_π^*, E_π^* are respectively the momentum and energy of the produced π in the τ rest frame, four-momentum conservation implies

$$P_\pi^* = P_{\nu_\tau}^* \tag{3.24}$$

$$E_\pi^* = \sqrt{P_\pi^{*2} + m_\pi^2} \simeq \frac{m_\tau}{2} \tag{3.25}$$

Making a boost to the laboratory frame in the s_τ direction, with $E_\tau = E_{beam}$ and P_τ the energy and momentum of the τ in the laboratory, one gets for the pion energy

$$E_\pi = \gamma \left(E_\pi^* + \beta \cdot P_\pi^* \cos \theta^* \right) \tag{3.26}$$

$$\gamma = \frac{E_\tau}{m_\tau} \quad , \quad \beta = \frac{P_\tau}{E_\tau} \tag{3.27}$$

After some simplification (neglecting the π mass, $E_\pi^* \simeq P_\pi^*, \alpha \simeq 1$), the last expression takes the form

$$E_\pi = \gamma \, \frac{m_\tau}{2} \left(1 + \cos \theta_\pi^* \right) \tag{3.28}$$

and it is immediate to conclude that:

• If $\cos \theta_\pi^* > 0$,

$$E_\pi \simeq \frac{E_{beam}}{2} \left(1 + \cos \theta_\pi^* \right) > \frac{E_{beam}}{2} \implies \underline{FAST\ PIONS} \tag{3.29}$$

• If $\cos \theta_\pi^* < 0$,

$$E_\pi \simeq \frac{E_{beam}}{2} \left(1 + \cos \theta_\pi^* \right) < \frac{E_{beam}}{2} \implies \underline{SLOW\ PIONS} \tag{3.30}$$

If it would happen to be $g_L^\tau = g_R^\tau$ (unpolarized τ) then

$$N_{s_\tau \cdot p_\tau > 0} = N_{s_\tau \cdot p_\tau > 0} \iff N_\pi (E_\pi > \frac{E_{beam}}{2}) = N_\pi (E_\pi < \frac{E_{beam}}{2}) \iff A^\tau{}_{POL} = 0 \tag{3.31}$$

and the pion spectrum in the laboratory would be flat. The complete analytic calculation[15] leads to the distribution of the energy distribution of the pions in the laboratory frame, in terms of the variable $X_\pi = E_\pi / E_{beam}$:

$$\frac{dN_\pi}{dX_\pi} \simeq 1 + A_{POL}^\tau \left(2X_\pi - 1 \right) \tag{3.32}$$

Writing

$$A_{POL}^{\tau} = -(P_L - P_R) \quad , \quad P_L = \frac{(g_L^{\tau})^2}{(g_L^{\tau})^2 + (g_R^{\tau})^2} \quad , \quad P_R = \frac{(g_R^{\tau})^2}{(g_L^{\tau})^2 + (g_R^{\tau})^2} \quad (3.33)$$

the energy distribution expression can be written as

$$\frac{dN_\pi}{dX_\pi} \simeq 1 + P_L(\ 1 - 2X_\pi\ ) + P_R(\ 2X_\pi - 1\ ) \qquad (3.34)$$

showing that the slope of the pion energy distribution results from the mixture of the pions coming from decaying τ's with negative helicity (left-handed) and pions coming from decaying τ's with positive helicity (right-handed). The full slope gives then the measure of the asymmetry:

- If negative slope $\Rightarrow (g_L^{\tau})^2 > (g_R^{\tau})^2$ (Negative Polarization)

- If positive slope $\Rightarrow (g_L^{\tau})^2 < (g_R^{\tau})^2$ (Positive Polarization)

From the last formulae and from the definition of A_{POL}^{τ}, it is clear that the measurement of the tau polarization results from counting the number of τ's decaying with a positive spin projection along the momentum direction of the τ in the laboratory and the number of τ's decaying with a negative spin projection along the same direction. Using the $\tau \rightarrow \pi\nu$ decay mode, this translates into the asymmetry between the number of pions with energy above and below the threshold $E_{thr} \simeq \frac{E_{beam}}{2}$:

$$A_\pi^E = \frac{N_\pi(E > E_{thr}) - N_\pi(E < E_{thr})}{N_\pi(E > E_{thr}) + N_\pi(E < E_{thr})} \qquad (3.35)$$

3.3.3 $\tau \rightarrow \rho \nu_\tau$, $\rho \rightarrow \pi \pi^0$ Polarimeter

Being a vector resonance, the rho produced in the decay $\tau \rightarrow \rho \nu_\tau$ is allowed to have helicity states 0 or -1 depending on the τ total angular momentum (J_z^τ) along the decay axis. As shown in the next figures , when the τ angular momentum along the decay axis is $+1/2$ ($-1/2$), the ρ must be produced with helicity 0 (-1). The magnitude for each helicity configuration is computed in [18].

ALLOWED   ALLOWED

FORBIDDEN
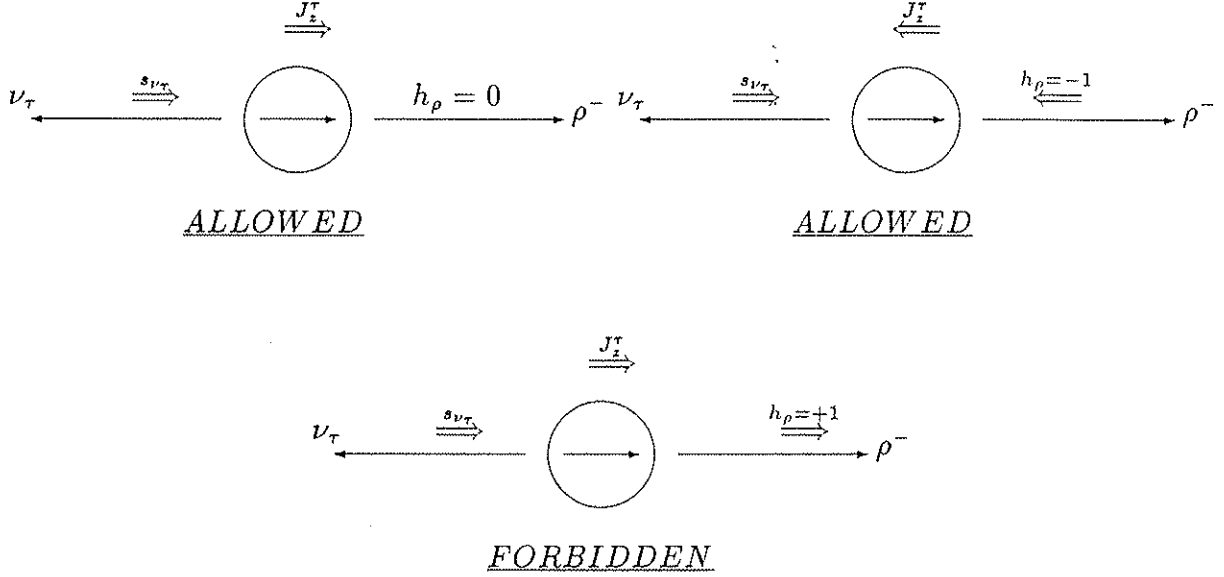
As for the decay $\tau \rightarrow \pi \nu_\tau$, the following set of equations can be deduced:

$$E_\rho = \gamma \left(E_\rho^* + P_\rho^* \cos \theta^* \right) \tag{3.36}$$

$$\cos \theta^* = \frac{E_\rho - \frac{E_\rho^{max} + E_\rho^{min}}{2}}{\frac{E_\rho^{max} + E_\rho^{min}}{2}} \tag{3.37}$$

$$E_\rho^{max} = \gamma \left(E_\rho^* + P_\rho^* \right) \approx E_\tau \tag{3.38}$$

$$E_\rho^{min} = \gamma \left(E_\rho^* - P_\rho^* \right) = E_\tau \left(\frac{m_\rho}{m_\tau} \right)^2 \tag{3.39}$$

with $E_\rho^*, P_\rho^*, E_\rho$ respectively the ρ energy and momentum in the τ rest frame, the ρ energy in the laboratory system and $\cos \theta^*$ is the ρ emission angle in the τ decay frame. This angular distribution is given by

$$\frac{dN}{d\cos\theta^*} \propto \frac{1}{2}\left(1 - \alpha\, h\, \cos\theta^*\right) \tag{3.40}$$

with $\alpha \approx 0.46$ a constant related to the magnitude of each of the different helicity final states in the tau decay. Making use of the transformations above, the ρ energy distribution in the laboratory is given by

$$\frac{dN}{dE_\rho} \propto \frac{1}{2}\left(1 - \alpha\, h\, \left(\frac{E_\rho - \frac{E^{max}_\rho + E^{min}_\rho}{2}}{\frac{E^{max}_\rho + E^{min}_\rho}{2}}\right)\right) \tag{3.41}$$

The τ polarization measurement consists in the asymmetry between the number of produced ρ's with energy respectively above and below the threshold $E_{thr} = \frac{E^{max}_\rho + E^{min}_\rho}{2}$:

$$A^E_\rho = \frac{N_\rho(E > E_{thr}) - N_\rho(E > E_{thr})}{N_\rho(E > E_{thr}) + N_\rho(E > E_{thr})} \tag{3.42}$$

Chapter 4

RADIATIVE CORRECTIONS TO THE Z^0 LINE SHAPE

The typical (lowest order) Breit-Wigner expression corresponding to the Z^0 boson resonance state of mass M_Z, total width Γ_Z and total angular momentum J, produced in e^+e^- annihilation and decaying into fermion pairs $f\bar{f}$ (f=quark,lepton), is [19]

$$\sigma^0(s) = \sigma^0_{peak} \; \frac{\frac{\Gamma_Z^2}{4}}{\left(\sqrt{s} - M_Z\right)^2 + \frac{\Gamma_Z^2}{4}} \tag{4.1}$$

with

$$\sigma^0_{peak} = \frac{4\pi}{M_Z^2} \, (2J+1) \, BR(Z^0 \to e^+e^-) \, BR(Z^0 \to f\bar{f}) \tag{4.2}$$

or, being Γ_{ee}, Γ_{ff} respectively the partial widths for the processes $Z^0 \to e^+e^-$ and $Z^0 \to f\bar{f}$,

$$\sigma^0_{peak} = \frac{12\pi}{M_Z^2} \, \frac{\Gamma_{ee}\Gamma_{ff}}{\Gamma_Z^2} \tag{4.3}$$

4.1   Radiative Corrections

The quantum behaviour of the electroweak theory implies that in e^+e^- annihilation processes, the physical phenomena are not exactly described by the lowest order (Born) graphs, but real and virtual processes of QED, QCD and electroweak nature must be taken into account, like:

- Radiation of real photons by the initial and/or final state particles (Initial and final state bremsstrahlung)

- Virtual photon loops on the fermion lines of the diagrams describing the process

- QED vertex corrections (virtual corrections)

- Weak vertex corrections (virtual corrections)

- γ, Z^0, W self energies, originated mainly by fermion loops in the boson propagators

- QCD corrections

The corrections due to initial and final state bremsstrahlung for an annihilation process occuring in a narrow resonance ($\frac{\Gamma}{M} \ll 1$) distort the measured resonance shape by introducing a tail at energies above the resonance mass, lowering the peak cross-section, shifting its position and modifying the resonance width.

The virtual quantum corrections, like the self-energies of the intermediate bosons have as effect the modification of the measured value of the resonance mass and width.

The QED and weak virtual corrections at the vertices, change the couplings of the fermionic current to the vector boson.

The uncertainties due to the top quark mass and the Higgs mass, entering in the calculation of the loop corrections to the propagators and in the vertex corrections, can be tested at LEP energies with the direct measurement of the Z^0 resonance parameters. The measurements of the Z^0 mass, total width, peak cross-section and partial widths, allow the estimation of the contribution to the measured parameters coming from the virtual graphs involving such particles and translate in the establishment of bounds in their masses.

4.2 QED radiation

The process of photon radiation by the initial state particles before the collision or by the particles produced in the Z^0 decay distorts the resonance shape leading to measurable quantities (σ_{peak} , $\sqrt{s(\sigma_{peak})}$, Γ_Z) that deviate from the tree-level theoretical expectations. The distributions of the final state fermions like acolinearity, acoplanarity, energy spectra, etc., are also influenced by the initial or final state radiation of soft and hard photons.

4.2.1 Initial State Radiation

If an incident beam particle of energy E_b radiates a photon of energy k, the centre of mass energy available in the $e^+ e^-$ collision changes as $s \longrightarrow s' = s(1 - \frac{k}{E_b})$. The measured lineshape of the Z^0 resonance can be modelled as the convolution integral of the lowest order cross-section $\sigma^0(s)$ with the function f(k,s) describing the radiative processes:

$$\sigma_{meas}(s) = \int_{k_{min}}^{k_{max}} f\left(\frac{k}{E_b}, s\right) \; \sigma^0\left(s(1 - \frac{k}{E_b})\right) dk \qquad (4.4)$$

Within the resonance range, the energy of the initial state radiated photons is constrained by the resonance shape due to the fact that radiation of hard photons shifts the centre of mass energy of the annihilation process to values of lower cross-section. The energy of the radiated photons must be such that the centre of mass energy after the radiation is still "on-resonance".

In the simplest approach, the function $f(k, s)$ describes the typical bremsstrahlung process and can be written as

$$f(k, s) \; dk \; \equiv \; \frac{2\alpha}{\pi} \left(\ln \frac{s}{m_e^2} - 1 \right) \frac{dk}{k} \qquad (4.5)$$

Imposing the constrain of staying "on-resonance" the last expression must be multiplied by $\sigma^0(s)$ describing the lowest order Breit-Wigner parametrization of the resonance. The differential cross-section for the bremsstrahlung process results

$$d\sigma_b \; \approx \; \frac{2\alpha}{\pi} \left(\ln \frac{s}{m_e^2} - 1 \right) \frac{dk}{k} \; \frac{\frac{\Gamma_Z^2}{4}}{\left(\sqrt{s} - M_Z\right)^2 + \frac{\Gamma_Z^2}{4}} \qquad (4.6)$$

Noticing that below the resonance

$$s \simeq 4E_b(E_b - k) \implies s - M_Z^2 \simeq 4E_b k \implies \sqrt{s} \simeq M_Z(1 - \frac{k}{2 \ E_b}) \qquad (4.7)$$

and introducing this simplification into the last expression, it is immediately seen that the bremsstrahlung spectrum on-resonance is modified from the typical 1/k dependence as

$$\frac{1}{k} \longrightarrow \frac{1}{k} \frac{1}{1 + \frac{4k^2}{\Gamma_Z^2}} \qquad (4.8)$$

showing clearly that the radiation is "damped" by the resonance shape softening the photon spectrum and introducing a dependence steeper than 1/k.

4.2.2   Effects In The Peak Cross-Section

Initial state radiation of soft photons leads to a reduction of about 30% in the peak cross-section, σ_{peak}, described typically by the simplified $\mathcal{O}(\alpha)$ expression ($s = M_Z^2$)

$$\Delta(\sigma_{peak}^0) = \frac{2\alpha}{\pi} \ln \left(\frac{M_Z}{\Gamma_Z}\right) \ln \left(\frac{M_Z^2}{m_e^2}\right) \qquad (4.9)$$

Assuming that soft photon emission obeys Poisson statistics (Bloch-Nordsieck theorem[20]) and that the probability of single photon emission goes to zero as its energy $k \to 0$, the radiation of multiple photons must be taken into account. This is accomplished with the exponentiation of the cross-section to include the corrections due to multiple soft photon radiation[21,22,23], modifying the cross-section at the peak as:

$$\sigma_{peak}^0 \longrightarrow \sigma_{peak}^0 \ (\ 1 + \Delta(\sigma_{peak}) \ ) \ \longrightarrow \ \sigma_{peak}^0 \left(\frac{\Gamma_Z}{M_Z}\right)^{\frac{2\alpha}{\pi} \ln \left(\frac{M_Z^2}{m_e^2}\right)} \qquad (4.10)$$

Also, the relation between $\sqrt{s(\sigma_{peak})}$ and M_Z is sizably influenced by the initial state bremsstrahlung that shifts the position of σ_{peak} from the lowest order Breit-Wigner value by a few dozens of MeV.

4.2.3 Final State Radiation

In this case the photon spectrum is not constrained by the resonance shape. As shown in ref.[21], the energy spectrum of the radiated photon is modified from the typical $1/k$ dependence to

$$\frac{1}{k} \longrightarrow \frac{1}{k} \left(1 - \frac{k}{E_b} + \frac{k^2}{2E_b^2}\right) \qquad (4.11)$$

which is harder than the $1/k$ spectrum.

4.2.4 Detectability of Radiated Photons

It can be shown that the angle $\theta_{p\gamma}$ between the radiated photon and the emitting particle follows in good approximation the law $\left(\gamma \simeq \frac{E_p}{M_p}\right)$

$$\frac{dN}{d\Omega} \sim \frac{\theta_{p\gamma}^2}{\left(\theta_{p\gamma}^2 + \frac{1}{\gamma^2}\right)^2} \qquad (4.12)$$

While for an emitting final state muon $(\gamma_\mu \simeq 460)$ this expression simplifies to

$$\frac{dN}{d\Omega} \sim \frac{1}{\theta_{p\gamma}^2} \qquad (4.13)$$

for an emitting final state tau $(\gamma_\tau \simeq 25)$ the same is no longer valid and a "shoulder effect" with maximum at

$$\theta_{max} \approx \frac{2}{\gamma_\tau} \qquad (4.14)$$

should be considered. Then, hard final state radiated photons can be measured with angular distributions roughly following that of the radiating particles $(1 + \cos^2 \theta)$.

As will be seen in next chapters, about 40% of τ leptons decay into final states with photons surrounding a charged track. Then, a good knowledge of the final state radiation spectrum is required to disentangle the photons from π^0 decays and the radiative photons.

4.3　Electroweak Corrections

4.3.1　s-dependent width, $\Gamma_Z(s)$

The lowest order width of the Z^0 boson resonance, Γ_Z^0, is related to the imaginary part of the Z^0 propagator through the one-loop weak corrections of the self-energy (Π^Z) type, through [22]

$$\Pi^Z \simeq \frac{1}{s - M_Z^2 + i M_Z \Gamma_Z^0} \quad , \quad M_Z \Gamma_Z^0 = Im\left\{\Pi^Z(s = M_Z^2)\right\} \tag{4.15}$$

The width is computed in lowest order to be

$$\Gamma_Z^0(f\bar{f}) = \sum_f N_C^f \frac{\alpha}{3} M_Z \sqrt{1 - 4\mu_f}\,[\, v_f^2\,(1 + 2\mu_f)\, +\, a_f^2\,(1 - 4\mu_f)\,] \tag{4.16}$$

with

$$N_c^f = 1\,,\, f = lepton \tag{4.17}$$

$$N_c^f = 3\,,\, f = quark \tag{4.18}$$

$$\mu_f = \left(\frac{m_f}{M_Z}\right)^2 \ll 1 \tag{4.19}$$

On-resonance, the lowest order cross-section for massless fermion pair production is ruled by the Z^0 exchange diagram of order $\mathcal{O}(1)$, whereas in the "continuum" region (γ exchange) it is of order $\mathcal{O}(\alpha^2)$. If first order corrections $\mathcal{O}(\alpha)$ are to be included in the cross-section computation, the total width value computed up to order α must be used. As Γ_Z is related to the imaginary part of the Z^0 self energy (one-loop correction to the propagator), then 2-loop corrections to the propagator must be taken into account in the resonance region.

"Non-photonic" electroweak corrections play an important role in the correct evaluation of the higher order value of the width, Γ_Z. They are mainly vertex corrections, self-energies and box diagrams. The latter can be neglected in the resonance region, and vertex corrections affect the couplings v_f, a_f of the Z^0 boson to the fermions, which are well parametrized by energy dependent form-factors. The main corrections come from the 2-loop self-energy diagrams and involve s-dependent corrections to the propagator.

It has been shown that the s dependence of the 2-loop corrections to the Z^0 propagator is well described near the resonance by the replacement

$$\frac{1}{s - M_Z^2 + iM_Z\Gamma_Z} \implies \frac{1}{s - M_Z^2 + is\frac{\Gamma_Z}{M_Z}} \qquad (4.20)$$

containing the crucial weak corrections that must be used to interpret the measurements of the Z^0 width and cross-section. Other sizable corrections to the Z^0 width come from:

- QED corrections to the decay $Z^0 \to f\bar{f}$

- QCD corrections to the decay $Z^0 \to q\bar{q}$

Altogether, besides the introduction of a Breit-Wigner form with an s-dependent width,

$$\Gamma_Z(s) = \frac{s}{M_Z^2}\Gamma_Z \qquad (4.21)$$

the other corrections can be written as[22]

$$\Gamma_Z = \Gamma_Z^0 \left[1 + \delta_{QCD} + \delta_{QED} + \delta_V + \delta_{Hff} \right] \qquad (4.22)$$

where δ_V groups all weak vertex corrections affecting the couplings, δ_{Hff} contains the effects on the Z^0 width of the Higgs boson, and by far the two main corrections are

$$\delta_{QCD} \simeq \frac{\alpha_s(M_Z^2)}{\pi} + \left(\frac{\alpha_s(M_Z^2)}{\pi}\right)^2 (1.98 - 1.15N_f) + \mathcal{O}(\alpha_s^3) \qquad (4.23)$$

$$\delta_{QED} \simeq \frac{3\alpha}{4\pi} Q_f^2 \qquad (4.24)$$

As M_Z is an experimentally determined quantity needed for the completion of the set of input parameters to be used in the renormalization scheme, and as its value can be extracted from the resonance shape measurement (related to the peak cross-section), it is then of crucial importance the knowledge of the accurate value of the width Γ_Z having a direct effect on the displacement of the measured value of the peak cross-section.

4.4 Z^0 Resonance Parametrization

In the last decade, several calculations were successfully made to estimate the effects of radiative corrections up to $\mathcal{O}(\alpha^2)$. The following (approximated) expressions reproduce with high accuracy the Z^0 resonance characteristics and include most of the effects mentioned or described above, and are particulary useful for experimental calculations concerning the processes $Z^0 \to f\bar{f}$.

4.4.1 $\sigma(s)$, Production Cross-Section

$$\sigma^f(s) = \sigma^f_{peak} \frac{s\Gamma_Z^2}{\left(s - M_Z^2\right)^2 + \frac{s^2}{M_Z^2}\Gamma_Z^2} \tag{4.25}$$

$$\Gamma_Z(s) = \frac{s}{M_Z^2}\Gamma_Z \tag{4.26}$$

4.4.2 σ_{peak}, Peak Cross-Section

$$\sigma^f_{peak} = \sigma^0_{peak}\left(\frac{\Gamma_Z}{M_Z}\right)^\beta \tag{4.27}$$

$$\sigma^0_{peak} = \frac{12\pi}{M_Z^2} \frac{\Gamma_{ee}\Gamma_{ff}}{\Gamma_Z^2} \tag{4.28}$$

4.4.3 $s^{1/2}(\sigma_{peak})$, Peak Cross-Section position

$$\sqrt{s(\sigma_{peak})} = M_Z + \frac{\pi}{8}\beta\Gamma_Z - \frac{\Gamma_Z^2}{2M_Z} \tag{4.29}$$

4.4.4 β, virtual radiator

$$\beta = \frac{2\alpha}{\pi}\left(\ln\frac{M_Z^2}{m_e^2} - 1\right) \tag{4.30}$$

4.5 Precision Measurements

4.5.1 Lowest order relations

In the framework of the Standard Model the four fermion interaction with Z^0 exchange is written at tree level as

$$M_{if} \sim G_\mu M_Z^2 \left[\mathcal{J}_i^3 - 2 \sin^2 \theta_w \, \mathcal{J}_i^{em} \right] \frac{1}{s - M_Z^2 + i M_Z \Gamma_Z} \left[\mathcal{J}_f^3 - 2 \sin^2 \theta_w \, \mathcal{J}_f^{em} \right] \tag{4.31}$$

with $\mathcal{J}^3, \mathcal{J}^{em}$ respectively the weak and electromagnetic components of the initial and final state fermion current. The weak mixing angle $\sin^2 \theta_w$ is defined by any of the following expressions,

$$\sin^2 \theta_w = \frac{\pi \, \alpha}{\sqrt{2} \, G_\mu \, M_W^2} \tag{4.32}$$

$$\sin^2 \theta_w \, \cos^2 \theta_w = \frac{\pi \, \alpha}{\sqrt{2} \, G_\mu \, M_Z^2} \tag{4.33}$$

$$\sin^2 \theta_w = 1 - \frac{M_W^2}{M_Z^2} \tag{4.34}$$

as a function of M_W and of the precisely measurable quantities:

- $\alpha = \frac{1}{137.03604(11)}$, from Thompson scattering

- $G_\mu = 1.16344(11) \cdot 10^{-5}$, from muon lifetime

- $M_Z = 91.17 \pm 30$ MeV, measured at Z scan (LEP,SLC)

4.5.2 Δr

The above lowest order expressions must be modified to include the effect of the radiative corrections. The QED and weak radiative corrections are taken into account by defining the factor Δr, absorbing the effects of the virtual quantum corrections (loops, self energies, vertex, ...) to the lowest order graphs. In the renormalization scheme commonly used, Δr is a function of the input parameters:

$$\Delta r \equiv \Delta r \left(M_{Higgs}, M_{top}, M_Z, \alpha, G_\mu, m_q\right) \tag{4.35}$$

It can be shown that the full effect of the radiative corrections results from a series of powers of Δr, yielding

$$1 + \Delta r + (\Delta r)^2 + ... \longrightarrow \frac{1}{1 - \Delta r} \tag{4.36}$$

The expressions 4.32, 4.33, modified to include the factor Δr become:

$$\sin^2 \theta_w = \frac{\pi \, \alpha}{\sqrt{2} \, G_\mu \, M_W^2 \, (1 - \Delta r)} \tag{4.37}$$

$$\sin^2 \theta_w \, \cos^2 \theta_w = \frac{\pi \, \alpha}{\sqrt{2} \, G_\mu \, M_Z^2 \, (1 - \Delta r)} \tag{4.38}$$

The main contributions to Δr come from fermion loops in the γ, Z, W propagators (boson self-energies) and from vertex corrections.

4.5.3 $\Delta \alpha$

The effect of fermion loops in the photon propagator is the running of the QED coupling constant, exhibiting a strong variation from $q^2 = 0$ to $q^2 = M_Z^2$. This variation is written as[30]:

$$\Delta \alpha = \frac{\alpha}{3\pi} \sum_{leptons} Q_l^2 \left[\ln\left(\frac{m_l^2}{q^2}\right) - \frac{5}{3} \right] + \Delta \alpha_{hadrons} \tag{4.39}$$

with

$$\alpha(M_Z) = \frac{\alpha}{1 - \Delta \alpha} \tag{4.40}$$

4.5.4 $\Delta\rho$

A set of important contributions to Δr come from the virtual radiative corrections due to the top quark and originating at the $t\bar{t}$ loop in the Z propagator and to $t\bar{b}$ loop in the W propagator. Also, as pointed out in [30], the vertex corrections from the diagrams shown in figure 4.2, contribute significantly to Γ_Z and $\Gamma_{b\bar{b}}$.
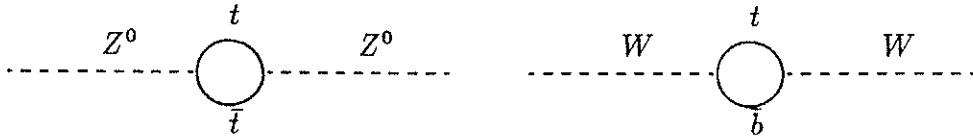
Figure 4.1: Top quark effects in the Z^0,W self energies
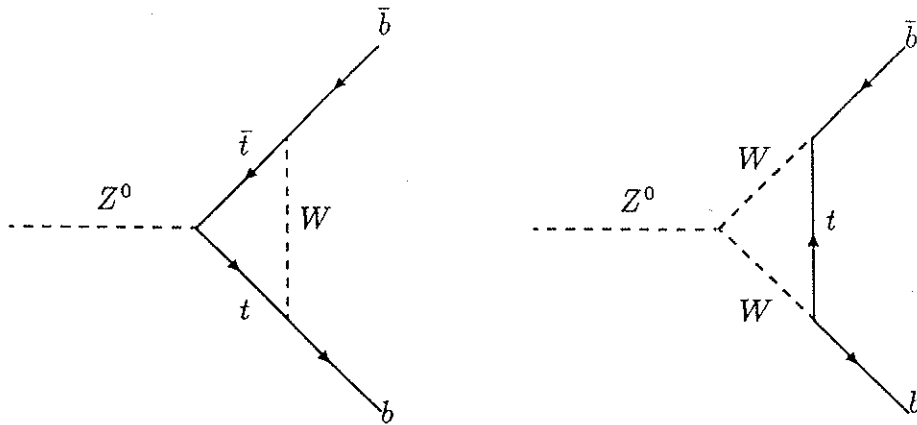
Figure 4.2: Vertex corrections due to top quark, affecting Γ_Z and $\Gamma_{b\bar{b}}$

The expression 4.31, modified to include the electroweak corrections (excluding the pure QED corrections) is written as[32,33]

$$M_{if} \sim G_\mu \, M_Z^2 \, \rho_{if} \left[\mathcal{J}_i^3 \; - \; 2 \, \kappa_i \, \sin^2 \theta_w \, \mathcal{J}_i^{em} \right] \frac{1}{s - M_Z^2 + i \frac{s}{M_Z} \Gamma_Z} \left[\mathcal{J}_f^3 \; - \; 2 \, \kappa_f \, \sin^2 \theta_w \, \mathcal{J}_f^{em} \right]$$

(4.41)

with

$$\rho_{if} = 1 + \Delta \rho_{if}$$

(4.42)

$$\kappa_{i,f} = 1 + \Delta \kappa_{i,f}$$

(4.43)

The correction $\Delta \rho_{if}$, absorbing the terms due to the top quark and Higgs boson contributions to the radiative corrections, respectively $\Delta \rho_{top}, \Delta \rho_{Higgs}$, can be written as[32,33]

$$\Delta \rho_{if} \;=\; \underbrace{\Delta \rho_{top} \;+\; \Delta \rho_{Higgs}}_{\Delta \rho} \;+\; h.c.$$

(4.44)

with

$$\Delta \rho_{top} \;\simeq\; \frac{3 \, G_\mu}{8 \, \pi^2 \, \sqrt{2}} \, m_t^2 \;+\; \mathcal{O}[(G_\mu m_t^2)^3]$$

(4.45)

$$\Delta \rho_{Higgs} \;\sim\; \ln \left(\frac{M_{higgs}^2}{M_W^2} \right)$$

(4.46)

and in the expression 4.45, logarithmic terms in $\frac{m_t^2}{M_W^2}$ have been neglected. In good approximation, the following expressions are valid:

$$\rho_{if} \;\simeq\; 1 \;+\; \Delta \rho$$

(4.47)

$$\kappa_{i,f} \;\simeq\; 1 \;+\; \frac{\cos^2 \theta_w}{\sin^2 \theta_w} \, \Delta \rho$$

(4.48)

and as shown in ref.[32], the relation between Δr, $\Delta \alpha$ and $\Delta \rho$ can be expressed as

$$\frac{1}{1 - \Delta r} \;=\; \frac{1}{1 - \Delta \alpha} \, \frac{1}{1 + \frac{\cos^2 \theta_w}{\sin^2 \theta_w} \Delta \rho} \;+\; small \; terms$$

(4.49)

or equivalently

$$\Delta r = \Delta \alpha - \frac{\cos^2 \theta_w}{\sin^2 \theta_w} \, \Delta \rho \;+\; small \; terms$$

(4.50)

Notice the high sensitivity of Δr to the top quark mass m_t, through the term $\Delta \rho$ ($\frac{\cos^2 \theta_w}{\sin^2 \theta_w} \approx 3.3$).

4.5.5 $\overline{\sin^2 \theta_w}$

Defining $\overline{\sin^2 \theta_w}$ as the effective weak mixing angle, measured at the $Z^0 \to f\bar{f}$ vertex with the Z^0 produced on-shell,

$$\overline{\sin^2 \theta_w} \equiv \kappa_{i,f} \sin^2 \theta_w \tag{4.51}$$

the expression 4.41 can be re-written as

$$M_{if} \sim G_\mu \, M_Z^2 \, \rho_{if} \left[\mathcal{J}_i^3 - 2 \, \overline{\sin^2 \theta_w} \, \mathcal{J}_i^{em} \right] \frac{1}{s - M_Z^2 + i \frac{s}{M_Z} \Gamma_Z} \left[\mathcal{J}_f^3 - 2 \, \overline{\sin^2 \theta_w} \, \mathcal{J}_f^{em} \right] \tag{4.52}$$

Expressions 4.32, 4.33, and 4.34 become

$$\overline{\sin^2 \theta_w} = \frac{\pi \, \alpha}{\sqrt{2} \, G_\mu \, M_W^2 \, (1 - \overline{\Delta r})} \tag{4.53}$$

$$\overline{\sin^2 \theta_w} \, \overline{\cos^2 \theta_w} = \frac{\pi \, \alpha(M_Z)}{\sqrt{2} \, G_\mu \, M_Z^2 \, \rho} \tag{4.54}$$

$$\overline{\sin^2 \theta_w} = 1 - \frac{M_W^2}{\rho \, M_Z^2} \tag{4.55}$$

with $\overline{\Delta r} = \Delta \alpha - \Delta \rho$, $\rho = 1 + \Delta \rho$ with $\Delta \rho$ as defined in the previous section. The relation between the 2 definitions of weak mixing angle and the term $\Delta \rho$ is given by[32]

$$\overline{\sin^2 \theta_w} \simeq \sin^2 \theta_w + \cos^2 \theta_w \, \Delta \rho \tag{4.56}$$

4.5.6   The Improved Born Approximation

Using the expressions of last sections, the improved Born approximation modifies the lowest order expressions to include the electroweak radiative corrections but conserving the simplified form of the Born terms and expressions. It consists in considering the Born expressions with the running α instead of fixed α, the propagator of the Z^0 with an s-dependent width, the presence of the parameter ρ multiplying G_μ and the use of the effective weak mixing angle $\overline{\sin^2 \theta_w}$ or equivalently the effective couplings of the Z^0 to the fermions. Technically, it consists of making the following replacements in the lowest order expressions:

$$\alpha \longrightarrow \alpha(M_Z) \tag{4.57}$$

$$\Gamma_Z \longrightarrow \frac{s}{M_Z} \Gamma_Z \tag{4.58}$$

$$G_\mu \longrightarrow G_\mu\, \rho \tag{4.59}$$

$$\sin^2 \theta_w \longrightarrow \overline{\sin^2 \theta_w} \tag{4.60}$$

The four fermion interaction via Z^0 exchange written in the context of the improved Born approximation is shown in equation 4.52. As an example, the partial width of the Z^0 into fermion pairs, written as

$$\Gamma_{ff} = \frac{G_\mu\, M_Z^3}{24\,\pi\,\sqrt{2}} \left[1 + \left(1 - 4\,|Q_f|\,\sin^2\theta_w \right)^2 \right] (1 + \delta) \tag{4.61}$$

with

$$\delta = \begin{cases} \left(1 + \frac{3\,\alpha}{4\,\pi}\, Q_f^2 \right) & leptons \\ 3\left(1 + \frac{3\,\alpha}{4\,\pi}\, Q_f^2 \right)\left(1 + \frac{\alpha_s(M_Z)}{\pi} \right) & quarks \end{cases} \tag{4.62}$$

becomes in the improved Born approximation

$$\Gamma_{ff} = \frac{G_\mu\, \rho\, M_Z^3}{24\,\pi\,\sqrt{2}} \left[1 + \left(1 - 4\,|Q_f|\,\overline{\sin^2\theta_w} \right)^2 \right] (1 + \delta) \tag{4.63}$$

From the this expression, using the result of equation 4.54, the relation between the partial width (measurable quantity) and the effective weak mixing angle is obtained:

$$\Gamma_{ff} = \frac{\alpha(M_Z)\, M_Z}{48\,\sin^2\theta_w\,\cos^2\theta_w} \left[1 + \left(1 - 4\,|Q_f|\,\overline{\sin^2\theta_w} \right)^2 \right] (1 + \delta) \tag{4.64}$$

Bounds on the top quark mass can be obtained using the last expressions and the value of Γ_{ff} measured at LEP.

Chapter 5

τ DECAY PHYSICS

The τ lepton is kinematically allowed to decay into lighter leptonic partners (electrons and muons) as well as into hadronic pseudoscalar and vector states (mesons and resonances). The study of the branching ratios into leptonic final states allows direct checks on universality, Lorentz structure of the decay vertex $\tau - W - \nu_\tau$ and setting bounds on the tau neutrino (ν_τ) mass. Measurement of the multi-π, multi-π^0 decay modes of the τ allows studies on the validity of PCAC,CVC "theorems" and the measurement of rare multi-pion decay modes allows to set upper limits on the tau neutrino mass. Measurement of the QCD scale parameter, $\Lambda_{\overline{MS}}$ from τ decays, is a direct consequence of the processes at the $u - W - d_C$ vertex.

Besides, measurements on multi-lepton decay modes allow the establishment of limits on lepton flavour violation and measurement of rare multi-π, multi-π^0 modes allow checks on the existence of second-class currents strongly suppressed in the framework of the Standard Model.

The topics discussed in this chapter are extensively treated in [2,7,37,38,39,40,41].

5.1 Decay Mechanism

In the framework of the Standard Model of Electroweak Interactions, the τ lepton decay proceeds via the W-boson emission diagram (fig. 5.1) The lagrangian term describing the W-boson coupling to the fermionic currents can be written as

$$\mathcal{L}_{CC}^\tau = \frac{g}{2\sqrt{2}} \, [\, \sum_l \bar{\nu}_l \, \gamma^\mu \, (\, 1 - \gamma_5 \,) \, l \, + \, \bar{u} \, \gamma^\mu \, (\, 1 - \gamma_5 \,) \, d_C \,] \, W_\mu \qquad (5.1)$$

with $d_C = d \, \cos\theta_C + s \, \sin\theta_C$. The leptonic weak current $\mathcal{J}_{lept}^\mu$
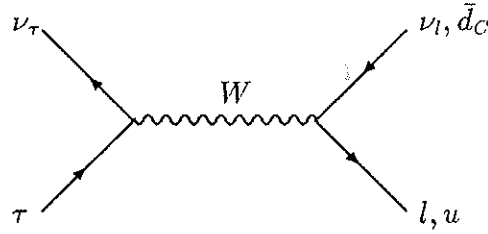
Figure 5.1: τ decays via W boson emission with leptonic (l=e,μ) or hadronic ($d_C = d \cos\theta_C + s \sin\theta_C$) final states

$$\mathcal{J}^\mu_{lept} = \bar{\nu}_l \, \gamma^\mu \, (\, 1 - \gamma_5 \,) \, l \quad , \qquad l = (e, \mu, \tau) \tag{5.2}$$

exhibits the V-A Lorentz structure of the (l, ν_l) weakly interacting doublet. Neglecting the masses one would expect, based on the diagram above, a branching ratio

$$BR(\tau^- \rightarrow \nu_\tau \, l^- \, \bar{\nu}_l \,) \simeq 20\% \tag{5.3}$$

due to the 3-coloured quarks coupling the W boson on the lower weak vertex of the diagram and that

$$R_H = \frac{\Gamma(\tau^- \rightarrow \nu_\tau l^- \bar{\nu}_l)}{\Gamma(\tau^- \rightarrow \nu_\tau + hadrons)} \simeq \frac{1}{N_C} \quad , \quad (N_C = 3) \tag{5.4}$$

5.2   Leptonic τ Decays $(\tau^- \rightarrow \nu_\tau \, l^- \, \bar{\nu}_l)$

The partial width for the process $\tau^- \rightarrow \nu_\tau \, l^- \, \bar{\nu}_l$, (l=e,$\mu$), asuming massless neutrinos, is [36]:

$$\Gamma(\tau^- \rightarrow \nu_\tau l^- \bar{\nu}_l) \simeq \frac{G_\mu^2 m_\tau^5}{192\pi^3} \, f(\frac{m_l^2}{m_\tau^2}) \left[1 + \frac{3}{5} \frac{m_\tau^2}{M_W^2} \right] \left[1 + \frac{\alpha}{2\pi}(\frac{25}{4} - \pi^2) \right] \tag{5.5}$$

where

$$f(y) = 1 - 8y + 8y^3 - y^4 - 12 \, y^2 \, \ln y \quad , \qquad y = \frac{m_l^2}{m_\tau^2} \tag{5.6}$$

is the correction factor accounting for the phase-space. The QED and weak radiative corrections enter in the terms between square brackets, and they are mainly dominated by the "running" of the Fermi constant G_μ normally defined at the energy scale of the muon decay processes ($Q^2 = m_\mu^2$), that must be "rescaled" to tau decay energy range ($Q^2 = m_\tau^2$). Also the QED running coupling constant is defined as $\alpha \equiv \alpha(m_\tau)$. Such corrections are small:

$$\left[1 + \frac{3}{5}\frac{m_\tau^2}{M_W^2} \right] \left[1 + \frac{\alpha}{2\pi}(\frac{25}{4} - \pi^2) \right] \simeq 0.996 \tag{5.7}$$

5.2.1 Universality

Measuring accurately the τ decays into l=e,μ stringent limits on lepton universality can be established by observing that

$$\frac{\Gamma(\tau^- \to \nu_\tau \mu^- \bar{\nu}_\mu)}{\Gamma(\tau^- \to \nu_\tau e^- \bar{\nu}_e)} = \left(\frac{g_\mu}{g_e} \right)^2 \frac{f(\frac{m_\mu^2}{m_\tau^2})}{f(\frac{m_e^2}{m_\tau^2})} \longrightarrow 0.973 \tag{5.8}$$

with g_μ, g_e coming from the lagrangean definition of equation 5.1. The experimental values extracted so far from the τ and π decays are

$$\left. \left| \frac{g_\mu}{g_e} \right| \right|_\tau = 1.023 \pm 0.017 \qquad (\tau \ decay) \tag{5.9}$$

$$\left. \left| \frac{g_\mu}{g_e} \right| \right|_\pi = 1.006 \pm 0.006 \qquad (\pi \ decay) \tag{5.10}$$

5.2.2 Lorentz Structure Of The Vertex $\tau - \nu_\tau - W$

Considering the leptonic decays $\tau^- \to \nu_\tau l^- \nu_l$, neglecting final state lepton masses and radiative corrections, and assuming a V-A structure for the vertex $l^- - \nu_l - W$ ($l = e, \mu$), the energy distribution of the l^- in the τ rest frame can be written as

$$\frac{1}{\Gamma}\frac{d\Gamma}{dx} \simeq x^2 \left[3(1 - x) + 2\rho \left(\frac{4}{3}x - 1 \right) \right] \tag{5.11}$$

with $x = \frac{E_l}{E_{max}}$. Assuming for the $\tau - \nu_\tau - W$ decay vertex a mixed Lorentz structure of the type

$$\alpha(V - A) \; + \; \beta(V + A) \tag{5.12}$$

the Michel parameter (ρ) can be written as

$$\rho \; = \; \frac{3}{4} \frac{\alpha^2}{\alpha^2 + \beta^2} \tag{5.13}$$

The averaged measurement of the Michel parameter from the study of lepton energy spectra in the τ decay modes into electron and muon is

$$< \rho > = 0.70 \pm 0.05 \tag{5.14}$$

excluding pure V+A,V,A types of vertex, leaving neverthless room for a V+A mixing in a dominant V-A Lorentz structure (remeber: pure V-A would lead to $\rho = 0.75$). A very poor upper limit (compared with μ decay) for the mixing is, at 95% CL

$$\frac{\beta}{\alpha} < 0.50 \tag{5.15}$$

5.2.3 τ Lifetime, Universality and V-A

Tests on lepton universality (same coupling strength of the electroweak bosons to each leptonic current) can be made by comparing the μ decay and τ leptonic decays. Assuming the leptonic doublet structure characteristic of the Standard Model, μ decay proceeds via the same graph as τ decay, changing the τ doublet by the muon doublet in the upper part of the decay diagram of figure 5.1 and allowing one only possible final state $\mu \to \nu_\mu e \bar{\nu}_e$ at the lower vertex. Then,

$$\frac{BR(\tau^- \to \nu_\tau e^- \bar{\nu}_e)}{BR(\mu^- \to \nu_\mu e^- \bar{\nu}_e)} \frac{\tau_\mu}{\tau_\tau} \; = \; \left(\frac{g_\tau}{g_\mu}\right)^2 \left(\frac{m_\tau}{m_\mu}\right)^5 \frac{\left[1 + \frac{3}{5}\frac{m_\tau^2}{M_W^2}\right]}{\left[1 + \frac{3}{5}\frac{m_\mu^2}{M_W^2}\right]} \frac{\left[1 + \frac{\alpha(m_\tau^2)}{2\pi}\left(\frac{25}{4} - \pi^2\right)\right]}{\left[1 + \frac{\alpha(m_\mu^2)}{2\pi}\left(\frac{25}{4} - \pi^2\right)\right]} \tag{5.16}$$

Present data from τ and μ lifetime direct measurements give

$$\left|\frac{g_\tau}{g_\mu}\right|_{lifetime} = 0.96 \pm 0.02 \tag{5.17}$$

while data from CERN $p\bar{p}$ Collider studies of the decays $W^- \rightarrow l^- \bar{\nu}_l$ establishes

$$\left|\frac{g_\mu}{g_e}\right|_{W^- \rightarrow l^- \bar{\nu}_l} = 1.00 \pm 0.07 \pm 0.04 \qquad (5.18)$$

$$\left|\frac{g_\tau}{g_e}\right|_{W^- \rightarrow l^- \bar{\nu}_l} = 1.01 \pm 0.10 \pm 0.06 \qquad (5.19)$$

5.3 Hadronic τ Decays ($\tau^- \rightarrow \nu_\tau + hadrons$)

Hadronic final states from τ decays must obey the usual conservation laws of strong and electroweak processes. Assuming a V-A Lorentz structure in the vertex coupling the W boson to the $u - d_C$ quark current ($\mathcal{J}^\mu_{HADR}$), one can split the vector (V) and axial-vector(A) components of the quark current writing

$$\mathcal{J}^\mu_{hadr} = \mathcal{J}^\mu_{V,hadr} - \mathcal{J}^\mu_{A,hadr} \qquad (5.20)$$

Some constrains must be imposed to the hadronic final state:

• Due to angular momentum conservation the hadronic final state in τ decays can only have total angular momentum 0 or 1.

• Since the current $\mathcal{J}^\mu_{hadr}$ is charged, both V and A parts must be isovectors (I=1).

• Both V and A parts contain strangeness-conserving ($\Delta S = 0$) and strangeness-changing ($\Delta S = 1$) contributions.

• From the definition of G-parity and from the known parity of a system of n-mesons,

$$G(n\pi) = C(n\pi)(-1)^I = (-1)^n \qquad (5.21)$$

it follows that for a multi-pion final state the C-parity must be opposite of the G-parity.

As a vector(axial-vector) current transforms odd(even) under C (charge conjugation), the vector part of the hadronic current $\mathcal{J}^\mu_{V,hadr}$ is the responsible for τ decays into an even number of pions and the axial part of the hadronic current $\mathcal{J}^\mu_{A,hadr}$ is the responsible for τ decays into an odd number of pions.

Using the constraints above, the following J^P hadronic states can be expected in τ decays:

$J^P = 0^+ \implies SCALAR$

$J^P = 0^- \implies PSEUDOSCALAR$

$J^P = 1^- \implies VECTOR$

$J^P = 1^+ \implies AXIAL - VECTOR$

5.3.1   Pseudoscalar States $(J^P = 0^-)$

5.3.1.1   • $\tau \to \pi\nu_\tau$

This decay is "technically" similar (in terms of computation) to the decay $\pi \to \mu\nu_\mu$ by exploiting time reversal invariance and making the corresponding replacements.
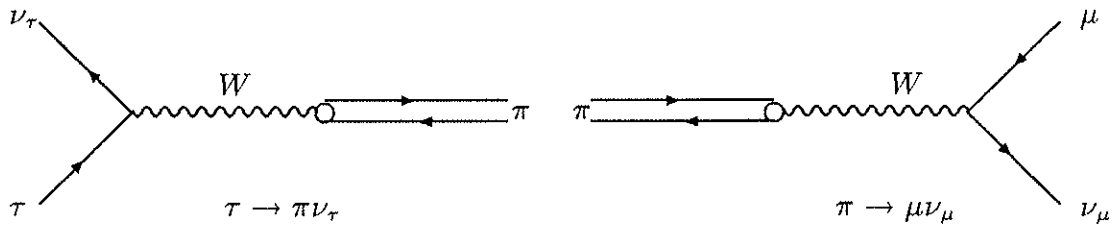
The decay width is

$$\Gamma(\tau \to \pi\nu_\tau) = \frac{G_\mu^2}{16\pi} \, f_\pi^2 \, \cos^2\theta_C \, m_\tau^3 \left(1 - \frac{m_\pi^2}{m_\tau^2} \right)^2 \tag{5.22}$$

and the theoretical expectation is

$$\frac{\Gamma(\tau \to \pi\nu_\tau)}{\Gamma(\tau \to \nu_\tau e^- \bar{\nu}_e)} \simeq 0.601 \tag{5.23}$$

5.3.1.2   • $\tau \to K \nu_\tau$

This decay is similar to the decay $\tau \to \pi \nu_\tau$ with the constraint of being Cabibbo suppressed. Besides, the pion "form-factor" (f_π) must be replaced by the kaon "form-factor" (f_K) to yield

$$\Gamma(\tau \to K \nu_\tau) = \frac{G_\mu'^2}{16\pi} \, f_K^2 \, \sin^2 \theta_C \, m_\tau^3 \left(1 - \frac{m_K^2}{m_\tau^2} \right)^2 \tag{5.24}$$

and the theoretical expectation is

$$\frac{\Gamma(\tau \to K \nu_\tau)}{\Gamma(\tau \to \nu_\tau e^- \bar{\nu}_e)} \simeq 0.039 \tag{5.25}$$

5.3.1.3   Meaurement of the Cabibbo angle, θ_C

A precise determination of the Cabibbo angle is possible with an accurate measurement of the last two decay modes. The ratio of the partial decay widths is

$$\frac{\Gamma(\tau \to K \nu_\tau)}{\Gamma(\tau \to \pi \nu_\tau)} = \tan^2 \theta_C \left(\frac{f_K}{f_\pi} \right)^2 \frac{\left(1 - \frac{m_K^2}{m_\tau^2} \right)^2}{\left(1 - \frac{m_\pi^2}{m_\tau^2} \right)^2} \tag{5.26}$$

5.3.2   Vector States ($J^P = 1^-$)

5.3.2.1   • $\tau \to \rho \nu_\tau$, $\rho \to \pi \pi^0$

The τ decay to non-strange isovector function is expected to be dominated by the ρ resonance. Invoking CVC (Conserved Vector Current), the decay width for this mode can be derived from analogy with the electromagnetic annihilation $e^+ e^- \to \rho$ to obtain

$$\Gamma(\tau \to \rho \nu_\tau) = \frac{G_\mu^2}{16\pi} \, \cos^2 \theta_C \, m_\tau^3 \, \frac{f_\rho^2}{m_\rho^2} \left(1 - \frac{m_\rho^2}{m_\tau^2} \right)^2 \left(1 + \frac{2m_\rho^2}{m_\tau^2} \right) \tag{5.27}$$

The theoretical expectation is

$$\frac{\Gamma(\tau \to \rho\nu_\tau)}{\Gamma(\tau \to \nu_\tau e^- \bar{\nu}_e)} \simeq 1.23 \tag{5.28}$$

5.3.2.2   • $\tau \to K^* \nu_\tau$, $K^* \to K\pi^0$

The $K - \pi^0$ system is analog to the $\pi\pi^0$ from the ρ resonance but Cabibbo suppressed. One can then expect

$$\Gamma(\tau \to K^* \nu_\tau) = \frac{G_\mu^2}{16\pi} \sin^2 \theta_C \, m_\tau^3 \, \frac{f_{K^*}^2}{m_{K^*}^2} \left(1 - \frac{m_{K^*}^2}{m_\tau^2} \right)^2 \left(1 + \frac{2m_{K^*}^2}{m_\tau^2} \right) \tag{5.29}$$

and

$$\frac{\Gamma(\tau \to K^* \nu_\tau)}{\Gamma(\tau \to \nu_\tau e^- \bar{\nu}_e)} \simeq 0.064 \tag{5.30}$$

5.3.2.3   • $\tau \to 2n\pi\nu_\tau$, $2n = N_{charged} + N_{neutral}$

These decays are like the ρ decay, estimated (not always a firm computation exists) from the CVC hyphotesis in analogy with the $e^+ e^- \to (2n\pi)^{0-charge}$ electromagnetic annihilation, and on some other theoretical assumptions. The main expected modes are $\tau \to \pi^- 3\pi^0 \nu_\tau$ and $\tau \to 3\pi^- \pi^0 \nu_\tau$ with decay widths

$$\frac{\Gamma(\tau \to \pi^- \pi^0 \pi^0 \pi^0 \nu_\tau)}{\Gamma(\tau \to \nu_\tau e^- \bar{\nu}_e)} \simeq 0.057 \tag{5.31}$$

$$\frac{\Gamma(\tau \to \pi^- \pi^+ \pi^- \pi^0 \nu_\tau)}{\Gamma(\tau \to \nu_\tau e^- \bar{\nu}_e)} \simeq 0.275 \tag{5.32}$$

5.3.3   Axial-Vector States $(J^P = 1^+)$

The theoretical predictions for these decays are much less based on robust theoretical basis. They are in some cases consistent with the data but in other cases, due to low statistics, the agreement is loose. Anyhow, experimental data serves as a stimulating way for checking the consistency of the theoretical predictions and for some decay modes it goes ahead of the (feasible) theoretical predictions. Some guesses can also be given, using PCAC (Pseudo Axial Conserved Current) assumptions and analogies with electromagnetic annihilation in the processes $e^+ e^- \to ((2n+1)\pi)^{0-charge}$.

5.3.3.1 • $\tau \rightarrow A_1 \nu_\tau$, $A_1 \rightarrow 3\pi$

The $J^P = 1^+$ decay mode is dominated by the $A_1(1260)$ resonance decaying in 3 pions. The theoretical predictions inspired in electromagnetic annihilation and on PCAC result in the following expression for the decay width

$$\Gamma(\tau \rightarrow A_1\nu_\tau) = \frac{G_\mu^2}{16\pi} \cos^2\theta_C \, m_\tau^3 \, \frac{f_{A_1}^2}{m_{A_1}^2} \left(1 - \frac{m_{A_1}^2}{m_\tau^2}\right)^2 \cdot \left(1 + \frac{2m_{A_1}^2}{m_\tau^2}\right) \qquad (5.33)$$

Setting (with theoretical prejudice) $\frac{f_\rho^2}{m_\rho^2} = \frac{f_{A_1}^2}{m_{A_1}^2}$ one expects

$$\Gamma(\tau \rightarrow A_1\nu_\tau) \simeq 0.37 \, \Gamma(\tau \rightarrow \rho\nu_\tau) \qquad (5.34)$$

$$\frac{\Gamma(\tau \rightarrow A_1\nu_\tau)}{\Gamma(\tau \rightarrow \nu_\tau e^- \bar{\nu}_e)} \simeq 0.46 \qquad (5.35)$$

which seems to agree with the experimental data analysed so far.

5.3.3.2 • $\tau \rightarrow 5\pi\nu_\tau$

Only very crude estimations can be given for this mode, experimental input is needed. The prediction is

$$\frac{\Gamma(\tau \rightarrow 5\pi\nu_\tau)}{\Gamma(\tau \rightarrow \nu_\tau e^- \bar{\nu}_e)} \simeq 0.03 \qquad (5.36)$$

5.3.3.3 • $\tau \rightarrow K\pi\pi\nu_\tau$

This mode is the Cabibbo supressed mode counterpart of the $\tau \rightarrow 3\pi\nu_\tau$ decay mode and the partial width can be estimated by the following relation

$$\Gamma(\tau \rightarrow K\pi\pi\nu_\tau) = tg^2\theta_C \, \Gamma(\tau \rightarrow \pi\pi\pi\nu_\tau) \simeq 0.025 \, \Gamma(\tau \rightarrow \nu_\tau e^- \bar{\nu}_e) \qquad (5.37)$$

An alternative method considers it as being a decay mode of the τ proceeding through the Q resonance, relating then this decay mode to the decay $\tau \rightarrow K^*\nu_\tau$.

5.3.4   Second-Class (G-Parity Violating) Currents

Second class weak currents are explained by making the asumption that strong isospin conservation is violated by the difference between the quark masses m_d and m_u. Such currents are strongly supressed in the framework of the Standard Model, and would manifest in τ decays by the existence of hadronic final states with G-parity values opposite to the ones exhibited by the hadronic final states related to the first class currents, which are characterized by the following spin-parity values[42]:

$$J^{PG} = \begin{cases} 0^{--} & (\pi) \\ 1^{-+} & (\rho) \\ 1^{+-} & (A_1) \\ 0^{++} & (exotic) \end{cases} \qquad (5.38)$$

Hadronic final states of opposite G-parity values would exhibit spin-parity values

$$J^{PG} = \begin{cases} 0^{-+} \\ 1^{--} \\ 1^{++} \\ 0^{+-} \end{cases} \qquad (5.39)$$

The measurement of hadronic final states with such G-parity values would be an indication of the existence of second-class currents or of G-parity violating mechanisms in the hadronic currents[43].

5.3.4.1   • $\tau^- \rightarrow \pi^- \eta \nu_\tau \ (J^{PG} = 0^{+-}, 1^{--})$

The $\pi\eta$ system has the parity

$$P(\pi\eta) \ = \ P(\pi)\, P(\eta)\, (-1)^J \ = \ (-1)\, (-1)\, (-1)^J \ = \ (-1)^J \qquad (5.40)$$

and its spin-parity values are then $J^P = 0^+, 1^-$. The G-parity of the η is

$$G(\eta) = C(\eta)(-1)^{I(\eta)} \quad , \quad C(\eta) = 1 \quad , \quad I(\eta) = 0 \implies G(\eta) = 1 \qquad (5.41)$$

and using the G-parity rule $G(n\pi) = (-1)^n$

$$G(\pi\eta) \ = \ G(\pi)\, G(\eta) \ = \ (-1)\, (+1) \ = \ -1 \qquad (5.42)$$

The $\pi\eta$ system, with spin-parity values $J^{PG} = 0^{+-}, 1^{--}$, exhibits G-parity opposite to that of a first class current. The measurement of this τ decay mode by HRS[44] with a branching fraction of $5.1\pm1.0\pm1.2$ % was not confirmed by other experiments. The upper limit for this decay is set to 2.1% at 90% Confidence Level[12].
Enhancement of the number of 1-prong or 3-prong τ decays, could be the manifestation of a non-standard G-parity violating mechanism with the existence of a decay

mode proceeding via η resonance formation and decay ($\eta \rightarrow \gamma\gamma$ or $\eta \rightarrow \pi^+\pi^-\pi^0$). The expectation of the branching ratio for this tau decay mode is[45]

$$B(\tau^- \rightarrow \pi\eta\nu_\tau) \simeq \left(\frac{m_d - m_u}{300\ MeV/c^2}\right)^2 B(\tau^- \rightarrow \pi^-\nu_\tau) \simeq 10^{-5} \qquad (5.43)$$

5.3.4.2 • $\tau^- \rightarrow \pi^-\omega\nu_\tau$

The ω resonance has well established spin-parity charge conjugation values $J^{PC} = 1^{--}$, $G(\omega) = -1$ and well established decay into 3 pions ($\omega \rightarrow \pi^+\pi^0\pi^-$). By analysing the 4-pion final states from τ decays proceeding from ω resonance formation and decay, no evidence was found so far for second class current in the $\omega\pi^-$ system.

5.4 $\Lambda_{\overline{MS}}$ Determination

The ratio between the leptonic and hadronic widths of the τ is theoretically predicted to be, in the $\overline{MS}$ renormalization scheme[41]

$$R_H = \frac{\Gamma(\tau \rightarrow \nu_\tau + hadrons)}{\Gamma(\tau \rightarrow \nu_\tau e\nu_e)} \approx 3r_H \left(1 + \frac{\alpha_s(m_\tau)}{\pi} + 5.2\left(\frac{\alpha_s(m_\tau)}{\pi}\right)^2 + 104\left(\frac{\alpha_s(m_\tau)}{\pi}\right)^3 + ...\right)$$

$$(5.44)$$

where $r_H = 1.0215 \pm 0.0050$ contains the efects of the electroweak corrections, and other non-negligible contributions to the calculation are not included. The total decay width of the τ written as

$$\Gamma_\tau = \Gamma(\tau \rightarrow \nu_\tau e\nu_e) + \Gamma(\tau \rightarrow \nu_\tau\mu\nu_\mu) + \Gamma(\tau \rightarrow \nu_\tau + hadrons) \qquad (5.45)$$

can be expressed in terms of the electron partial width and the ratio R_H defined above, as

$$\Gamma_\tau = \Gamma(\tau \rightarrow \nu_\tau e\nu_e)\ (1.9728 + R_H) \qquad (5.46)$$

using the theoretical prediction $\Gamma(\tau \rightarrow \nu_\tau\mu\nu_\mu) = 0.9728\ \Gamma(\tau \rightarrow \nu_\tau e\nu_e)$ due to the different masses of the muon and electron.

The determination of Γ_τ (from the τ lifetime measurement) and of $\Gamma(\tau \rightarrow \nu_\tau e\nu_e)$ (from the branching ratio measurement) allows the determination of the R_H value from experimental data, to be confronted with the theoretical expectations.

The experimental value for R_H, obtained after averaging on different methods of calculating the electron width in tau decays (direct measurement, from muon measurement or from lifetime measurement), is

$$R_H^{exp} = 3.54 \pm 0.08 \tag{5.47}$$

The above calculations to order α_s^3, make the R_H ratio strongly dependent on the QCD scale $\Lambda_{\overline{MS}}$. Expanding α_s in series of powers of $\ln(m_\tau/\Lambda_{MS})$ and using as input in the expression 5.44 the value R_H^{exp}, a determination of $\Lambda_{\overline{MS}}$ can be obtained in the range from 100 to 200 MeV.

5.5   Branching Ratios For τ Decays

τ DECAY MODE	BRANCHING RATIO (%)
$\tau \longrightarrow e\bar{\nu}_e\nu_\tau$	17.5$\pm$ 0.4
$\tau \longrightarrow \mu\bar{\nu}_\mu\nu_\tau$	17.8$\pm$ 0.4
$\tau \longrightarrow \rho\nu_\tau$	22.3$\pm$ 1.1
$\tau \longrightarrow \pi\nu_\tau$	10.8$\pm$ 0.6
$\tau \longrightarrow \pi\pi\pi\nu_\tau$	6.8 $\pm$ 0.6
$\tau \longrightarrow \pi\pi\pi\pi^0\nu_\tau$	4.4 $\pm$ 1.6
$\tau \longrightarrow \pi\pi^0\pi^0\nu_\tau$	7.5 $\pm$ 0.9
$\tau \longrightarrow \pi\pi^0\pi^0\pi^0\nu_\tau$	3.0 $\pm$ 2.7
$\tau \longrightarrow K^*\nu_\tau$	1.4 $\pm$ 0.3
$\tau \longrightarrow K\nu_\tau$	0.66$\pm$ 0.2
$\tau \longrightarrow K\pi\pi\nu_\tau$	0.3 $\pm$???
$\tau \longrightarrow \pi\omega\nu_\tau$	1.6 $\pm$ 0.5
$\tau \longrightarrow \pi\pi\pi\pi\pi\nu_\tau$	0.056$\pm$ 0.022

Table 5.1: World averaged measurements of main decay modes of τ lepton

Part II

Apparatus

LAYOUT OF THE LEP EXPERIMENTS

LEP

SPS

CERN

L3   P2

ALEPH   P4

P8   DELPHI

P6   OPAL
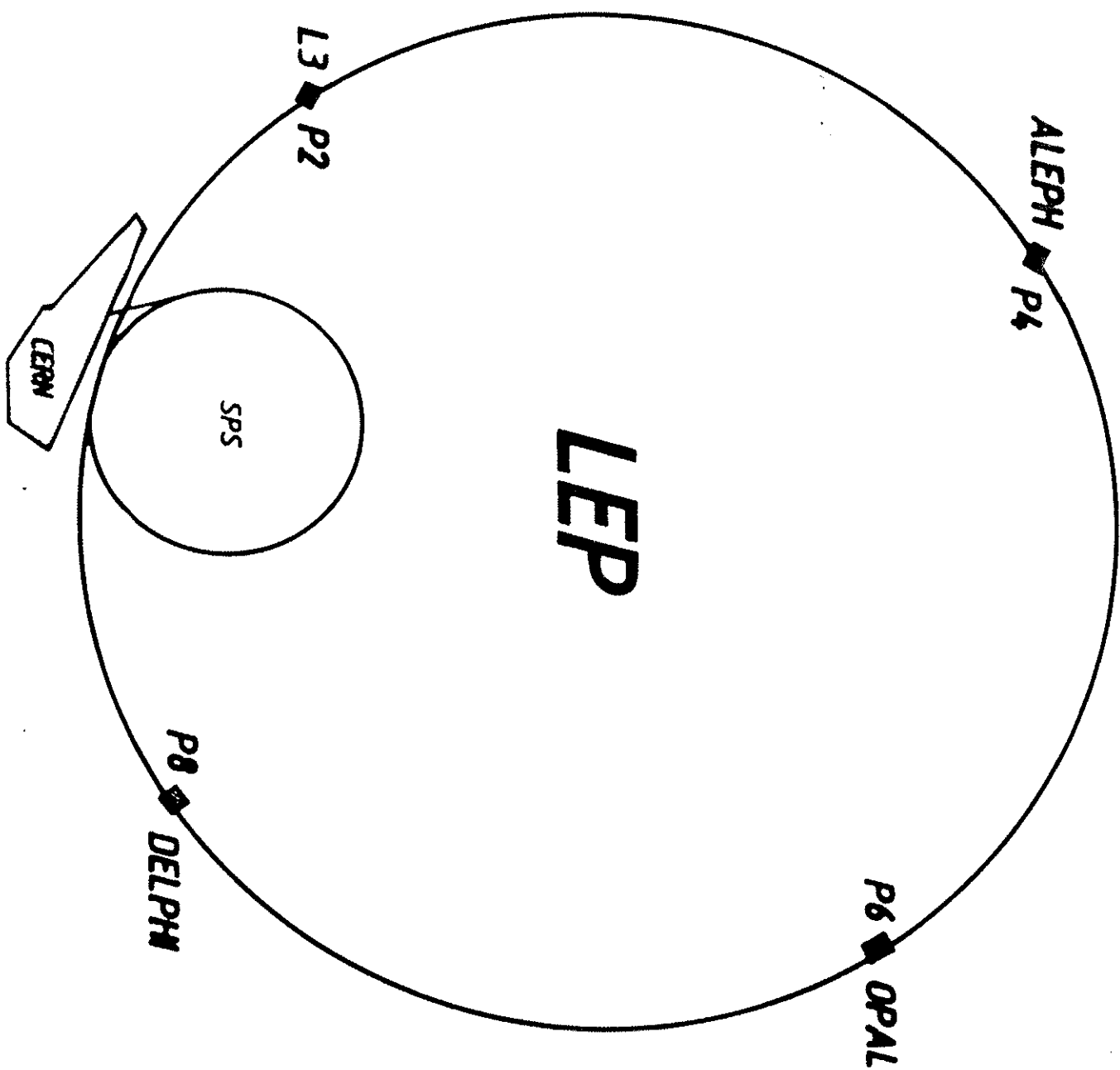
Chapter 6

ACELERATOR

LEP (Large Electron Positron) is a colliding beam facility at CERN . It is a storage ring designed to accelerate e^+ and e^- beams and make them collide at 4 interaction points surrounded by detectors. Each beam consists of 4 bunches of $5 \cdot 10^{11}$ particles travelling in a vacuum tube where the pressure is mantained at about 10^{-10} Torr. The beam particles are kept in their trajectories by a complex system of magnets (bending magnets, focusing quadrupoles, dipoles, sextupoles, etc.) positioned along the perimeter of the acelerator (26.7 Km). The frequency of revolution (f) of the circulating particles is about 10^4 Hz, meaning that the time interval between 2 bunch crossings at the experimental areas is 23 μs.

In the first phase of operation (LEP 100) the energy of each beam can be varied in the range from 20 to 55 GeV. During this period, the center of mass energy of the e^+e^- collisions produced at LEP is tuned to cover the Z^0 resonance ($\sqrt{s} \sim 91$ GeV), allowing the collection of $10^7 Z^0$ events per experiment. In a later stage of operation (LEP 200) the energy range will be extended to a maximum energy of 95 GeV per beam, to cover the center of mass energy threshold for W^+W^- production ($\sqrt{s} \simeq 160$ GeV) and beyond.

The focusing and bending elements of the beam optics system correcting for errors in position and angle induce betatron oscillations of the beam particles around the nominal orbit. It can be shown that the amplitude of such transversal oscilations can be described by a β function varying with s, the pathlength corresponding to a given orbit. An electron beam consists of many particles oscillating with different amplitudes (close orbits). The emittance ϵ is defined as the average area corresponding to all the trajectories in the phase space defined by the amplitude and beta values of the oscillations. It is of common use the assumption of gaussian density distributions for the transverse beam dimensions (horizontal,vertical) [1], with the rms values being

---

[1]The transverse bunch density is assumed to be $N_\pm \ e^{-\frac{x^2}{2\sigma_h^2}} \ e^{-\frac{y^2}{2\sigma_v^2}} / 2 \ \pi \ \sigma_h \ \sigma_v$

determined by

$$\sigma_{h,v} \; = \; \sqrt{\epsilon_{h,v} \; \beta_{h,v}} \tag{6.1}$$

The typical emittance and beta function values for the LEP machine are

$$\epsilon_h \; = \; 100 \; nm \; , \; \epsilon_v \; = \; 10 \; nm \; , \; \beta_h \; = \; 1.75 \; m \; , \; \beta_v \; = \; 7 \; cm \tag{6.2}$$

defining rms beam radii dimensions in the X (horizontal) and Y (vertical) directions

$$\sigma_x \; = \; 300 \; \mu m \tag{6.3}$$

$$\sigma_y \; = \; 10 \; \mu m \tag{6.4}$$

The rms bunch length along the Z (longitudinal) direction is

$$\sigma_z \; = \; 12 \; mm \tag{6.5}$$

The luminosity at each interaction point with $N_\pm$ particles per bunch and n_b bunches per beam is given by

$$L \; = \; \frac{N_\pm^2 \; f}{4 \; \pi \; n_b \; \sigma_x \; \sigma_y} \; \approx \; 1.6 \cdot 10^{31} \; cm^{-2} \; s^{-1} \tag{6.6}$$

The luminosity can be further improved by superconducting low-beta quadrupoles, placed a few meters away from the interaction point. Such quadrupoles, reduce the value of β_v to 4.2 cm, squeezing the beam dimensions near the experimental areas and improving the rate of collisions (beta squeeze).

The moving charged particles loose energy due to sinchroton radiation in the bending sections (arcs) of the ring with radius of curvature $\rho = 3096 \; m$. Defining r_e and m_e respectively as the classical radius and the electron mass, the sinchroton radiation loss per turn for $E_{beam} = 45.5$ GeV is given by [2]

$$E_{loss} = \frac{4\pi \; r_e \; m_e \; c^2 \; \gamma^4}{3} \frac{}{\rho} \; \simeq \; 140 \; MeV/particle/turn \tag{6.7}$$

These losses are restored by the 2 systems of 128 copper radiofrequency (RF) cavities fed by 16 klystrons (1 MW each) located in 2 opposite straight sections of the ring, which provide the accelerating electric field.

Due to the fact that a change in the energy of a particle describing a given close orbit implies a change of its reference trajectory [3], the energy distribution of the particles in the beam core is assumed to be Gaussian, and the beam energy spread can be shown to be

$$\frac{\sigma_{E_{beam}}}{E_{beam}} \; \approx \; \frac{1}{2} \sqrt{\frac{E_c}{E_{beam}}} \; \approx \; 0.6 \cdot 10^{-3} \tag{6.8}$$

with $E_c \simeq 70 \; KeV$ is the critical energy characteristic of the synchroton radiation spectrum for 45 GeV beam particles.

---

[2] $\gamma \; = \; \frac{E_{beam}}{m_e \; c^2}$

[3] At LEP, $\frac{ds}{s} \; \simeq \; \frac{dE}{E}$, with s,E respectively the length and energy for a given orbit

The determination of the beam energy is made by measuring the line integral of the magnetic field strength (B_{dipole}) over the dipole length (L_{mag}):

$$E_{beam} \simeq \int_0^{L_{mag}} B_{dipole} \, dz \simeq B_{dipole} \, L_{mag} \tag{6.9}$$

with the accuracy on the energy measurement given by

$$\frac{\Delta E_{beam}}{E_{beam}} \simeq \frac{\Delta B_{dipole}}{B_{dipole}} + \frac{\Delta L_{mag}}{L_{mag}} = \pm (2 + 1) \cdot 10^{-4} \tag{6.10}$$

The corresponding uncertainty in the centre of mass energy, at $\sqrt{s} = 45.5$ GeV, is approximately 20 MeV.

LEP 100 MACHINE PARAMETERS	
Maximum Energy	55 GeV
Dipole field	0.0645 Tesla
Injection energy	20 GeV
RF System	
Frequency	352 MHz
Peak voltage	400 MV
Length of 128 cavities	272 m
Peak power per klystrons	1 MW
Interaction Region	
Quadrupoles Position (Z)	± 3.5 m
β functions	$\beta_h=1.75$ m , $\beta_v=7$cm
RMS beam radii	$\sigma_x=300\mu$ m , $\sigma_y=10\mu$ m
RMS bunch length	$\sigma_z=12$ mm
RMS energy spread	$0.6 \cdot 10^{-3}$
Performance	
Current in 4 bunches	3 mA
Nominal Luminosity	$1.6 \cdot 10^{31}$ cm^{-2} s^{-1}

6.1   LEP Cycle

A cycle (*FILL*) of LEP operation can be divided in the following phases:

• During the filling time, beams are injected, ramped to the nominal energy of the fill and acumulated. The beam current varies from I_{min} to I_{max} in a time interval of less than 1 hour. LEP typical values of I_{max} are around 3 mA. During this period collimators are tuned up to the final settings.

• Only after the beam current reaches I_{max}, the data taking period in the detectors starts, with the raising of the high voltages. During this period, the beam currents decay exponentially like $e^{-\frac{t}{\tau_{beam}}}$ with typical values for τ_{beam} of some hours. Collisions with stable beams start a few minutes after the data taking period has started and the high voltages are at their nominal values.

• When the beam currents are close to I_{min}, the data taking period is finished for the fill, the beams are dumped and a new fill starts.

6.2   Machine Backgrounds

The main sources of background are:

I) *Low energy photons from synchroton radiation*. The synchroton radiation spectrum is characterized by the critical energy value [4]

$$E_c = \frac{3}{2} \frac{\lambda_{Comp}\; m_e\; c^2\; \gamma^3}{2\; \pi\; \rho} \tag{6.11}$$

Half of the radiation power is in quanta of energy $E_\gamma > E_c$. At 45 GeV, the critical energy in LEP is $E_c = 70$ KeV. The number of emitted photons is approximately $2 \cdot 10^3/turn \approx 2 \cdot 10^7\; s^{-1}$. These photons are emitted relative to the radiating particles at angles $\theta \sim \frac{1}{\gamma} \approx 10\; \mu rad$.

II) *Off − momentum particles*. High energy beam particles (e^+ or e^-) at energies below the nominal beam energy are commonly called off-momentum particles. These particles are originated in the bending sections of the acelerating system (energies 1% to 2 % below the beam energy) or by beam-gas bremsstrahlung, a few hundred meters away from the interaction points. These particles affect the trigger rates in the detector. Also, the rate of counts in the luminosity monitoring detectors (see next sections) at small angles near the beam line can be affected by off-momentum particles.

---

[4] $\lambda_{Comp} = \frac{h}{m_e\; c}$ is the Compton wavelength, h is the Planck constant

A complex system of collimators exists along the perimeter of the accelerator and near the experimental areas to reduce the machine backgrounds. The collimators are tuned during the setup of the beams, until the backgrounds are minimized in the interaction points.

The geometry and dimensions of the beam pipe surrounding the interaction regions play also an important role in the background rates.

6.3 Typical Rates

At LEP, the estimated rates of radiated photons and bremsstrahlung off-momentum electrons for beam energy values in the range 45 to 55 GeV are[46]:

- Number photons/second ($E_\gamma > 10\ KeV$) $\sim 10^{17}$

- Number e^-/second $\sim 2 \cdot 10^6$

Altough only a fraction of these background particles reach the experimental areas and the detectors, an efficient system of collimators was designed close to the interaction regions, to reduce by several orders of magnitude the remaining flux of such particles into the detectors. In addition, a special configuration of the beam pipe profile was adopted. The typical rates of background particles[46] in the experimental areas, per bunch crossing, are given in Table 6.1.

BACKGROUND TYPE	REGION	No collimator	Collimator
Low energy photons	Central	$4.5 \cdot 10^8$	5.
	Forward	$4.5 \cdot 10^8$	$1.5 \cdot 10^2$
Beam-halo electrons		$5 \cdot 10^2$	$1.5 \cdot 10^{-3}$
Off-momentum particles	Detector	$3 \cdot 10^{-2}$	$2 \cdot 10^{-2}$
	Luminosity	$2 \cdot 10^{-1}$	10^{-2}

Table 6.1: Typical rates of background particles per bunch crossing.

6.4   Tolerable Backgrounds

Photons striking the beam pipe have energies of the order of several hundred KeV being scattered into the detector. About 10 % of these photons convert in the tracking chambers degrading the pattern recognition. Fluxes up to 10^7 photons/second are not expected to provoke degradation in the pattern recognition. The tolerable rate for electrons striking the beam pipe is of about 10^3/second.

6.5   The Beam-Pipe

The dimension of the vacuum chamber surrounding the interaction point obeys to several requirements of multiple origin [47,48]:

I) The need to have tracking devices with very good spatial resolution (few microns) as close as possible to the interaction point in order to minimize the uncertainty due to the multiple scattering in the beam pipe material, when extrapolating the tracks back to the vertex region. These Vertex Detectors are specially adequated for the studies of short-lived particles, where the accurate measurement of secondary decay vertices determines the lifetime of the decaying particles (e.g. b quark, τ lepton) and more generally for all physics channels where a good determination of the impact parameter of tracks is needed.

II) Background rates in the detector due to particle-wall interactions near the interaction point. Like:

i) Off-momentum particles swept out into the vacuum walls by the focusing quadrupoles

ii) Hard radiated photons by the electrons in the quadrupole magnetic fields, that reach the interaction point directly or after being scattered in the surrounding collimators or beam pipe. These photons are emitted at very low angle relative to the electrons and can reach the walls of the vacuum chamber if emitted by particles with energies on the edge of the gaussian profile of the beam halo. The photon background rate into the detector away from the low angle regions close to the beam pipe depends strongly on the diameter of the vacuum chamber around the interaction region.

The intersection region at LEP near DELPHI experimental area is surrounded by a vacuum chamber of aluminium walls 1.2 mm thick (1.35 % of a radiation lenght), 32 cm long and 158.4 mm in diameter. The vacuum pipe dimensions were chosen assuming conservative beam and background conditions.

Barrel Muon Chambers
Forward Muon Chambers
Barrel Hadron Calorimeter
Forward Hadron Calorimeter
Scintillators
Forward E.M. Calorimeter
Barrel E.M. Calorimeter
Forward Chambers B
Outer Detector
Forward RICH
Barrel RICH
Forward Scintillators
TPC
Inner Detector
Small Angle Tagger
Vertex Detector
Forward Chambers A
Superconducting Coil

e⁺
e⁻

DELPHI

Chapter 7

DETECTOR

DELPHI[1], Detector with Lepton, Photon and Hadron Identification, is one of the 4 detectors at LEP. Installed in a cavern 100 meters below ground it consists of a cylindrical section, _the barrel_, closed by _two endcaps_. The barrel is surrounded by the barracks housing the electronics and equipment computers for each subdetector and by the gas, cryogenics and power supply systems. Altough it has a "conventional" detector architecture for e^+e^- collider, DELPHI explores in a pioneering way the Ring Image Cerenkov techniques, through a set of complex detectors (RICH) that complemented by the accurate vertex determination using the silicon MicroVertex Detector (μV) make of it a unique detector in what concerns particle identification. Other detectors like the Time Projection Chamber (TPC) and the High Density Projection Chamber (HPC) allow three dimensional reconstruction of charged tracks and showers with good resolution and granularity.

The apparatus, operating in a magnetic field of about 1.2 Tesla (5000 Ampers) created by the world largest superconducting coil, can be divided in sets of detectors performing specific tasks, like follows:

- _Tracking Chambers_

- _Calorimeters_

- _Muon Chambers_

- _Luminosity monitoring detectors_

- _Scintillators and Hodoscopes_

- _Ring Imaging Cerenkov Detectors (RICH)_

---

[1]for a more detailed description see refs.[49,50,51]

The figures of merit of DELPHI detector are:

- I) Reconstruction of tracks (momentum,charge,angles) in the region $13° < \theta < 167°$, with good momentum resolution extended up to the very low angles. Track momentum resolution is

$$\frac{\sigma_P}{P} \simeq \begin{cases} 0.0015 \ P(GeV) & BARREL \\ 0.0037 \ P(GeV) & ENDCAPS \end{cases} \tag{7.1}$$

- II) Good azimuthal resolution for tracks. Expected $R\Phi$ resolution at the beam pipe is

$$\sigma_{R\Phi} \simeq \begin{cases} 100 \ \mu m & Without \ \mu Vertex \ detector \\ 5 \ \mu m & With \ \mu Vertex \ detector \end{cases} \tag{7.2}$$

- III) Electromagnetic calorimetry coverage in about 90 % of the solid angle allowing 3-D reconstruction of the showers in the barrel region. The aimed energy resolution is

$$\frac{\sigma_E}{E} \simeq \begin{cases} \frac{0.20}{\sqrt{E(GeV)}} & BARREL \\ \\ \frac{0.11}{\sqrt{E(GeV)}} & ENDCAPS \end{cases} \tag{7.3}$$

- IV) Hadronic calorimetry coverage in about 98 % of the solid angle with energy resolution of

$$\frac{\sigma_E}{E} \simeq \frac{1.20}{\sqrt{E(GeV)}} \tag{7.4}$$

- V) Muon chambers coverage in about 93 % of solid angle

- VI) Good discrimination between π/k up to 20 GeV, based on the RICH detectors and between e/π up to 8 GeV based on the $\frac{dE}{dX}$ measurement in the TPC.

- VII) Good measurement of track impact parameter and of decay vertices of particles with lifetimes in the range $(1 - 15) \cdot 10^{-13}$ seconds (e.g. weak (semi-leptonic) decays of heavy quarks (b mainly) and leptons (tau)). The expected error on projected impact parameter is

$$\sigma_{imp}^2 = (\frac{153}{p})^2 + (25)^2 + (11)^2 \ (\mu m)^2 \tag{7.5}$$

Heavy flavour (b-quark mainly) physics is intended to result from a combined good vertex reconstruction (μVertex) and good hadron identification (RICH)

7.1 Tracking System

It consists of several drift chambers that can be combined to give the overall track reconstruction (P, θ, ϕ). Up to 4 different detectors can be combined to fit a track by using the track segments recorded in each detector. They are:

7.1.1 Barrel Tracking Chambers

7.1.1.1 ID, Inner Detector

Consists of 2 cylindirical chambers of different characteristics:

- *Jet Chamber*, starting at a radius of 13 cm from the beam line, covers the angular region $17° < \theta < 163°$ and the range $-40\ cm < Z < 40\ cm$. It is segmented in 24 $R\Phi$ sectors of $15°$, symmetrically divided by 24 radial wires. The measurement of the drift time to each wire allows the measurement of 20 points (in average) along the trajectory of the track. The $R\Phi$ accuracy per point measurement is 100 μm. The transverse momentum can be reconstructed for tracks up to 5 GeV.

- *Trigger Chamber*, covering the region $33° < \theta < 147°$. Starting at $R = 25\ cm$ from the beam line, consists of 5 cylindrical layers each with 192 wires azimuthally distributed operating in proportional mode (MWPC) and 192 circular cathode strips. This chamber participates in the fast trigger of the detector. Measurement of $R\Phi$ and Z coordinate of the hits along the wires are performed.

The number of measured points in the ID is a function of theta like follows:

$$N_{hits} = 29 \qquad 33° < \theta < 147° \qquad (7.6)$$
$$= 2\theta - 33 \qquad 17° < \theta < 30° \qquad (7.7)$$

Typical detector resolutions are

$$\sigma_{R\Phi} \simeq .025\ mm \qquad (7.8)$$

$$\sigma_Z \simeq 600\ \mu m \qquad (7.9)$$

$$\sigma_\phi \simeq 1\ mrad \qquad (7.10)$$

$$\sigma_\theta \simeq 40\ mrad \qquad (7.11)$$

$$\frac{\sigma_{P_T}}{P_T} \simeq 0.20\ P_T \qquad (7.12)$$

and for 2-track separation:

$$\Delta(R\Phi) \simeq 1\ mm \qquad (7.13)$$

$$\Delta(Z) \simeq 1\ cm \qquad (7.14)$$
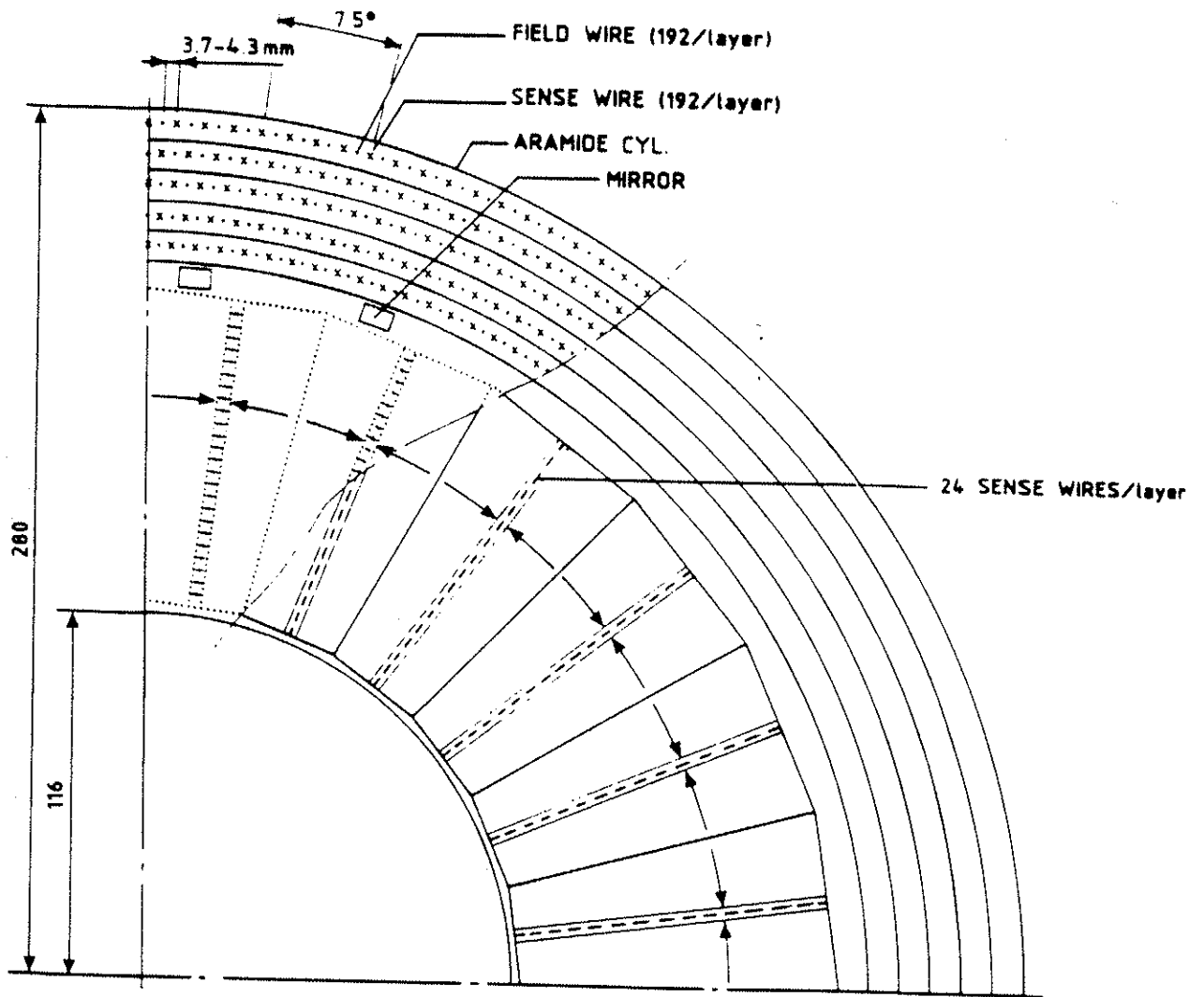
Figure 7.1: Transverse view of one quarter of the Inner Detector (ID). Six (out of 24) $R\Phi$ sectors in the Jet Chamber and the 5 layers of the Trigger Chamber are shown.

7.1.1.2   TPC, Time Projection Chamber

It is a drift chamber consisting of 2 half cylinders of 130 cm length, inner and outer radius respectively 30 cm and 120 cm, that are separated by a central wall plane at Z=0. It is operated at a pressure of 1 atm with typical drift velocity values of 6.5 cm/μs. Electrons created by particle ionization in the gas volume (starting at a radius of approximately 39 cm) drift towards the end-wall, under the action of an applied electric field parallel to the Z axis, where they induce a signal in the readout pads by avalanche near the walls . Each endcap wall is azimuthally divided into 6 sector plates with 16 circular pad rows and 192 sense wires. The number of pads per row, multiple of 16, varies with the radius to give a total of 1680 pads per sector.

This detector measures a number of points (maximum 16) along the particle trajectory that is variable with θ. It allows 3-dimensional reconstruction of the track segment within its sensitive volume, and is used as a "pivot" to start the track reconstruction in the angular range $22° < \theta < 158°$ where at least 4 points are measured along the particle trajectory. The dimensions of the cathode pads are 7.5 x 8 mm^2, allowing good two-track separation. The central wall (Z=0), of few cm thickness, amounts to an effective dead or inefficient angular region of 2 degrees.

The material constitutive of this detector amounts to 0.1 radiation lengths (X_0) mainly in the inner wall. The end-wall crossed by tracks in the forward region amounts to about .45 X_0. This, as will see in next chapters, represents a source of photon conversions in the detector.

Information about the $\frac{dE}{dX}$ of the crossing particles, obtained from the pulse height induced in the wires, allows e/π separation in the energy range below 8 GeV with a resolution of 5.5%.

The typical resolutions are

$$\sigma_{R\Phi} \simeq 250 \ \mu m \tag{7.15}$$

$$\sigma_Z < 0.9 \ mm \tag{7.16}$$

$$\left(\frac{\sigma_P}{P}\right)^2 \simeq \left[(.7P)^2 + (.48)^2 \right] \ (\%) \quad \theta = 90° \tag{7.17}$$

$$\left(\frac{\sigma_P}{P}\right)^2 \simeq \left[(.5P)^2 + (.58)^2 \right] \ (\%) \quad \theta = 50° \tag{7.18}$$

$$\frac{\sigma_P}{P} \simeq \left[(.7P)^2 + (.48)^2 \right] \ (\%) \quad P \gg 1, \quad \theta > 35 \tag{7.19}$$

and for 2-track separation is,

$$\Delta(R\Phi) \simeq 2 \ cm \tag{7.20}$$

$$\Delta(Z) \simeq 1 \ cm \tag{7.21}$$

6 secteurs identiques à chaque extrémité

enceinte en matériaux composites

plaque H.T.

cage isolante

cage électrostatique

2x6 passages Laser

0.29

1.216

3.340 m

axe du faisceau

16 rangées de damiers

192 fils sensibles
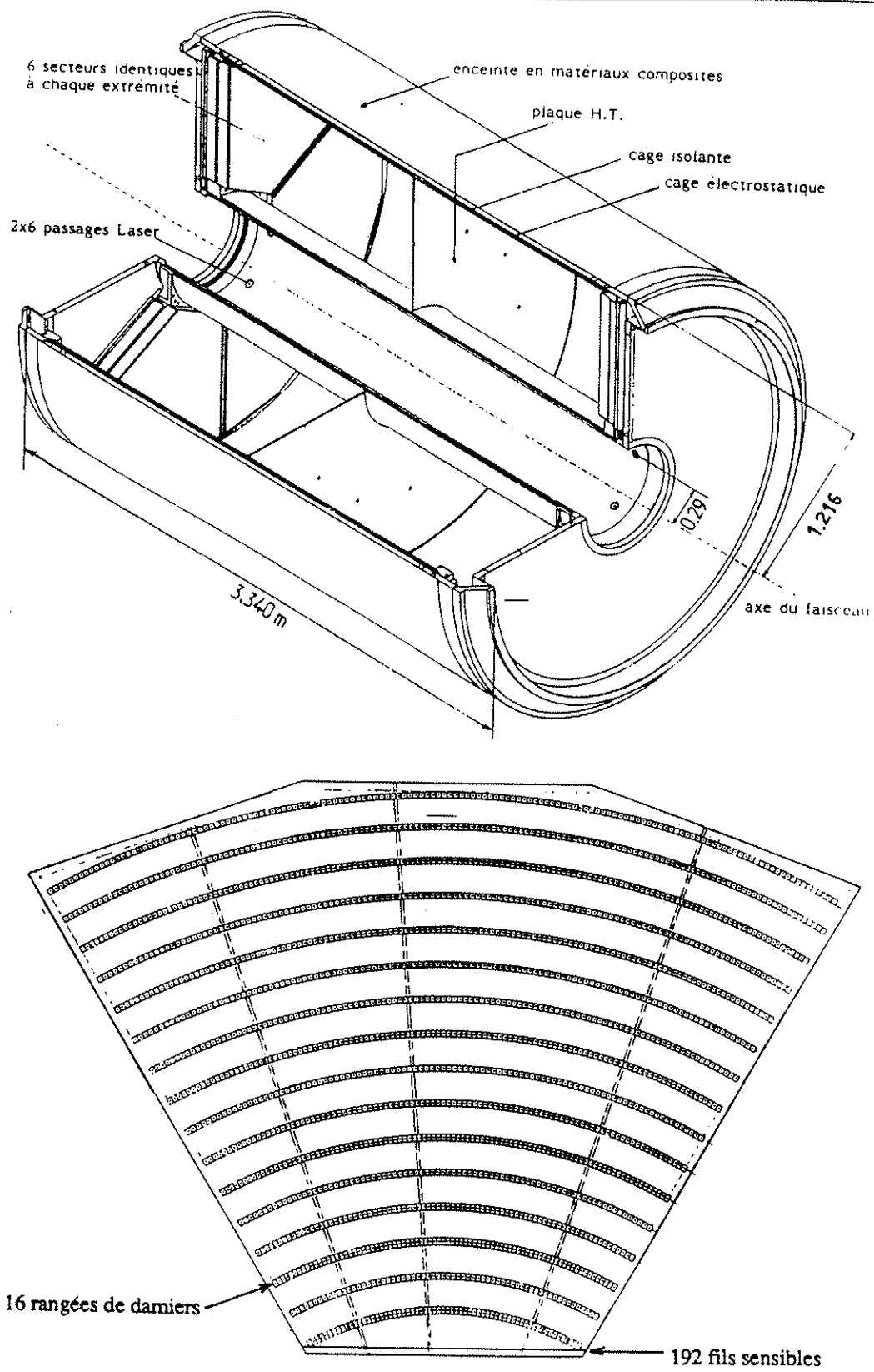
Figure 7.2: View of the TPC structure (top) and of one TPC sector with the 16 pad rows visible (bottom).
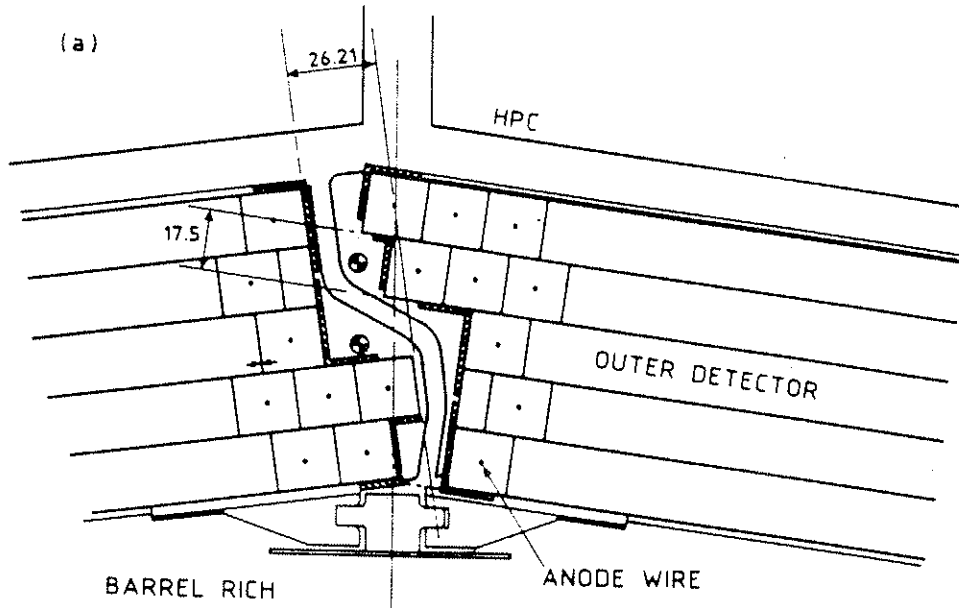
Figure 7.3: Partial (zoomed) $R\Phi$ view of the Outer Detector with 5 layer of drift tubes per plank. Dead zones in the transition between azimuthal sectors are seen

7.1.1.3   OD, Outer Detector

Starting at a radius of about 197 cm from the beam line and covering the angular region $43° < \theta < 137°$, is segmented in 24 $R\Phi$ sectors (planks), each consisting of 145 drift tubes of 4 meters length along Z, and grouped in 5 staggered layers.

This detector participates in the fast trigger decisions, providing $R\Phi$ and Z information. Each layer of drift tubes contributes with at least one point (number of points dependent on the angle of the crossing track) to the track reconstruction. Measurement of $R\Phi, \phi$ coordinates is done by processing of the drift time in each tube, being the Z coordinate reconstructed by the delay time measured at the end of the wires. Typical measurement errors are:

$$\sigma_{R\Phi} \simeq 110 \ \mu m \tag{7.22}$$

$$\sigma_Z \simeq 4 \ cm \tag{7.23}$$

7.1.1.4   Features Of The System

• TPC is the main detector of the system, used as the "pivot" in the track search and track fit during the complex track reconstruction procedure. It is a detector with good spatial resolution $(R\Phi, Z)$, about 1 m radius and 1.3 m long. Being a drift device does not participate in the fast trigger decisions (see next chapter).

• ID, very good point resolution, detector close to the interaction region participates (Trigger Chamber) in the T1 level of trigger (see next chapter)

• OD, very good spatial resolution in $R\Phi$ and ϕ at 2 meters from the interaction point in the transverse plane, increases the lever arm for the track reconstruction, improving then the momentum resolution for high momentum tracks. In addition, 3 out of 5 layers in each sector provide measurement of Z coordinate. Participates in the barrel track sub-trigger and in the first level of trigger decision (T1). Is very useful for $\mu^+\mu^-$ physics where good reconstruction of tracks with momentum close to the beam energy is needed. Also useful information for the calorimeters about pre-showering and photon conversion can be suplied.

The summarized information about the type and number of track measurements from each detector contributing to the track reconstruction in the barrel is shown in the table below.

Detector	# Points	Point Measurement	Track Measurement
ID (Jet)	24	$R\Phi$	P_T ϕ
ID (Trigger)	5	$R\Phi$ Z	ϕ
TPC	16	R $R\Phi$ Z	P_T θ ϕ
OD	5	$R\Phi$ Z	ϕ

7.1.2 Forward Tracking Chambers

7.1.2.1 FCA, Forward Chamber A

This detector is mounted directly behind the TPC endplate, perpendicular to the beam direction and covers the angular regions $11° < \theta < 33°$ and $147° < \theta < 169°$. Each arm of the detector consists of 3 chambers rotated with respect to each other by $120°$ and built as 2 half-discs of inner and outer radii 29 cm and 101 cm respectively. Each half disc has 2 staggered planes of 64 wires, the first disc starting at $Z = \pm 155$cm. These chambers participate in the track subtrigger in the forward/backward direction and provide the measurement of up to 2x3 coordinates for tracks in the endcaps (forward or backward) down to the very low angle regions. The achieved resolutions are

$$\sigma_{X,Y} \simeq 600 \ \mu m \tag{7.24}$$

$$\sigma_\theta \simeq 20 \ mrad \tag{7.25}$$

$$\sigma_\phi \simeq 50 \ mrad \tag{7.26}$$

7.1.2.2 FCB, Forward Chamber B

This detector consisting of 2 arms, one per endcap, covers the angular regions $13° < \theta < 35°$ and $145° < \theta < 167°$. Each endcap consists of 2 half discs with inner and outer radii 48 cm and 211 cm respectively, perpendicular to the beam axis in the region defined by $|Z| \simeq 260 - 274 \ cm$. The 2 half discs, at positive and negative X, are separated by a dead zone of few cm around $\Phi = 90°, \Phi = 270°$.

The chambers in each endcap have 12 sense wire Z-planes separated by 1.1 cm, with 3 different orientations and grouped in staggered pairs rotated by $120°$ with respect to each other. The distance between sense wires in the same plane is of about 2 cm, imposing a driftlength of about 1 cm. This detector participates with FCA (and TPC) in the track subtrigger in the forward/backward regions and with the measurement of 4x3 coordinates allows the precise determination of the track parameters with significant improvement on the momentum resolution for tracks in the endcap regions down to the very low angle regions. The expected resolution values are:

$$\sigma_{X,Y} \simeq 200 \ \mu m \tag{7.27}$$

$$\sigma_{\frac{dx}{dz}}, \sigma_{\frac{dy}{dz}} \simeq 0.006 \tag{7.28}$$

FORWARD CHAMBER B

FORWARD CHAMBER A
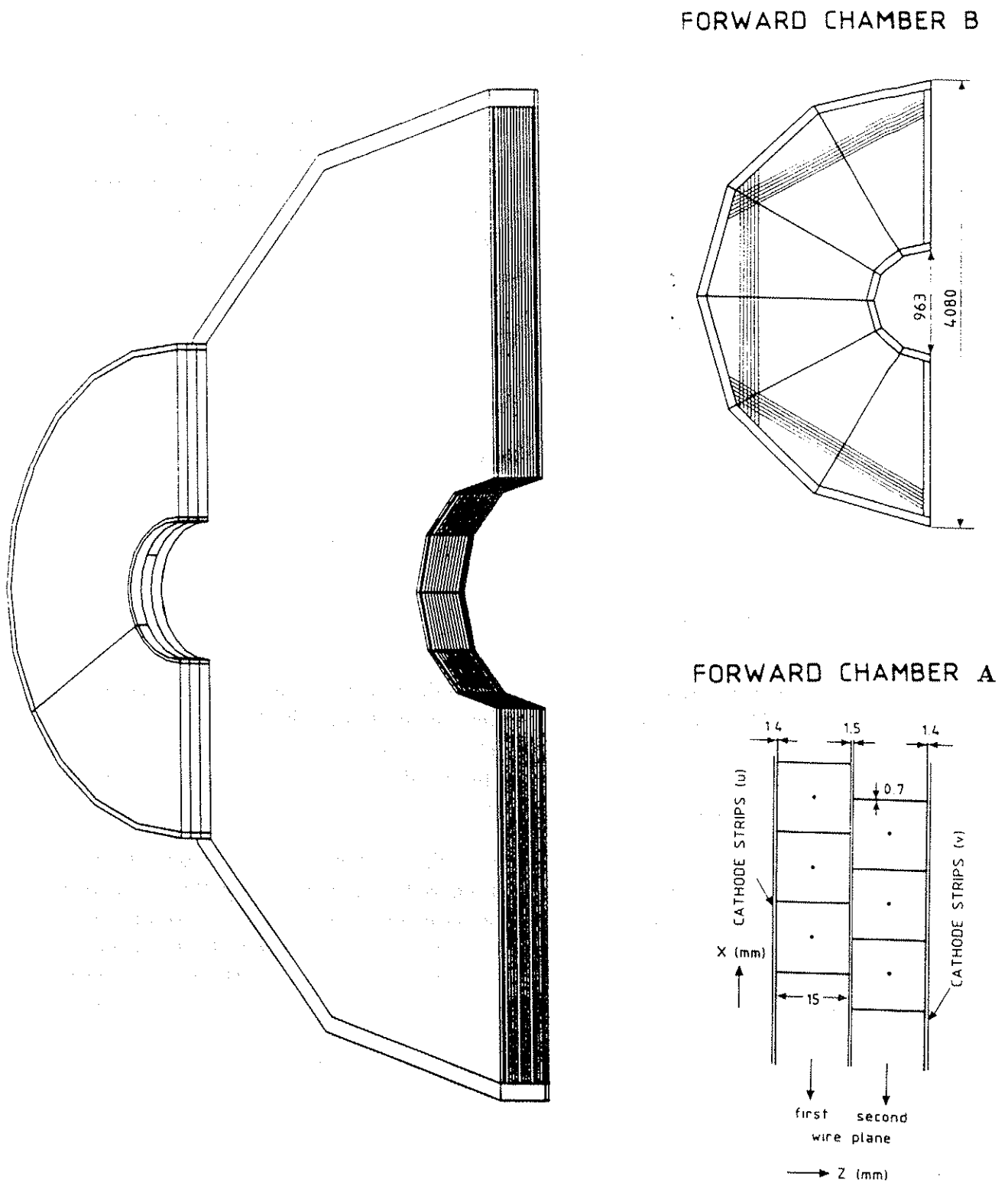
Figure 7.4: View of one half-disc of chambers A and B, with the z-planes of wires visible in the sliced region. The 3 different orientations of the wires in FCB, rotated 120° with respect to each other, and the relative position of the wires in two consecutive planes of FCA, are shown.

7.1.2.3   Characteristics Of The System

Below $\theta = 22°$ and above $\theta = 158°$, the number of TPC pads "seing" the track
is less than 3 and below $\theta = 18°$ and above $\theta = 162°$ no pad information (only
wire) is available from the TPC. With the aim of extending the track reconstruction
capabilities to the very forward/backward region where no TPC information is given,
and to improve the track reconstruction in the regions where it is not fully seen
(less than 16 pads up to about 35°) by the TPC, the Forward Chambers A and B
placed after the TPC and respectively before and after the Forward RICH detectors
make of DELPHI one of the e^+e^- detectors with highest coverage in what concerns
track measurement at low angles. Tracks in the forward-backward direction, in the
region where TPC does not give valid information (less than 3 pads seen), can be
reconstructed by the FCA+FCB+(ID-JET) measurements. Track reconstruction is
expected up to low angles (13°) due to the long arm available with the Chamber B,
with deterioration of the momentum resolution below 20°. Up to 35°, combination
of TPC information with 3-D track information available from the Chambers A+B,
allow a good determination of the track parameters.

Cathode strips outside and between the 2 staggered planes of FCA, ORed with wires
of FCB provide the first level of trigger for tracks in the forward/backward direction.
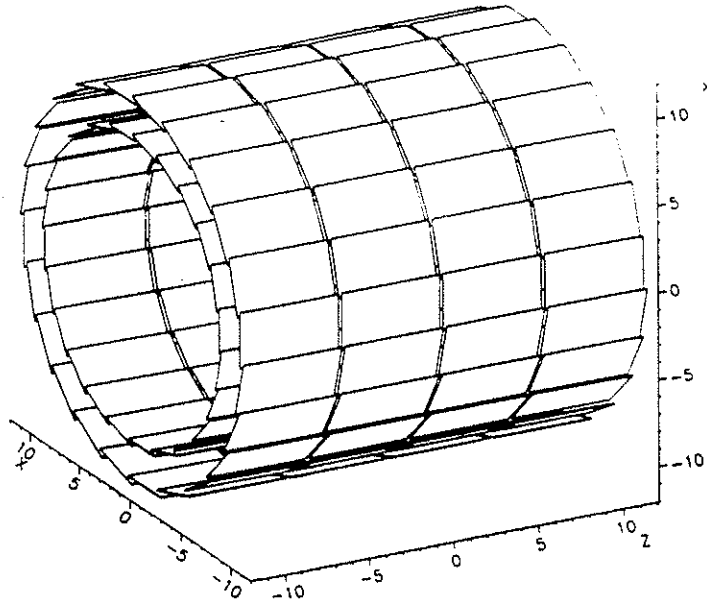
Figure 7.5: Perspective view of the μVertex detector, 24 cm length, being visible the 2 silicon layers (at R=9 cm and R=11 cm) and the 2x24 $R\Phi$ sectors in each layer

7.1.3 VD, μVertex Detector

Covering the angular region $42° < \theta < 138°$, it consists of 2 cylindrical shells, at radius 9 and 11 cm from the beam line, 24 cm length extending in Z from -12 cm to +12 cm. Each shell is segmented in 2x24 $R\Phi$ layers of microstrip silicon detectors. Consecutive layers have an overlap of about 10% in Φ. This is the closest detector to the interaction region, and its radiation thickness is of about 1.1% of a radiation length.

Due to a very accurate measurement of the transverse ($R\Phi$) coordinate only a few centimeters from the interaction region, it can substancially improve track momentum and direction resolution when its measurements are combined with ID, TPC and OD information. The $R\Phi$ resolution that can be achieved with this detector is

$$\sigma_{R\Phi} \simeq 5 \ \mu m \qquad single \ track \qquad (7.29)$$

$$\sigma_{R\Phi} \simeq 100 \ \mu m \qquad two \ track \ separation \qquad (7.30)$$

The resolution in the impact parameter for tracks fitted including the μV detector meausrements is:

$$\sigma_{imp}^2 = (\frac{153}{p})^2 + (25)^2 + (11)^2 \ (\mu m) \qquad (7.31)$$

Altough being a small detector, it has more than 50000 readout strips.

7.2   Calorimetry

Due to a complex structure of cable ducts and suports for detectors like TPC,FCB and RICH there is a gap in the angular electromagnetic coverage of DELPHI. The barrel and endcap regions are physically separated by cables and suports in the regions $35° < \theta < 42°$ and $138° < \theta < 145°$. One electromagnetic calorimeter covers the barrel region and another covers the 2 endcap regions of the detector.

7.2.1   Barrel Electromagnetic Calorimeter

7.2.1.1   HPC, High Density Projection Chamber

It is the barrel electromagnetic calorimeter, covering the angular region $43° < \theta < 137°$. Longitudinally (Z) it is segmented in 6 rings separated by 1 cm gap [2], each ring being azimutally ($R\Phi$) divided in 24 modules with gaps (_cracks_) of 1 cm between modules. Each of the 144 modules starts radially at 208 cm from the beam line and extends up to 260 cm consisting of 41 lead-converter slabs with an acordeon-like structure, imersed in the sensitive gas volume (8 mm gaps between slabs). A total of 18 radiation lengths is distributed over 9 radial layers. The lead layers are used as field cage establishing an electric field along the Z axis in the gas gaps. For trigger purposes, a plane of scintillators exists in one of the sampling gaps, at a depth of 4.5 radiation lengths.

The mode of operation is inspired in the same time projection technique used in the TPC: the electrons from the lead converter layers emerging in the gas sampling gaps drift towards a proportional chamber (single wire plane) at the Z-end plane of the module. There, a 2-D pad readout structure (100 pads distributed over 6 staggered layers) samples the collection of the amplified charge in time slots of 70 ns, allowing the reconstruction of the Z coordinate. The pad pattern defines the granularity of radial and azimuthal coordinate sampling. This technique applied to calorimetry allows the reconstruction with good accuracy of the shower position ($R, R\Phi$,Z). In addition, due to the good granularity, radial sampling in the 9 layers of the HPC modules allows accurate 3-dimensional reconstruction of the shower. Typical values for the granularity of this device are:

$$Z \simeq 4\ mm \tag{7.32}$$

$$R \simeq 4.5\ cm \tag{7.33}$$

$$R\Phi \simeq 4.0\ cm \tag{7.34}$$

---

[2]with the exception of the modules joining at Z=0 separated by a 7.5 cm gap

The achieved resolutions in the shower direction and energy reconstruction are:

$$\sigma_\theta \simeq 25 \; mrad \tag{7.35}$$

$$\sigma_\phi \simeq 50 \; mrad \tag{7.36}$$

Two showers are separated if

$$\Delta Z > 2 \; cm \tag{7.37}$$

$$\Delta R\Phi > 4 \; cm \tag{7.38}$$

The fractional energy resolution achieved in the reconstruction of 45.5 GeV showers from Bhabha events during the 1990 run is

$$\frac{\sigma_E}{E} \simeq 10 \; \% \tag{7.39}$$

7.2.2   Endcap Electromagnetic Calorimeter

7.2.2.1   FEMC, Forward Electromagnetic Calorimeter

This is the electromagnetic calorimeter covering the endcap angular regions defined as $10° < \theta < 36.5°$ and $143.5° < \theta < 170°$. Each endcap consists of 4500 lead-glass blocks with a "pyramidal" geometry pointing to the interaction region, in a bidimensional array of 5 x 5 cm^2 ($\simeq 1°\text{x}1°$) counters distributed in a disc with inner and outer radius 45 cm and 240 cm, front planes at $Z = \pm284cm$ and extending 40 cm in depth (Z). The constitutive material has 2 cm radiation length (X_0) and Moliere radius of 5 cm.

The expected accuracy in the energy and shower position reconstruction is

$$\frac{\sigma_E}{E} \simeq \left[\left(0.35 + \frac{5}{\sqrt{E}} \right)^2 + \left(\frac{6}{E} \right)^2 \right]^{1/2} (\%) \tag{7.40}$$

$$\sigma_{X,Y} \simeq \frac{8.2}{\sqrt{E}} (mm) \tag{7.41}$$

The fractional energy resolution achieved in the reconstruction of 45.5 GeV showers from Bhabha events during the 1990 run is

$$\frac{\sigma_E}{E} \simeq 9 \; \% \tag{7.42}$$
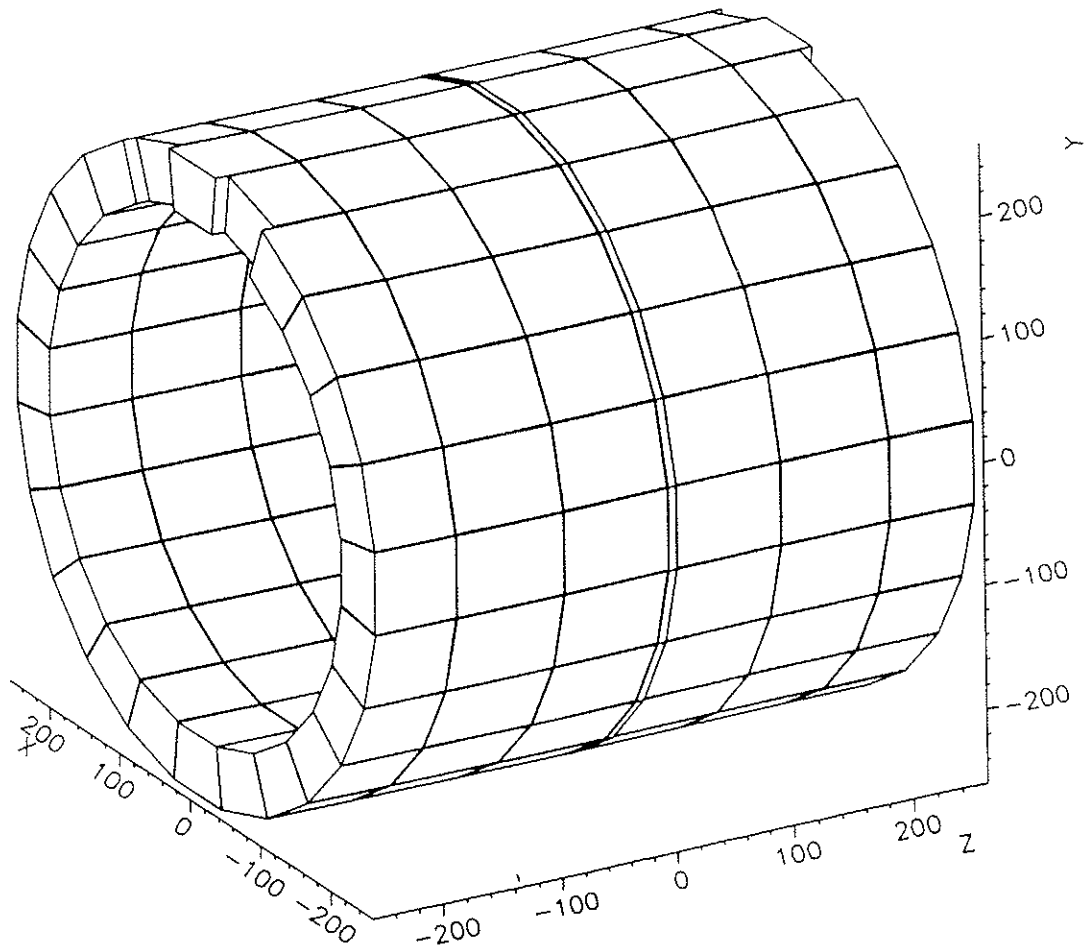
Figure 7.6: View of the barrel electromagnetic calorimeter (HPC), at 208 cm from the interaction point in the radial coordinate, and about 4 m long. In the figure, the 6 Z-ring segmentation is exhibited, with 24 $R\Phi$ modules in each of these rings
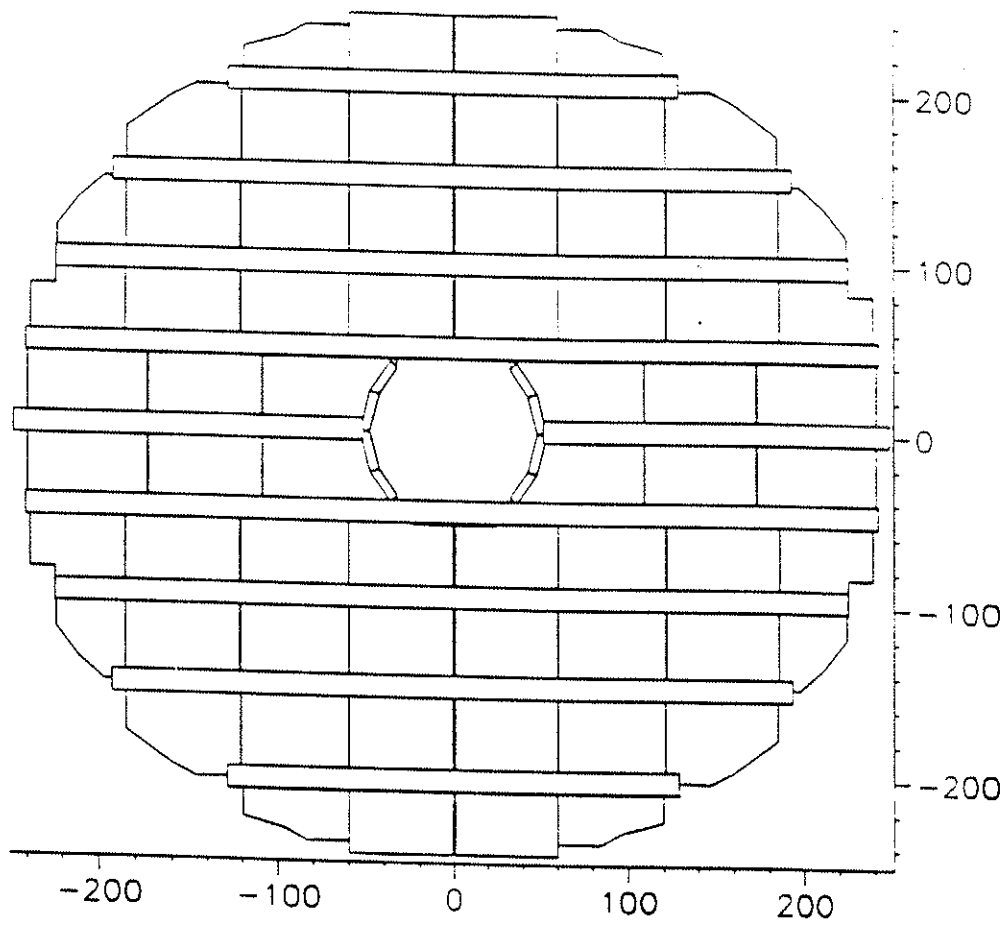
Figure 7.7: Front view of the endcap lead glass electromagnetic calorimeter (FEMC), with the modular structure shown. Each endcap consists of about 4500 lead glass blocks.

7.2.3   Hadronic Calorimeter

7.2.3.1   HAC, Hadron Calorimeter, Barrel & Endcaps

It consists of a barrel and 2 endcap pieces, non-separated, altogether covering the angular region $10° < \theta < 170°$.

- *Barrel* - It is a 8 meters length cylinder, segmented in 24 $R\Phi$ modules. Each module is formed by 19 iron plates, 5 cm thick, 2 iron plates 2.5 cm thick and outside, enclosing the Inner Muon Chamber layer, a 10 cm thick iron plate. The total radial length of about 110 cm of iron (6 interaction lenghts for pions), starting radially at about 320 cm from the beam line. Streamer tubes operating in limited mode fill the space between consecutive iron plates. A structure of readout pads, glued to the streamer tubes, collects the charge induced by the crossing particles.

- *Endcaps* - Consist of 2 big "discs" (polygonal shape) 105 cm length and 4.6 m radius, to which are attached circular pieces of 40 cm length and 2.4 m radius. Each endcap is segmented into 12 equal sector shaped modules, with 21 iron plates 5 cm thick, spaced by 17 mm. The detector sensitive elements between iron pieces are multicell wire chambers, working in limited streamer mode. The readout pads, at different planes, obey a projective geometry, pointing to the beam crossing region.

For readout,trigger and analysis purposes the calorimeter is organized in *towers* pointing to the interaction region covering an angular region $\Delta\theta \simeq 3°, \Delta\Phi \simeq 3.75°$ and with typical dimensions 25x25x35 cm^3 in the barrel. Sixteen adjacent towers in one plane define a *supertower* and are read by the same electronic card. Supertowers are grouped in *hipertowers*, consisting of all supertowers along the same angular (θ) interval. Each half of the barrel (at positive or negative Z) consists of 232 towers (15 supertowers, 4 hipertowers) and each endcap consists of 176 towers (13 supertowers, 4 hipertowers).

The achieved energy resolution is

$$\frac{\sigma_E}{E} \simeq \frac{120}{\sqrt{E}}(\%) \qquad\qquad (7.43)$$

with a granularity (dictated by the size of each tower) of about 10 cm.

7.3   Muon Chambers

They are splitted in 2 groups of chambers covering respectively the barrel and endcaps regions. The coverage is not complete and besides the inevitable low angle dead zones, also the regions $45° < \theta < 53°$ and $127° < \theta < 135°$ are not covered by muon chambers.

7.3.1   MUB, Barrel Muon Chambers

They consist of 3 layers of drift-chambers covering the angular region $50° < \theta < 130°$. Each layer is segmented in 2x24 $R\Phi$ sectors (planks), with drift chambers of length 3.65 m operated in proportional mode. The drift tubes are 20.8 cm wide and 2.6 cm high and the delay line acts as the central field shaping electrode.

- *Inner layer*: inserted inside the return yoke after 90 cm of iron, consists of 2x24 planks. Each plank, 104 cm wide, has 3 staggered planes of drift tubes, but only 2 are read out.
- *Outer layer*: mounted on the outer surface of the iron yoke, each plank 83 cm wide, consists of 2 staggered layers of drift tubes.
- *Peripheral layer*: 50 cm outside the iron yoke, each plank 83 cm wide, covers the the dead zones left by the inner and outer layers and consists of 2 staggered layers of drift tubes.

While for the Inner and Outer layers a sector of chambers covers partially the corresponding yoke sector of the Hadron Calorimeter, for the Peripheral layer, each sector overlaps partially with the 2 adjacent sectors of the Inner and Outer layers and the corresponding adjacent yoke sectors. The Z coordinate is determined by measuring the time difference of arrival of the pulse at each end of the delay line, while the determination of the $R\Phi$ coordinate follows from the drift time to the wire. Most of the muon tracks cross 2 layers of chambers producing ideally 4 sets of $R\Phi, Z$ measurements (hits). For the subset of tracks crossing the regions where the 3 layers of chambers overlap, up to 6 hits can be produced.

The delay line and drift velocity values are:

$$Delay\ lines\ v^{-1} \simeq 180\ nsec/m \tag{7.44}$$

$$Drift\ velocities \simeq 40\ \mu m/nsec \tag{7.45}$$

The achieved $R\Phi$ and Z resolutions (dictated respectively by the drift to the wires and by the propagation of the pulse in the delay line) are:

$$\sigma_{R\Phi} \simeq 4\ mm \tag{7.46}$$

$$\sigma_Z \simeq 2.5\ cm \tag{7.47}$$
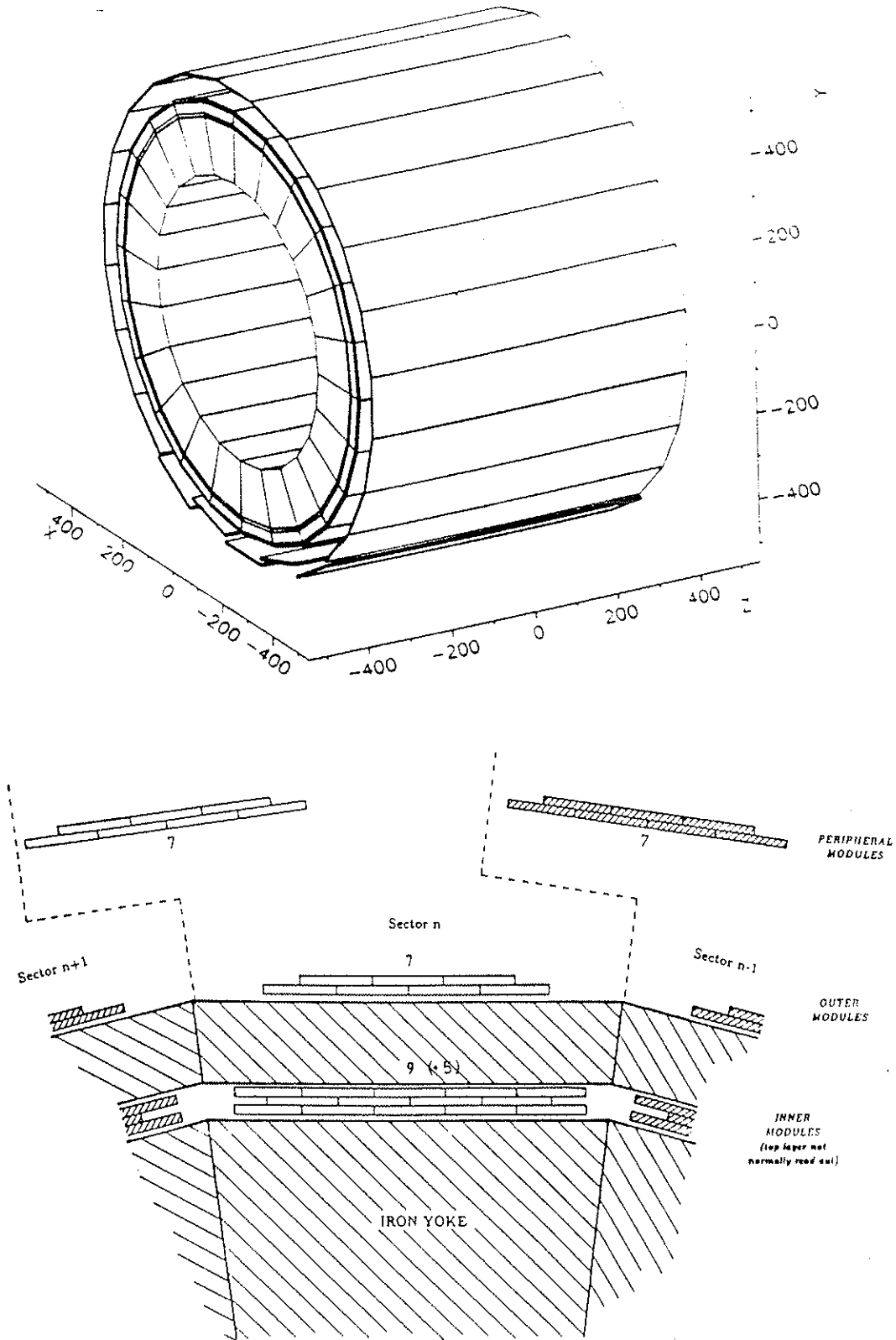
Figure 7.8: The barrel hadronic calorimeter (HAC) and muon chambers (MUB) in perspective (a) and partial transverse section (b). From the drawings it is visible the $R\Phi$ segmentation (24 modules) of both detectors, and the three layers of muon chambers

7.3.2   MUF, Endcap Muon Chambers

Each endcap consists of 2 planes of chambers (at constant Z) covering the angular regions $15° < \theta < 45°$ and $135° < \theta < 165°$, operated in the limited streamer mode. Each plane is built in 4 quadrants of 448 x 448 cm^2 and each quadrant has 2 orthogonal layers of 22 drift chambers with the anode wires crossed at 90°. The sensitive area of each quadrant is defined by 12 $cm < |x, y| < 448$ cm excluding the region defined by $|x| < 91$ cm and $|y| < 91$ cm. The first plane is inserted inside the yoke, behind 85 cm of iron. The second plane is outside the yoke, 30 cm away from the first plane, after 20 cm of iron. In a similar way as for the barrel muon chambers, the X,Y coordinates are derived from the drift time to the anode wire and the 2 delay times corresponding to the signal propagation to both ends of the chamber. Muon tracks crossing the 2 planes of chambers produce 4 hits (2 sets of X,Y measurements per layer).

The typical values for delay line and drift velocities in this detector are

$$Delay\ lines\ v^{-1} \simeq 600\ nsec/m \tag{7.48}$$

$$Drift\ velocities \simeq 10\ \mu m/nsec \tag{7.49}$$

resulting in the spatial resolution averaged over all the layers in one endcap:

$$\sigma_{x,y} \simeq 3\ mm \tag{7.50}$$
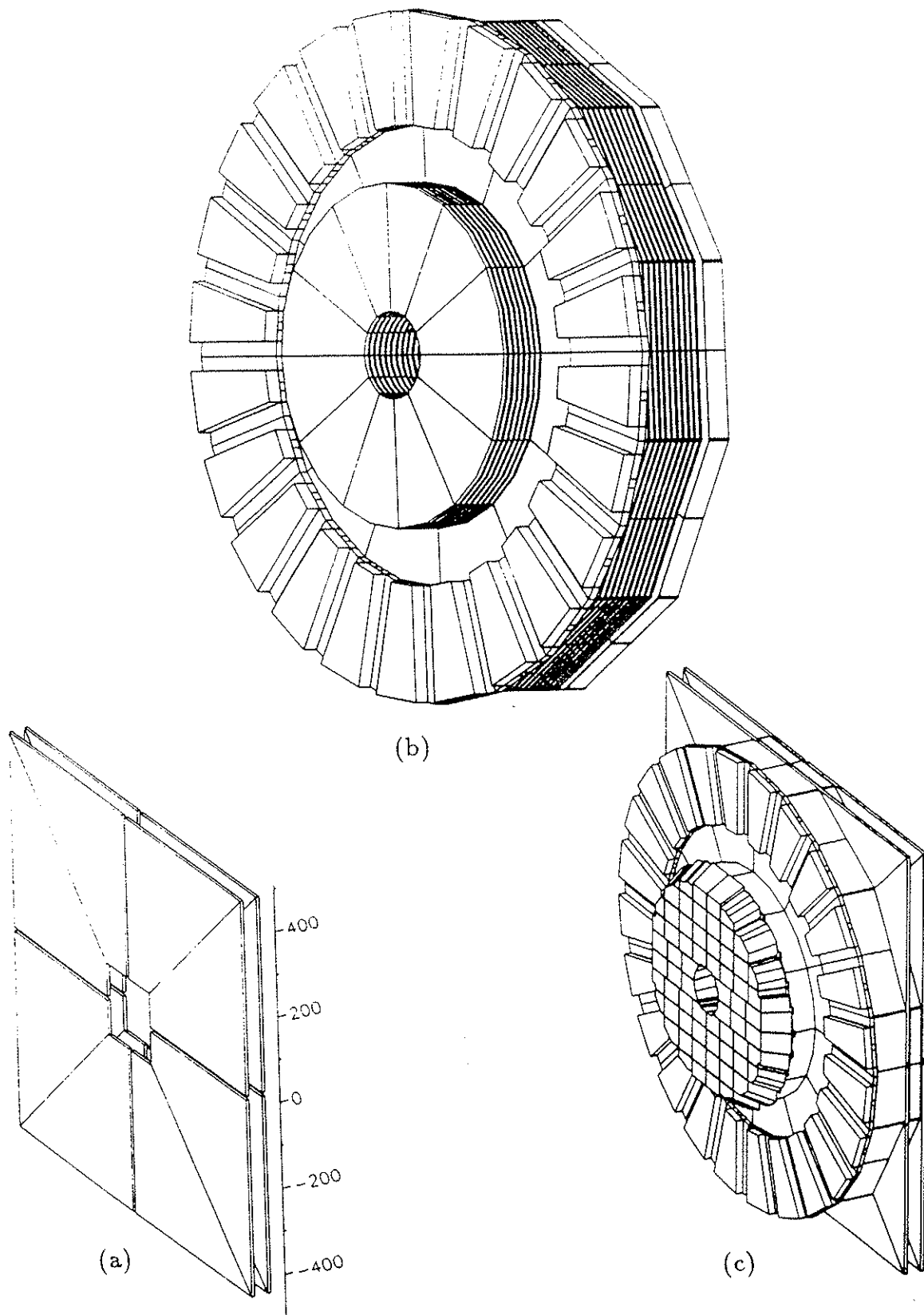
Figure 7.9: View of MUF (endcap muon chambers) quadrants in (a), of the several endcap components of the hadronic calorimeter (inner and outer disk)in (b), and of combination between FEMC, HAC and MUF in one endcap (c). The relative positioning of the muon chamber layers with respect to the hadronic calorimeter is shown in (c)

7.4 Luminosity Detectors

7.4.1 SAT, Small Angle Tagger

Consists of 2 arms covering the polar angles from 43 mrad (3°) to 135 mrad (7.7°) starting from the beam line (at positive and negative Z), with front planes at $Z = \pm 250 cm$. Each arm is divided in two half-disks separated by a dead region of 2 cm and has an electromagnetic _calorimeter_ with 28 radiation lengths thickness, composed of lead sheets concentric with the beam axis and alternating with scintillating fibres parallel to the beam. Photodiodes receive from conical lightguides the signals from bundles of 144 fibers. For readout purposes, azimuthal segmentation exists: the 4 inner rings are divided in 15° sectors while the 4 outer rings are segmented in 7.5° sectors.

The lead-scintillating fiber calorimeters in each arm are complemented by a _tracker_ made of 3 planes of silicon detectors at $Z = \pm 203, \pm 216, \pm 230$ cm and inner radius 10 cm, covering the angular region from 43.5 mrad to 120 mrad. These detectors reconstruct and define with an accuracy of $\sigma_\theta = 1.5$ mrad, the particle direction and the impinging point in the calorimeter, allowing the definition of the inner radius of acceptance to about 40 μm.

This detector performs the task of counting and measuring accurately the number of Bhabha events in its fiducial region. Survey of the beam position and interaction point are also performed.
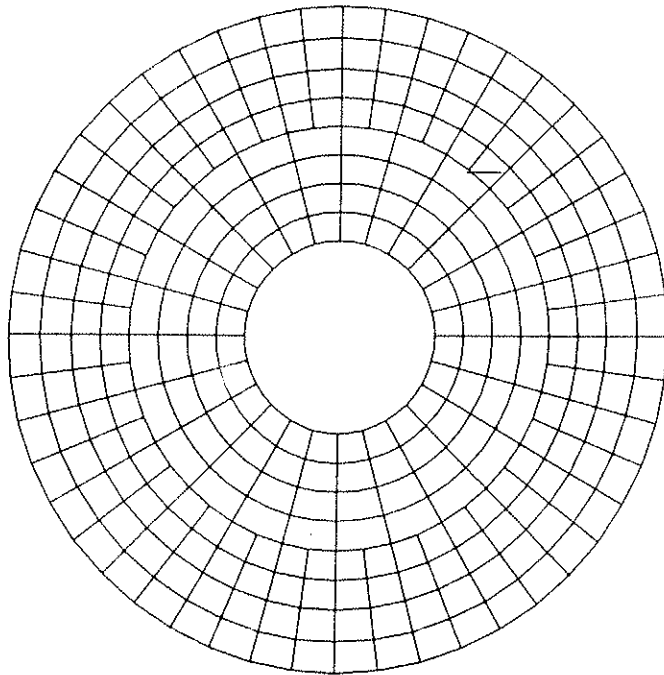
Figure 7.10: Front view of a SAT arm, where the radial ring structure is evidenced and the azimuthal segmentation for different rings is shown

7.5   Scintillators and Hodoscopes

Two detectors, consisting of scintillators, cover the barrel and endcap regions. Their main functions are:

- Participate in fast trigger decisions.

- Measure the time of flight of particles (barrel scintillators)

- Provide information about cosmic particles and the cosmic trigger.

7.5.1   TOF, Time Of Flight

It consists of a barrel of scintillators at radius 310 cm, between the superconducting coil and the hadron calorimeter, covering the angular region $41° < \theta < 139°$ with a dead zone 6 cm wide around 90°. A single layer of 172 scintillation counters, 3.5 meters long, with corresponding light guides and photomultipliers is segmented in 24 $R\Phi$ sectors. With an attenuation length of 135 cm and a response of 40 photoelectrons for a minimum ionizing particle, the time resolution is of the order of 1.2 ns and the spatial resolution of about 20 cm.

This detector gives the cosmic trigger signal in the barrel (on and off beam) and contributes to the high redundancy of the trigger in the barrel. Time of flight measurement can be used to veto cosmic muons.

7.5.2   HOF, Hodoscopes Forward

It consists of 2 planes of scintillator counters (1 per endcap), after the yoke of the Hadron Calorimeter and before the second plane of forward muon chambers. Each plane is segmented in 4 sectors (quadrants) of 28 hodoscopes. The attenuation length is of the order of 1.5 m and the time resolution is 5 ns.
This detector participates with the TOF in the cosmic trigger and is the only detector triggering the muons from the beam halo used for alignment of the endcap tracking chambers. It contributes as an independent trigger to the redundancy of the muon trigger in the endcap regions extending and improving the muon detection and trigger efficiency down to the very low angle region.
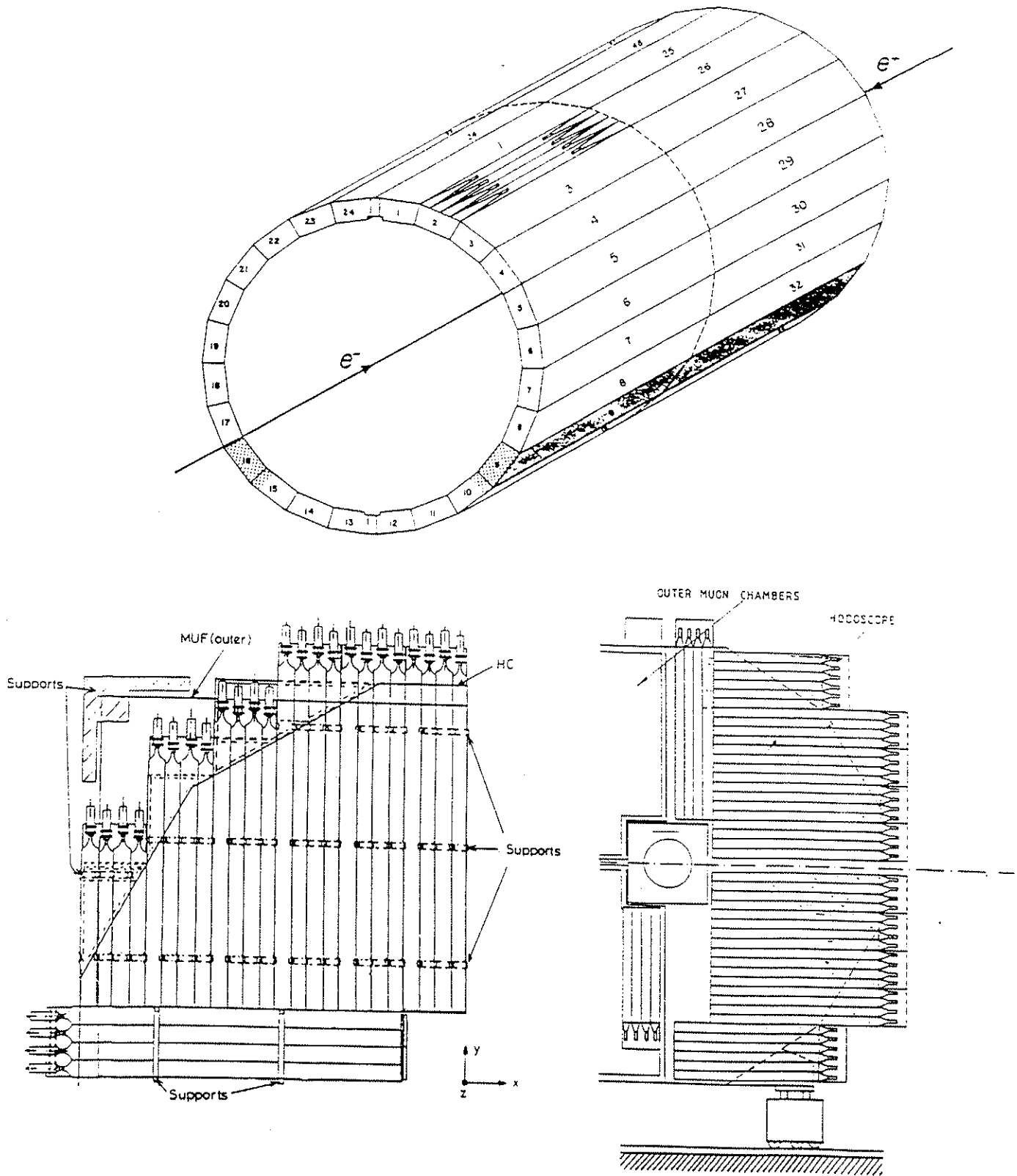
Figure 7.11: a) View of the TOF scintillators and photomultipliers, at about 312 cm from the beam line covering the barrel region b) View of the HOF scintillators and photomultipliers covering the endcap region
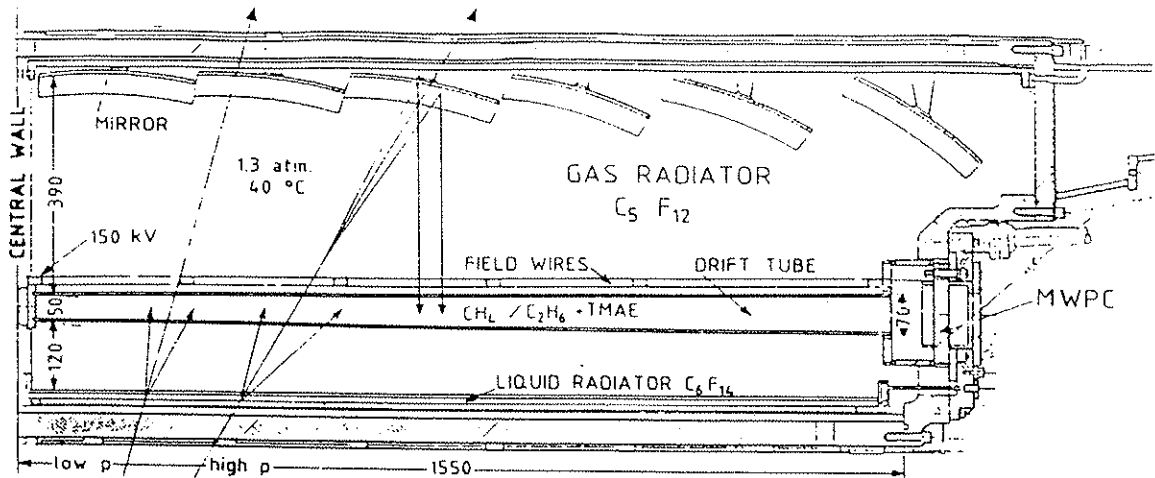
Figure 7.12: Cross-section of the barrel RICH.

7.6 Ring Imaging Cerenkov Detectors (RICH)

The aim of the DELPHI Cerenkov counters is the identification of hadrons (π, K, p) in a wide range of the momentum spectrum. Separation π/K up to 20 GeV and K/p up to 30 GeV is foreseen in the Barrel RICH. This detector is a 3.5 meters cylinder with inner and outer radii respectively 123 cm and 192 cm covering the angular region $41.5° < \theta < 138.5°$. It is segmented in 24 $R\Phi$ sectors in each Z hemisphere, each with a liquid radiator box mounted near the inner radius, followed by a drift tube and a gas radiator medium. A total of 288 parabolic mirrors cover the outer surface of the detector.

Cerenkov photons produced by the particles crossing the liquid radiator medium enter the drift tubes, where they are absorbed by a photo-ionizing agent (TMAE). The electrons produced by ionization drift along the tubes to the end plate where they are detected by a Multi Wire Proportional Chamber (MPWC). The hit anode wire gives the ϕ coordinate and the drift time gives the z coordinate of the Cerenkov photon. The cathode strip barycenter gives the R coordinate at which the ionization occurred.

Photons produced by Cerenkov effect and emitted in a cone centered in the particle trajectory in the gas radiator medium are reflected by the parabolic mirrors and focused in the drift tubes, defining the characteristic ring images. As before, the produced photoelectrons drift to the readout chamber. The depth coordinate measured by the cathode strips allows separation between electrons from the two kinds of Cerenkov rings. The velocity of the particle can be determined from the size of the detected ring of Cerenkov photons.

The Barrel RICH has collected data during the running period of 1990 and is expected to be fully operational during 1991.

Chapter 8

TRIGGER & DAS

At LEP, the time interval between bunch crossings in the interaction points of the beams is 22.35 μs. If one interaction would be registered in the detector at each bunch crossing, the typical event rate would be about 44.5 KHz.

Given the designed machine luminosity $\mathcal{L} \sim 10^{31} \, cm^{-2} \, s^{-1}$ and the theoretical cross-section for e^+e^- annihilation ($\sigma \sim 35 \, nb$) at the resonance peak ($\sqrt{s} = 91.1 \, GeV$), the expected rate of Z^0 events, dN_{Z^0}/dt, would be

$$\frac{dN_{Z^0}}{dt} = \mathcal{L} \, \sigma \simeq 0.35 \, Hz \tag{8.1}$$

To the cross-section for e^+e^- annihilation must be added the cross-section for the other processes occuring in e^+e^- interaction. The more important arise from the t-channel interactions, namely Bhabha scattering and the $\gamma^*\gamma^*$ interactions, which cross-sections, integrated over the full solid angle, submerge by some orders of magnitude the cross section for Z^0 production.

In the real detector, no full coverage of the solid angle exists for technical reasons. The uncovered regions are the very small angle regions (close to the beam line), accounting for the bulk of the cross-section of the t-channel processes characterized by a steep variation of the differential cross-section at very small angle. Neverthless, the remaining cross-section integrated over the detector acceptance region is still sizable.

The total rate of events recorded in the detector has the following components [1]:
• The rate of produced γ, Z^0 events, dependent on the center of mass energy of the annihilation process: 0.35 Hz on the peak of the resonance, diminishing off peak.

---

[1]These rates correspond to a value of $\mathcal{L} \simeq 10^{31} \, cm^{-2} \, s^{-1}$. In practice, during the 1990 data taking period, the LEP peak luminosity was of about $7 \cdot 10^{30} \, cm^{-2} \, s^{-1}$.

● The Bhabha event rate in the small angle luminosity detectors, approximately constant in the resonance range. It is of the same order of magnitude (see Chapter 12) of the Z^0 event rate at the peak: 0.3 Hz.

● The rate of events from $\gamma^*\gamma^*$ interactions, due to a sizable cross-section for this process within the detector acceptance.

● The contribution from the machine background events (off-momentum beam particles, scattered photons, beam gas collisions, etc.). The event rates from these processes can be controlled by a sophisticated system of collimators along the beam line and by the dimensions and geometry of the vacuum chamber surrounding the interaction point.

● The rate of cosmic events crossing the detector volume. Such rate can be estimated and controlled to desired levels. Cosmic events are useful for monitoring, survey and calibration of the detector.

● Noisy detector components can generate signals faking real interactions and contribute to the total rate of recorded events.

It is commonly accepted that the signal(S) over background(B) event ratio at LEP is at the Z^0 peak:

$$\left(\frac{S}{B}\right)_{LEP} \simeq 0.1 \div 0.2 \qquad (Z^0\ peak) \tag{8.2}$$

depending on the machine background conditions, and of a few parts per thousand off the peak.

The task of gathering all events of physics interest with a tolerable amount of background events is performed by the Data Acquisition System(DAS) and Trigger System. The architecture of the DAS and Trigger System for the LEP experiments was designed with main objective[57] "to read,filter and record basic event data after successive trigger and filter levels of increasing selectivity power".

8.1   DELPHI Trigger and Data Acquisition System

The simplified block diagram of the Data Acquisition System of the DELPHI experiment is sketched in figure 8.1, with the typical rates and timings at each decision level.

The system is organised in several levels of triggering and buffering. Once a Beam Crossing Signal (BCO) is received, the information of the fast detectors (response time of few hundreds of nanoseconds) is used to perform the *first level trigger* $(T1)$. The processing time is limited to 3.5 μs. If the first decision level is positive, the system takes the next 39 μs to perform the *second level trigger* $(T2)$. It uses the information from the drift detectors like the TPC and HPC, which is available only 10-20 μs after the BCO. The quality of this information allows a high degree of selectivity. However, each time the second level of trigger is activated, one beam crossing is lost. If the

Figure 8.1: Typical configuration, rates and timings of the DELPHI Data Acquisition System

$T2$ decision is negative, the system has about 5 μs to reset the front end electronic before the next BCO. If on the contrary, the decision is positive, the information available in the front-end buffers is read into local buffers and the front-end electronics is reset to the next interaction. This operation called Front-End Freeing takes about 500 μs except for a few detectors for which it can take a few miliseconds. The local buffers have the capacity to store several events (minimum 4) in order to deal with the statistical fluctuations of the $T2$ arrival time. This also means that the readout of the local buffers into a global event buffer is asynchronous with the $T2$ front-end freeing operations. Typically there is one local buffer per detector. Associated to it there is one processor that controls the data transfer operations and performs a more sophisticated trigger selection, the *third level trigger* ($T3$). The third level trigger information from each detector is centralized in a global third level trigger processor. Associated to the global event buffer, a battery of parallel processors performs the last level of filtering and tagging, the *fourth level trigger* ($T4$), before data is transfered to the central computer and stored in magnetic cartridge.

For the purposes of readout and trigger, DELPHI is divided in *partitions*. Most of the partitions correspond to a detector or part of a detector (e.g. TPC,HPC subdivided in 2 partitions each) but in some cases several detectors are grouped in the same partition (e.g. TOF/MUB , FCA/FCB). Additional partitions are reserved to the Trigger System (Trigger Partition) and to the hardware not assigned to any detector (Central Partition). All data transfers are made according to FASTBUS protocol and interconnections.

The Data Acquisition System in operation is a simplified version of the architecure shown in figure 8.1 with 2 levels of control and decision inspired in the first 2 levels of figure 8.1 but with different decision rates at each level. The full integration of the third and fourth levels in the readout and trigger systems is expected to be soon operational.

Some of the limitations constraining the timings of each level of decision or readout and the selectivity achieved at each reduction step are due to:

Intrinsic Detector Limitation
• The TPC has typical values of drift velocity of 6 cm/μs. Due to the length of the detector drift volume (maximum drift distance of about 1.2 meters), at least 20 μs are necessary to read and make a first raw processing of the information registered in the detector. This means that the TPC information on the track multiplicity and topology can only be used in the second or higher trigger levels. However, in the forward region when the tracklength within the TPC is less than 10 cm, the drift time is much shortened (less than 1.5 μs) allowing the use of the TPC in the fast trigger for forward tracks.

• In the HPC, the maximum drift distance corresponds to a module lenght (80 cm). So, about 10 to 12 μs are necessary to read the HPC information. For fast trigger

purposes, only the information available from the layer of scintillators in each module can be used as an energy trigger.

- Forward Muon Chambers, where the typical drift time is of 14 μs, imposes that this detector cannot participate in a fast muon trigger.

Front — End electronics limitation
This corresponds to the minimum time needed by the front-end electronics to be ready to accept a new event after a reset. It is mainly a hardware limitation due to the speed of the electronics, dimension of buffers and propagation of signals. While most of the DELPHI partitions need less than $1\mu s$ to be ready before the next BCO signal, some detectors need a few μs to reset their front-ends.

Readout Time and Event Size
This is the intrinsic time needed by the readout system to get and assemble the data from the multiple buffers to build the event structure. The volume of data per event and the bandwidth of the communication buses affects the rate at which events can be transfered and are recorded in the data storage medium.

8.2 Trigger System

The 2 main tasks of the DELPHI trigger system are:

- Select events to be recorded by the Data Aquisition System (DAS).
- Control and synchronization of the readout of the individual detectors and of the status of their front-end electronics and Front End Buffers (FEB).

The typical timing of the trigger system is sketched in figure 8.2. The reference time is taken from the BCO (Beam Cross Over) signal, comming from beam pick-up detectors placed upstreams from the experimental areas, detecting the crossing of the beams and sending a signal to the experimental areas. The 2 main entities of the trigger system are the Trigger Supervisor (TS) and the Local Trigger Supervisor (LTS).

8.2.1 The Trigger Supervisor

The Trigger Supervisor main functions are:

- Distribute the timing signals to the detectors.
- Receive the subtrigger data and make the first (and second) level trigger decision.
- Control the readout sequence and receive from each detector the signal of Front End Ready (FE_RDY), after the freeing of the FEBs.
- Comunication with the Event Supervisor at different steps of the readout process.
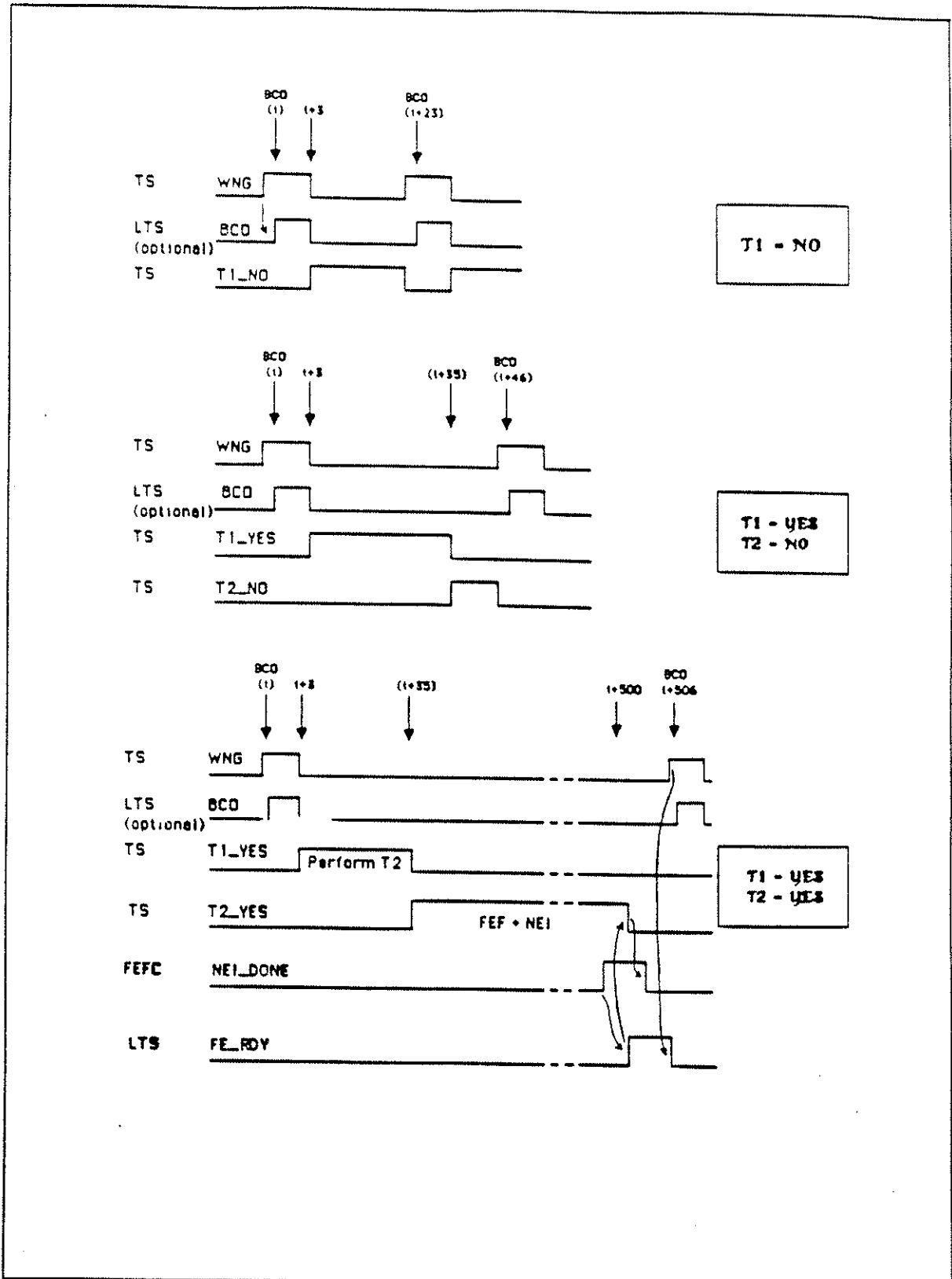
Figure 8.2: Timings and sequence of signals in the data acquisition and trigger system

The architecture of the Trigger Supervisor System is implemented using the following modules:

- Trigger Supervisor Control Box (*ZEUS*).

- Trigger Supervisor Decision Box (*PYTHIA*).

8.2.1.1   ZEUS

The main functions of this module are:

- Reception of the radio-frequency (RF) signals from the LEP control system.
- Reception of the Beam Cross Over signal (BCO) from the beam pick up detectors.
- Selection of the partitions participating in the trigger and data acquisition and checking of their status.
- Distribute to each partition (through PANDORA) the timing sequence for the trigger and the sinchronization signals (BCO,Cosmic,Test,Random) necessary for the readout.
- Receive and broadcast the timing signals needed by the front-end electronics related to the front-end buffering and freeing procedures (FE_READY signal), conditioning them to the status of the readout process.
- Exchanges timing and decision signals with PYTHIA.
- Inform the Event Supervisor of the completion of the Front End Freeing (FEF).

ZEUS receives the BCO signals and generates the CLK_BCO (Clock-BCO) signal at each beam crossing, and the WNG_BCO (Warning-BCO) when all FE_RDY (Front-End Ready) signals (from each detector) are received, informing the Event Supervisor of the completion of the Front-End Freeing.

8.2.1.2   PYTHIA

PYTHIA is the source of decision used by ZEUS for physics triggers, during the normal sequence of data taking with beam (trigger type BCO). After the subtrigger data from each detector (participating in the trigger) is encoded, a DATA_READY signal is sent to PYTHIA. This module combines the signals from individual detectors on the basis of pre-loaded and programmable look-up tables containing the logical combinations of the input signals and takes the central decision of accepting or rejecting an event. The pattern of fired triggers is saved at each event in the Trigger Partition data. Once a trigger decision is taken in PYTHIA, it is sent to ZEUS and the corresponding signal (T1_YES,T1_NO,T2_YES,T2_NO) is sent to the PANDORAs.

8.2.2   Local Trigger Supervisor

8.2.2.1   PANDORA

It is is the Local Trigger Supervisor Decision Box. Most partitions are controlled by a single PANDORA and a few partitions require more than one box. The functions of PANDORA are:

• Knowledge of the operating mode of the partition: *global*, if the partition is taking data integrated in the central data acquisition system (Central Partition) or *local* if the detector is taking data in standalone mode.
• The transmission of timing and synchronization signals from ZEUS to the front-end detector electronics.
• The transmission of the FEF signals from the partitions.

8.2.3   T1, the first level trigger

T1, the first level of decision, is a fast hardware trigger synchronous with the event, using crude detector information from MWPC wires or cathode pads and from scintillators. The detector information available at this level is of the kind yes/no tracks, yes/no energy deposition above threshold, yes/no back to back topology of tracks or energy depositions.

After the FE_RDY from all partitions have been received, the WNG_BCO signal is sent by ZEUS to all front-end electronics. The subtrigger data from the detectors that provide a fast response (few hundred nanoseconds to 2 μs) is assembled by the Trigger Supervisor and its decision (via PYTHIA) is issued 3.5 μs after the BCO was sent, in one the following terms:

• T1_YES if the first level trigger decision is positive relative to the selected criteria and thresholds (tracks,energy,back-to-back,etc.). Only after this decision, the TPC gate is opened and remains active for about 35 μs, time during which the T1_YES signal is permanently kept active. Once a T1_YES signal is issued, a second process of event validation is initiated, called the second level trigger (T2).

• T1_NO if the first level trigger decision is negative relative to the selected criteria and thresholds (tracks,energy,muon,bhabha,etc.). Once a T1_NO has been decided, it stays up (active) until the next beam crossing, at which time a new WNG_BCO signal is sent.

In the implemented system the measured rate of T1_YES signals is approximately $\leq$ 12 Hz. One BCO signal is lost in case a T1_YES signal is issued.

8.2.4   T2, the second level trigger

T2, the second level of decision, is a hardware trigger synchronous with the event, using more detailed information from individual detectors like TPC or HPC after a first processing of their data. More refined estimation of the energy in the calorimeters and more granular track information are available. The signal T2_YES or T2_NO must be issued about 39 μs after the T1_YES, following the digitization of detector data.

• After a T2_YES signal, ZEUS disables the distribution of timing signals and detectors complete the digitization of their raw data. A deadtime of about 500 μs is introduced in order to read the data from the Front End Buffers and reset the front end electronics. When the front end freeing is completed, each partition sends back the FE_RDY signal to ZEUS. The availability of a new event is then comunicated to the Event Supervisor.

• In case a T2_NO is active 39 μs after last BCO was sent to the front end electronics, this signal stays active for 7 μs more (after about 46 μs since last BCO) when a new BCO signal is again sent by the trigger system. One beam crossing is lost when a T2_NO signal is generated.

In the implemented system the measured rate of T2_YES signals is 1.5 Hz. About 300 BCO signals are lost in case a T2_YES signal is issued.

8.2.5   Dead Time

Being f_i the rate (in Hz) of signals at the i-th level of trigger decision and f_{BCO} the frequency of the Beam Cross Over signal (bunch crossing rate), the dead time on a machine like LEP is defined as[58]:

$$Dead\ Time\ =\ \frac{\sum \left[(Number\ of\ BCO's\ lost)_{level\ i}\ \cdot\ f_i \right]}{f_{BCO}} \tag{8.3}$$

In the case of DELPHI, with $f_1 \approx 12\ Hz$ and $f_2 \approx 1.5\ Hz$, the dead time is

$$(\ Dead\ Time\ )_{DELPHI}\ =\ \frac{(\ 1\ \cdot\ f_1\ +\ 300\ \cdot\ f_2\ )}{44500}\ \simeq\ 1\ \% \tag{8.4}$$

This estimation is consistent with the deadtime measured offline (2-3 %). During the last weeks of the 1990 data taking period, new triggering conditions were tested, allowing higher f_1 rates (several hundreds Hz), with the corresponding increase of the dead time.

8.3   The Readout System

The multiple readout operations performed by the Data Acquisition System (DAS), asynchronously with the crossing of the beam bunches can be grouped in two main tasks namely:

• The transfer of the data from each detector front end buffer to the local multi event buffer and formatting of the detector data.

• The assembly of the global event structure followed by the transfer of the event raw data to the main computer for permanent storage.

Each front-end module (ADC's, flash ADC's, TDC's) has one or more front-end buffers (FEB) where the digitized data is stored. The digitization time is detector dependent and ranges from a few hundred nanoseconds up to 20 μs for the detectors with longest drift times.

These buffers are read by the Crate Processors (CP) into the Crate Event Buffers (CEB) of 256 kbyte size. The number of CP per partition is variable (depending in the amount of data to be handled in the partition), the total CEB space being of 15 Mbytes in DELPHI. The maximum number of events that can be stored in the CEBs, dependent on the event size for the partition, varies from 20 up to 256. At this level, the data from each partition is formatted and structured in sequences of blocklets of few dozens or few hundreds words. The readout of the CEB(s) of each partition into the corresponding Multi-Event Buffer (MEB) is coordinated by the Local Event Supervisor (LES) and takes typically 1 ms. The Local Event Supervisors are under the control of the global Event Supervisor (ES).

The data in the 15 Multi-Event Buffers (one per detector) is asynchronously transfered to the Global Event Buffer (GEB, with a 2 Mbyte RAM memory) by the Block Mover, being this task coordinated by the Global Event Controller (GEC). This transfer takes typically 30 ms. Once stored in the GEB, the final stage of data transfer is performed by an optical fiber link connecting the detector at 100 meters depth and the Data Acquisition computer at the surface, where the data is finally recorded in the data storage medium (magnetic tape or cartridge).

The processors controlling the data transfer are Fastbus masters, namely Fastbus Intersegment Processors (FIP) controlling the crate readout and General Purpose Masters (GPM) in the readout phases controlled by the LES,ES or GEC.
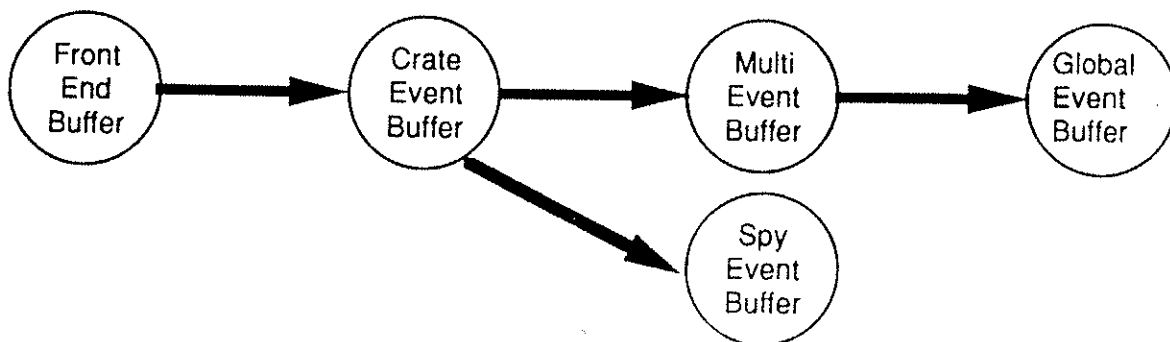
8.4 T3 & T4, the third and fourth filtering steps

The DELPHI readout system in operation until the end of the 1990 data taking period did not include the third and fourth levels of trigger, not yet fully integrated in the DAS environment. Both are software triggers, asynchronous with the event.

The third level of trigger, when in operation, will perform a first processing of the data from some detectors, with the crude computation of some quantities which are used to decide the readout of the data in the Multi-Event Buffers into the Global Event Buffer. The time available to this level is of the order of 20 ms.

The fourth level of trigger is extensively tested in offline conditions. It will allow to run online, in IBM 3081/E emulators, simplified versions of the pattern recognition algorithms, processing the event data stored in the Global Event Buffer and performing the tagging of events. The maximum time to process one event is of the order of 500 ms.

Acting on the data before the transfer to the data logger computer, this level will ensure the selectivity needed to perform the fast filtering of events for hot physics channels and will reduce the amount of background events to be handled in the offline analysis.

The efficiency of the reconstruction algorithms, studied from real data, and the tunning of the tagging criteria extensively done in offline environment, were carried on during the 1990 data taking period.

8.5   The "B1 Trigger"

A simpler but very efficient trigger system[59] was used during the whole period of data taking as the main trigger system. It consisted of counting and combining in room B1, with simple NIM electronics, the signals coming from several detectors, generating and broadcasting the T1_YES signal.

The scalers counting the signals sent by individual detectors (or group of detectors in coincidence) participating in the trigger were recorded on the raw data structure on an event by event basis, allowing offline studies of their differential contents or in other words of the signals used to decide upon the triggering of each event. These studies were of great importance in the understanding of the trigger efficiencies for different topologies and final states as a function of momentum, energy, track multiplicity, for different angular regions (θ, Φ) of the detector.

For trigger purposes, HPC and TOF barrels were Φ-segmented in 8x90° octants (4 in each hemisphere) and the layer of scintillators inside HPC modules (at 4.5 X_0 depth) was adjusted to an energy of about 2 GeV. The HOF layer of scintillators in each endcap was segmented in quadrants, and for the energy trigger in the forward/backward region, the total energy in each endcap of the FEMC calorimeter was used.

The main types of triggers are:

BACK TO BACK triggers, require coincidence of signals from back to back detector elements:
- *Track triggers* - coincidence of signals from tracking detectors (ID-OD, FCA-FCB).
- *Scintillator triggers* - combine signals from TOF,HPC or HOF sectors.
- *Energy triggers* - back to back energy depositions above a given threshold in the HPC,FEMC or SAT calorimeters.

MAJORITY TRIGGERS, requiring a number of signals coming from at least N (determining the type of majority) TOF,HPC,OD octants.

The main types of signals (from single detectors or coincidence of detectors) and corresponding mnemonics are described as follows.

8.5.1   Barrel Trigger

- *IDOD* - Back to back trigger resulting from coincidences of back to back Φ octants of OD in coincidence with ID. Signals from 3 out of 5 layers in OD or ID Trigger Chamber could be used to set this trigger. Highly efficient, it was the main back to back track trigger for the barrel region.

• *IOMJ* - Trigger requiring signals in the ID in coincidence with at least 2 signals (majority two) in the OD octants.

• *HPBB* - Back to back trigger, using the HPC scintillators. Energy depositions above a given threshold (2 GeV) in 2 back to back HPC octants activate this trigger signal.

• *TOBB* - Back to back trigger combining TOF counters information. The coincidence of signals from 2 opposite octants sets this trigger signal.

• *HPMJ* - Majority trigger requiring energy depositions above a given threshold (2 GeV) in at least 2 HPC octants.

• *TOMJ* - Majority trigger requiring signals coming from at least 2 TOF octants.

• *THMJ* - Majority trigger requiring coincidence between 1 TOF octant and the geometrically corresponding HPC octant.

• *SCOD* - Trigger requiring a signal from 1 TOF octant in coincidence with a signal from any OD sector.

8.5.2 Forward-Backward Trigger

• *FEHI* - Electromagnetic energy trigger requiring energy deposition in any FEMC endcap above an energy threshold of 6 GeV.

• *FEBH* - Trigger for low angle Bhabha in the forward-backward region covered by FEMC. Requires energy deposition in both endcap calorimeters above a threshold of 4 GeV.

• *HOBB* - Trigger requiring coincidence of signals from back to back HOF counters (hodoscopes).

• *FWMJ* - Forward majority trigger. At least 2 of the 6 following components were required:
1) Signals from at least 1 HOF quadrant (in the forward or in the backward hemisphere).
2) Energy deposition above 2 GeV in the forward endcap of FEMC.
3) Energy deposition above 2 GeV in the backward endcap of FEMC.
4) At least one signal from the combined FCA/FCB subtrigger in the forward endcap.
5) At least one signal from the combined FCA/FCB subtrigger in the backward endcap.
6) Single arm coincidence of ID and OD signals in the barrel region.

8.5.3   Bhabha Trigger

This trigger was done in PYTHIA with the following components:

- *SABH* - Main Bhabha trigger, requiring coincidence of back to back energy depositions above a given threshold (10 GeV) in each arm of SAT calorimeter.

- *SAAR* - Single arm SAT trigger, requiring total energy deposition above threshold in one arm of SAT calorimeter.

8.5.4   B1 efficiency for physics

The efficiency of the B1 set of triggers for the main types of Z^0 events and the efficiency of the PYTHIA trigger for Bhabha events are shown in next table[1]. The efficiencies are computed using events detected in the following angular regions of the detector:
- $25° < \theta < 155°$ for $Z^0 \rightarrow hadrons$ events.
- $43° < \theta < 137°$ for $Z^0 \rightarrow \mu^+\mu^-$ and $Z^0 \rightarrow \tau^+\tau^-$ events.
- $50° < \theta < 130°$ for $Z^0 \rightarrow e^+e^-$ events.
- $43 \, mrad < \theta < 135 \, mrad$ for Bhabha events.

Physics channel	B1 trigger efficiency (%)
$Z^0 \rightarrow hadrons$	99.5 ± 0.2
$Z^0 \rightarrow e^+e^-$	99.7 ± 0.1
$Z^0 \rightarrow \mu^+\mu^-$	97.0 ± 1.0
$Z^0 \rightarrow \tau^+\tau^-$	97.0 ± 1.0
Bhabha (SAT)	>99.9

---

[1]Quoted numbers are extracted from DELPHI published results

Part III

Detection and Analysis of $\tau^+\tau^-$

Chapter 9

OFFLINE SOFTWARE

The software of reconstruction and simulation of events in a complex detector like DELPHI, plays a very important role in all the analysis chain. The event reconstruction programs convert the raw data provided by the detectors into the information on the particles produced in the interactions. This information is used to get the physics results. The simulation programs start from the physical particles produced by a given generator and use Monte Carlo methods to simulate their behaviour when traversing the detector. The comparison between real and simulated data is extensively used in the several stages of the analysis, from the understanding of detector behaviour, its alignment, calibration and efficiencies, up to the extraction of the final physics results.

The event viewing software is of crucial importance for the interactive analysis. Scan of interesting events, monitoring and debugging of the results obtained from the reconstruction programs or the study of the individual detectors response and efficiencies to the multiple final states and topologies, are some of the tasks that can be performed with the interactive event viewing software.

The availability of good and accurate Monte Carlo generators of e^+e^- interactions is also a major requirement to precision measurements foreseen at LEP. This is acomplished by a set of programs reproducing the effects of the radiative corrections with uncertainties at the level of below 1% for most of the physics channels. In the following, the general features of such a generator developed for the studies of tau pair production and decay at LEP energies, are described.

9.1 Generation

KORALZ[61,62] is the Monte Carlo generator especially adapted and suited for the the study of τ pair production, decay and detection. In particular, it allows to evaluate how the physical spectra of final states from tau decays are "dressed" by the QED and electroweak radiative corrections, at LEP energies. The event generation has a modular structure corresponding to the consecutive stages from the initial state radiation followed by the Z^0 production and decay into $\tau^+\tau^-$, the individual τ radiation and decay, ending with the eventual radiation by the final state particles.

QED radiative corrections are treated by allowing multiple soft photon radiation using a method related to the Yennie-Fraustchi-Suura [63] prescription and the corresponding exponentiation of photon spectra.

Electroweak radiative corrections including vacuum polarization, corrections to the propagators, top quark mass and Higgs mass effects, are included in a very complete electroweak library used during the generation.

A complete menu of options allows to switch on/off the final state QED radiation, the vacuum polarization functions and changes of the "free parameters": unknown masses (m_{top}, M_{Higgs}, m_{ν_τ}), the resonance parameters (M_Z, Γ_Z), the weak mixing angle ($\sin^2\theta_w$), the number of neutrinos. The selection of the decay mode for each tau and parameters like the soft/hard photon cut are under user control.

The spin of τ is properly taken into acount in the implemented matrix elements used for the decays and correlation between τ spins is properly accounted for.

This generator includes almost all τ decay modes, adding to the major decay modes ($e, \mu, \pi, \rho, A_1, K, K^*$) the rare multipion and kaon decays [64]. The generated energy spectra of final state particles for the main decay modes are shown in figure 9.1.

KORALZ allows the study at the level of the event generation, of:

- Energy spectra of radiated photons from initial state beam particles, from the produced τ leptons and from the final state particles coming from τ decays (figure 9.2).
- Angular distribution of the emitted photon(s) (figure 9.2).
- Relative importance of the different kinds of radiative corrections (initial and final state radiation, electroweak corrections, etc.) contribution to the above spectra.
- Deformation of particle energy spectra by the radiation at the several stages and estimation of the correction factors in the measured spectra.
- Study of the effects of radiative corrections in the determination of the "observables" (e.g., τ polarization, forward-backward asymmetry).
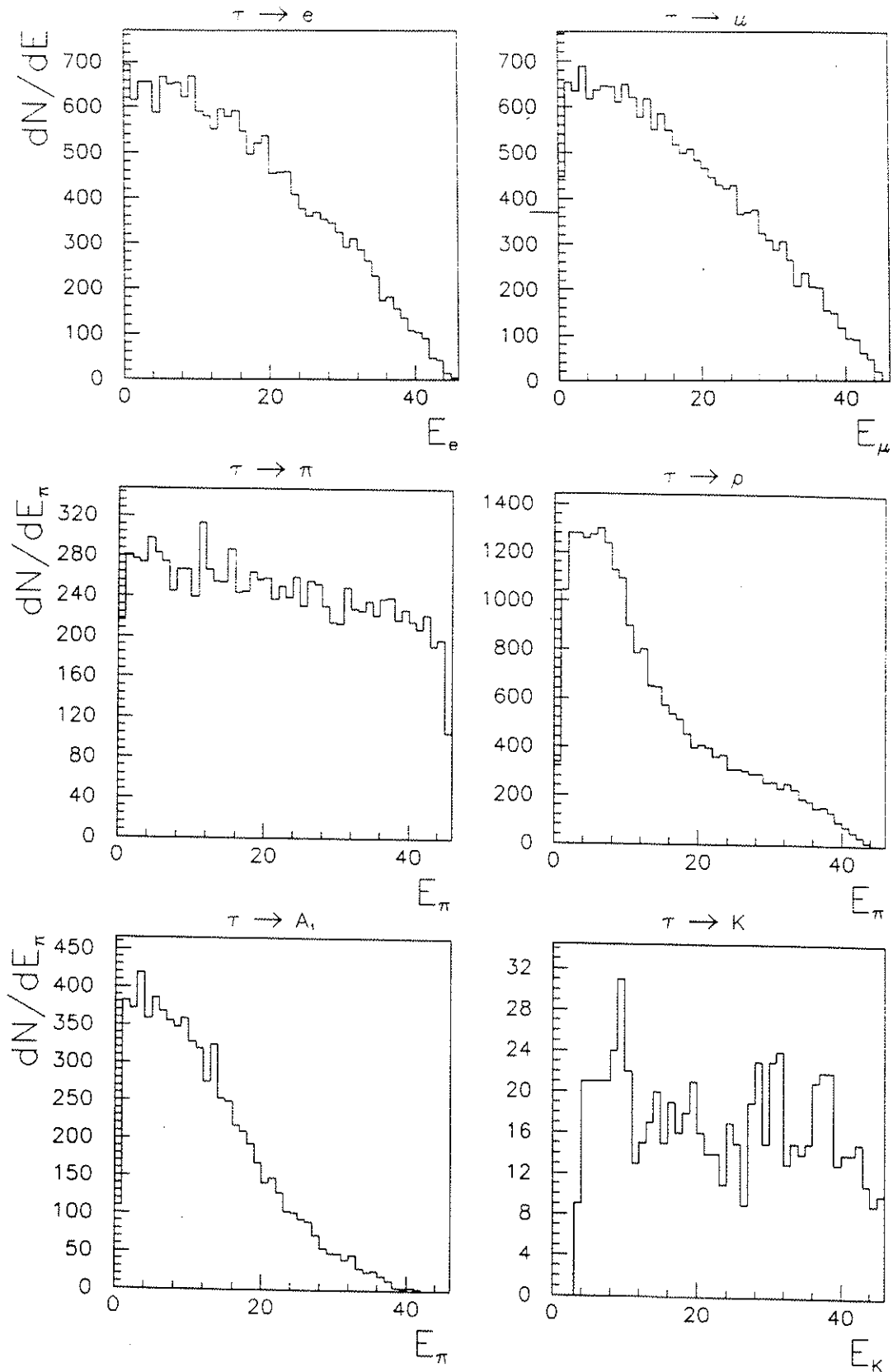
Figure 9.1: Energy spectra (QED,weak radiative corrections effect included) of the particles produced in the main τ decay modes, generated by KORALZ
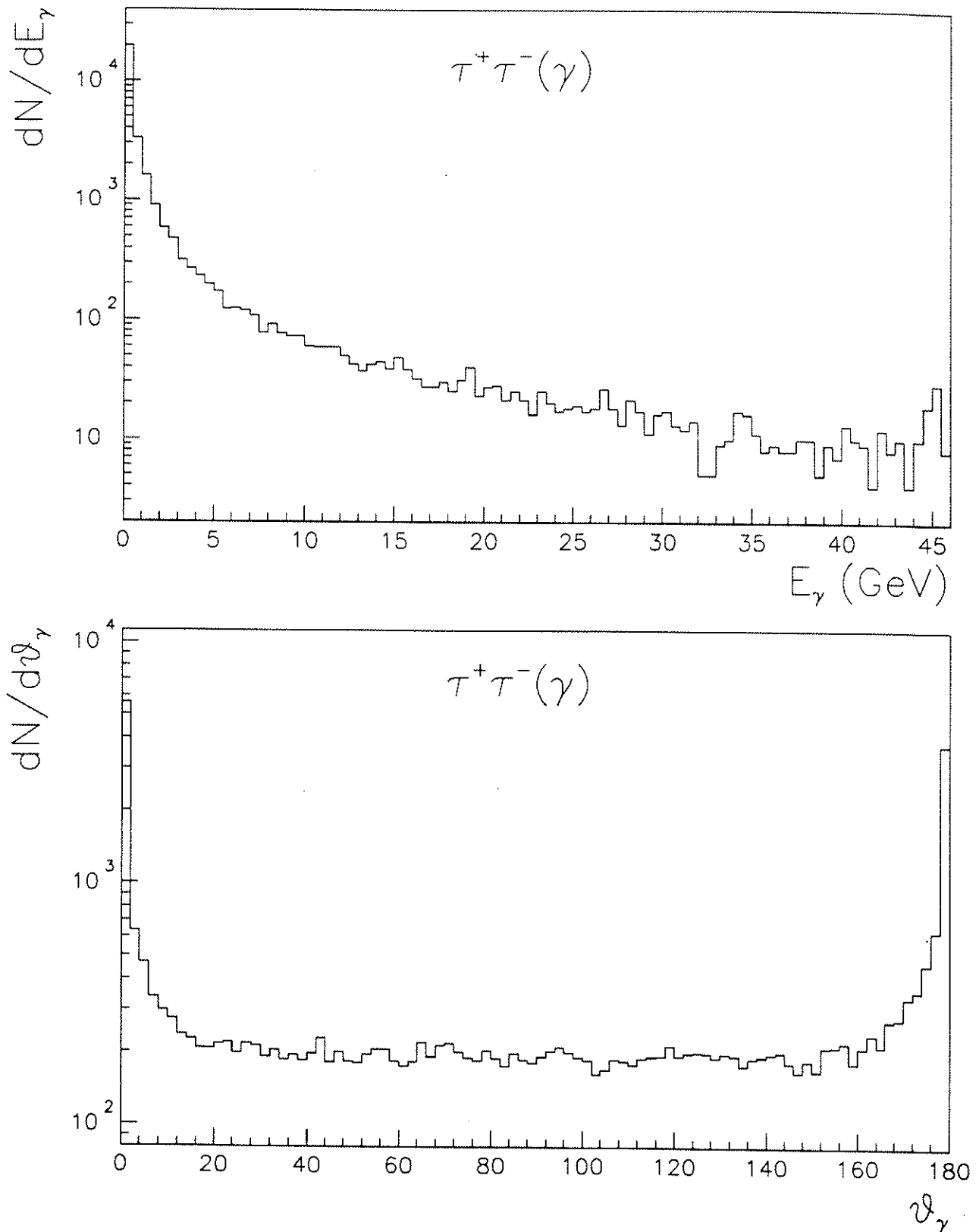
Figure 9.2: Energy (a) and angular distribution with respect to the τ direction (b) of the (initial or final state) radiated photons

9.2 Simulation

DELSIM[65] is the DELPHI simulation program. It consists of 2 main parts, one dealing with the generation of the particles and its decays and the other doing the tracking of the particles through the detector materials.

9.2.1 Generation

The generation part includes DELSIM own generators for all $e^+ e^- \rightarrow f\bar{f}$ processes, via Z^0 or γ exchange and generators for $Z^0 H^0$, $H^+ H^-$, 2γ events, among others. The fragmentation and/or decays of final state quarks is done via LUND MC routines. Radiative corrections to Z^0 production are not very accurately taken into account. However, external generators like MUUSTRAL, EUROJET, JETSET, KORALZ, DYMU3, etc. can be easily interfaced with DELSIM.

The "story" of the generation (mother-daughter-sister relation between particles in decay processes, story of fragmentation processes) is saved along the full chain to be later used (after reconstruction) in the physics analysis studies.

Single or multiple particle generators allow the study of the detectors response to particles of momentum and direction in the range specified by the user. These generators are specially useful to study the detector efficiency and resolution as a function of momentum, energy, angle, etc..

9.2.2 Tracking

The tracking part of DELSIM consists of a complex set of routines responsible for the transport of the particles through the detector after generation. It takes into account secondary processes of several nature:

- Tracking in the magnetic field

- Multiple scattering

- Energy loss

- Bremsstrahlung

- Photon conversion

- Compton scattering

- Nuclear interaction and absorption

One of the relevant features of this program is the simulation of the raw data for each detector up to the digitizations of pulse heights, drift times etc., as if they would have been produced in the real data taking conditions. This allows the study and tuning of detector response to crossing particles, and the determination of several parameters to be used in the reconstruction of real data. For detectors measuring quantities with the accuracy of few dozens or hundreds of microns, a very detailed tracking and simulation of the physical processes occuring inside the detector are needed. Also, detailed studies of the particle showers inside the dense materials of the calorimeters are necessary. For this, each module (detector) of the program provides a set of routines responsible for the simulation of detector response to the crossing particle. During the tracking of each particle, control is given at the end of each step to detector routines, where the signal left by the particle is calibrated and evaluated to simulate the detector response.

9.2.3   Detector description

For this purpose, a very detailed description of the materials, sensitive volumes, boundaries, shapes, etc., is needed. That exists under the form of a database containing for every detector, volume, structure, support or electronic box, the detailed description of the constitutive materials its shape and position. Also, the position of the sensing devices (wires, pads) inside each detector volume are described in this detector description database. Modifications to this database are made whenever the geometry of a detector changes or when the whole set is realigned by software.
The detector database also contains the calibrations for all the components of the different detectors, as well as the parameters (like voltages, pressure, temperature, etc.) to calculate quantities needed for the reconstruction, such as drift velocities or delay times. During data taking the calibration files which will be used for event reconstruction are updated by a Slow Control Software System.

9.3 Reconstruction

DELANA[66], the DELPHI reconstruction and analysis program, is the responsible for assembling and collecting the information from different modules at different levels and stages of the reconstruction pass. The architecture of DELANA [67,68] contains, in addition to all commom ideas implemented in reconstruction programs, constrains and pioneering ways of combining information in a setup with 16 detectors some of them split (physically or for readout purposes) into 2. Some features of the event reconstruction in DELPHI can be summarized as:

- The track reconstruction results in most of the acceptance region from the combination of 4 detectors (ID-JET,ID-TRIG,TPC,OD or ID-JET,TPC,FCA,FCB) physically separated and with different measurements and errors.

- A "natural" separation exists between barrel tracking chambers and endcap tracking chambers, raising the problems of track reconstruction in regions where both barrel (ID-JET,TPC) and endcap detectors (FCA,FCB) measure the same track, namely, how to combine their different measurements and how to weight their errors.

- For high multiplicity events with jets spanning over the barrel and endcap regions (simulateneously), unambiguous association of track segments in the several barrel and endcap detectors is very difficult. This raises combinatorial problems and a very delicated logic is needed to disentangle the correct association of track segments.

- Reconstruction of Ring Image Cerenkov data, imposing very stringent requirements on track reconstruction and extrapolation accuracy.

9.3.1 First stage pattern recognition

DELANA consists of a set of modules (1 per detector + general purpose modules) operating in two stages. In the first stage of pattern recognition, each detector individually processes its raw data, reconstructing the space points and the track segments inside the tracking chambers, or the energy clusters and showers in the calorimeters. At this level, each detector works independently. However, after this stage of reconstruction some ambiguities remain. Some examples are:

- VD - The Z coordinate corresponding to each of its $R\Phi$ measurements remains undefined due to the fact that this detector does not measure the longitudinal coordinate.

- ID - Left-Right ambiguity in its JET part: the measured drift time values do not allow to raise the ambiguity about the position (left or right) of the crossing track relative to the wire position. The association of the JET chamber information with
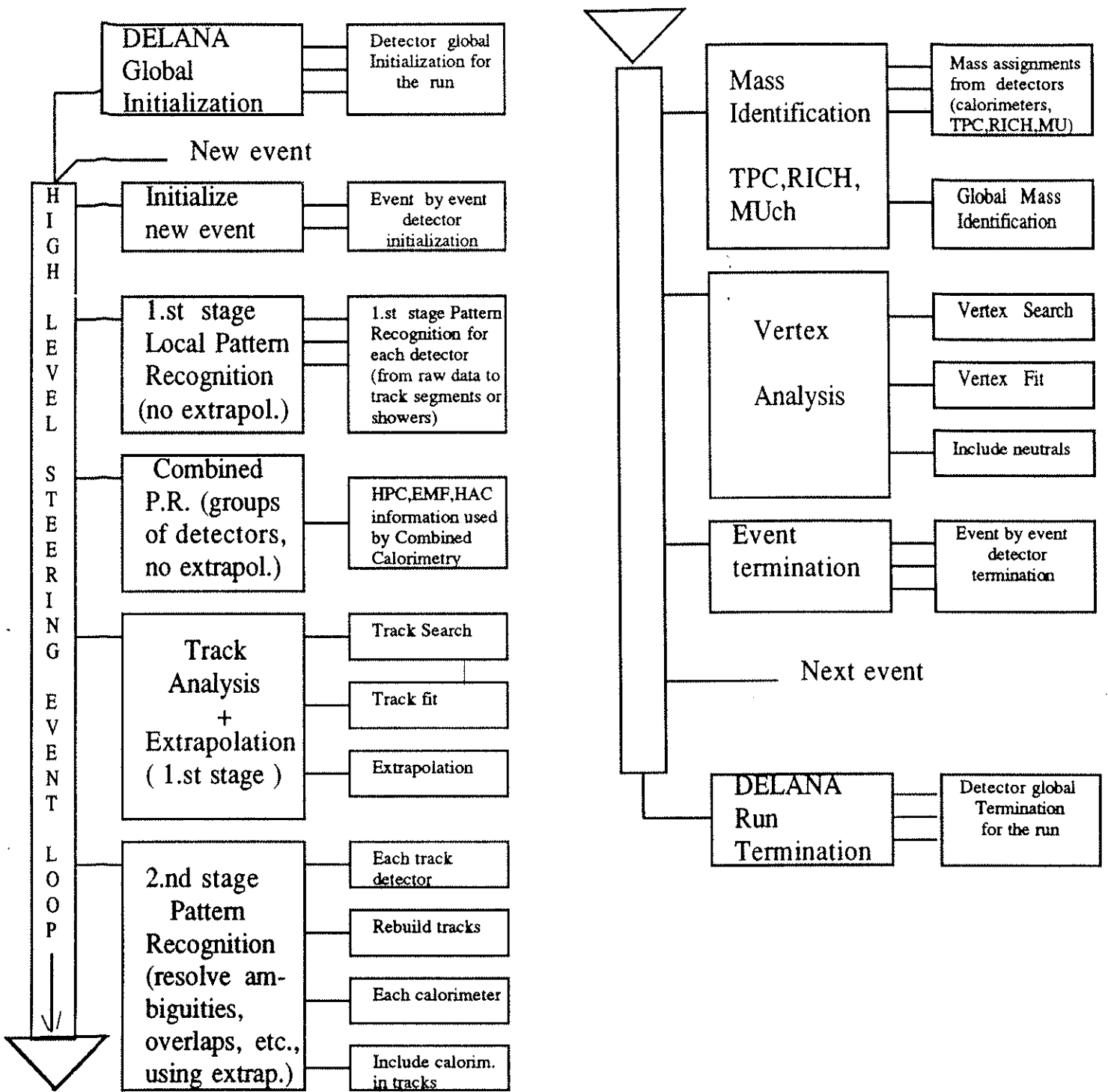
Figure 9.3: Flow diagram and processing stages of DELANA.

the TRIGGER chamber information is not always possible at this stage, being in this case both measurements independently used for track reconstruction.

- OD - If clusters of drift cells are reconstructed in the detector, due for instance to pre-showering of particles, the technique of the track segment reconstruction by fitting the tangent to the drift circles in each cell gives poor results.

- HPC - In case of overlapping showers, the absence of any information about the incoming tracks constrains the reconstruction performance of this calorimeter (shower separation, position, direction)

- FCB - Due to noise or secondaries generated by showering particles in neighbouring cables, lots of ghost hits degrade the pattern recognition performance in the chamber.

- MUB/MUF - Association of hits in different layers of chambers cannot be done in the absence of track extrapolation information.

At the end of this first pass of pattern recognition for each detector, track search and track fit processors combine the information from the tracking chambers and build the possible tracks, after which another processor extrapolates each track to a set of reference surfaces (1 at least per detector). A combined calorimetry processor combines the information from each calorimeter separately, to associate showers developing in both the electromagnetic and hadronic calorimeters. The following list of modules are involved in the first stage reconstruction:

- Pattern Recognition (1 module per detector except RIB/RIF)

- Combined Calorimetry

- Track Search

- Track Fit

- Track Extrapolation

9.3.2 Second stage pattern recognition

Each tracking detector accesses the predictions (track extrapolations) to a pre-defined reference surface (normally close to the reference point of its measurements) and compares it with its own reconstruction. Ambiguities are eliminated and information on detector track measurements (direction and position) is improved. After tracking detectors finish this second pass of pattern recognition, track search and track fit processors combine again the improved information from each tracking detector to build new tracks or improve already existing track parameters. At this level, the best set of track measurements exists for the event. The tracks in this "final" set are then

extrapolated superseeding the results of the first extrapolation pass. Calorimeters can then make the best track-shower matching and improve the shower position and direction measurement, with knowledge of the extrapolated track position. The combined calorimetry package performs the final attempt to associate showers in both calorimeters. The second stage pattern recognition can be summarized as follows:

- Tracking Chambers Pattern Recognition (2.nd pass)

- Track Search (2.nd pass)

- Track Fit (2.nd pass)

- Track Extrapolation (2.nd pass)

- Calorimeters Pattern Recognition (2.nd pass)

- Combined Calorimetry (2.nd pass)

9.3.3   Mass Identification

The mass assignment stage, after the second pass reconstruction, consists in the assembly of detector information about the identity of the particle based in several techniques. While TPC gives dE/dX information from the reconstructed pulse height in the wires, RICH detectors based on track extrapolation into a reference plane (close to liquid radiators) analyse the dimension of the reconstructed ring defined by the "focused" Cerenkov photons in a plane, ending up with probability values for a given track to be e, π, k, p. Individual calorimeters and combined calorimetry previously have defined the shower classification at their second stage pattern recognition. Muon chambers give the μ, π probability for an extrapolated track matched with hits in the layers. This stage can be summarized as follows:

- TPC: $dE/dX \rightarrow P(e), P(\pi), ...$

- RIB: $Rings \rightarrow P(e), P(\pi), P(K), P(p)$

- HPC,EMF: $Shower \rightarrow \gamma, e, MIP, hadron$

- HAC: $Shower \rightarrow \pi, \mu$

- CCAL: $Shower \rightarrow P(\mu), P(\pi)$

- MUB,MUF: $Hits\ matching\ track \rightarrow P(\mu), P(\pi)$

9.3.4 Vertex Fit

After this step, with the most complete information about the reconstruction and mass assignment of each track, a vertex fit package performs the search for a primary vertex using as input the existing charged tracks. In case a vertex is successfull fitted, the neutral particles (showers in calorimeters non-asociated to any charged track) are included in the fitted vertex.

9.4 Data handling and reduction

The TANAGRA (Track Analysis and Graphics) package[71] builds the structure of the reconstructed events in a hierarchic chain of banks containing the information about the space points, track elements, showers, tracks or vertices, preserving the logical relations between them (which detector banks were used to build track banks, which track banks were used to create vertex banks, what calorimeter banks were associated with charged track banks, etc.) and the status of each bank within the event strucuture (active, deactive, disabled, replaced). The status of each bank is of special relevance during the event reconstruction, when the information of several independent detectors is put together into tracks and ambiguous solutions can be fitted, or when the contents of a bank is modified or replaced in order to improve the quality of the reconstructed quantities.

With a detector independent structure of banks, TANAGRA allows to save, retrieve or modify the relevant information at the several steps of data reduction and processing by the different offline programs (simulation, reconstruction, DST or event viewing). The information relevant for the physics analysis is stored and manipulated in a coherent and universal way by all the programs interfering with the event structure, to save, retrieve, modify or display event data.

In figure 9.4 are shown the multiple levels of data reduction and the corresponding TANAGRA entities (types of banks) at each step.

RAW DATA

TANAGRA

CALIBRATION

TD — PATTERN RECOGNITION INPUT DATA

PATTERN RECOGNITION

TE — TRACK ELEMENT

TRACK SEARCH

TS — TRACK STRING

TRACK FIT

TK — FITTED TRACK

VERTEX SEARCH

TB — BUNDLE OF TRACKS

VERTEX FIT

TV — VERTEX

D E T E C T O R   D E P E N D.

G E N E R A L   P U R P O S E
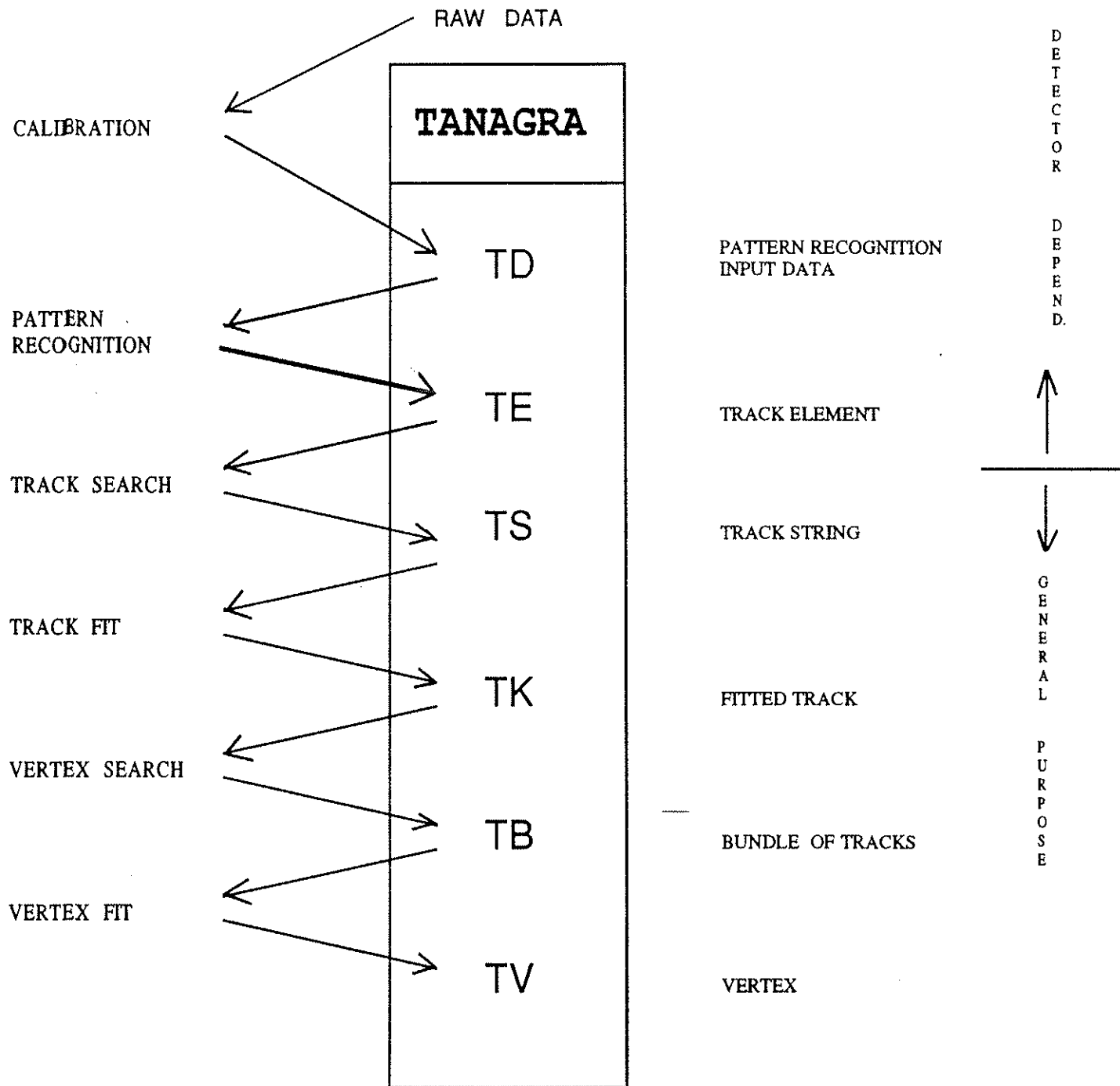
Data reduction and TANAGRA entities at each processing step

Figure 9.4: Data reduction steps and TANAGRA entities (banks) in the reconstructed event structure.

9.4.1   Track Reconstruction

The acceptance of the detector for charged tracks can be defined in first approximation by the angular region covered by tracking chambers:

$$13° < \theta < 167°$$

Track reconstruction efficiency and resolution is poor in some intervals of the polar (θ) and of the azimuthal (Φ) angle. This is related to the existence of dead regions for track measurement. These are:

The θ regions of inefficient track measurement

• The central wall of the TPC, few centimetres wide, results in an angular innefficient region for track reconstruction defined as

$$88° < \theta < 92° \tag{9.1}$$

• The very forward/backward regions in the endcaps below the region covered by the TPC. Below 22° less than 4 points are measured by the TPC and below 17° (limit of angular region covered by ID JET chamber) only FCA and FCB contribute to the track measurement. In general, the efficiency decreases rapidly to zero in the intervals

$$13° < \theta < 20° \tag{9.2}$$

$$160° < \theta < 167° \tag{9.3}$$

The Φ regions of inefficient track measurement

• The azimuthal regions corresponding to the geometrical gap between TPC sectors, where no track measurement is done. Such gaps, define the following low efficiency intervals defined as
$$29.5° < mod (\Phi , 60°) < 30.5° \tag{9.4}$$

• Gap between chamber hemispheres in FCB. This gaps, 10 cm wide, in the vertical plane, define in the endcaps inefficient regions for track reconstruction as:

$$89° < \Phi < 91° \tag{9.5}$$
$$269° < \Phi < 271° \tag{9.6}$$

9.4.1.1   Momentum Measurement

The acuracy in the track momentum measurement is related to the ability to recon-
struct its radius of curvature in the magnetic field or equivalently the dimensions
of the sagitta of the circular trajectory along which the detector measurements are
performed. For high momentum straight tracks (e.g. in $Z^0 \rightarrow \mu^+\mu^-$ events) when
the sagitta dimensions become comparable to the detector resolution to measure the
$R\Phi$ coordinate, the reconstruction with accuracy of the track curvature becomes hard
with consequent deterioration of the reconstructed momentum and charge.

Being B the magnetic field, P_T the track transverse momentum, L the radial track
length, $\Delta\phi = 0.3\ BL/P_T$ the deflection angle of the track in the magnetic field and
$R = P_T/0.3\ B$ the radius of curvature of the particle trajectory, the sagitta $\underline{s}$ is in
good approximation given by[70]

$$s \simeq \frac{R\,(\Delta\phi)^2}{8} \quad \overset{\Delta\phi \ll 1}{\Longrightarrow} \quad s \simeq 0.3\,\frac{BL^2}{8P_T} \tag{9.7}$$

The level of accuracy in the track transverse momentum (P_T) and polar angle (θ) mea-
surement in a central tracking detector (e.g. TPC) imersed in a solenoidal magnetic
field parallel to the z-axis and with accuracy $\sigma_{R\Phi}$, σ_z respectively in the measurement
of the transverse and longitudinal coordinate, can be estimated from[69]:

$$\frac{\sigma(P_T)}{P_T} = \frac{\sigma_{R\Phi}P_T}{0.3BL^2}\sqrt{\frac{720}{N+4}} \tag{9.8}$$

$$\sigma_\theta = \frac{\sigma_z}{L}\left(\frac{12(N-1)}{N(N+1)}\right)^{1/2} \tag{9.9}$$

with B,L defined as above and N the number of equidistant measured points along
the track. Typical values in the DELPHI TPC at B=1.2 Tesla are:

$$L \simeq 0.8\ m \quad , \quad N = 16 \quad , \quad \sigma_{R\Phi} = 250\ \mu m \quad , \quad \sigma_z < 1\ mm \tag{9.10}$$

Equation 9.8 shows that the momentum resolution improves mainly with the product
BL^2 but also with $\sqrt{N}$ (the multiple scattering contribution is neglected). In the
case of DELPHI barrel ($43° < \theta < 137°$), in order to extend L, the OD measurements
(maximum of 5 points) at 2 meters radius from the beam line and with an accuracy
better than $\sigma_{R\Phi} \sim 100\ \mu m$ improve the momentum resolution by a considerable
factor, especially for 45 GeV muon tracks when the sagitta of the circular orbit in the
TPC is of the order

$$\frac{s}{\sigma_{R\Phi}} \sim 3 \tag{9.11}$$

The improvement in the momentum resolution, when the OD measurements are in-
cluded in the fitted track, are displayed in figures 9.5,9.6. The distributions of the
reconstructed momentum for simulated tracks generated at two fixed values of P (10
and 45 GeV), in the region $45° < \theta < 135°$, are shown.
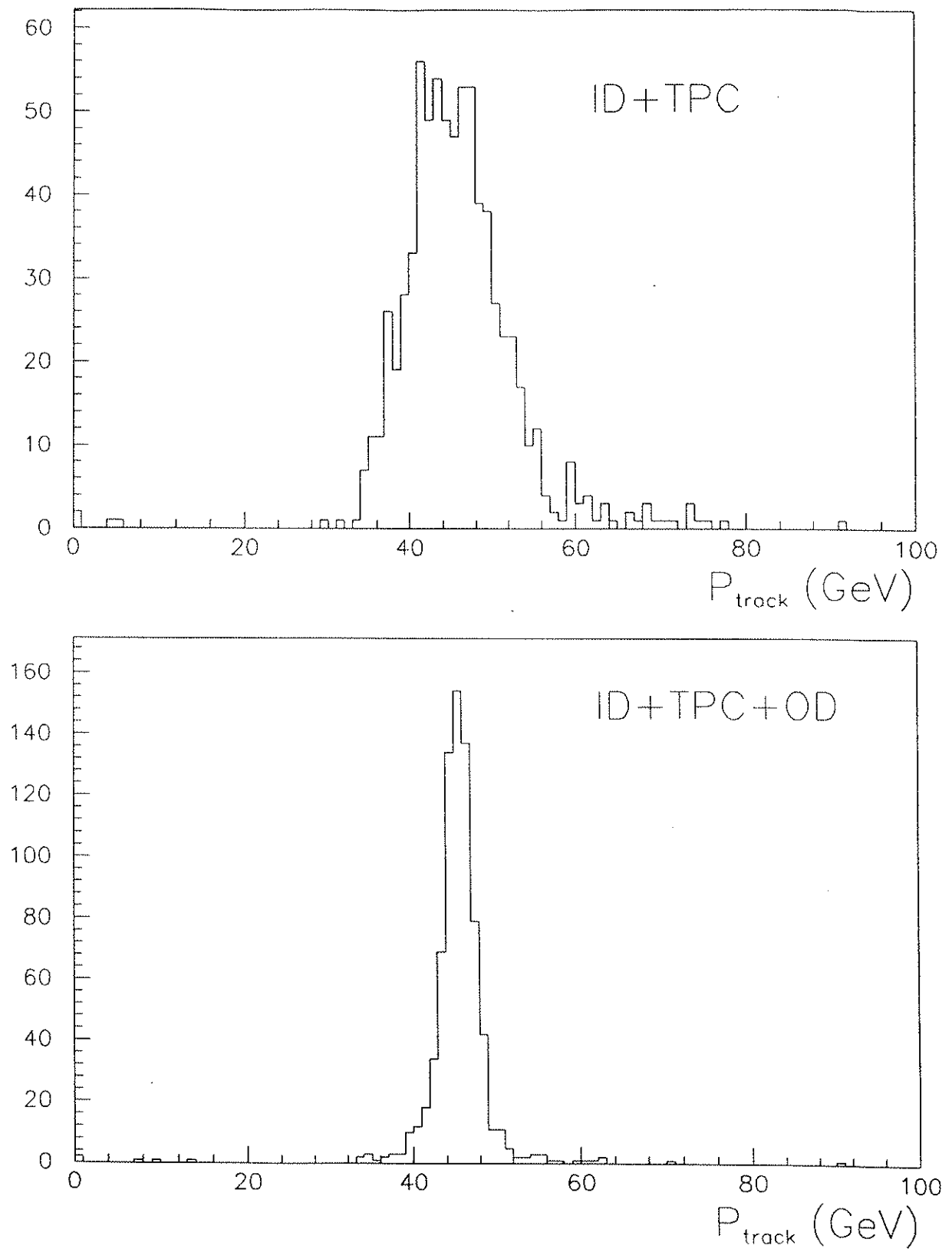
Figure 9.5: Reconstructed momentum distribution for generated tracks in the barrel with P=45.5 GeV, in the two situations: 1) OD measurements are not used to fit the tracks and 2) OD measurements are used to fit the tracks. Simulated results are shown.
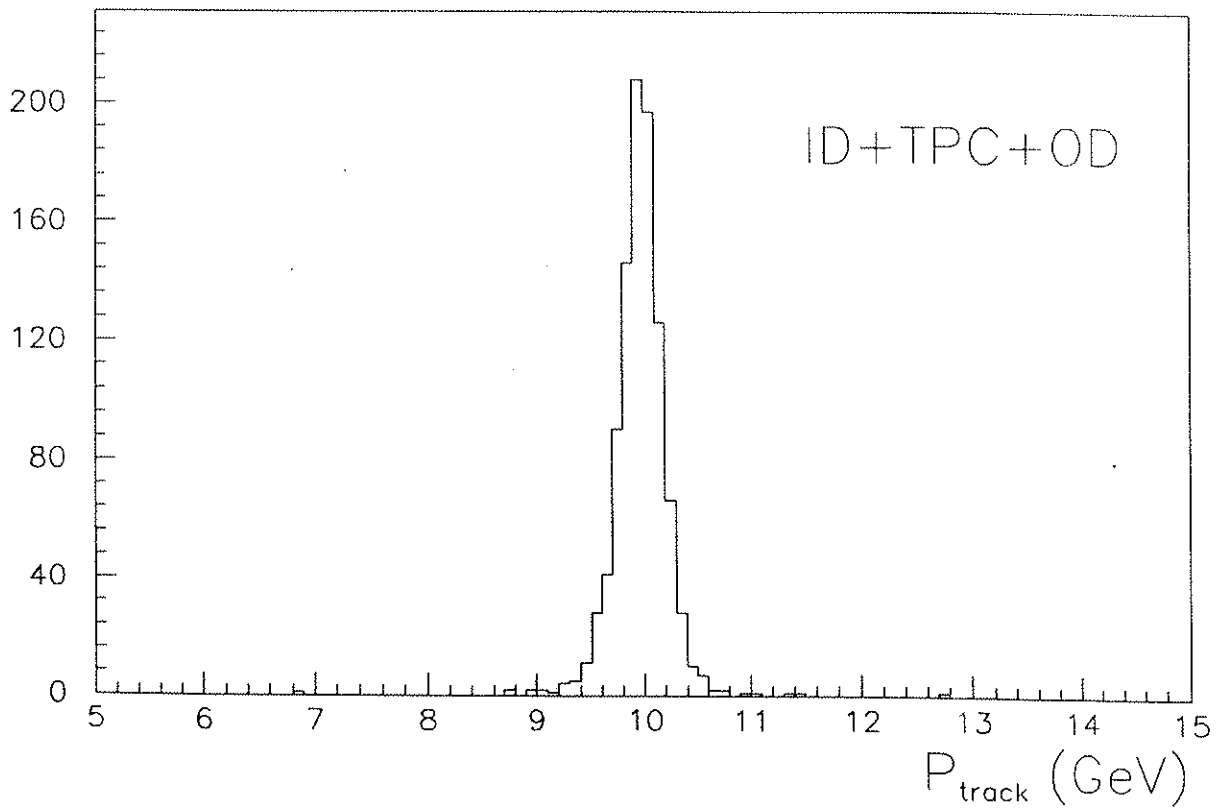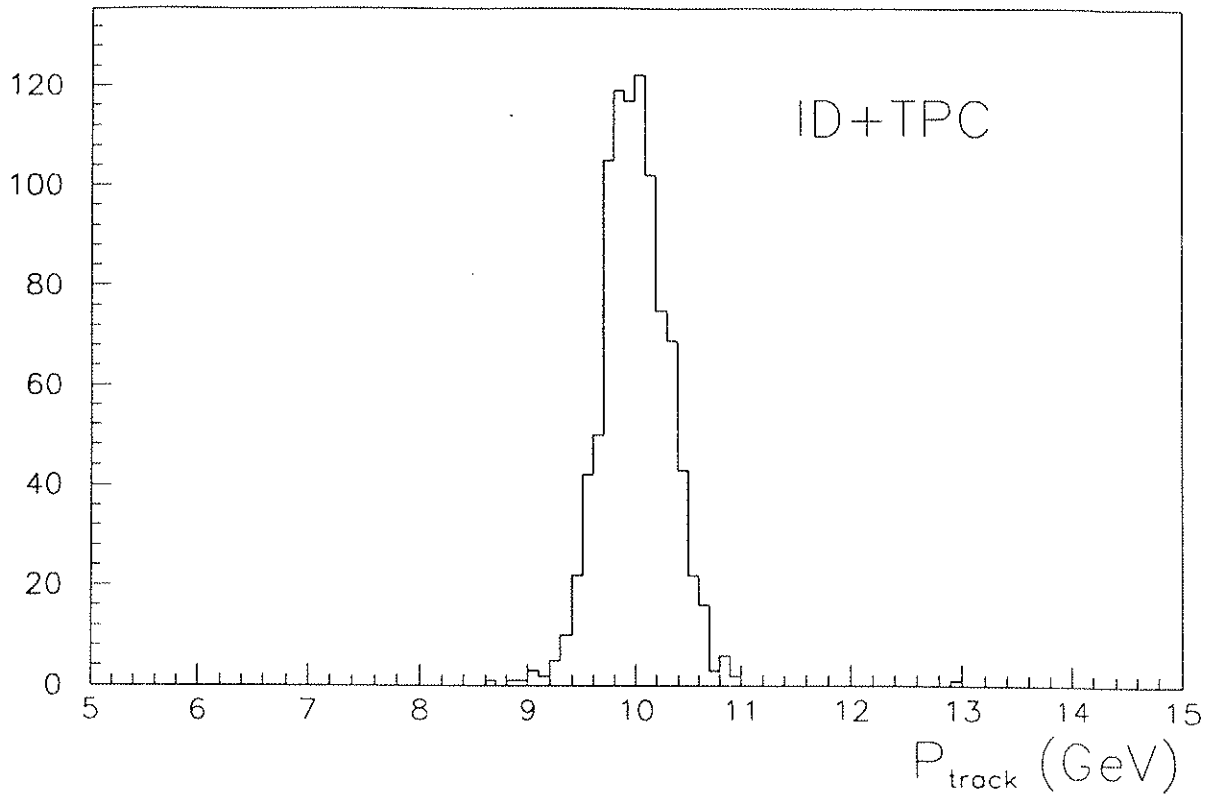
Figure 9.6: Same as previous figure for tracks generated with P=10 GeV.

9.4.2 Energy Reconstruction

Electromagnetic energy reconstruction is affected by the existence of zones not covered by any electromagnetic calorimeter and by dead zones corresponding to the separation between the 144 modules of the electromagnetic calorimeter in the barrel.

The θ dead zones for electromagnetic energy reconstruction are:

- "40° hole": common designation for the 2 angular regions separating the barrel and encap electromagnetic calorimeters, filled with the cables and support structures for the RICH detectors, the TPC and FCB. These regions are defined as:

$$35.5° < \theta < 41.5° \tag{9.12}$$

$$138.5° < \theta < 144.5° \tag{9.13}$$

- θ Cracks: the 6 θ-rings (24 $R\Phi$ modules each) are separated by 4 cm wide Z-gaps. Particles pointing towards the gaps will develop showers split between 2 different modules with the corresponding inefficient procedure of energy recovery in the pattern recognition algorithms. The region centered at $\theta = 90°$, about 4° wide, is dead or inefficient for energy measurement.

The Φ dead zones (gaps) in the barrel electromagnetic calorimeter are:

- Φ Cracks: The 24 azimuthal modules in each ring of the calorimeter are separated by gaps (cracks) about 1 cm wide, in practice affecting the energy recover procedure in a corresponding angular region of about ±1° centered in the gap. The energy of showers developing at the edge of the modules are badly reconstructed and photons pointing to the cracks are undetected. The HPC gaps produce a global effect of about 14% dead zones.

The reconstruction of energy in the hadronic calorimeter is performed in the angular range

$$11° < \theta < 169° \tag{9.14}$$

9.4.2.1 Reconstruction of Showers

The HPC has good granularity and allows tri-dimensional reconstruction of showers. The pattern recognition for this calorimeter reconstructs the θ and ϕ angles determining the direction of the showers and allows the reconstruction of the X,Y,Z coordinates of the baricenter of the energy deposited in each of its nine radial layers. The R, $R\Phi$, Z coordinates of the starting point of the shower are also reconstructed. In figures 9.9,9.7,9.8 the HPC measurements for the θ, ϕ and Z of showers are compared with the corresponding values from the matched extrapolated tracks in real leptonic (e^+e^-, $\mu^+\mu^-$ and $\tau^+\tau^-$) events. From the plotted difference, the level of accuracy of each measurement is displayed.
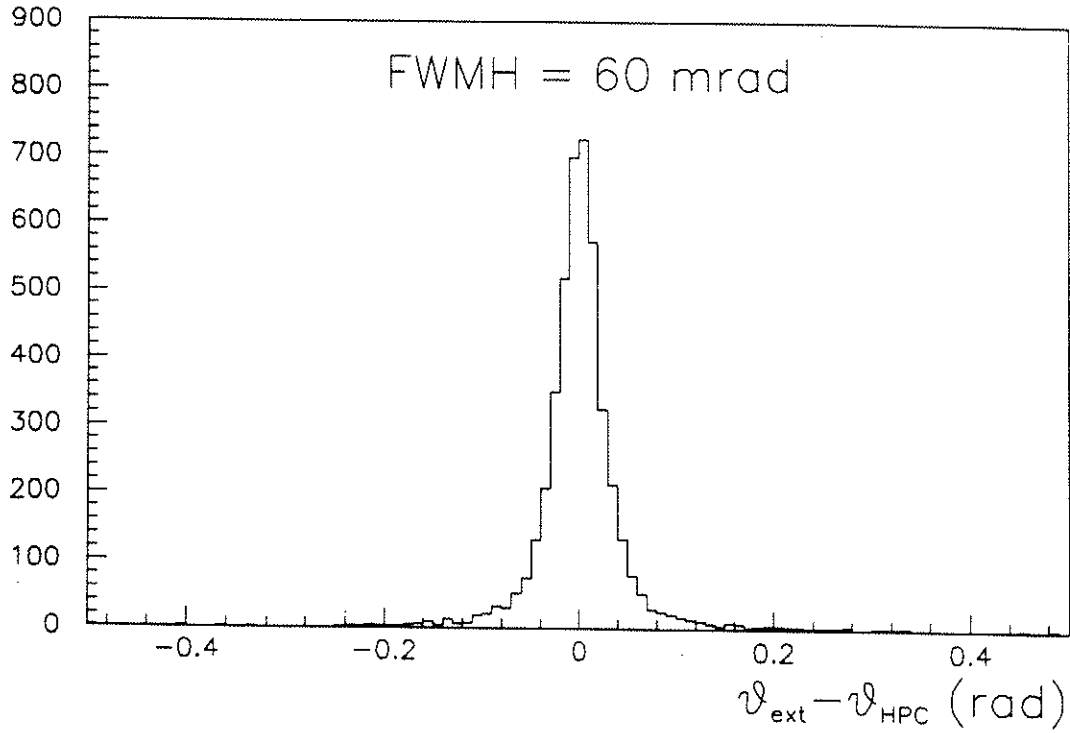
Figure 9.7: Difference $(\theta_{ext} - \theta_{hpc})$, between the θ of the shower measured by the HPC and the θ angle of the associated track, extrapolated to the entry of HPC.
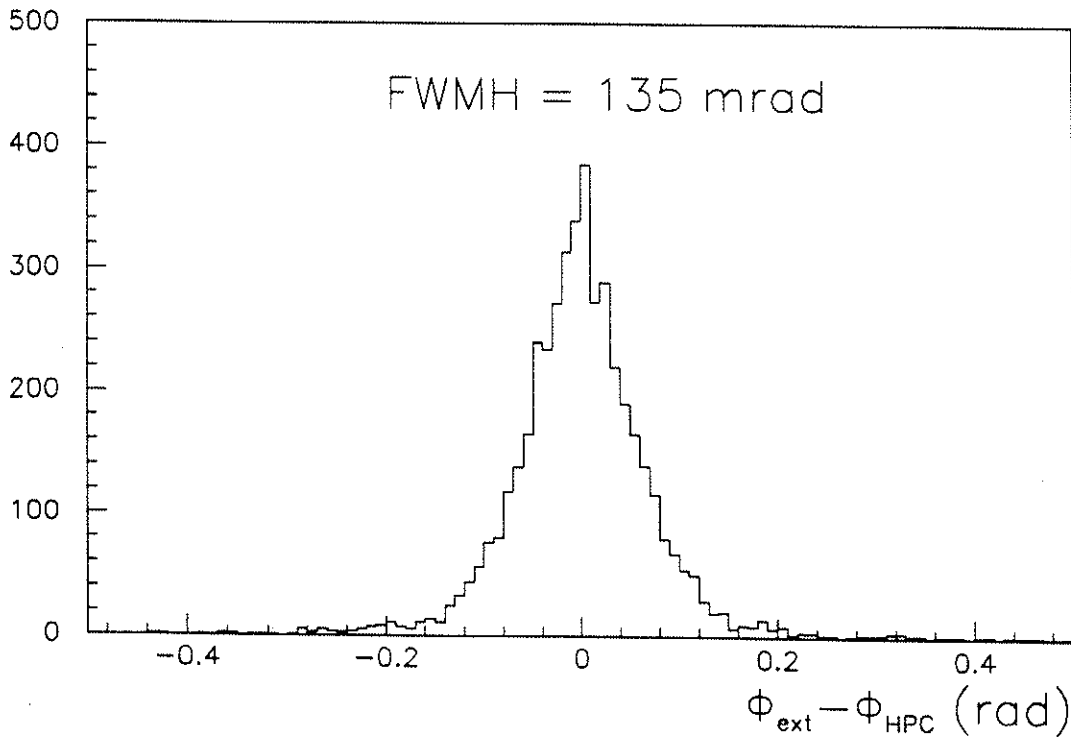
Figure 9.8: Difference $(\phi_{ext} - \phi_{hpc})$, between the ϕ of the shower measured by the HPC and the ϕ angle of the associated track, extrapolated to the entry of HPC.
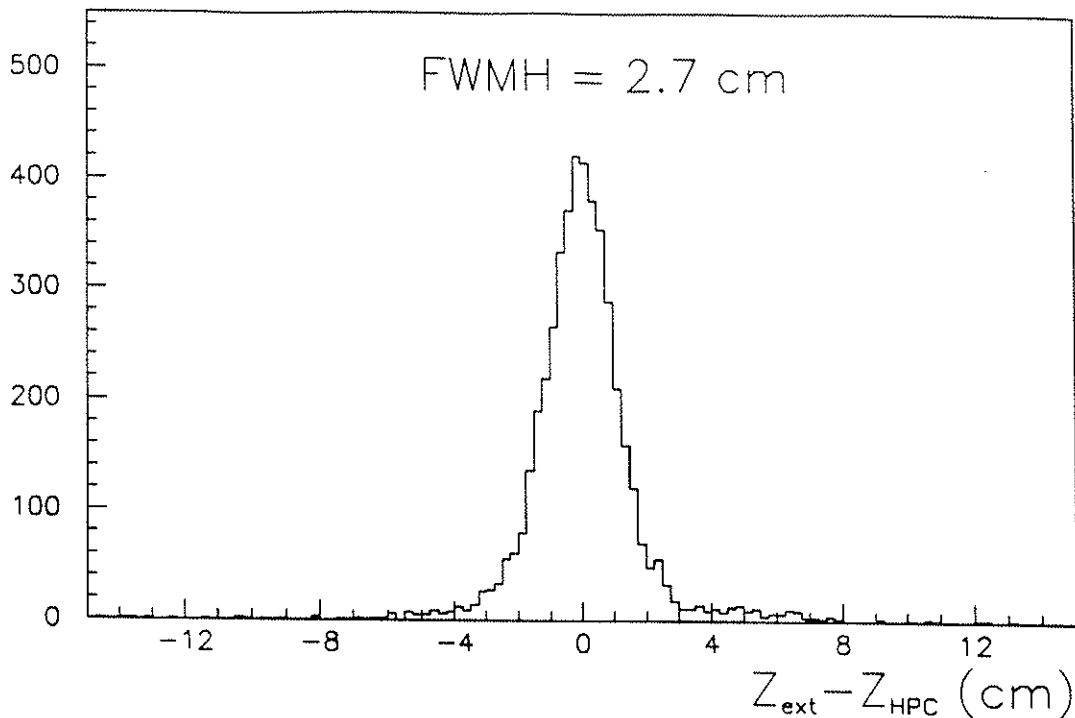
Figure 9.9: Difference ($Z_{ext} - Z_{hpc}$), between the shower Z coordinate measured by the HPC and the Z coordinate of the associated track, extrapolated to the entry of HPC.

9.5   Event Viewing

DELGRA[72], the DELPHI event viewing program, is the backbone of the interactive physics analysis. It performs the 3-D graphics display of the detector environment superimposed with the reconstructed event quantitities stored in the TANAGRA event structure, from the space points (TD) up to the fitted vertices (TV).

Displaying graphically the reconstructed space points, tracks, showers, vertices, etc.) for the event, it allows to examine and display the numerical values of the represented quantities (track momentum, energy of showers, direction and position of track elements, etc.) for the reconstructed event and to dump the full information in the TANAGRA banks.

Allowing to zoom, rotate, translate or pick the "bits and pieces" of the reconstructed event, it is a tool to check visually the simulation results, the quality of the reconstruction, the alignment of the detectors, etc. and is therefore a very useful debugging tool of the offline software.

It constitutes an indispensible tool for the physics analysis, allowing to get an insight into the detector response to the signature of each physics channel and to check visually the efficiency of the reconstruction and analysis programs. Results of jet search algorithms, lego plots, computation of invariant masses, etc., activated by the interactive user, can be superimposed to the displayed events. In figures 9.10,9.11 the transverse and longitudinal view of a $Z^0 \rightarrow 3 - jets$ hadronic event are displayed.
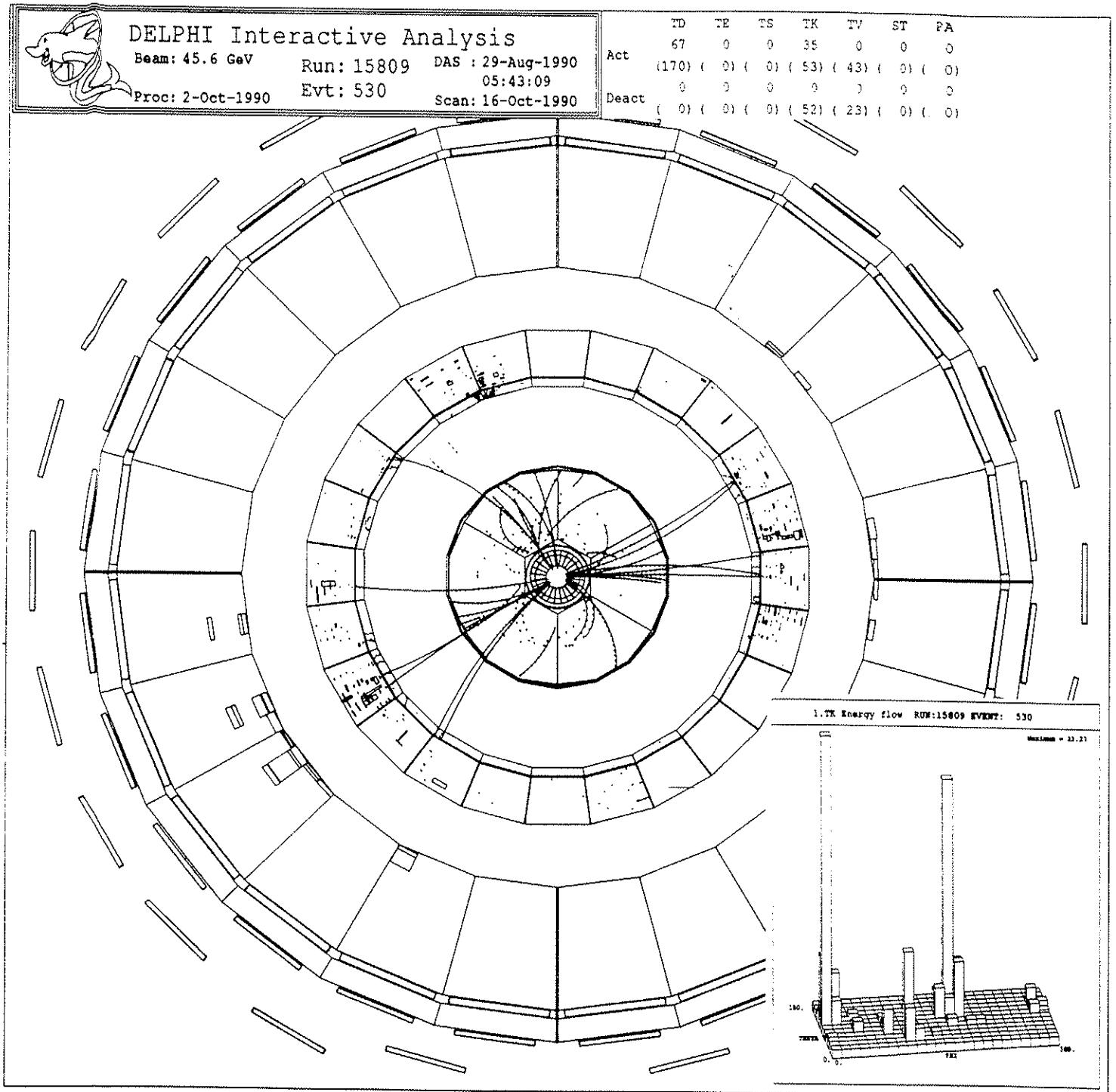
Figure 9.10: $R\Phi$ view of a typical $Z^0 \to hadrons$ event. The following reconstructed entities are displayed: space points, track elements, showers, fitted tracks. The lego-plot of the energy flow for the event is superimposed.
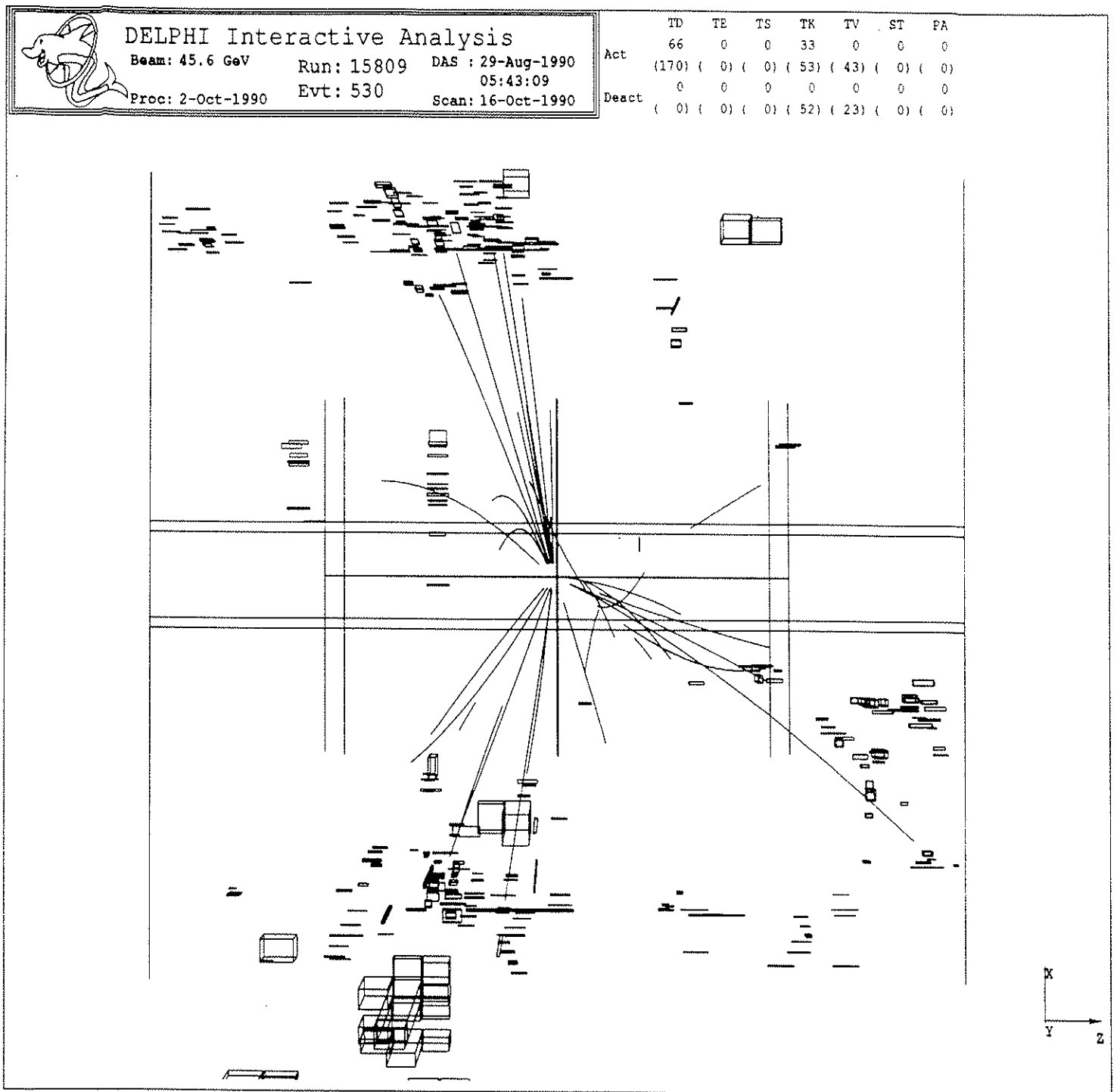
Figure 9.11: Longitudinal view of the $Z^0 \rightarrow 3 - jets$ event shown in previous figure, with two of the jets in the barrel region and the third one pointing forward.

Chapter 10

$\tau^+\tau^-$ DETECTION IN DELPHI

The establishment of a set of cuts to select the $\tau^+\tau^-$ events is closely related to a good understanding of the e^+e^- and $\mu^+\mu^-$ final states and their relevant distributions (momentum, energy, acolinearity, acoplanarity, etc.), as well as to the ability to perform particle identification in each hemisphere of the event. In this chapter, the signature in the detector of the $Z^0 \to e^+e^-$ and $Z^0 \to \mu^+\mu^-$ final states is described and the more complex signature of the $Z^0 \to \tau^+\tau^-$ final states is emphasized. Using Monte Carlo events simulated and reconstructed through the complete analysis chain previously described, we show how photon conversions and pion interactions "distort" the charged multiplicity of the final states from $\tau^+\tau^-$ decays.

The efficiency of the barrel subtriggers to each category of lepton pairs is analysed and the trigger efficiency for $\tau^+\tau^-$ final states is discussed in detail.

The topological characteristics of lepton pairs produced in Z^0 decays are analysed and the typical distributions of the acolinearity (θ_{acol}) and acoplanarity (θ_{acop}) angles are presented. Finally it is shown that each lepton family occupies a well defined region in the 2-dimensional distributions of pairs of variables like visible momentum, total electromagnetic energy, acolinearity, acoplanarity, etc., and that separation between e^+e^-, $\mu^+\mu^-$ and $\tau^+\tau^-$ events can be achieved by imposing sets of cuts acting on those variables.

The event selection and the $\tau^+\tau^-$ selection criteria are discussed in the next chapter, with numerical estimation of the efficiencies and backgrounds.

Whenever justified, comparison is made between the reconstructed quantities for real and simulated events.
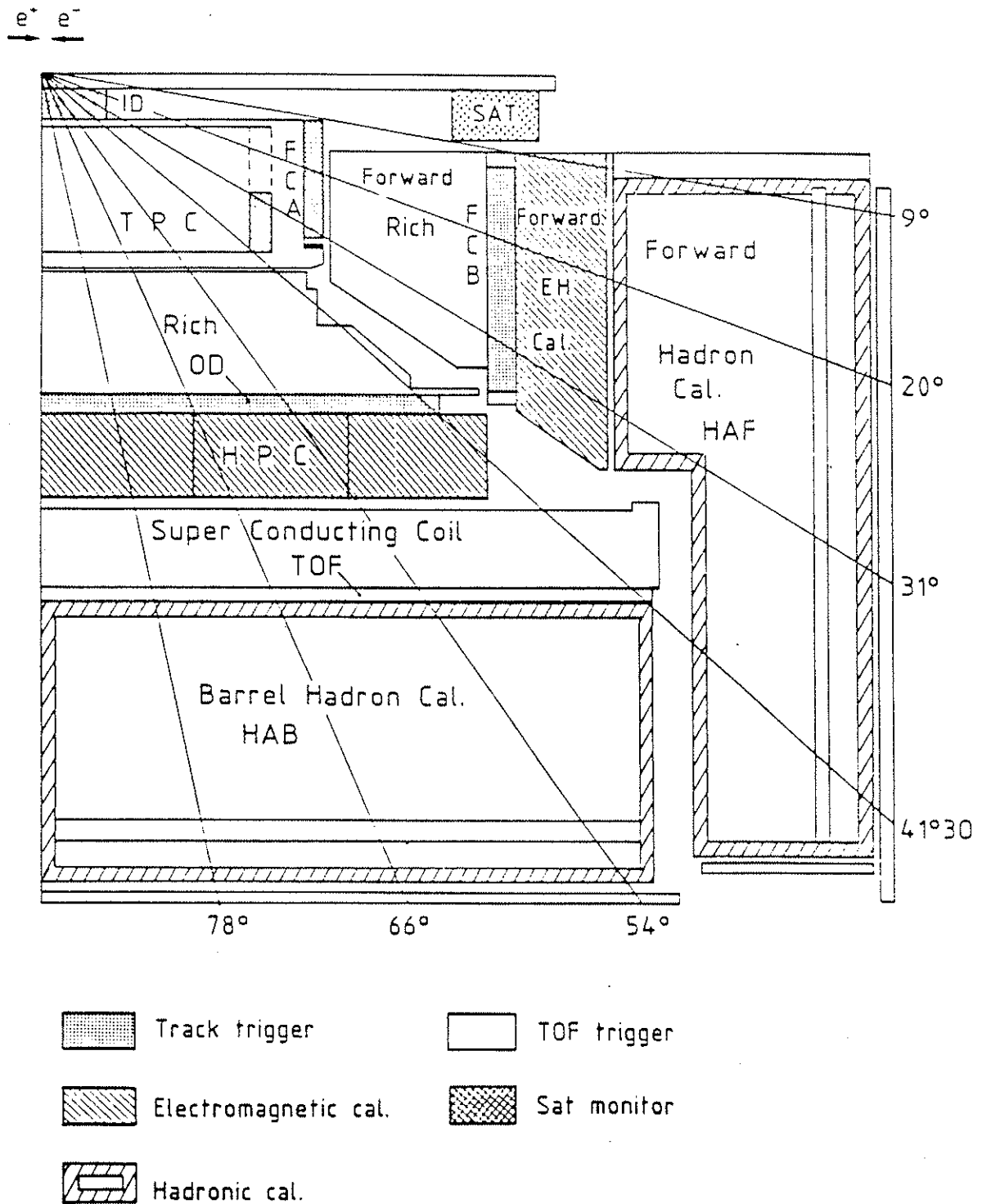
Figure 10.1: R-Z view of DELPHI, with discrimination of the detectors covering the barrel,endcap and transition regions

10.1 $e^+e^- \rightarrow Z^0 \rightarrow \mu^+\mu^-$

The typical signature of a reconstructed $Z^0 \rightarrow \mu^+\mu^-$ event in DELPHI can be summarized as[1]

• Two back to back charged tracks with high momentum and $P_{track} \sim E_{beam}$ for each track.

• 3 or 4 hits in Muon Chamber layers, matching each track.

• Minimum Ionizing Particle signal in the electromagnetic calorimeter, associated to each track. This signal is of about 200 MeV in the HPC and of about 600 MeV in the FEMC.

• Minimum Ionizing Particle signal ($\sim 4\ GeV$) in the hadronic calorimeter, associated to each track.

The momentum distribution for tracks reconstructed in real $Z^0 \rightarrow \mu^+\mu^-$ events, shown in figure 10.3 is peaked at $P_{track} \simeq E_{beam}$ with a tail extending towards the low momentum region of the spectrum, due to events with radiation of hard photon or to events with at least one badly reconstructed track. Tracks with momentum close to the beam energy ($P_{track} \simeq 45.5\ GeV$) are reconstructed in the DELPHI tracking system with a resolution

$$\sigma_P/P \simeq 10\%$$

The visible momentum, defined as the scalar sum of the momentum of the 2 tracks, exhibits a distribution showed in the figure 10.4, peaking at $P_{vis} \approx M_Z$ with a tail extending towards values $P_{vis} \approx M_Z/2$, due to the radiative $\mu^+\mu^-(\gamma)$ events or to $\mu^+\mu^-$ events with bad track reconstruction:

$$P_{vis} = \sum_{i=1}^{2} |\vec{P_i}| \simeq M_Z \tag{10.1}$$

The total energy in the electromagnetic calorimeter, E_{em}, also shown in figure 10.4, is peaked at

$$E_{em} \simeq 2\ E_{mip} \tag{10.2}$$

with E_{mip} is the reconstructed signal in the calorimeter for crossing minimum ionizing particles.

---

[1]Quoted are the average values of the distributions

DELPHI Interactive Analysis

Beam: 45.7 GeV

Proc: 8-Aug-1990

Run: 14473   DAS : 5-Aug-1990
                      07:44:59
Evt: 5470   Scan: 15-Oct-1990

	TD	TE	TS	TK	TV	ST	PA
Act	9	8	0	2	0	0	0
	(28)	(24)	(0)	(2)	(3)	(0)	(0)
Deact	0	0	0	0	0	0	0
	(0)	(5)	(0)	(2)	(0)	(0)	(0)

Y
Z   X
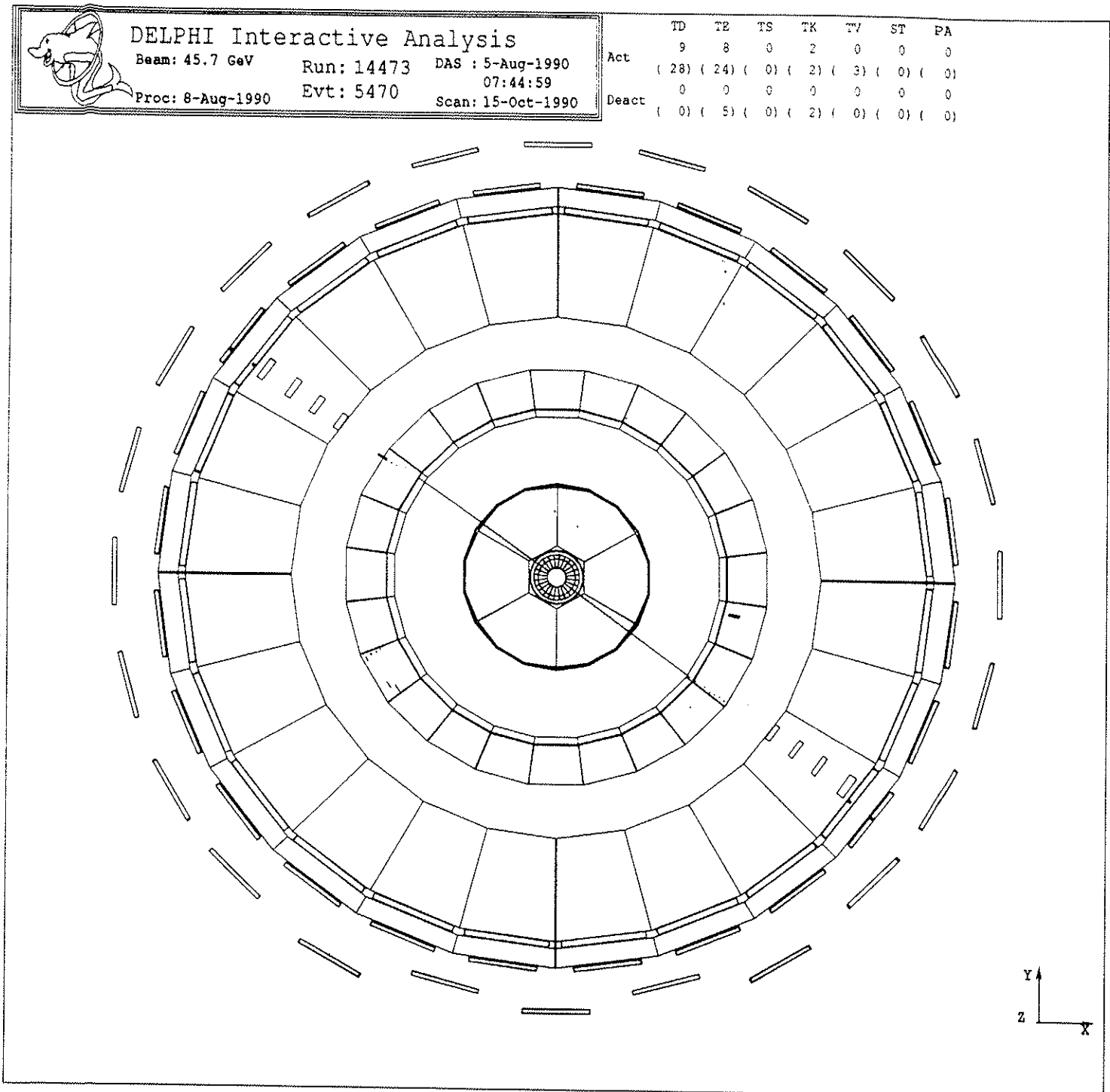
Figure 10.2: Characteristic signature of a $Z^0 \to \mu^+\mu^-$ event.
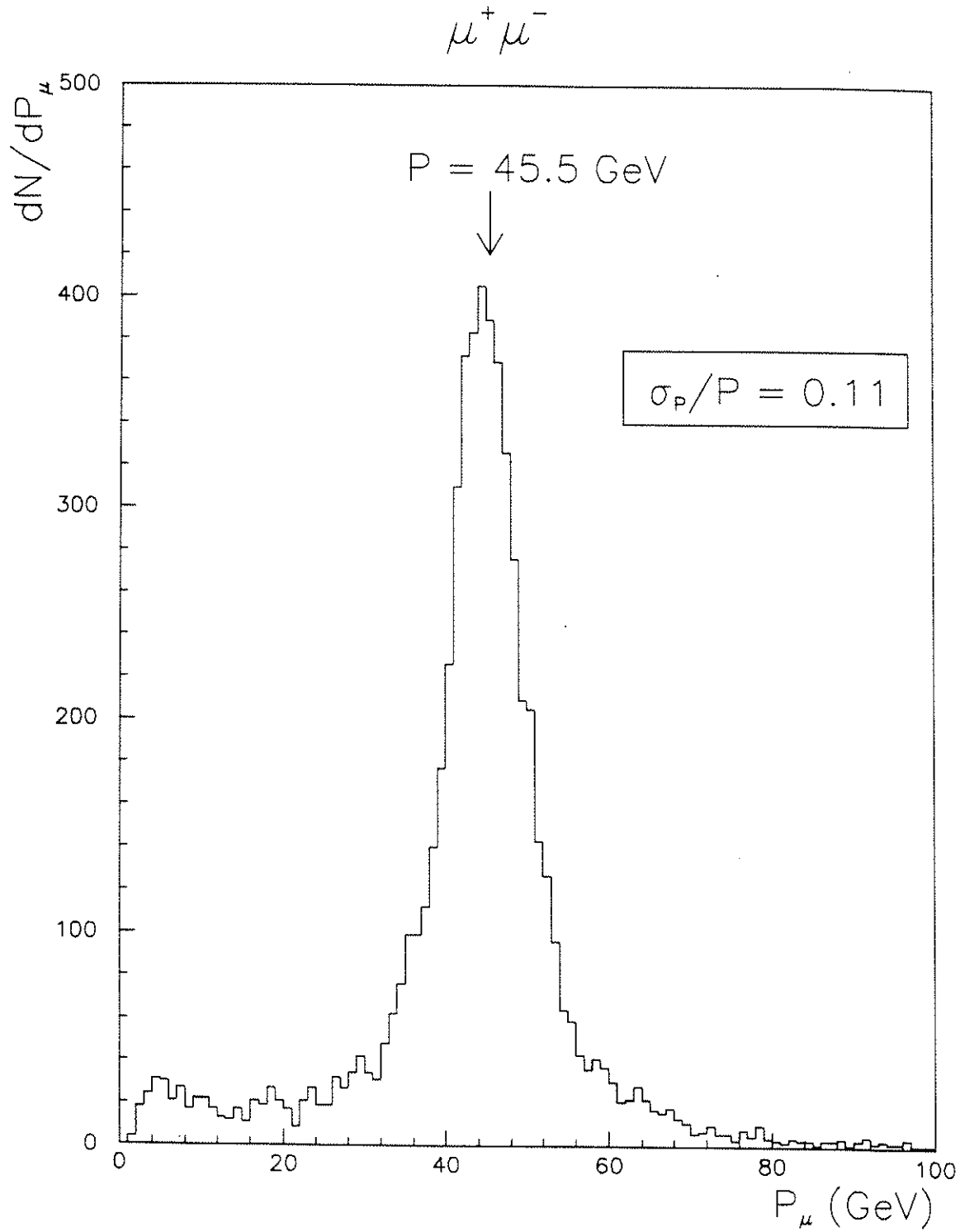
Figure 10.3: Distribution of track momentum for reconstructed $\mu^+ \mu^-$ events. The peak at $P_{track} \simeq M_Z/2$ is the characteristic signature of muons from $Z^0 \rightarrow \mu^+ \mu^-$ events.
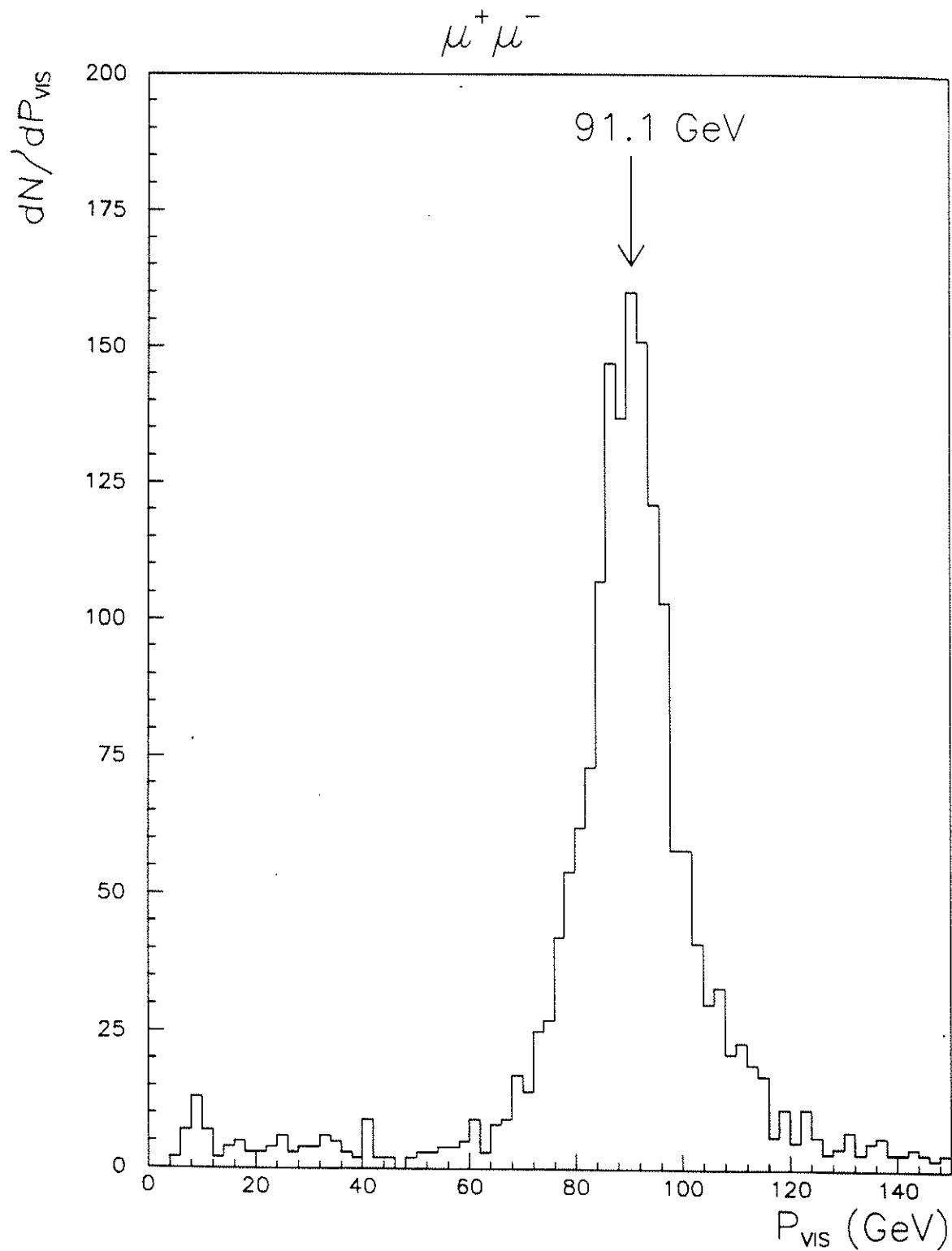
Figure 10.4: Distribution of visible momentum for reconstructed $\mu^+\mu^-$ events. The peak at $P_{vis} \simeq M_Z$ is the characteristic signature from $Z^0 \to \mu^+\mu^-$ events.

10.1.1   Track Reconstruction for $\mu^+ \mu^-$ events

The reconstruction of the 2 tracks from the $Z^0 \rightarrow \mu^+ \mu^-$ events is affected by the Φ dead zones of the TPC, of periodicity of 60°. Due to the back to back topology, both straight tracks fall simultaneously in these dead regions and the tracklength is almost fully contained within the dead zone. The Φ distribution of the reconstruced tracks, 6-folded to one TPC sector, is shown in figure 10.5. The track reconstruction efficiency for $Z^0 \rightarrow \mu^+ \mu^-$ events estimated from real events is

$$\varepsilon_\mu^{track} = 95 \%$$

The major contribution to the inefficiency is estimated by the fraction of tracks falling in the TPC Φ dead zones (the dip area in the figure).
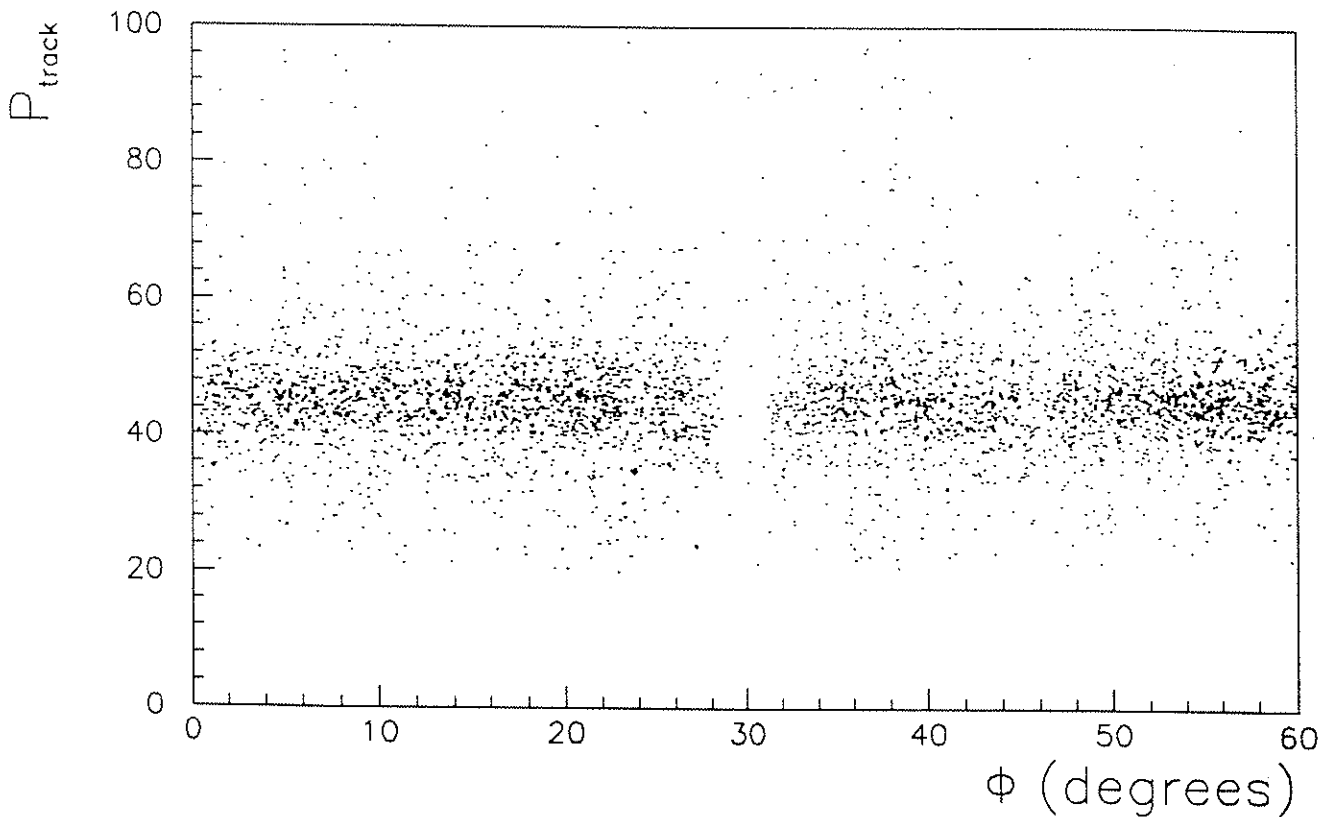
Figure 10.5: Reconstructed track momentum in $Z^0 \rightarrow \mu^+ \mu^-$ events as a function of the azimuthal angle folded to the interval $0° < \Phi < 60°$. The TPC dead region centered at $\Phi = 30°$ correspond to the physical separation between consecutive sectors

10.1.2 Single μ Identification

The identification efficiency of each muon is estimated from the real data, using the redundant information of the 3 independent detectors flagging the muon signature: the muon chambers (MUB), the electromagnetic calorimeter (HPC) and the hadronic calorimeter (HAC). The HPC efficiency for identifying a m.i.p. [2] outside the cracks is determined by measuring the number of tracks flagged as a m.i.p. by the HPC that were at the same time identified as a muon by the muon chambers:

$$\varepsilon_\mu^{hpc} = 98 \% \tag{10.3}$$

The muon identification efficiency of the barrel muon chambers (MUB) is estimated by measuring the number of tracks identified as a muon in the chambers, that were simultaneously identified as a m.i.p. by the HPC:

$$\varepsilon_\mu^{mub} = 95 \% \tag{10.4}$$

The inefficiency is mainly due to the regions not covered by muon chambers (about 4%). The combined single muon identification in the barrel region $50° < \theta < 130°$ is:

$$\boxed{\varepsilon_\mu > 99.5 \% \quad (\text{MUB+HPC+HAC})}$$

In the barrel regions $43° < \theta < 50°$ and $130° < \theta < 137°$, not covered by muon chambers, only HPC and HAC can be used to identify the isolated muon. The muon identification efficiency is lower but not smaller than 98% (smaller near the border of HPC):

$$\boxed{\varepsilon_\mu > 98 \% \quad (\text{HPC+HAC})}$$

The muon signal in the three barrel detectors contributing to the muon identification is shown in figure 10.6.

---

[2] m.i.p stands for "minimum ionizing particle"
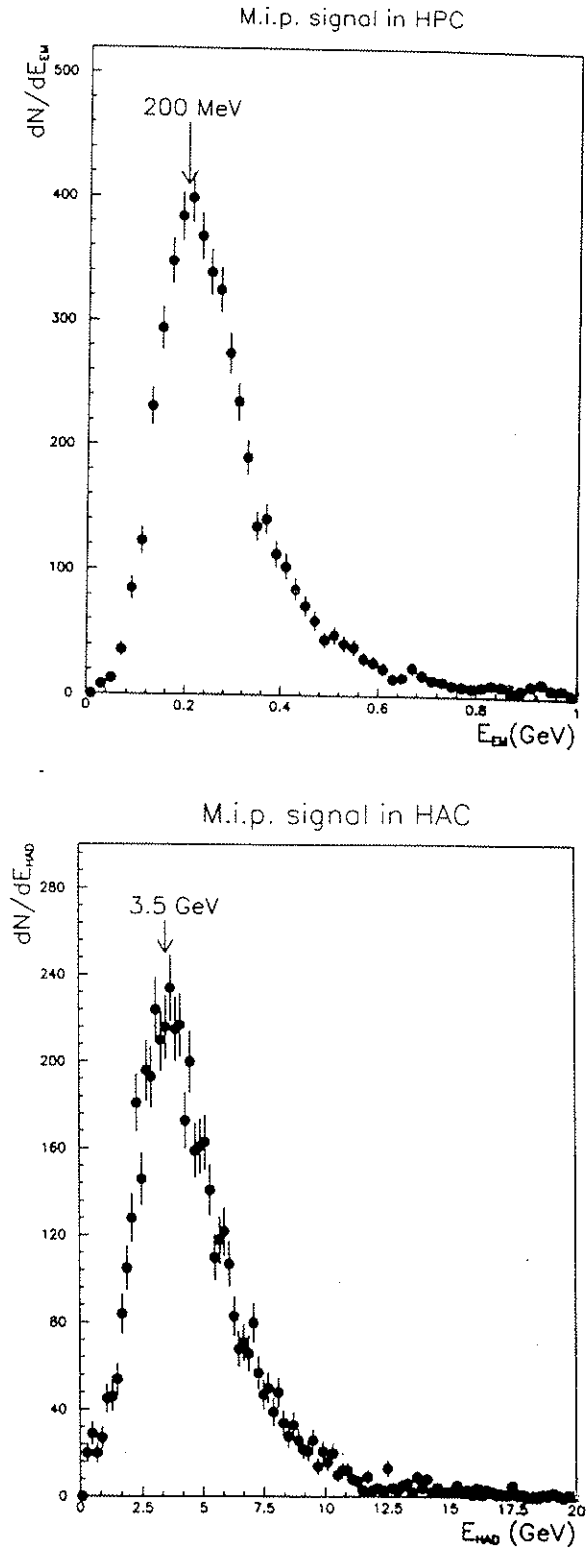
Figure 10.6: Muon signature : a) Reconstructed MIP signal in the HPC
b)reconstructed energy in the hadron calorimeter

10.2 $e^+e^- \to Z^0 \to e^+e^-$

In the barrel the t-channel contribution is small and the cross-section is dominated by the s-channel. In the endcaps the cross-section is dominated by the t-channel contribution. The expected number of events in the endcaps is about 4 times bigger than in the barrel. The typical final state from a reconstructed $Z^0 \to e^+e^-$ event consists of:

- Two back to back high energy showers in the electromagnetic calorimeter with $E_{shower} \sim E_{beam}$ for each shower.

- Each shower matching a high momentum charged track.

- No energy deposited in the hadronic calorimeter.
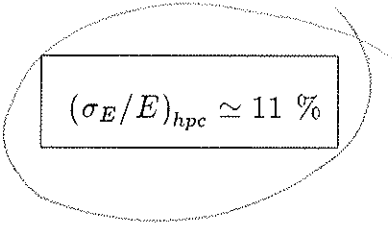
Additional energy clusters of smaller energy can be reconstructed in the neighbourhood of a more energetic cluster corresponding to photons radiated by the final state particles. The distribution of the total electromagnetic energy reconstructed for the $Z^0 \to e^+e^-$ events is shown in figure 10.10, peaking at value close the Z^0 mass with a tail extending towards smaller energies due to radiative $e^+e^-(\gamma)$ events and to inneficiencies in the energy reconstruction:

$$E_{em}^{ee} = \sum_{i=1}^{N_{cl}} E_{cl}^i \approx M_Z \tag{10.5}$$

10.2.1   Energy Reconstruction for e^+e^- events

In the barrel
The energy distribution of the 2 most energetic showers, shown in figure 10.8 peaks at values $E_{shower} \simeq E_{beam}$ with a tail extending to lower energies, corresponding to the radiative events $Z^0 \to e^+e^-(\gamma)$ or to inefficiencies in the energy reconstruction. These are mainly due to the dead zones between HPC modules (cracks). The reconstructed energy as a function of the azimuthal angle, 24-folded to the interval $0° < \Phi < 15°$ is shown in figure 10.9. The effect of the cracks, centered at $mod(\Phi,15) = 7.5°$, is visible in the degradation of the reconstructed energy.

$$(\sigma_E/E)_{hpc} \simeq 11 \ \%$$

DELPHI Interactive Analysis
Beam: 45.6 GeV   Run: 15622   DAS : 26-Aug-1990
                                      09:20:00
Proc: 3-Oct-1990   Evt: 1119   Scan: 16-Oct-1990

	TD	TE	TS	TK	TV	ST	PA
Act	15	0	0	2	0	0	0
	(32)	(0)	(0)	(5)	(6)	(0)	(0)
Deact	0	0	0	0	0	0	0
	(0)	(0)	(0)	(4)	(3)	(0)	(0)
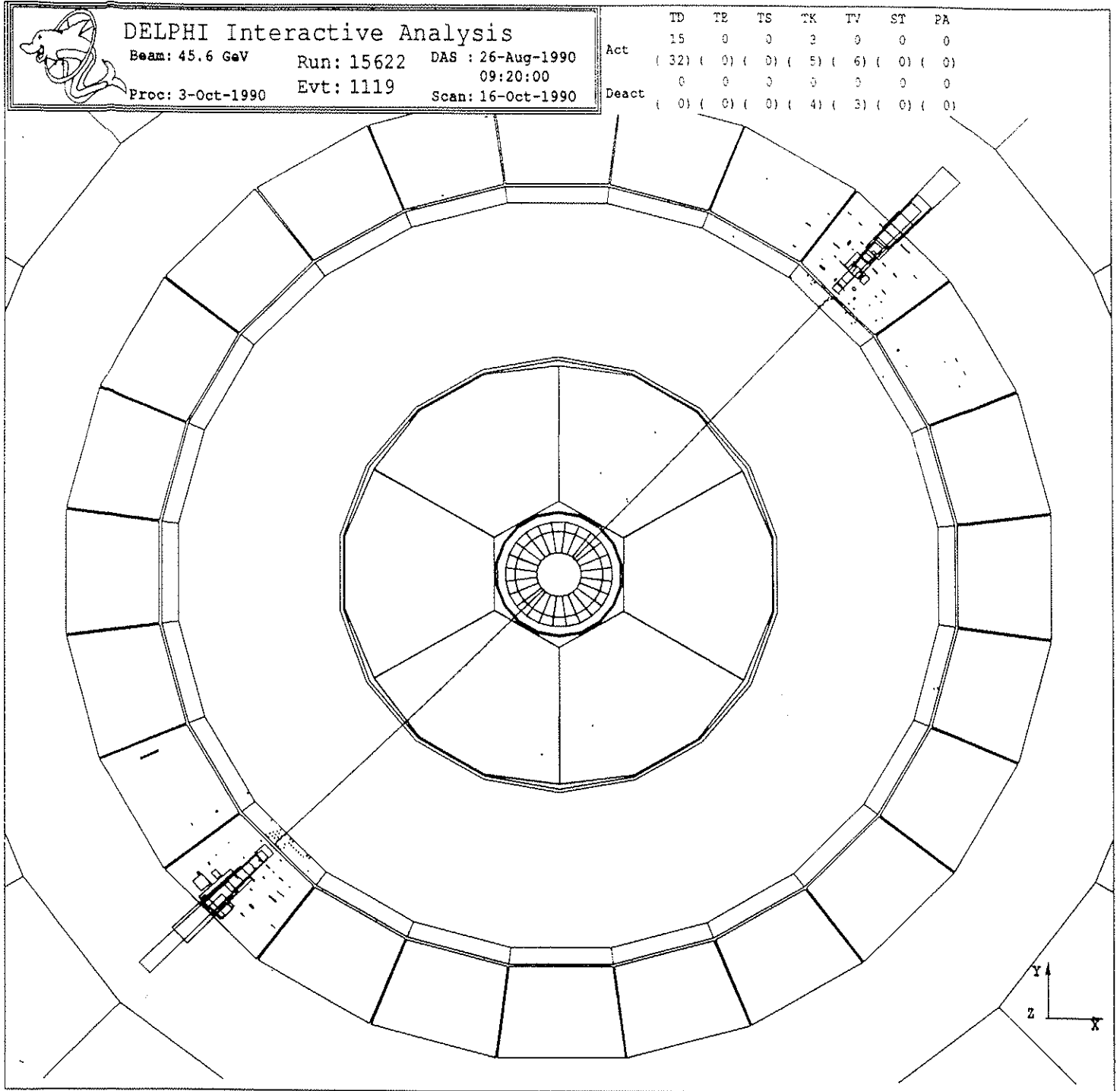
Figure 10.7: Characteristic signature of a $Z^0 \to e^+e^-$ event.
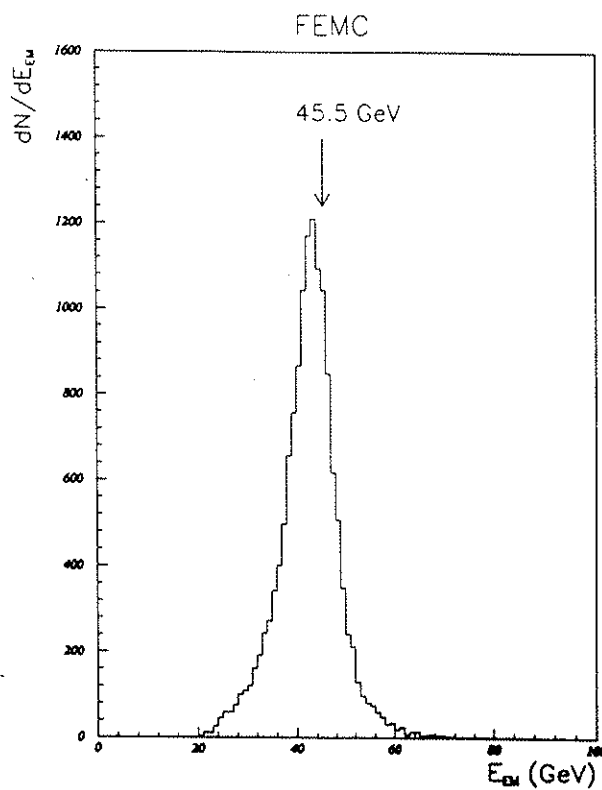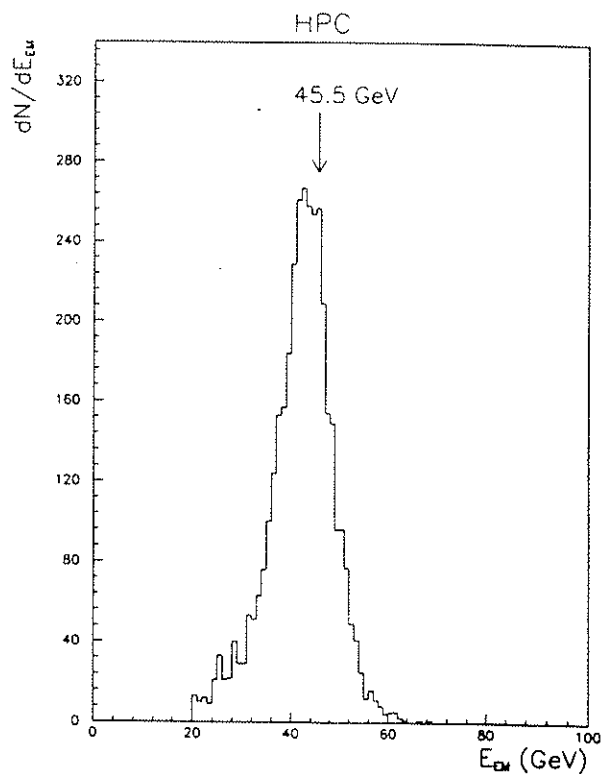
Figure 10.8: Reconstructed shower energy in the electromagnetic calorimeter, for events with 2 energetic back to back electromagnetic showers. The peak close to $E_{EM} \simeq M_Z/2$ is the characteristic signature of $Z^0 \to e^+e^-$ events in the barrel (HPC) and from t-channel $e^+e^- \to e^+e^-$ events in the endcap (FEMC).
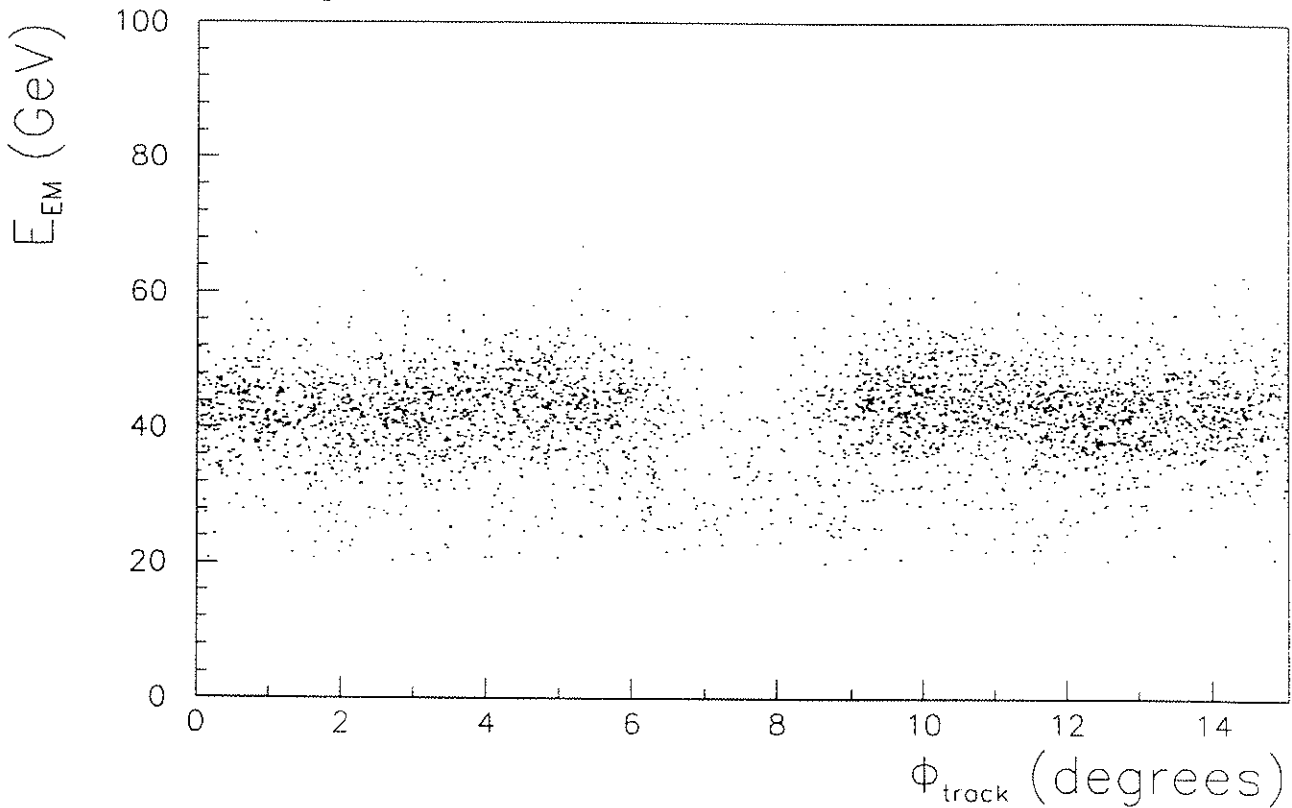
Figure 10.9: Reconstructed shower energy in HPC for $Z^0 \rightarrow e^+e^-$ events as a function of the azimuthal angle folded to the interval $0° < \Phi < 15°$. The HPC dead regions (cracks) centered at $\Phi = 7.5°$ correspond to the physical separation between consecutive modules

In the endcaps

With more than 1 radiation length of material (TPC end-wall, cables, FCA, FCB) before the calorimeter, the degradation of the track energy along the path is significant. Besides, radiated photons along the electron path can convert before reaching the calorimeter. The reconstructed energy in each endcap, shown in figure 10.8, results from the sum of the energies of several clusters scattered in a wide region surrounding the impact point of the particle. The energy resolution of the FEMC for 45 GeV showers is

$$(\sigma_E/E)_{femc} \simeq 9 \%$$
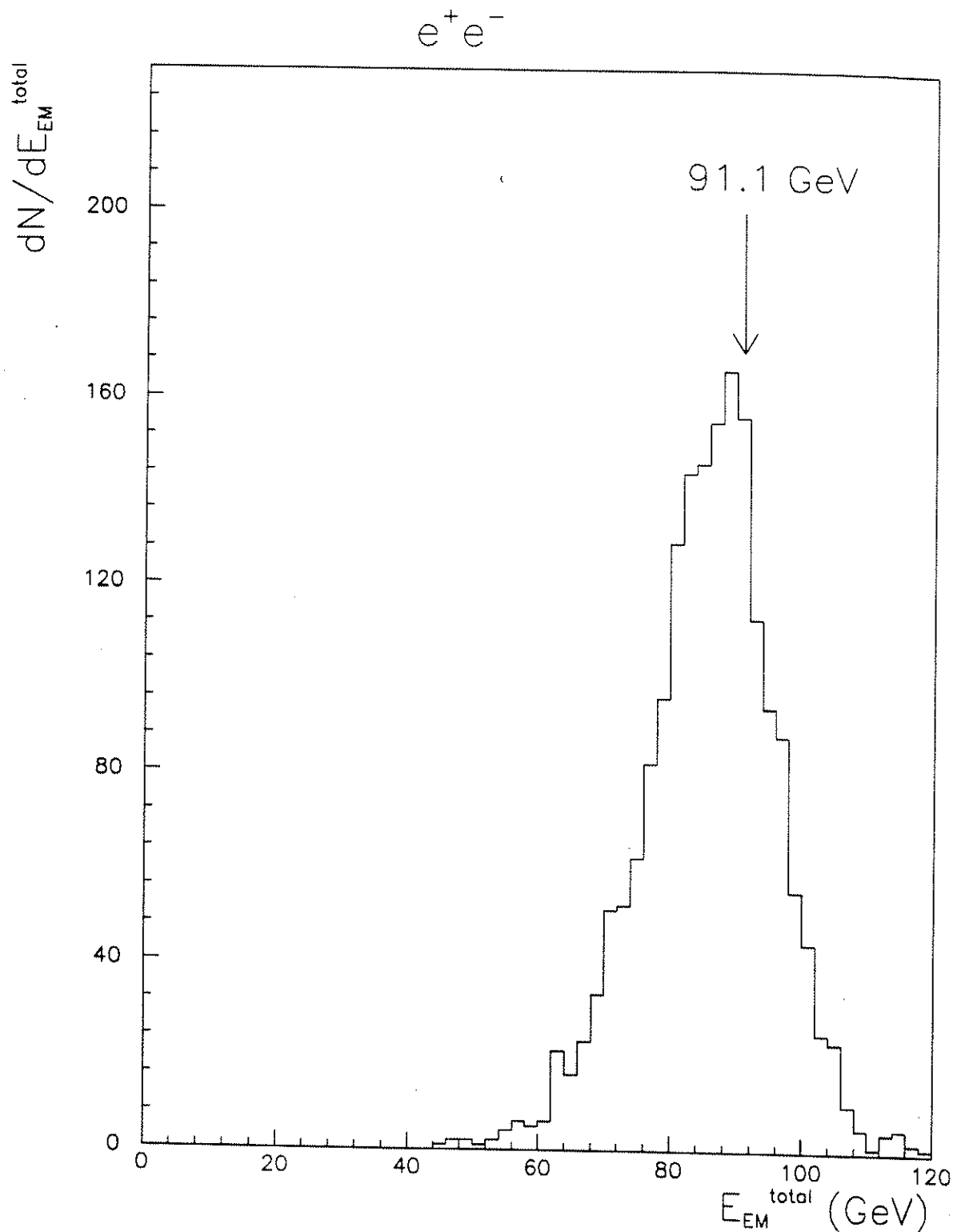
Figure 10.10: Total electromagnetic energy for events with 2 energetic back to back showers in the electromagnetic calorimeter. The peak close to $E_{EM}^{total} \simeq M_Z$ is the characteristic signature of $Z^0 \to e^+e^-$ events in the barrel (HPC) and from t-channel $e^+e^- \to e^+e^-$ events in the endcap (FEMC).

10.2.2 Track Reconstruction for e^+e^- events

In the barrel
Photon radiation by the final state particles occurs before the HPC. The reconstructed track results from the association of the measured track segment in the OD after the radiation has occured, with the track segments measured by TPC and ID before the radiation. If radiation of hard photon(s) occur, failure of the fit procedure or rejection of the OD track segment can happen. The momentum resolution for the tracks from $Z^0 \rightarrow e^+e^-$ is worse and the distribution broader, when compared to the same distribution in $Z^0 \rightarrow \mu^+\mu^-$ events. The track reconstruction efficiency, estimated from real events

$$\varepsilon_e^{track} = 93 \%$$

In the endcaps
The track reconstruction is very difficult due to the showering of the electrons before FCA and FCB that complicates the pattern recognition. The efficiency for reconstructing tracks is low.

10.3 $e^+e^- \rightarrow Z^0 \rightarrow \tau^+\tau^-$ Signature

In an ideal detector, the measured final states from $\tau^+\tau^-$ events would show up in more than 99 % of the decays, in one of the following categories :

- 2 nearly back-to-back tracks + neutrals (in one or both hemispheres)

- 1 track back-to-back with 3 tracks + neutrals (in one or both hemispheres)

- 3 tracks back-to-back with 3 tracks + neutrals (in one or both hemispheres)

In the real detector, final states from $\tau^+\tau^-$ events are observed with sometimes different characteristics: even number of tracks in one or both hemispheres, bundles of tracks (similar to jets) or no tracks in one hemisphere, undetected neutrals, etc. . The number N_{ij}^{rec} of _reconstructed_ events in the topology i-j (i tracks in one hemisphere versus j tracks in the opposite hemisphere) must be estimated by an elaborated analysis taking into account the inefficiencies of several procedures (trigger, data acquisition, reconstruction, analysis, etc.), the physical processes occuring for the particles crossing the detector (pion interaction, photon conversion, electron bremsstrahlung) and the contamination from background events:

$$N_{ij}^{rec} = N_{ij}^{background} + \sum_{k,l} \varepsilon_{i,j \leftarrow k,l} \, N_{k,l}^{produced} \qquad (10.6)$$

with $\varepsilon_{i,j \leftarrow k,l}$ represents the probability that events with topology k-l are detected as having topology i-j. These probabilities can be estimated via Monte Carlo methods, which take into account the inefficiencies affecting the detection and reconstruction of the event all along the chain of trigger, reconstruction and analysis. The reconstructed i-j topologies after full detector simulation, for generated $\tau^+\tau^-$ events decaying into k-l final states are shown in tables 10.1 and 10.2. Two events, one illustrating a photon conversion in the inner wall of the TPC and the other the interaction of a pion before entering the TPC, are shown in figure 10.11. In table 10.12 the comparison between the generated and the reconstructed (after detailed simulation and tracking in the detector) multiplicities are shown. Also from simulation, a scatter plot with the R-Z coordinates at the conversion point for the process $\gamma \rightarrow e^+e^-$ is shown.

$\varepsilon_{1,1 \rightarrow i,j}$	i=0	i=1	i=2	i=3	i=4	i=5	i=6	i=7	i=8
j=0	.042	.031	.004	.001	.000	.000	.000	.000	.000
j=1	.025	.673	.033	.040	.007	.006	.002	.000	.000
j=2	.003	.035	.008	.006	.002	.001	.000	.000	.000
j=3	.001	.039	.005	.004	.002	.001	.000	.001	.000
j=4	.001	.009	.002	.000	.000	.000	.000	.000	.000
j=5	.000	.004	.001	.000	.000	.000	.000	.000	.000
j=6	.000	.002	.001	.000	.000	.000	.000	.000	.000
j=7	.000	.001	.001	.000	.000	.000	.000	.000	.000
j=8	.000	.001	.001	.000	.000	.000	.000	.000	.000

Table 10.1: $\varepsilon_{1,1 \rightarrow i,j}$, the probability that events with 1-1 topology at the level of generation are reconstructed with topology i-j

$\varepsilon_{1,3 \rightarrow i,j}$	i=0	i=1	i=2	i=3	i=4	i=5	i=6	i=7	i=8
j=0	.055	.007	.002	.001	.000	.000	.000	.000	.000
j=1	.015	.011	.002	.001	.000	.000	.000	.000	.000
j=2	.010	.056	.006	.004	.002	.001	.000	.000	.000
j=3	.012	.529	.033	.026	.011	.004	.001	.000	.000
j=4	.002	.071	.013	.009	.004	.002	.000	.000	.000
j=5	.001	.041	.012	.004	.004	.002	.000	.000	.000
j=6	.000	.011	.004	.004	.000	.000	.000	.000	.000
j=7	.000	.009	.004	.003	.000	.000	.000	.000	.000
j=8	.001	.003	.002	.000	.000	.000	.000	.000	.000
j=9	.000	.002	.000	.000	.000	.000	.000	.000	.000
j=10	.000	.000	.000	.000	.000	.000	.000	.000	.000

Table 10.2: $\varepsilon_{1,3 \rightarrow i,j}$, the probability that events with 1-3 topology at the level of generation are reconstructed with topology i-j
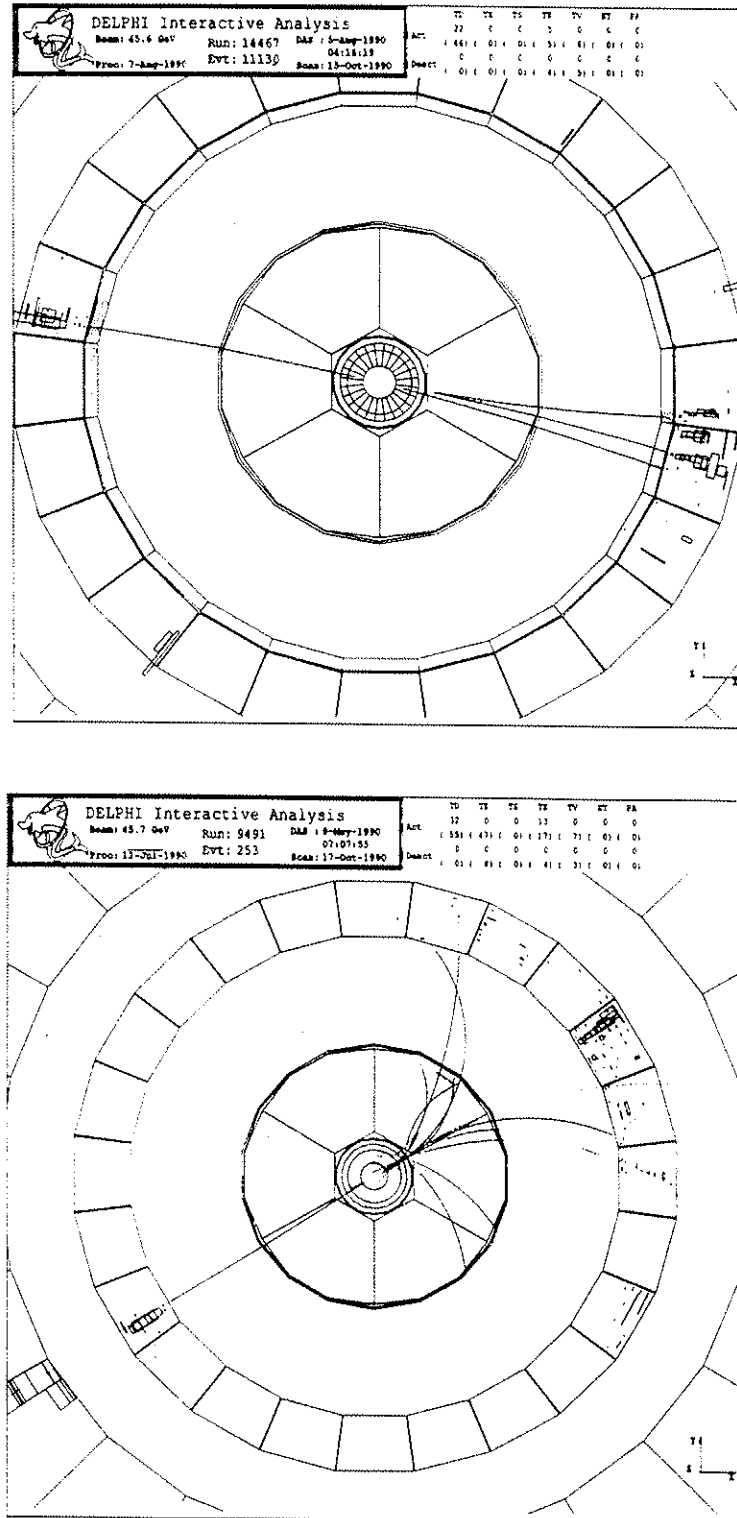
Figure 10.11: Photon conversion in the inner wall of the TPC (top) and interaction of a pion before entering the TPC (bottom) for real $\tau^+\tau^-$ events.

14	18	6		
22	33	10		
28	59	15	2	
56	93	27	1	
122	208	85		
170	254	21		
604	1250	8		
484	205	5		
4647	72	6		
430	52	2		
237	57	1		

TRACKS (REC) vs TRACKS(SIM)

RV VS ZV
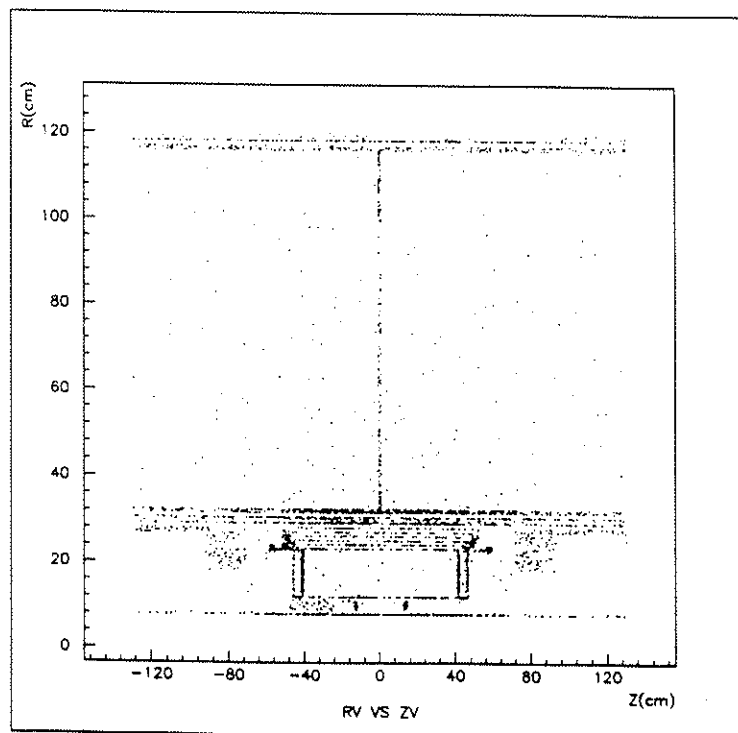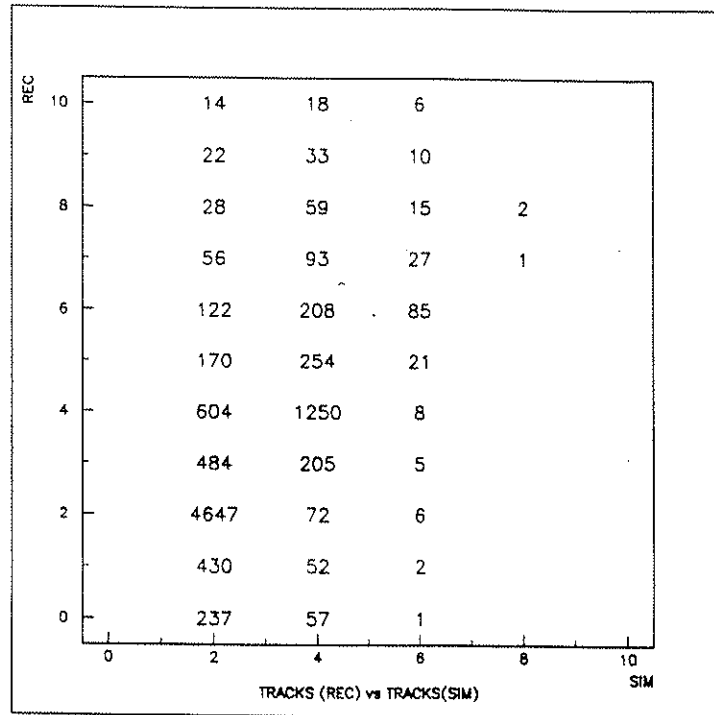
Figure 10.12: Generated and reconstructed multiplicities for Monte Carlo events (top) R-Z coordinates of conversion point of photons (bottom)

10.4   Trigger for $\tau^+\tau^-$ events

$\tau^+\tau^-$ events can be triggered independently by several detectors or by coincidences of detector responses to the multiple types of signatures (track multiplicity, neutral and charged electromagnetic energy, penetrating pions and muons) and their topology (back to back tracks, electromagnetic energy surrounding charged tracks, etc.).

As explained in the following, a set of redundant triggers for charged back to back topologies (plus neutrals) exists in the barrel, allowing for a global trigger efficiency for $\tau^+\tau^-$ events at the level of 97% $\pm$ 1%. In the endcaps, the redundancy and the number of independent triggers is smaller, with a corresponding reduction of the trigger efficiency for $\tau^+\tau^-$ events. Finally, the angular region between barrel and endcaps, $35° < \theta < 42°$ and $138° < \theta < 145°$, is covered by the TPC track trigger (second level) and by the back to back trigger from the HOF scintillators.

10.4.1   Track trigger

The most efficient type of trigger for $\tau^+\tau^-$ events is the track trigger requiring the coincidence of ID and OD signals (IDOD and IOMJ) or the coincidence of OD and TOF signals (SCOD). This trigger selects the $\tau\tau$ decays in the barrel region. It has three components [4]:

Back to back trigger (IDOD)

Majority trigger (IOMJ)

Single track trigger (SCOD)

The computation of the efficiencies of the several subtriggers was done using as "reference" the IDOD trigger, due to its high efficiency, computed from the $ee, \mu\mu, \tau\tau$ event samples and its back to back requirement.

$$\epsilon_{trig}^{IDOD} \simeq 90\%$$

---

[4]For the trigger mnemonics see Chapter 8

10.4.2   Scintillator trigger (back-to-back)

The TOF scintillators covering approximately the same angular region as the OD, provide an independent way of triggering events with back to back topology. Together with the IDOD and IOMJ track triggers, they give high redundancy in the barrel trigger. The efficiency of the TOF counters to single (minimum ionizing or penetrating) tracks is of the order of 60 %, accounting for the geometric dead zones (15 %) and other inefficiences. For $\tau^+\tau^-$ events, the TOF trigger for back to back topologies, TOBB, gives the necessary redundancy to trigger on final states with charged tracks in opposite hemispheres like

- μ versus μ

- μ versus $m\pi + n\pi^0$ $m = 1 \; or \; 3 \; , \; n \geq 0$

- $k\pi + l\pi^0$ versus $m\pi + n\pi^0$ $m, k = 1 \; or \; 3 \; , \; n, l \geq 1$

TOF counters are also sensitive to low energy stuff, leaking from the HPC due to non full containment of showers developed by high energy electrons or photons and are therefore rather efficient detectors for these particles.

10.4.3   Electromagnetic energy trigger (back-to-back)

The HPC trigger for back to back topologies, HPBB, requiring coincidence of signals from back to back octants (scintillators set to 2 Gev threshold) allow an independent way of triggering the following final states:

- e versus e

- e versus $m\pi + n\pi^0$ $m = 1 \; or \; 3 \; , \; n \geq 1$

- $k\pi + l\pi^0$ versus $m\pi + n\pi^0$ $m, k = 1 \; or \; 3 \; , \; n, l \geq 1$

This trigger is important not only for a final state with electrons but also for all the hadronic final states with charged π accompanied by at least one energetic γ (from π^0). These final states, triggered by the track trigger will be redundantly triggered by the HPBB and possibly also by the TOBB (when in both hemispheres particles hit TOF counters or the energy leaking from the HPC is enough to produce signals in the TOF scintillators).

10.4.4   Majority triggers

TOMJ (at least 2 TOF octants with hits in counters), HPMJ (at least 2 HPC octants with energy deposition above scintillator threshold) contain the previous ones. THMJ (signal from any TOF octant in coincidence with a signal from any HPC octant) is another type of trigger signal that can improve the redundancy for $\tau^+\tau^-$ events.

10.4.5   TOF-OD coincidences

In addition mixed triggers like a coincidence between TOF octants and OD can improve the redundancy to trigger $\tau^+\tau^-$ events.

10.4.6   Efficiency of the barrel triggers for leptons

The trigger for $Z^0 \rightarrow \mu^+\mu^-$ events in the barrel region, relies on the track trigger sub-components (IDOD,IOMJ,SCOD) and on the back to back trigger from the TOF counters (TOBB). The threshold of the HPC scintillators is such that these counters are not sensitive to mip's.
The trigger for $Z^0 \rightarrow e^+e^-$ events in the barrel region is highly redundant (efficiency close to 100%). Events are independently triggered by the HPC/TOF scintillators (THMJ,HPBB,TOMJ) and by the track trigger. The most efficient trigger component results from the coincidences (majority 1) between the HPC and TOF scintillators. The efficiency of the several trigger components in the barrel region is displayed in next table.

Efficiency (%)	e^+e^-	$\mu^+\mu^-$	$\tau^+\tau^-$
TOBB	57.4	38.7	51.3
TOMJ	62.4	40.2	62.6
HPBB	66.3	0.7	26.9
HPMJ	68.4	1.1	31.0
THMJ	88.9	13.9	74.3
SCOD	73.3	66.8	74.8
IOMJ	95.8	96.6	96.4

Table 10.3: Efficency of the main barrel subtriggers computed with respect to the IDOD trigger in the region $45° < \theta < 135°$, for each of the three leptonic channels.
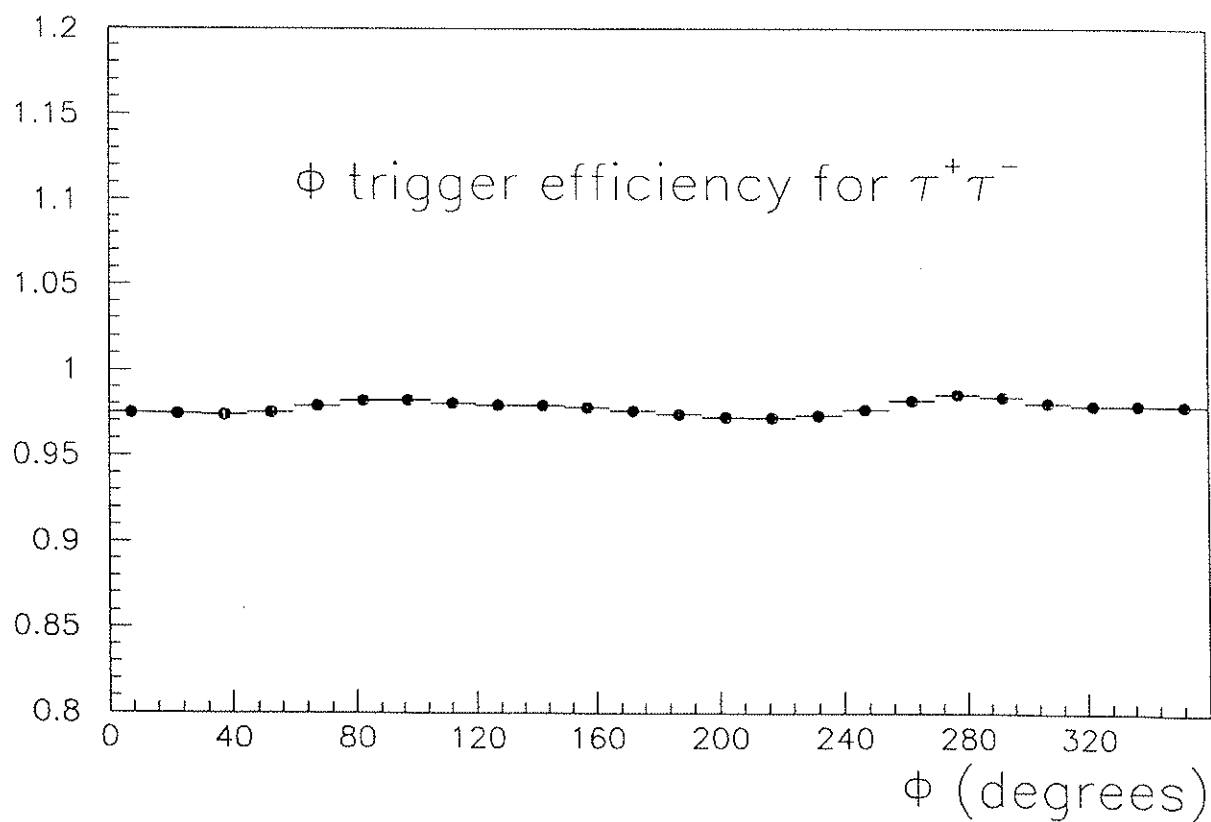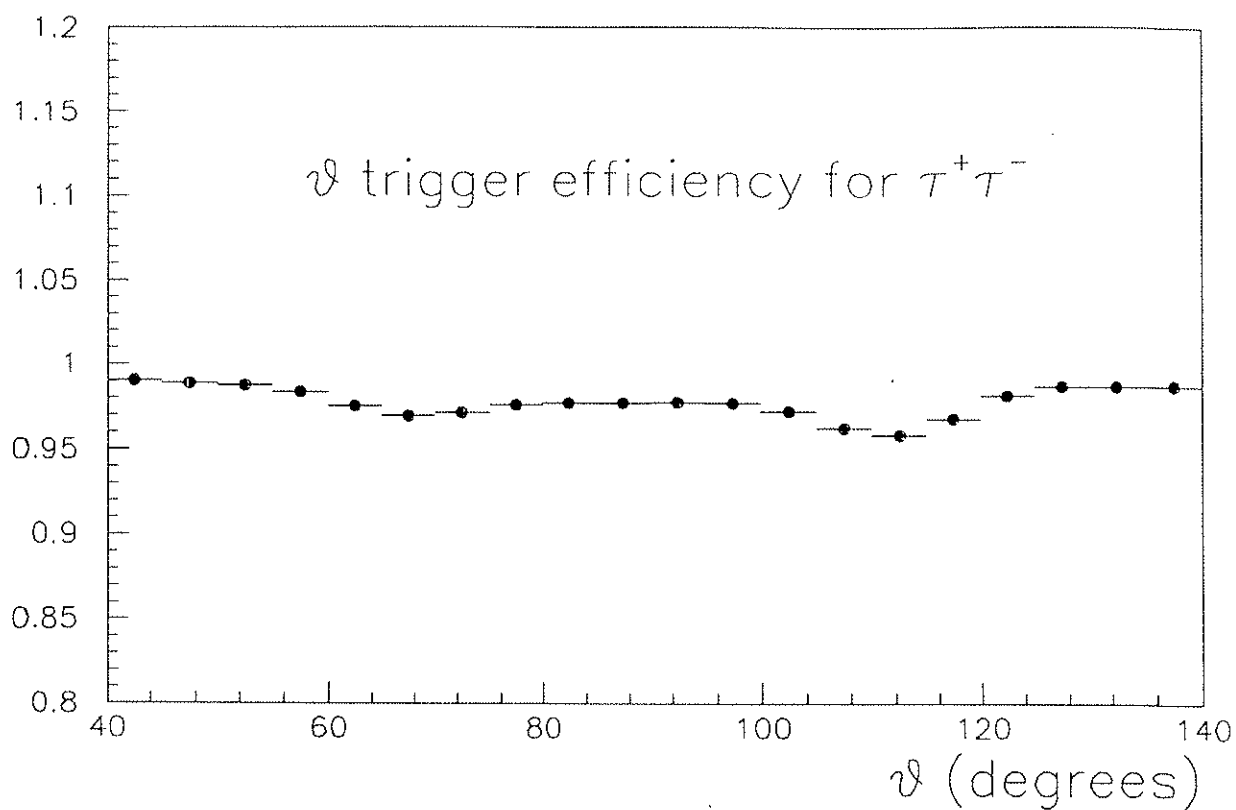
Figure 10.13: Efficiency of the barrel trigger for $\tau^+\tau^-$ events, as a function of θ, Φ. The efficiency is computed using the 2 independent triggers: track trigger (IDOD+IOMJ) and scintillator trigger (THMJ)

10.5   Separation of e^+e^- , $\mu^+\mu^-$ and $\tau^+\tau^-$ events

In $Z^0 \to e^+e^-$ and $Z^0 \to \mu^+\mu^-$ events, the produced pair of leptons carries all the centre of mass energy available in the collision (neglecting radiation): the energy distribution of the electromagnetic showers associated to each electron track and the momentum distribution of each muon track peak at the beam energy. The missing energy or missing momentum respectively for each class of events, is negligible.

In $Z^0 \to \tau^+\tau^-$ events, each τ decays into one or two neutrinos. Missing energy and missing momentum are then characteristic of $\tau^+\tau^-$ events, with the distributions of momentum of the individual tracks and of the energy of the showers covering all the kinematically allowed range. In addition, due to neutrinos, the topology of the events is different, as discussed in the sequence.

10.5.1   Acolinearity(θ_{acol}) and Acoplanarity(θ_{acop})

For events with 2 charged tracks in final state and measured momentum vectors $\vec{P}_1, \vec{P}_2$, the acolinearity angle is defined as

$$\cos\ \theta_{acol} = -\frac{\vec{P}_1 \cdot \vec{P}_2}{|\vec{P}_1||\vec{P}_2|} \tag{10.7}$$

and the acoplanarity angle is defined as the angle between the 2 planes defined by each of the particles and one of the beam particles (electron here) direction $\vec{P}_{e^-}$.

$$\cos\ \theta_{acop} = -\frac{(\vec{P}_1 \times \vec{P}_{e^-}) \cdot (\vec{P}_2 \times \vec{P}_{e^-})}{|\vec{P}_1 \times P_{e^-}||\vec{P}_2 \times P_{e^-}|} \tag{10.8}$$

The acolinearity distributions in e^+e^- and $\mu^+\mu^-$ final states reflect mainly the initial state radiation processes and their intensity. Initial state radiation of collinear photons (with respect to the emitting beam particle) that are lost along the beam tube imposes by 4-momentum conservation that the final state particles are not exactly back-to-back but still coplanar.

The acoplanarity distributions in e^+e^- and $\mu^+\mu^-$ final states, peaking at very small angles, reflect mainly the final state radiation.

The acolinearity and acoplanarity distributions in $\tau^+\tau^-$ final states reflect in addition to the same radiative mechanisms described for $e^+e^-, \mu^+\mu^-$, the decay of a more massive object (the τ is 17 times more massive than the muon and 3500 more massive than the electron) with the 4-momentum carried away by the undetected neutrinos.

The simulated distributions of $\theta_{acol}, \theta_{acop}$ in $e^+e^-, \mu^+\mu^-$ and $\tau^+\tau^-$ events are shown in figures 10.14,10.15 and 10.16 respectively. From the the figures it is clear that:

• $e^+e^-, \mu^+\mu^-$: about 80% of the pairs have acolinearity and acoplanarity values $\theta_{acol} < 1°, \theta_{acop} < 1°$ while the fraction of events with acolinearity or acoplanarity angles greater than 10° is of the order of 2-3 %.

• $\tau^+\tau^-$: the acolinarity and acoplanarity distributions are contained below 20°, more than 90% of the pairs have $\theta_{acol} > 1°$ and more than 80% of the pairs have $\theta_{acop} > 1°$.

The effects of acolinearity and acoplanarity cuts applied to minimize the $e^+e^-, \mu^+\mu^-$ contamination in the $\tau^+\tau^-$ sample can be seen in the tables 10.4 and 10.5, displaying the fraction of events of each lepton family surviving the cuts.

LEPTON PAIR	$\theta_{acol} > 1°$	$\theta_{acol} > 2°$	$\theta_{acol} > 3°$
e^+e^-	19.1%	10.8%	7.3%
$\mu^+\mu^-$	15%	5%	3%
$\tau^+\tau^-$	92%	75%	58%

Table 10.4: Fraction of events of each leptonic family with acolinearity angle greater than 1°, 2° and 3° respectively.

LEPTON PAIR	$\theta_{acop} > 1°$	$\theta_{acop} > 2°$	$\theta_{acop} > 3°$
e^+e^-	8.3%	4.9%	3.6%
$\mu^+\mu^-$	15%	7%	6%
$\tau^+\tau^-$	80%	62%	48%

Table 10.5: Fraction of events of each leptonic family with acoplanarity angle greater than 1°, 2° and 3° respectively.

Acolinearity and acoplanarity cuts also contribute to remove the background events from $\gamma^*\gamma^* \rightarrow (e^+e^-) \, l^+l^-$ characterized by pairs of high acolinearity (pairs of close tracks).
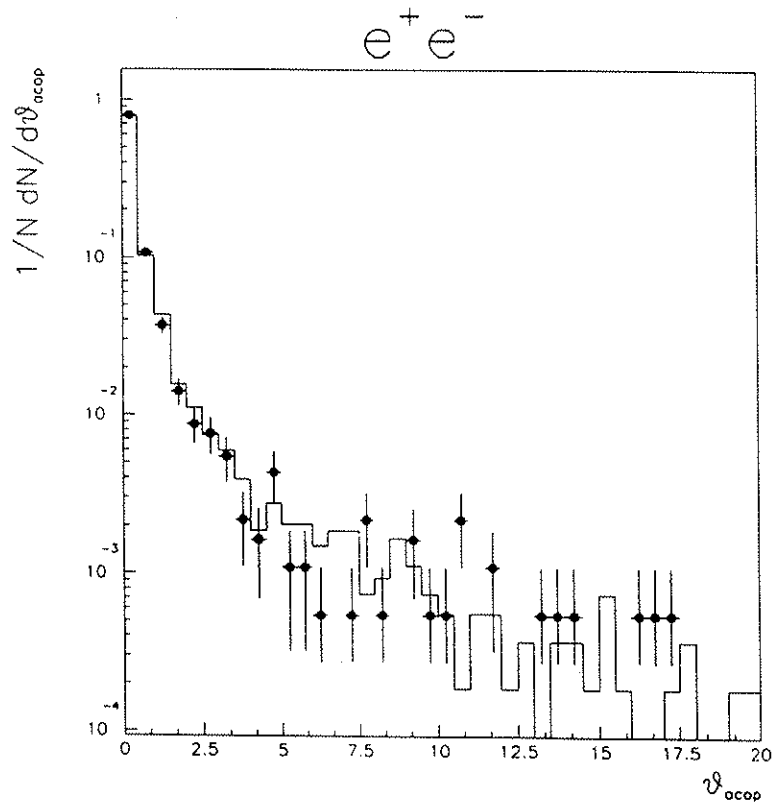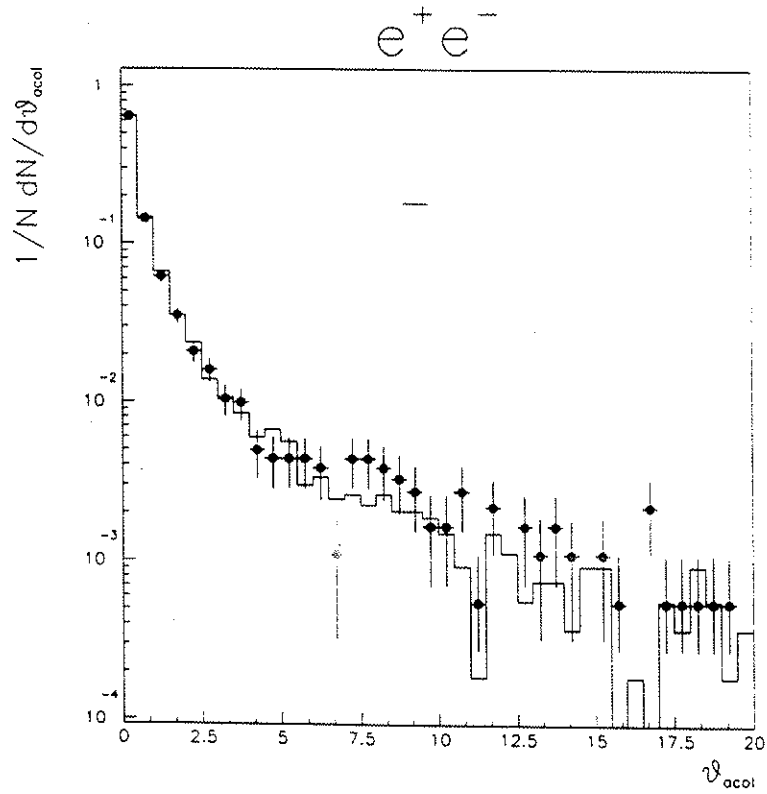
Figure 10.14: Reconstructed acolinearity and acoplanarity distributions for simulated $Z^0 \rightarrow e^+e^-$ events. Superimposed are the corresponding distributions obtained from a sample of 2500 real events.
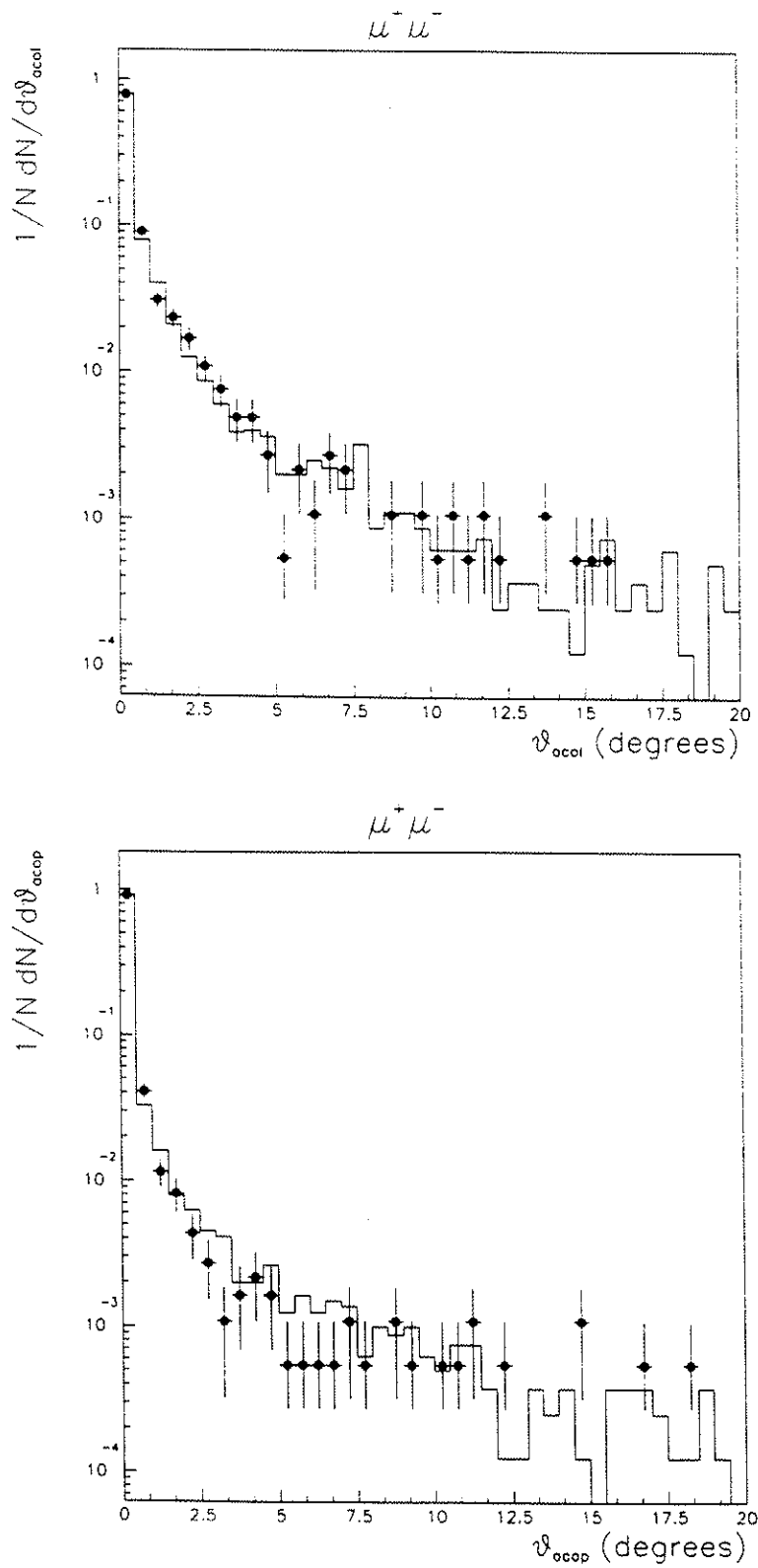
Figure 10.15: Reconstructed acolinearity and acoplanarity distributions for simulated $Z^0 \to \mu^+\mu^-$ events. Superimposed are the corresponding distributions from a sample of 3000 real events.
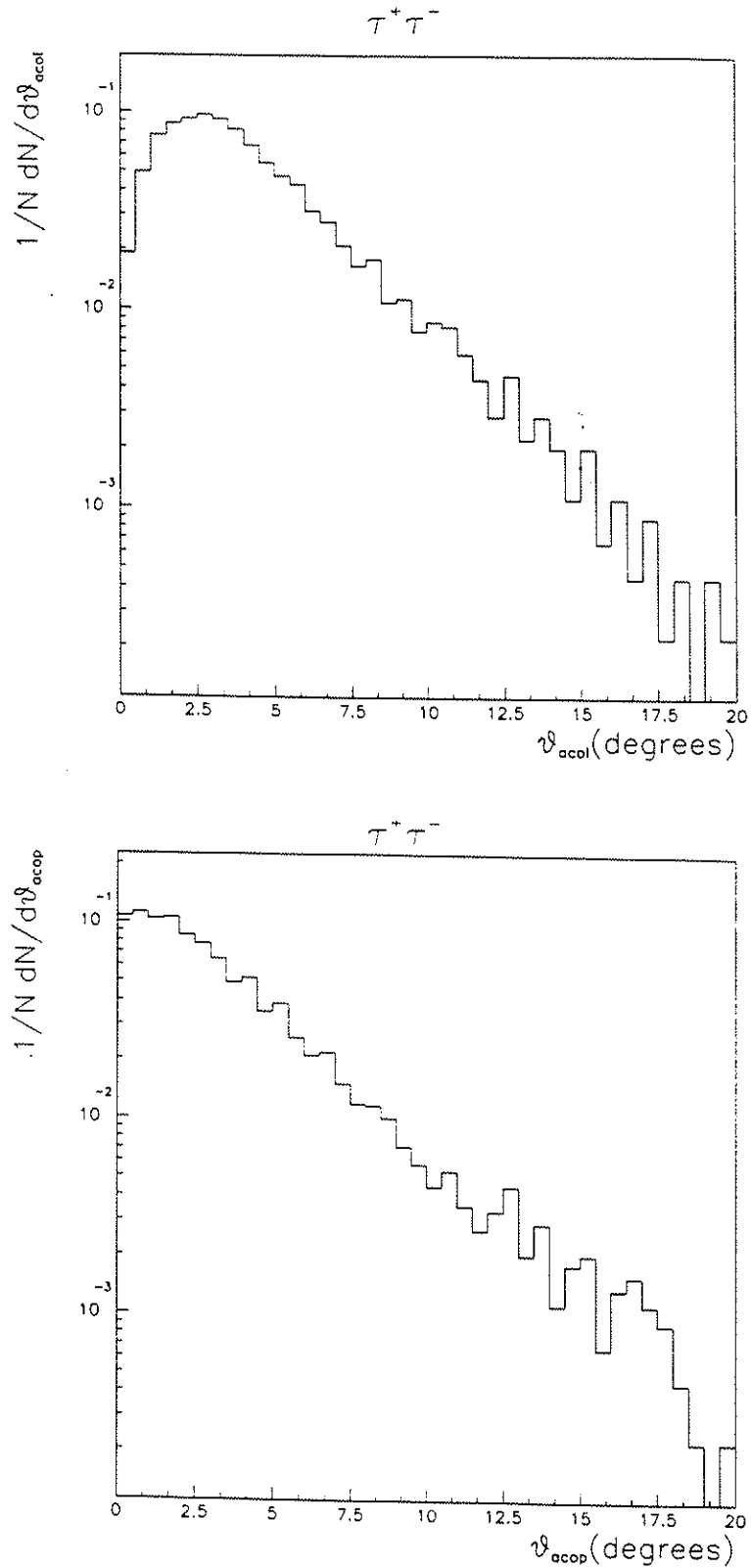
Figure 10.16: Reconstructed acolinearity and acoplanarity distributions in simulated $Z^0 \rightarrow \tau^+\tau^-$ decays

Using global event variables like the visible momentum (P_{vis}), the total electromagnetic energy (E_{em}), the acolinearity (θ_{acol}) or the acoplanarity (θ_{acop}), or the variables related to each track (momentum P_{trk} and energy of matched shower E_{sh}), the events belonging to each leptonic family can be identified by the region they populate in the 2-dimensional distribution of pairs of variables. The correlated distributions of the following pairs of variables can be used to disentangle e^+e^- from $\tau^+\tau^-$ or $\mu^+\mu^-$ from $\tau^+\tau^-$ events :

$$(E_{em} \ vs \ \theta_{acol}) \qquad e^+e^- \ \Leftrightarrow \ \tau^+\tau^- \qquad\qquad (10.9)$$

$$(E_{em} \ vs \ \theta_{acop}) \qquad e^+e^- \ \Leftrightarrow \ \tau^+\tau^- \qquad\qquad (10.10)$$

$$(E_{sh \ 2} \ vs \ E_{sh \ 1}) \qquad e^+e^- \ \Leftrightarrow \ \tau^+\tau^- \qquad\qquad (10.11)$$

$$(P_{vis} \ vs \ \theta_{acol}) \qquad \mu^+\mu^- \ \Leftrightarrow \ \tau^+\tau^- \qquad\qquad (10.12)$$

$$(P_{vis} \ vs \ \theta_{acop}) \qquad \mu^+\mu^- \ \Leftrightarrow \ \tau^+\tau^- \qquad\qquad (10.13)$$

$$(P_{trk \ 2} \ vs \ P_{trk \ 1}) \qquad \mu^+\mu^- \ \Leftrightarrow \ \tau^+\tau^- \qquad\qquad (10.14)$$

In figures 10.17, 10.18, 10.19, 10.20, the _simulated_ 2-D distributions of some of the pairs of variables above are displayed.
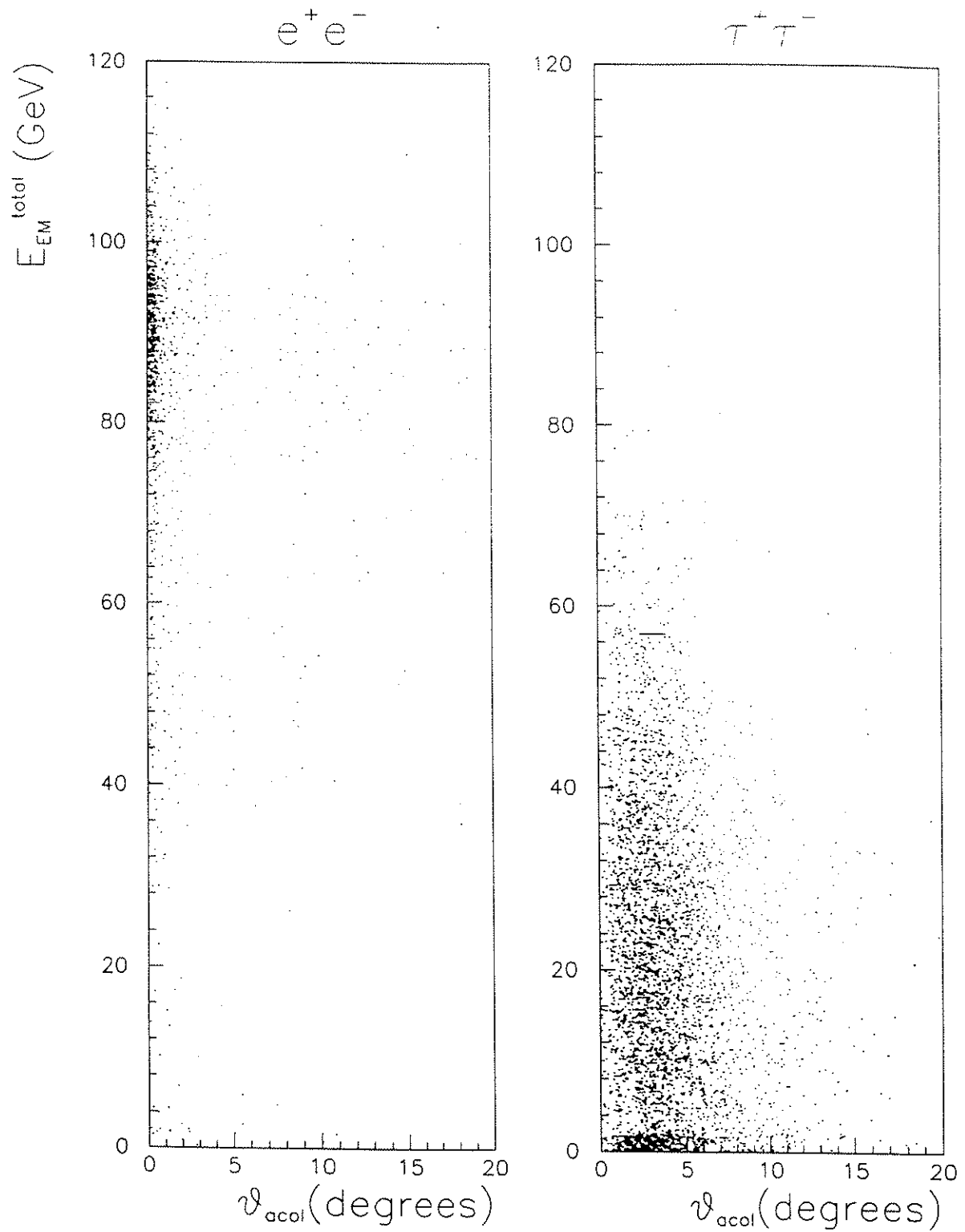
Figure 10.17: Distribution of the total reconstructed electromagnetic energy versus acolinearity for simulated $Z^0 \to e^+e^-$ and $Z^0 \to \tau^+\tau^-$ decays.
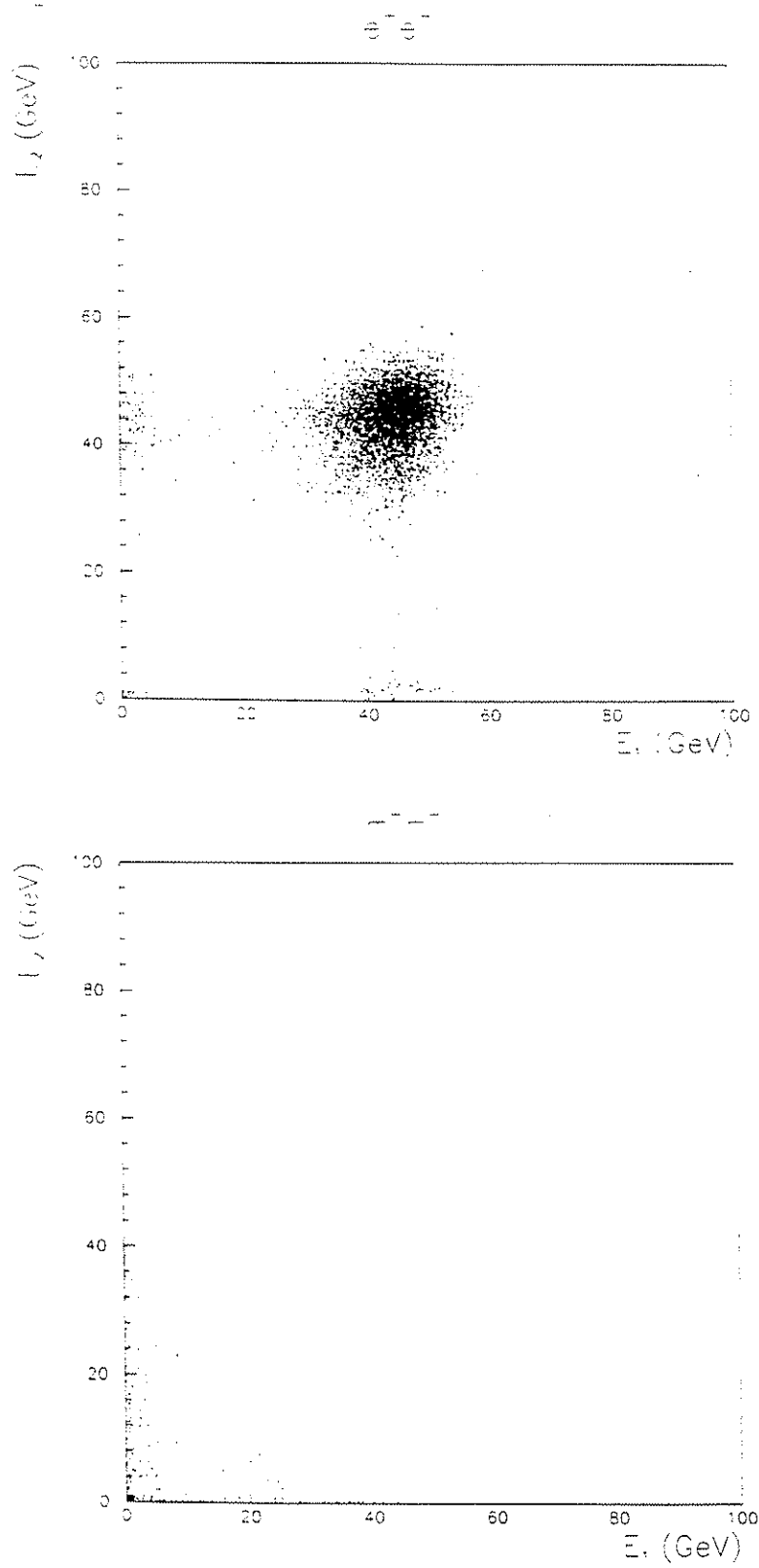
Figure 10.18: Electromagnetic energy associated to one of the tracks versus the electromagnetic energy associated to the other, for simulated $Z^0 \rightarrow e^+e^-$ and $Z^0 \rightarrow \tau^+\tau^-$ events.
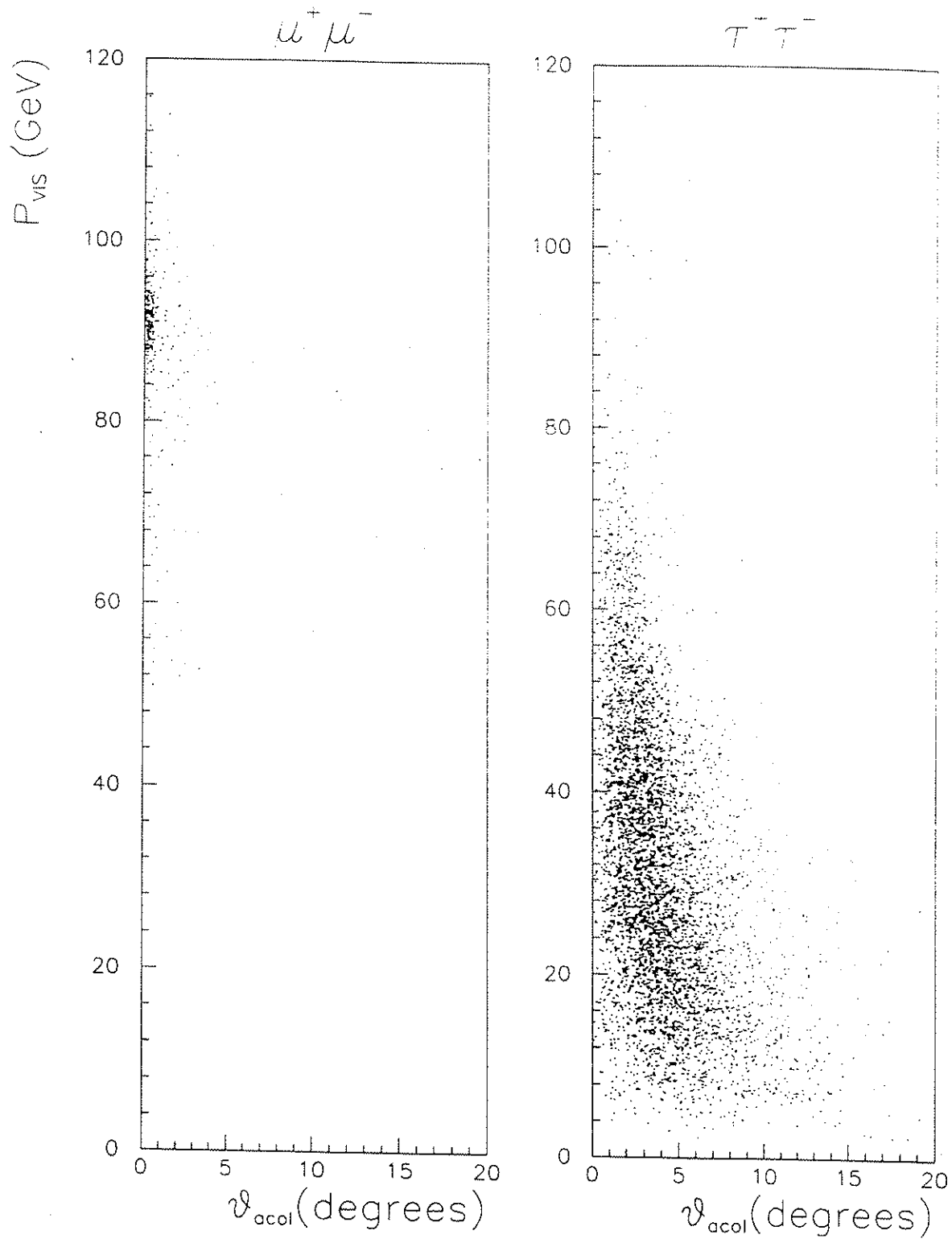
Figure 10.19: Distribution of reconstructed visible momentum versus acolinearity for simulated $Z^0 \rightarrow \mu^+\mu^-$ and $Z^0 \rightarrow \tau^+\tau^-$ decays.
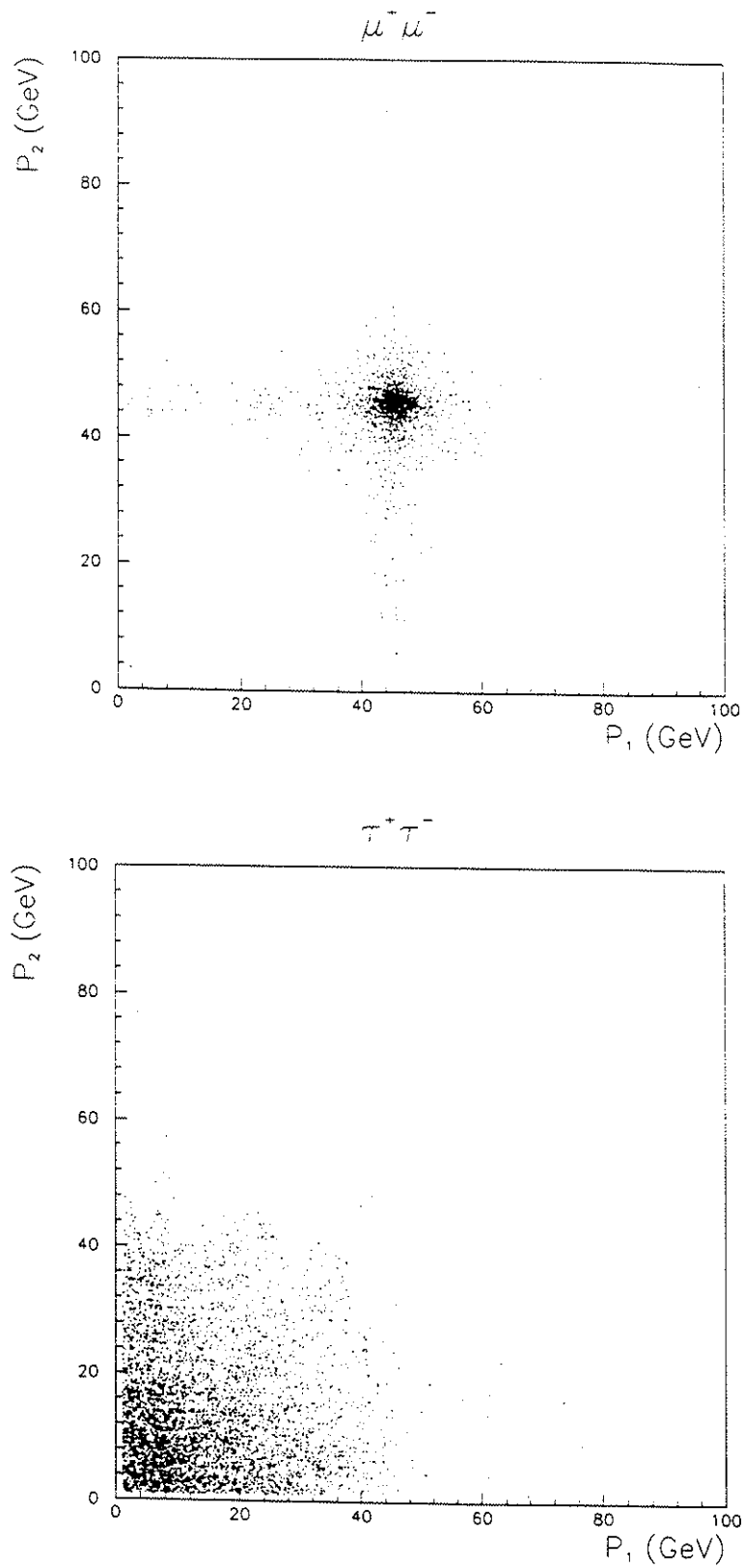
Figure 10.20: Momentum of one of the tracks versus the momentum of the other, for simulated $Z^0 \rightarrow \mu^+\mu^-$ and $Z^0 \rightarrow \tau^+\tau^-$ events.

Chapter 11

EVENT SELECTION AND ANALYSIS

The first stage in the offline filtering of events, occuring at the raw data processing phase by DELANA, consists in the selection of a sample containing the leptonic candidates. The cuts imposed at this level are very loose and the selection criteria are such that most of the hadronic, cosmic and beam gas events are not selected into the sample of leptonic events. At this level no attempt is made to give a more detailed event tag or classification (e.g. $e^+e^-, \mu^+\mu^-, \tau^+\tau^-, \gamma^x\gamma^x$). The fraction of real leptonic events from Z^0 decays in this sample is of about 10 to 15 %, depending on the centre of mass energy (on/off peak) and triggering conditions.

In a second stage, another analysis program (TAUANA) reads the Master DST [1] files containing the leptonic candidates and after decoding the reconstructed event structure creates the μDST files, consisting of n-tuples[73] filled with the relevant variables describing and summarizing the event (150 variables per event).

A set of cuts on the ntuple variables is then imposed to tag and select the $\tau^+\tau^-$ events. Selection of the e^+e^- and $\mu^+\mu^-$ events and study of their typical distributions is also possible. The background contamination and the efficiency of cuts are determined from the same leptonic μDST.

Further data reduction steps are possible, leading to smaller event samples, the personal DST's. The data with the reduction factors in the number of events and in the volume of data at the several stages of the analysis chain is shown in figure 11.1.

---

[1]DST is the common abreviation for Data Summary Tape
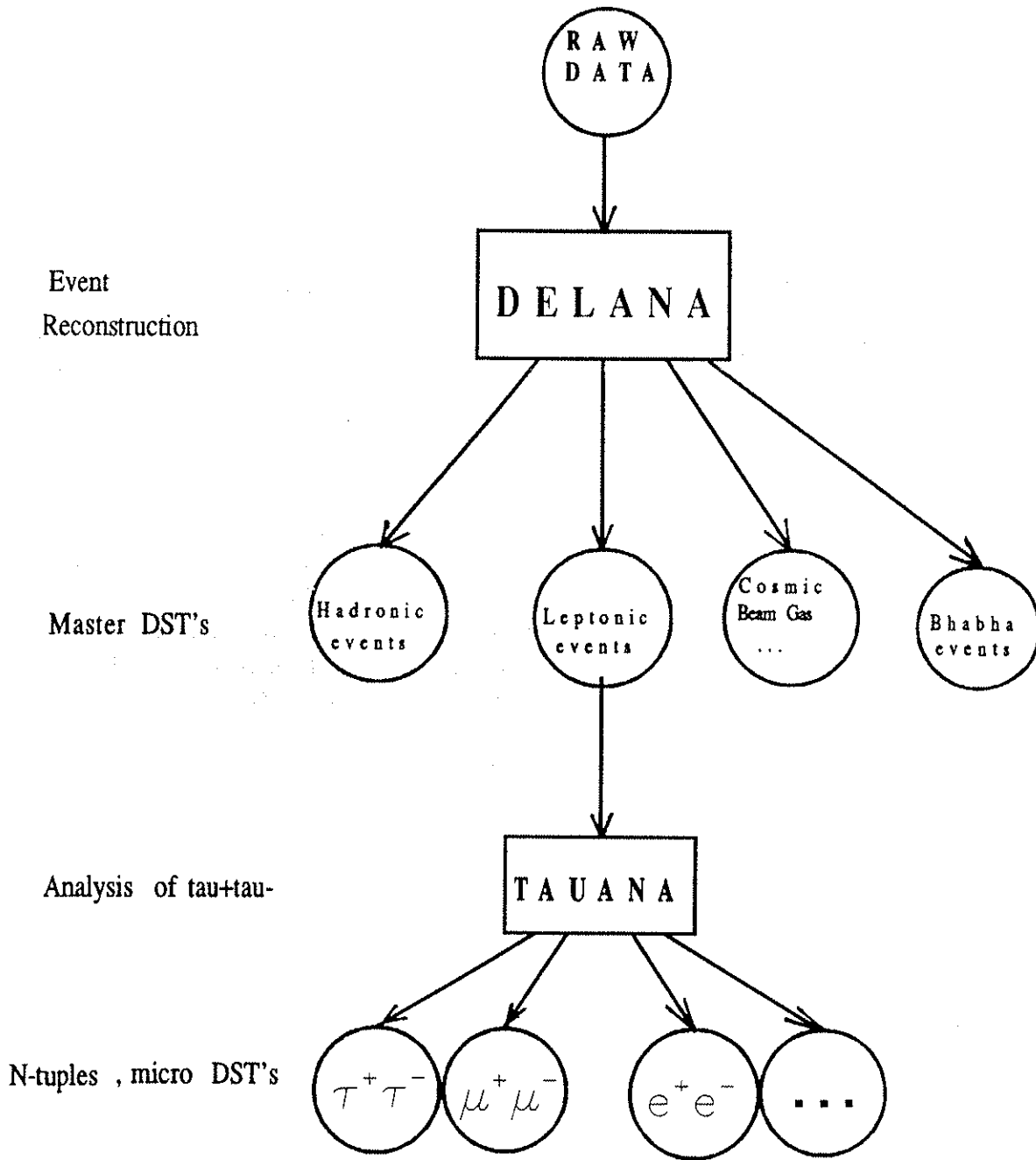
Figure 11.1: Event and data flow in the offline analysis chain.

11.1   Selection of Leptonic Events

Leptonic events are filtered in a first pass (DELANA) by the folowing set of cuts:

For the event :

- C1) Number of reconstructed tracks less than 9

$$\#tracks < 9 \tag{11.1}$$

- C2) Total energy (tracking chambers momentum + energy in calorimeters) > 8 GeV

$$E_{TOT} > 8 \ GeV \tag{11.2}$$

For at least one track :

- C3) Distance of closest approach to the interaction point in the transverse plane (e.g. impact parameter) to the beam line smaller than the beam-pipe radius

$$d_{IP} < 8 \ cm \tag{11.3}$$

- C4) Z-distance to the interaction point smaller than 10 cm

$$Z_{IP} < 10 \ cm \tag{11.4}$$

- C5) Momentum of the track greater than .5 GeV

$$P_{track} > .5 \ GeV \tag{11.5}$$

Cut C1 filters all low multiplicity events: lepton pairs ($\tau^+\tau^-$ decays, $\mu^+\mu^-$, e^+e^-), $\gamma^*\gamma^*$ events ($e^+e^-l^+l^-$), beam-gas events, cosmics, low multiplicty hadronic events.

Cut C2 rejects mainly $\gamma^*\gamma^*$ (low-mass pairs) and beam-gas events (low energy tracks)

Cut C3 and C4 rejects most of the tracks from beam gas events and also cosmics events crossing the detector outside the beam-pipe and away from the interaction point of the beams.

This set of broad cuts, altough selecting the wanted leptonic events from Z^0 decays and leaving room for the $\tau^+\tau^-$ final states with additional tracks coming from γ conversion and π interactions, also keeps some of the undesired background from cosmic events, beam-gas interactions, $\gamma^*\gamma^*$ or from low multiplicity hadronic events.

11.2   Track quality cuts

In the second stage of the analysis (TAUANA), checks are made on the quality of the reconstructed tracks in the event.

For the majority of tracks originating in the primary vertex of the $e^+e^-, \mu^+\mu^-$ events and from the secondary vertices in $\tau^+\tau^-$ decays, the reconstructed values for the impact parameter and z-distance of closest approach to the interaction point are contained within a cylinder of radius 1.5 cm and halflength 3.0 cm centered in the interaction point of the beams and called the *interaction region* (see figure 11.2). In the sequence, for a track to be considered as coming from the interaction region, its distance of closest approach to the interaction point in the transverse (d_{IP}) and longitudinal (Z_{IP}) direction must obey:

$$|d_{IP}| < 1.5 \; cm \quad , \quad |Z_{IP}| < 3 \; cm \tag{11.6}$$

Neverthless, given the fact that a significant part of $\tau^+\tau^-$ decays have π^0's in the final state, the signature of such events in the detector is sometimes "polluted" by additional tracks coming from $\gamma \rightarrow e^+e^-$ conversions, pointing to the interaction point in the longitudinal view, but missing the interaction region in the transverse view. Also, the majority of the hadronic τ decays contain at least one charged π. In some events, due to interaction of the pions crossing the materials, bundles of low energy tracks can appear superimposed to the other tracks of the event, faking multiplicities and topologies.

The analysis method used tries to distinguished the "secondary" (<u>BAD</u>) tracks (from γ conversion, pion interaction and also bad reconstruction) from the "main" (<u>GOOD</u>) tracks. Looping over the total number of tracks reconstructed in the event, checks are made on

- Track impact parameter (d_{IP})
- Track z-distance to the interaction point (Z_{IP})
- Track momentum
- Track origin from γ conversion vertex
- Track origin from π interaction vertex

Bad tracks do not point to the interaction region (in the transverse or longitudinal plane) or have momentum less than 1 GeV or belong to a fitted vertex with other charged track of opposite sign ($\gamma \rightarrow e^+e^-$ conversion) and the invariant mass of the 2 opposite charged tracks defining the fitted vertex is smaller than 200 MeV.
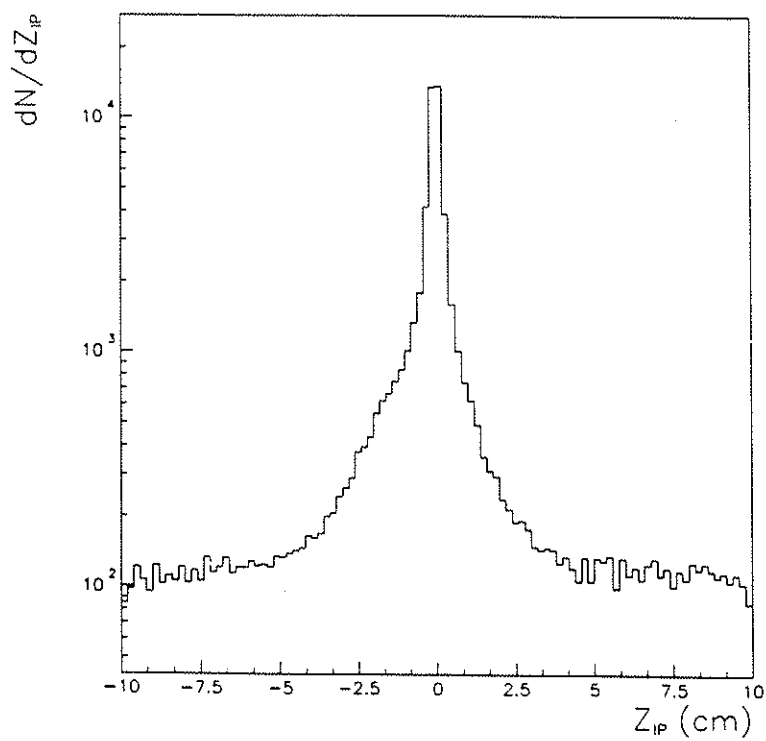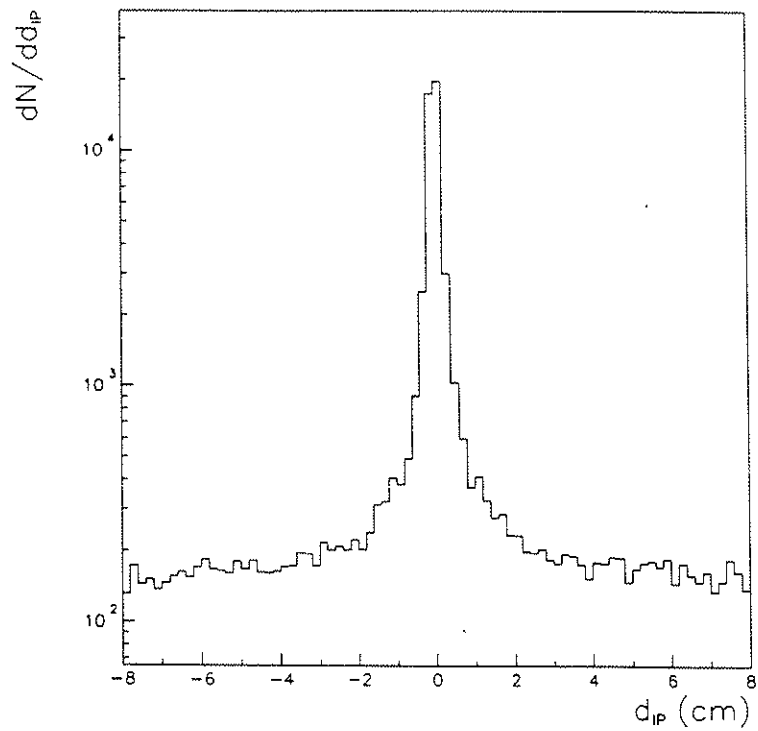
Figure 11.2: Distributions of track impact parameter and z distance of closest approach to the interaction point for leptonic events

11.3   Selection Criteria For $\tau^+\tau^-$ Events

Three categories of $\tau^+\tau^-$ events are considered. Their mnemonics are related to the number of charged tracks in each hemisphere of the event:

- $1 - 1$ $\equiv$ 1 track vs 1 track.
- $1 - 2$ $\equiv$ 1 track vs 2 tracks.
- $1 - N$ $\equiv$ 1 track vs N>2 tracks.

The geometrical acceptance considered in the selection and analysis of $\tau^+\tau^-$ events is defined as $43° < \theta < 137°$, coinciding with the DELPHI barrel region.

11.3.1 $\tau^+\tau^- \Rightarrow 1 - 1$ Final States

The following cuts select events with both τ's decaying into one charged track:

- 2 "good" charged tracks with at most 2 additional "bad" tracks

- Angle between the 2 good tracks bigger than 160° (θ_{acol} smaller than 20°).

$$
\left.
\begin{array}{l}
\bullet\ 43° < \theta < 137° \\[1em]
\bullet\ |d_{IP}| < 1.5\ cm \\[1em]
\bullet\ |Z_{IP}| < 2.5\ cm \\[1em]
\bullet\ E_{EM} < 30\ GeV
\end{array}
\right\} \text{For each good track} \tag{11.7}
$$

- $E_{EM}^{total} > 3\ GeV$ $\underline{OR}$ $((\#hits_{\mu CH})^{track\ 1} \cdot (\#hits_{\mu CH})^{track\ 2} = 0)$

- $\theta_{acol} > 3°$ $\underline{OR}$ $\theta_{acop} > 1°$

- $P_{VIS} < 60\ GeV$

- Sum of charges of both good tracks is zero

This cuts require 2 (good) tracks, allowing for 2 additional (bad) tracks due to γ conversion to account for the decay modes with π^0 in the final state. The angle between the 2 good tracks must be bigger than 160 degrees (equivalent to acolinearity smaller than 20 degrees) and both tracks must come from the interaction region. To reduce the background from $Z^0 \rightarrow e^+e^-$ events, the electromagnetic energy associated to each track must not exceed 30 GeV. The background from $Z^0 \rightarrow \mu^+\mu^-$ events is reduced by requiring more than 3 GeV for the total electromagnetic energy or that at least one of the tracks is not matched by muon hits. Before the cuts on acolinearity,

acoplanarity and visible momentum, the background from the other leptonic channels is estimated of be 30%. The cuts on acolinearity and acoplanarity eliminate 80% of the contamination from $e^+e^-, \mu^+\mu^-$ final states, while causing a loss of about 20% of $\tau^+\tau^-$ events. The cut on the visible momentum of the pair of tracks reduces the contamination to the level of 0.5%.

A typical event belonging to this category is shown in figure 11.3. The distributions of the acolinearity and acoplanarity angles for events passing the selection cuts for the 1-1 category are shown in figure 11.4, superimposed to the corresponding distributions obtained by applying the same cuts to a sample of 10000 simulated $Z^0 \rightarrow \tau^+\tau^-$ events.

11.3.2 $\tau^+\tau^- \Rightarrow 1 - N$ (N>1) Final States

These events, are characterized by one isolated good track in one hemisphere and N good tracks in the opposite hemisphere. The isolation angle of a track is defined as the angle between that track and the closest of the other N tracks.

11.3.2.1   1 vs 2 (N=2)

These events are mainly due to:

i) $\tau^+\tau^-$ final states with a γ conversion when one of the tracks from the conversion is lost or has low momentum.

ii)   1 vs 3 prong final state, with 1 of the tracks in the 3-prong arm lost.

The following cuts are imposed:

- 3 good charged tracks with at most 4 additional bad tracks

- Isolation angle of one of the tracks bigger than 150°.

- $43° < \theta < 137°$

- $|d_{IP}| < 1.5\ cm$ $\Big\}$ *For each good track*   (11.8)

- $|Z_{IP}| < 2.5\ cm$

- $E_{EM} < 30\ GeV$, for each hemisphere

- $E_{EM}^{total} > 3\ GeV \vee ((\#hits_{\mu CH})^{track1} * (\#hits_{\mu CH})^{track2}) = 0$

Three good tracks are required, all coming from the interaction region. The isolation angle must bigger than $150°$. The electromagnetic energy in each hemisphere must not exceed 30 GeV in order to reduce the $Z^0 \rightarrow e^+e^-$ background. The $Z^0 \rightarrow \mu^+\mu^-$ events are rejected by requiring the total electromagnetic energy for the event to be bigger than 3 GeV or that at least one of the 2 main good tracks (the isolated and the most energetic of the other two) is not matched to muon hits.

A typical event belonging to this category is shown in figure 11.5.

11.3.2.2   1 vs N (N>2)

This category of events is mainly originated from 1 vs 3 final states from $\tau^+\tau^-$ decays. The events with $N > 3$ are mainly due to bad reconstruction of the 3-prong decay in the TPC (related to the 2-track resolution) or from γ conversions.

The following set of cuts are imposed:

- $3 \leq N \leq 5$ good tracks, with at most 2 additional bad tracks

- Isolation angle of one of the tracks bigger than $150°$.

- $43° < \theta < 137°$

- $|d_{IP}| < 1.5\ cm$ $\Big\}$ *For the isolated track only*   (11.9)

- $|Z_{IP}| < 2.5\ cm$

These cuts require one good track, recoiling against three, four or five good tracks in the opposite hemisphere. Two additional bad tracks from bad reconstruction or photon conversion are allowed. The isolation angle must be bigger than $150°$. Due to inefficiencies in the reconstruction of the collimated tracks from 3-prong decays of tau, only the isolated track must originate from the interaction region.

An example of a typical 1-3 final state produced in $\tau^+\tau^-$ decays is shown in figure 11.7.
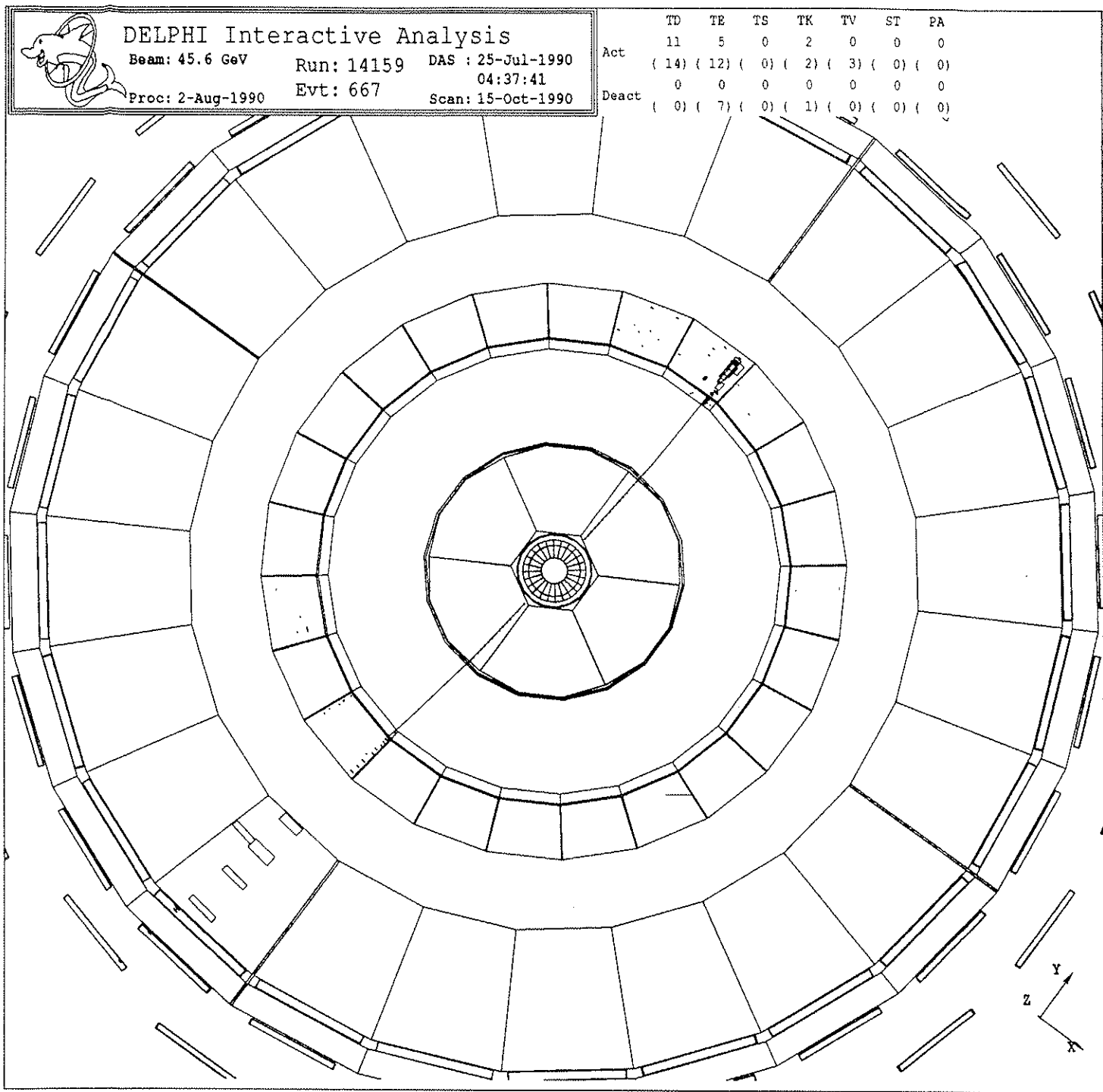
Figure 11.3: Event falling in the category 1-1 of $\tau^+\tau^-$ decays. A muon recoiling against an electron are seen in the final state.
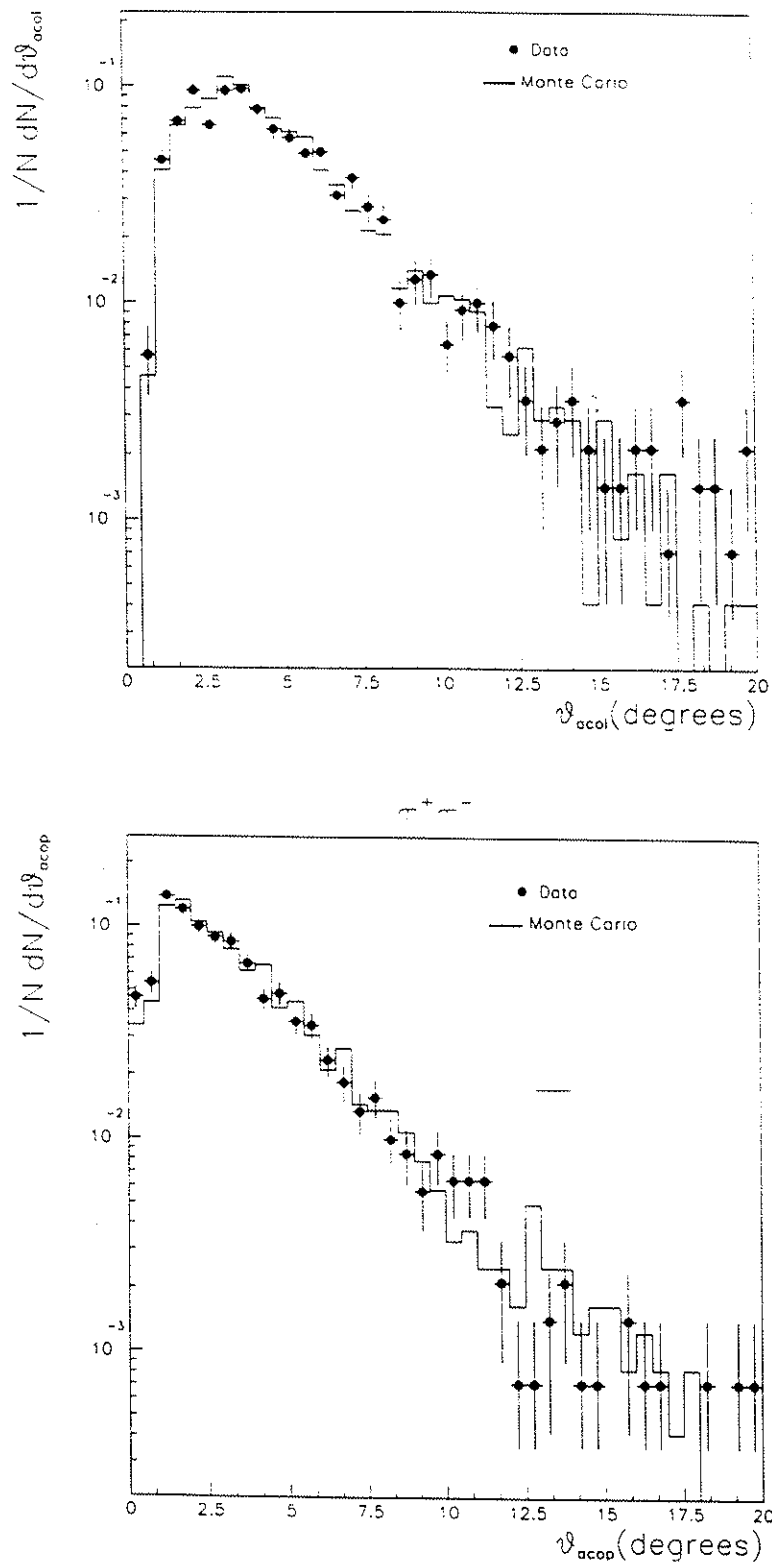
Figure 11.4: Acolinearity and acoplanarity distributions for events surviving the 1-1 selection cuts superimposed to the corresponding distributions obtained by applying the same cuts to a sample of 10000 simulated $Z^0 \to \tau^+\tau^-$ events.
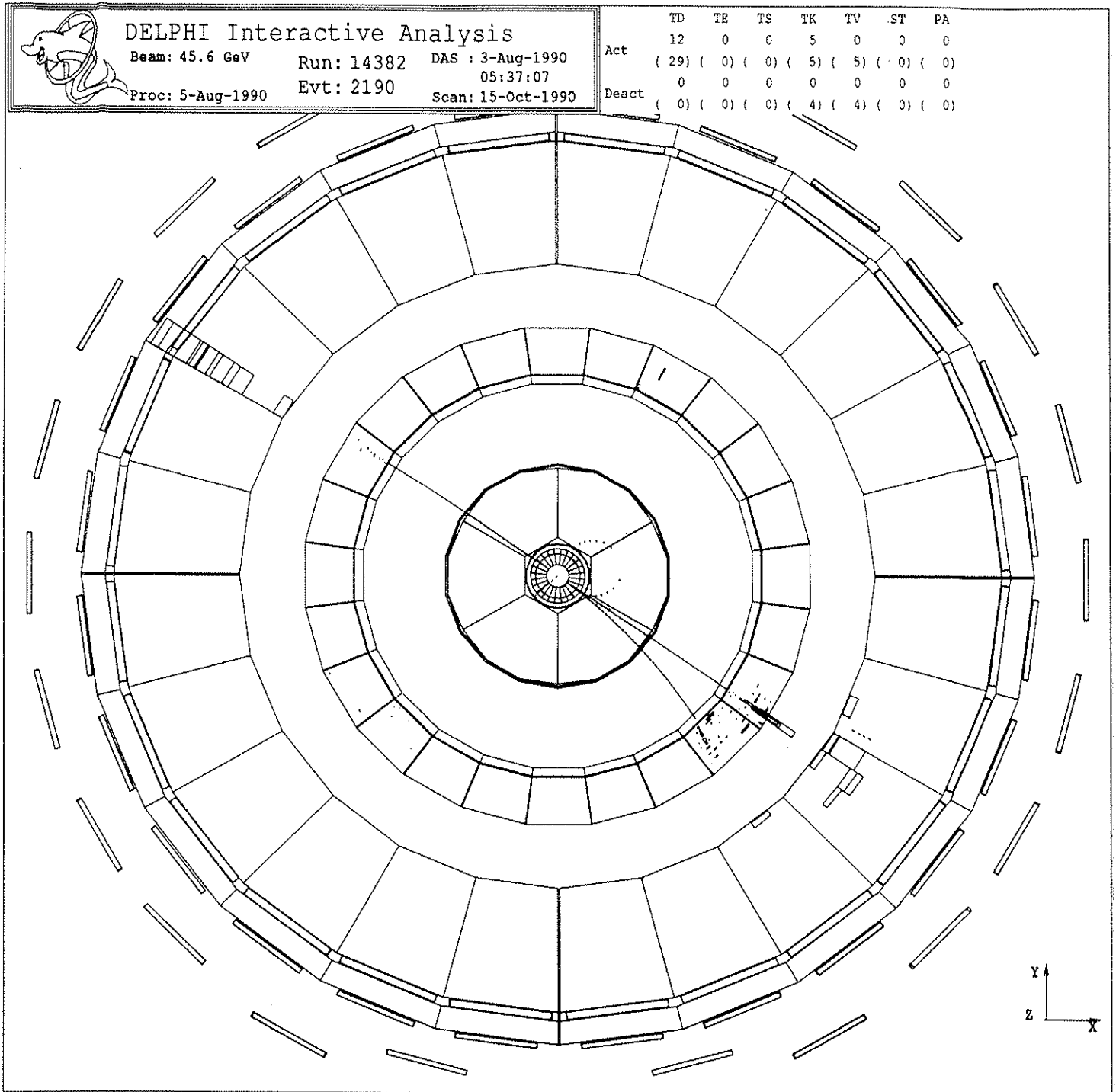
Figure 11.5: Isolated track recoiling against 2 other tracks in the opposite hemisphere, thus belonging to the 1-2 category of $\tau^+\tau^-$ decays.
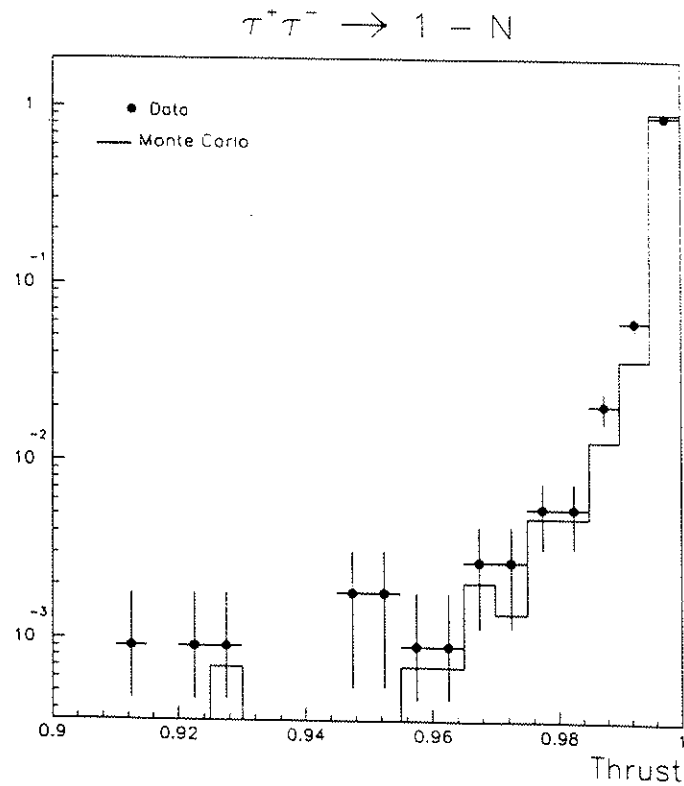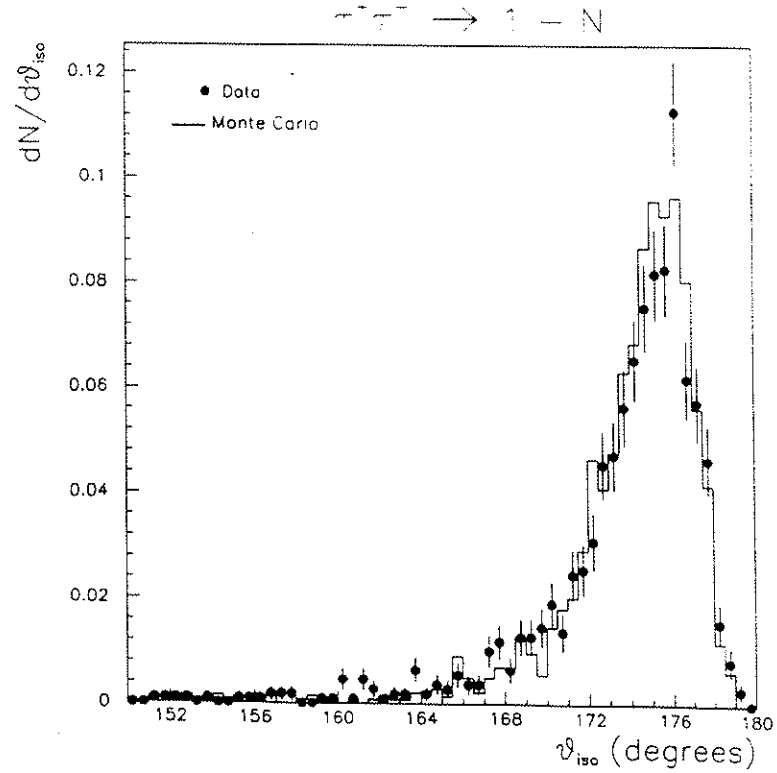
Figure 11.6: (a) Isolation angle, (b) Thrust distribution, for final states surviving 1-N selection cuts, superimposed to the corresponding distributions obtained by applying the same cuts to a sample of 10000 simulated $Z^0 \to \tau^+\tau^-$ events.

	TD	TE	TS	TK	TV	ST	PA
	11	3	0	5	0	0	0
Act	(39)	(136)	(0)	(5)	(6)	(0)	(0)
	0	0	0	0	0	0	0
Deact	(0)	(7)	(0)	(7)	(5)	(0)	(0)

DELPHI Interactive Analysis

Beam: 45.6 GeV

Run: 14384   DAS : 3-Aug-1990
                      05:58:41

Proc: 4-Aug-1990   Evt: 720   Scan: 15-Oct-1990

1.X-Y

2.Z-Y
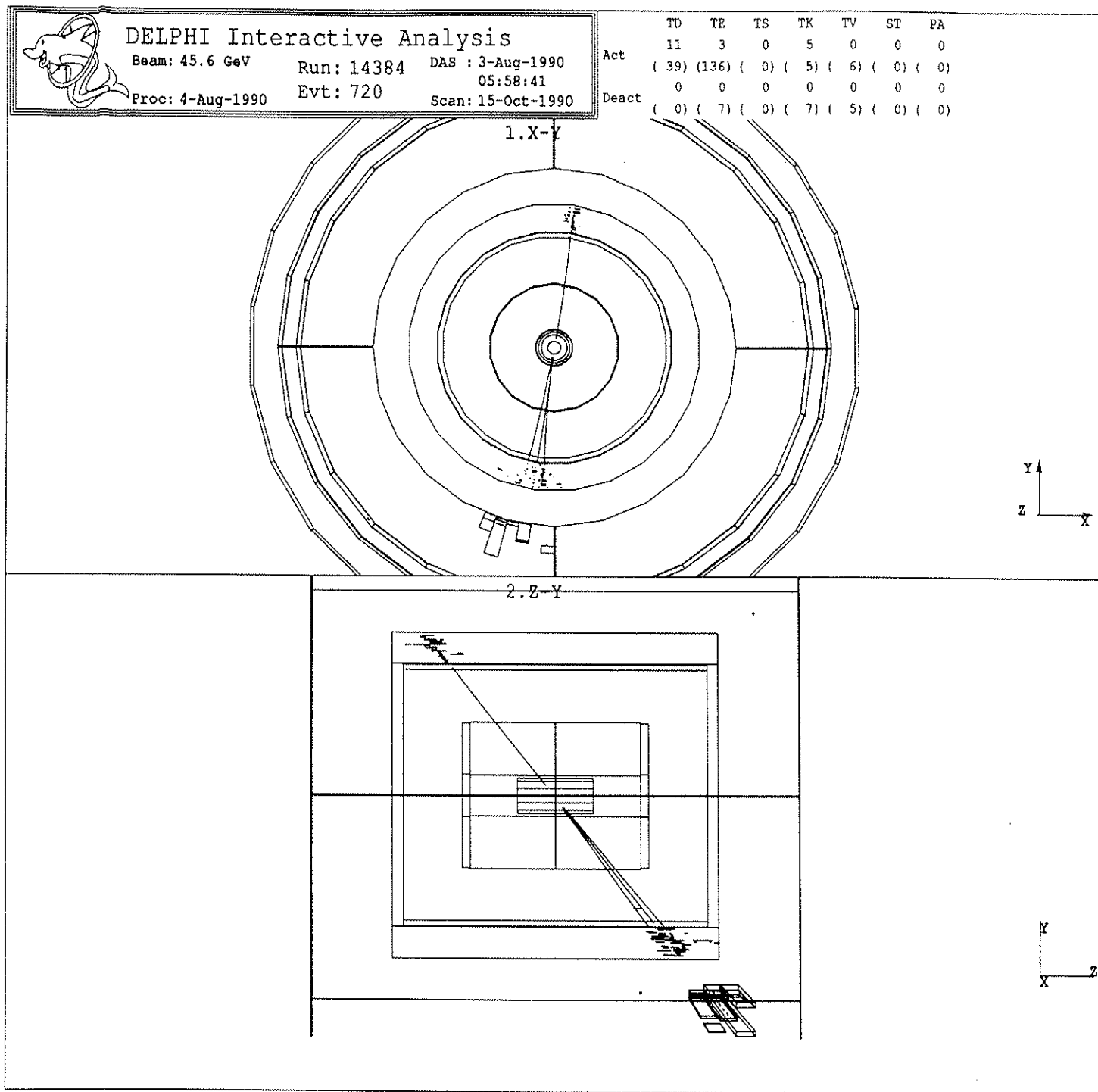
Figure 11.7: Isolated track recoiling against 3 other tracks in the opposite hemisphere, seen in two different projections.

11.4   Efficiency of the $\tau^+\tau^-$ selection cuts

The efficiency of the selection cuts is studied using Monte Carlo generated $\tau^+\tau^-$ events (using KORALZ), simulated with DELSIM and reconstructed with DELANA. The same cuts used to select the tau events from the the real data are applied to the reconstructed events to estimate the losses due to the multiple selection criteria.

Table 11.1 shows ε_{cuts}, the efficiency of the selection cuts applied to each of the three considered categories of $\tau^+\tau^-$ events. The percentage of real events found in each of the three categories is also displayed. The reference sample, before any cuts, consists is of 10000 events, generated in the full solid angle (4π). The defined geometrical acceptance, $43° < \theta < 137°$, rejects 35.5% of the $\tau^+\tau^-$ events.

The total systematic error is estimated by studying the stability and sensitivity of the number of selected events to the value of the cuts. The quoted error receives as major contribution the uncertainties in the visible momentum, acolinearity and acoplanarity cuts applied to select the 1-1 final states. By comparing the variation of the number of simulated and real events passing the full set of selection criteria when the value of these cuts is varied slightly from their nominal values, a systematic uncertainty of 1.8 % is assigned to the determination of the global efficiency.

TOPOLOGY	Fraction of events (%)	ε_{cuts}(%)
1-1	57	37.5
1-2	16	6.8
1-N	27	20.2
Global	100	64.5 ± 1.8

Table 11.1: Efficiency of cuts for the topologies 1-1,1-2,1-N determined from simulated $\tau\tau$ decays. The percentage of real events found in each of the three categories considered in the analysis is also displayed.

In figures 11.8,11.9,11.10,11.11, the distributions of visible momentum, total electromagnetic energy, acolinearity and individual track momentum, are shown for real events surviving the $Z^0 \rightarrow \tau^+\tau^-$ selection cuts.
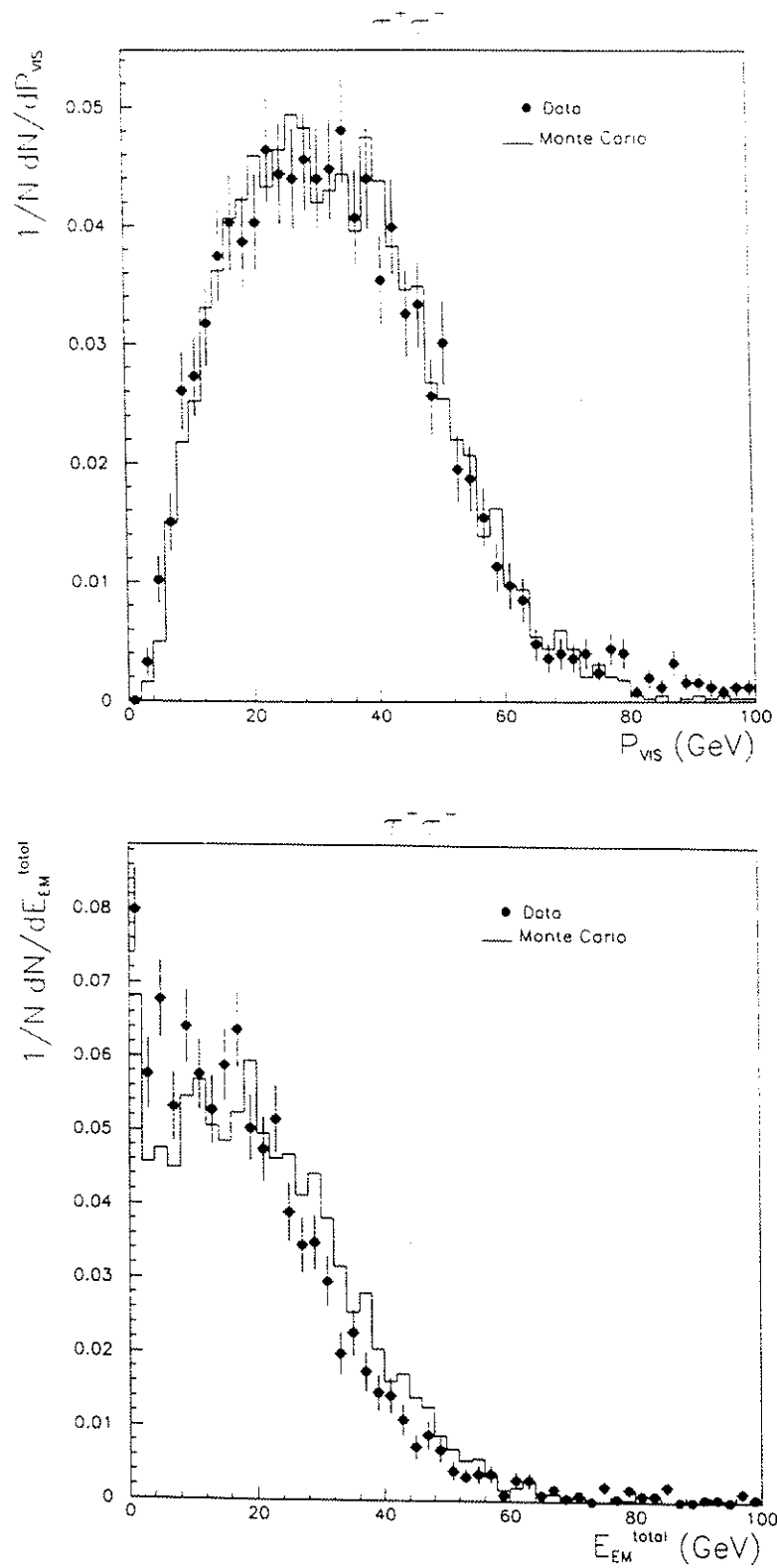
Figure 11.8: Distribution of the visible momentum and total electromagnetic energy for events passing the $Z^0 \rightarrow \tau^+\tau^-$ selection cuts, superimposed to the corresponding distributions obtained by applying the same cuts to a sample of 10000 simulated events.

$\tau^+\tau^-$

$\mu^+\mu^-$
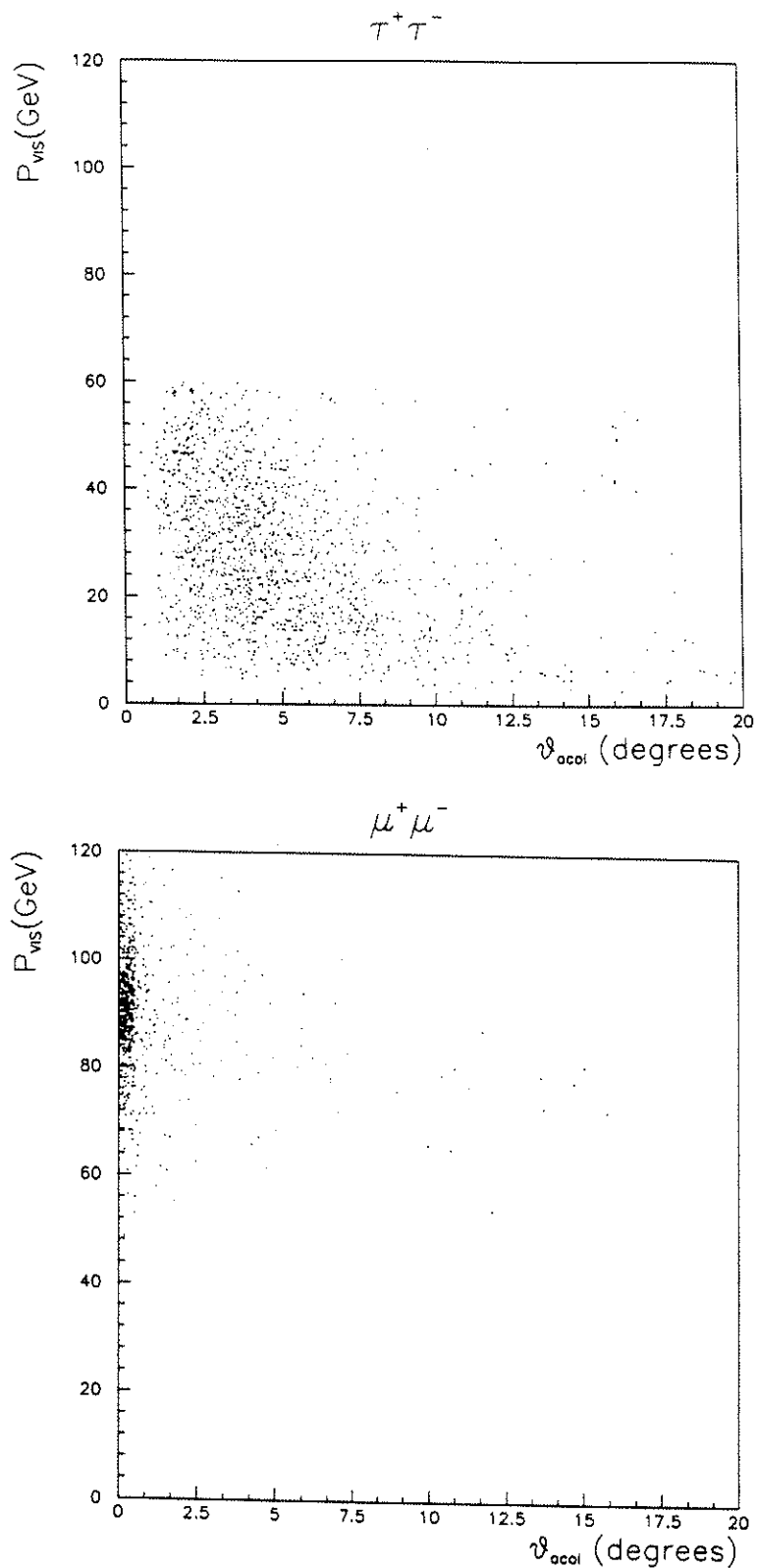
Figure 11.9: Distribution of the visible momentum versus acolinearity for events passing the 1-1 selection cuts. The corresponding distribution for $Z^0 \rightarrow \mu^+\mu^-$ events is also shown.

$\tau^+\tau^-$

e^+e^-
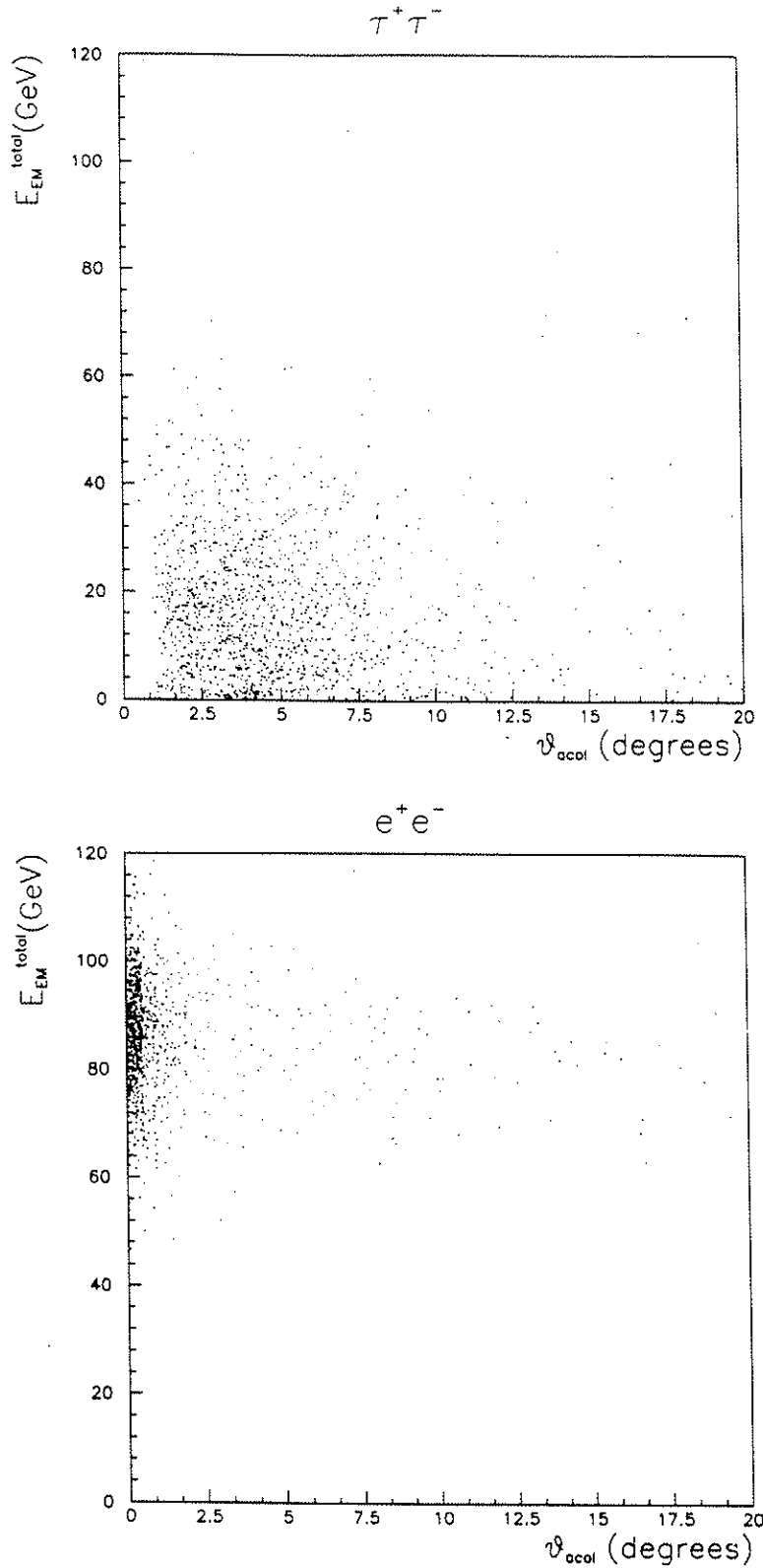
Figure 11.10: Distribution of the total energy in the electromagnetic calorimeter versus acolinearity for events passing the 1-1 selection cuts. The corresponding distribution for $Z^0 \to e^+e^-$ events is also shown.

$\tau^+\tau^-$

$\mu^+\mu^-$

Figure 11.11: Distribution of the momentum of one of the tracks versus the momentum of the other, for selected $Z^0 \rightarrow \tau^+\tau^-$ falling in the 1-1 category. The corresponding distribution for $Z^0 \rightarrow \mu^+\mu^-$ events is also shown.

11.5   Backgrounds

Due to multiple final states allowed in τ decays, $\tau^+\tau^-$ events represent a source of background to multiple other physics channels (leptonic and hadronic) and suffer from background contamination of multiple channels. In the sequence the most important backgrounds contaminating the $\tau^+\tau^-$ channel are examined.

11.5.1 $e^+e^- \to e^+e^-\gamma^*\gamma^* \to e^+e^-l^+l^-$

This process can be seen as developing in 2 steps: in the first step, both e^+ and e^- "radiate" virtual photons (γ^*) and in the second step, from the $\gamma^*\gamma^*$ collision blob (X), a pair of fermions is produced. Like:

- $e^+e^- \to e^+e^-\gamma^*\gamma^*$

- $\gamma^*\gamma^* \to X \to l^+l^-$

The amplitude for this process is evaluated mainly from the multiperipheral t-channel diagram, shown in figure 11.12.
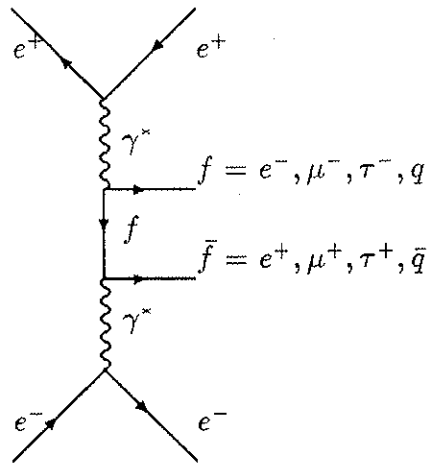
Figure 11.12: The basic $e^+e^- \to \gamma^*\gamma^* \to e^+e^-f\bar{f}$ processes.

The final state (analysed here) is $e^+e^-l^+l^-$ with a detected pair of leptons (l^+l^-) when the beam particles are lost in the beam tube. Extensive treatement exist on the literature to simplify the calculation of this process. In the Weisacker-Williams approximation, (Equivalent Photon Approximation, EPA), the normalized energy

spectrum of the virtual photon, $w = \frac{E_{\gamma^*}}{E_{beam}}$, for small deflection angles of the beam particles (small Q^2) and when these are not seen in the acceptance region of the detector, is given by [75]

$$\frac{dN}{d\omega} = \frac{\alpha}{2\pi} \ln \left(\frac{E_{beam}^2}{m_e^2}\right) \frac{1 + (1 - \omega)^2}{\omega} \tag{11.10}$$

The angular differential cross-section of the lepton pair in the process $\gamma^*\gamma^* \to l^+l^-$ is strongly peaked along the photon direction like

$$\frac{d\sigma}{d\cos\theta^*} \approx \frac{1 + \cos^2\theta^*}{\sin^2\theta^*} \tag{11.11}$$

In good aproximation, when the deflection angle is small, the 2-photon centre of mass system moves along the beam line. The simplified expression of the cross-section for producing a lepton pair of invariant mass M_{ll} in the $\gamma^*\gamma^*$ collision is

$$\sigma_{\gamma^*\gamma^*} \simeq \frac{4\pi\alpha^2}{M_{ll}^2} \tag{11.12}$$

The total cross-section for the final state $(e^+e^-l^+l^-)$ can be written $(l = e, \mu, \tau)$ as[75]

$$\sigma(e^+e^- \to e^+e^-l^+l^-) \simeq \frac{8\alpha^4}{\pi} \frac{1}{m_l^2} \ln^2 \left(\frac{E_{beam}}{m_e}\right) \ln\left(\frac{E_{beam}}{m_l}\right) \tag{11.13}$$

From the above expressions, the characteristics and importance of these background processes can be summarized as:

• The total $\gamma^*\gamma^*$, $\mathcal{O}(\alpha^4)$ cross-section rises logarithmically with the beam energy and is, without cuts, at the Z^0 resonance energies much bigger than the cross-section for leptonic pair production.

• Cuts in the invariant mass of the measured pair (M_{ll}), in the event transverse momentum (P_T) or in the acolinearity angle (θ_{acol}) between the tracks, can reduce by some orders of magnitude the cross-section for the process. The cut in M_{ll}, is implicitely applied through the E_{TOT} cut (8 GeV) used to select the leptonic events. The cut in θ_{acol} is explicitly formulated in the $\tau^+\tau^-$ selection criteria, through the isolation angle cuts (160° for 1-1 and 150° for 1-N). The cut in P_T is derived from the defined geometrical acceptance together with the cut on the minimum momentum of the tracks, used in the selection of the leptonic events and the back to back topology required for the $\tau^+\tau^-$ events through the isolation angle.

With these cuts the cross-section is lowered to the level of few picobarns and the contamination of each the 3 main contaminating channels

$$e^+e^- \to (e^+e^-)\, e^+e^- \tag{11.14}$$

$$e^+e^- \to (e^+e^-)\, \mu^+\mu^- \tag{11.15}$$

$$e^+e^- \to (e^+e^-)\, \tau^+\tau^- \tag{11.16}$$

is expected to be negligible (at the level of few per mil).

11.5.2 $e^+e^- \to Z^0 \to \mu^+\mu^-$

$Z^0 \to \mu^+\mu^-$ events represent a contamination to the $Z^0 \to \tau^+\tau^-$ final states with topology 1-1, if at least one of the following situations happens:

- Badly measured momentum of one or both tracks (mainly due to the dead zones of the TPC).

- Non identified muon in one or both hemispheres, due to inefficiencies in Muon Identification procedure.

- Hard radiative $Z^0 \to \mu^+\mu^-\gamma$ events with undetected photon.

The reconstructed visible momentum for these events, falls in the tail of the distribution for $Z^0 \to \mu^+\mu^-$ events. Such events, with missing momentum, fake the following $\tau^+\tau^-$ final states:

$$\tau^+\tau^- \to \mu + x + \not{p} \tag{11.17}$$

$$\tau^+\tau^- \to \mu + \mu + \not{p} \tag{11.18}$$

As explained in a previous section, to reduce the contamination from the $Z^0 \to \mu^+\mu^-$ channel, events with muon hits matching both tracks are not considered. In addition cuts in the following reconstructed quantities are applied:

- Total electromagnetic energy (> 3 GeV)
- Visible momentum (< 60 GeV)
- Acoplanarity ($> 1°$) or Acolinearity ($> 3°$)

Contamination of $Z^0 \to \tau^+\tau^-$ final states in the 1-2 or 1-3 topologies happens in radiative $Z^0 \to \mu^+\mu^-\gamma$ events followed by photon conversion with one or both the tracks detected.

11.5.3 $e^+e^- \rightarrow Z^0 \rightarrow e^+e^-$

$Z^0 \rightarrow e^+e^-$ events represent a contamination to $\tau^+\tau^-$ final states with topology 1-1, if at least one of the following situations happens:

- Inefficiencies in energy reconstruction (mainly due to the HPC cracks)

- Hard radiative $Z^0 \rightarrow e^+e^-\gamma$ events with undetected photon.

The reconstructed energy for such events falls in the tail of the energy distribution for $Z^0 \rightarrow e^+e^-$ events. Such events with missing energy fake the following $\tau^+\tau^-$ final states:

$$\tau^+\tau^- \rightarrow x + y + \not{E} \qquad x = e,\rho \ , \ y = e,\rho \qquad (11.19)$$

As explained in a previous section, in order to reduce the contamination from $Z^0 \rightarrow e^+e^-$ events cuts are applied on the following quantities:

- Electromagnetic energy per track or hemisphere (< 30 GeV)
- Visible momentum (< 60 GeV)
- Acoplanarity ($> 1°$) or Acolinearity ($> 3°$)

As for muons, contamination of $Z^0 \rightarrow \tau^+\tau^-$ final states in the 1-2 or 1-3 topologies happens in radiative $Z^0 \rightarrow e^+e^-\gamma$ events followed by photon conversion with one or both tracks detected.

11.5.4 $e^+e^- \to Z^0 \to hadrons$

The branching ratio for the process $Z^0 \to hadrons$ is about 20 times bigger than the branching ratio for $Z^0 \to \tau^+\tau^-$ decays. Hadronic events with an isolated track in one hemisphere and N tracks (N$\leq$ 7) in the opposite hemisphere represent a source of background contaminating the $\tau^+\tau^-$ event sample. To reduce such contamination, cuts can be applied in the global event variables or in the topological and kinematical quantities in each hemisphere of the event. These cuts are:

Multiplicity cut
The measured mean charged multiplicity for hadronic events at $\sqrt{s} = 91.1$ GeV is

$$< n_{ch} > \simeq 21 \tag{11.20}$$

To remove the hadronic background, the following charged multiplicity cut is used to select the leptonic events

$$n_{ch} \leq 8 \tag{11.21}$$

Isolation cut
Further rejection of the hadronic events is obtained with the isolation cut used to select the categories 1-2 and 1-N of $Z^0 \to \tau^+\tau^-$ events. By requiring a single track in one hemisphere, isolated by more than 150° from the closest track in the other hemisphere, this cut turns out to be equivalent to a cut in the jet charged multiplicity.

The distributions of the charged multiplicity for hadronic events and charged multiplicity per jet are shown in figure 11.13.

Thrust cut
The thrust (T) of an event is defined as

$$T = max \frac{\sum_i |\vec{n} \cdot \vec{p_i}|}{\sum_i |\vec{p_i}|} \quad (\frac{1}{2} < T < 1) \tag{11.22}$$

with $|\vec{n}| = 1$, T=1 for an ideal back to back event and T=1/2 for a perfectly isotropic event. The direction $\vec{n}$ at which the thrust is maximum defines the thrust axis. The distribution of the thrust for hadronic events is shown in figure 11.14. From the figure results that at LEP energies, 3% of the hadronic events have $T > 0.99$. The following cut can be imposed to select $\tau^+\tau^-$ events remove most of the hadronic background:

$$T > 0.99 \tag{11.23}$$

Invariant Mass cut
The invariant mass of the N tracks in the hemisphere opposite to the isolated track is likely to be of the order of the tau mass (1.72 GeV) for $\tau^+\tau^-$ events while for low multiplicity jets from hadronic events exhibits higher values. The hadronic background can be significantly reduced by requiring that the invariant mass of the N-track system is

$$M_{N-track} < 2 \; GeV \tag{11.24}$$
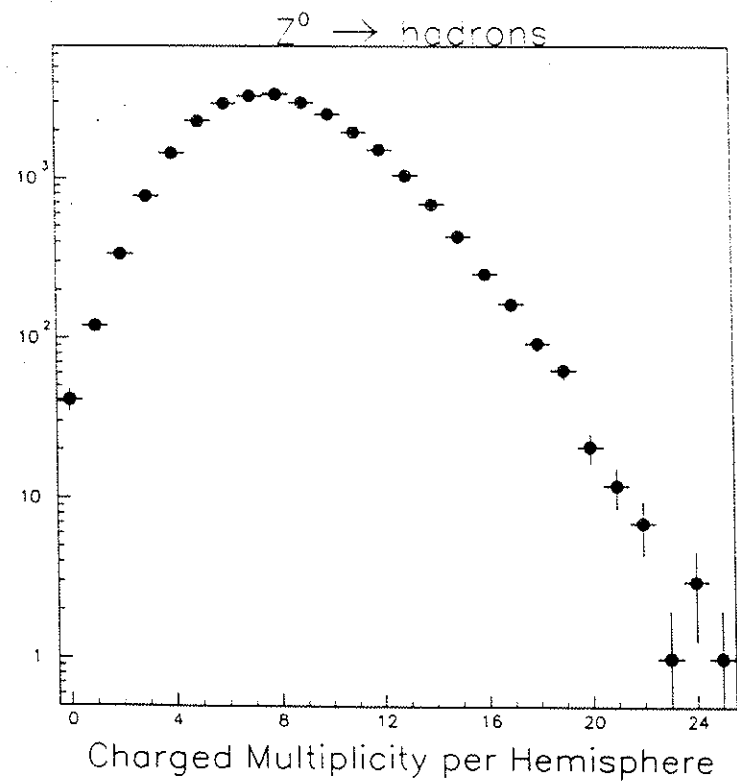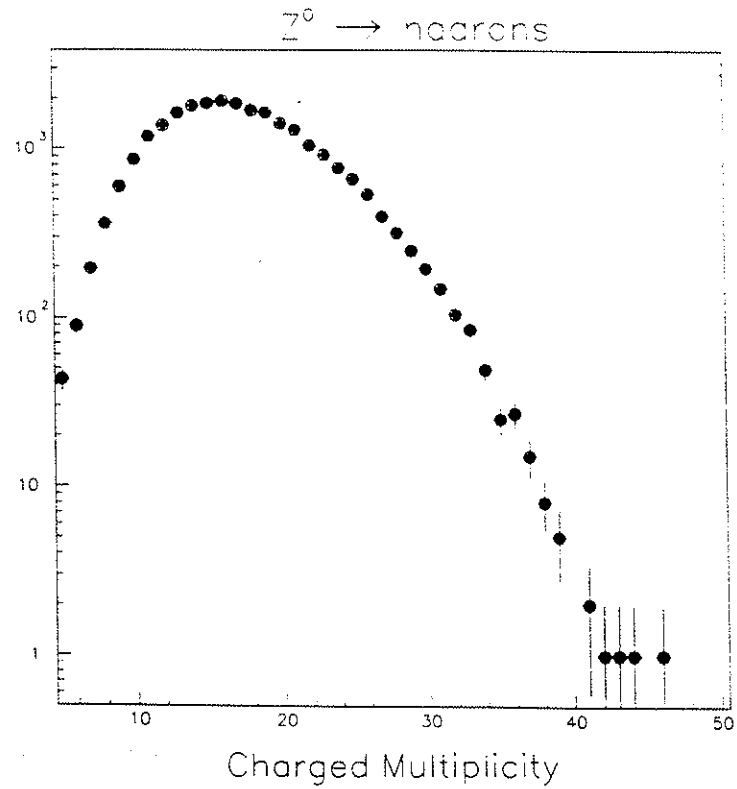
Figure 11.13: Total charged multiplicity and jet charged multiplicity distributions for real $Z^0 \to hadrons$ events.
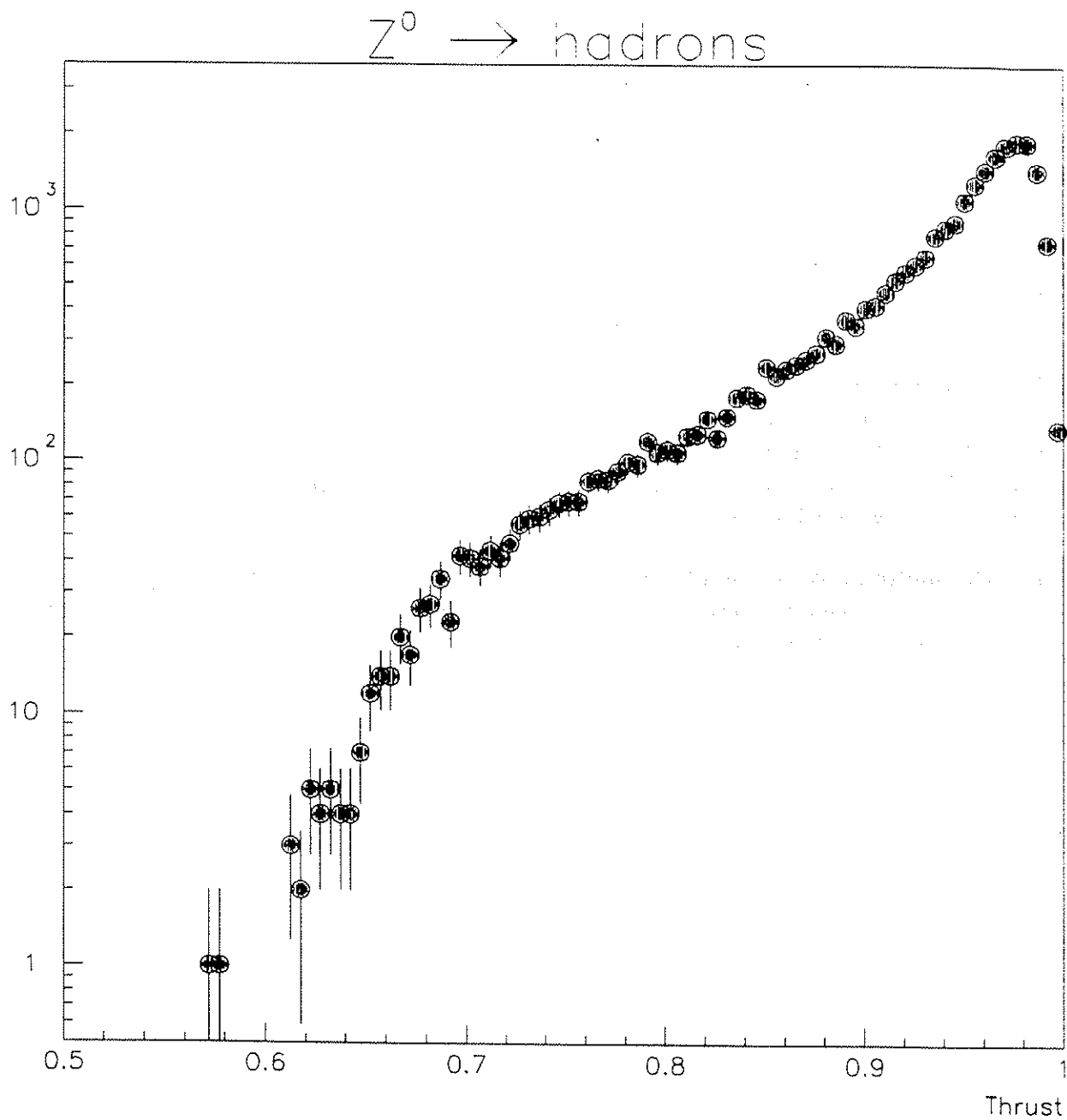
Figure 11.14: Thrust distribution for real $Z^0 \rightarrow hadrons$ events.

11.5.5   Background estimation

For the estimation of the background contamination from several channels, Monte Carlo simulated events (hadronic, e^+e^- and $\mu^+\mu^-$) are used. The levels of contamination from each channel are determined by the number of events passing the cuts used to selected the real $\tau^+\tau^-$ events, making the corresponding normalization for the total number of real events and taking into account the ratios of the cross-sections.

Concerning the $e^+e^- \to \gamma^*\gamma^* \to e^+e^- l\bar{l}$ background, the DIAG36 generator[76] was used to determine the efficiency of the $\tau^+\tau^-$ cuts to the $e^+e^-e^+e^-$, $e^+e^-\mu^+\mu^-$ and $e^+e^-\tau^+\tau^-$ final states and estimate their contamination on the $\tau^+\tau^-$ sample. As expected[77][78], before cuts the visible cross-section is dominated by the $e^+e^-\mu^+\mu^-$ final states. After the cuts are applied total contamination is estimated to be below 0.3%.

The contamination from $Z^0 \to \mu^+\mu^-$ events affects mainly the 1-1 category of $\tau^+\tau^-$ events, while the contamination from $Z^0 \to e^+e^-$ events affects also to the 1-N category. Due to the severe cuts on acolinearity, acoplanarity and visible momentum, the contamination from these 2 channels on the tau sample is determined to be below a few per mil, with a loss of about 20% of $Z^0 \to \mu^+\mu^-$ events.

For the hadronic background, the $\tau^+\tau^-$ selection cuts were applied to a sample of 10600 $Z^0 \to q\bar{q}$ events generated in the full solid angle. About 5 events passed the cuts, 4 surviving the 1-2 cuts and 1 falling in the class 1-N. The estimated contamination from hadronic events in the $\tau^+\tau^-$ sample, in the angular region $43° < \theta < 137°$ is then 2%.

Background type	Contamination (%)
$e^+e^-e^+e^-$	<0.2
$e^+e^-\mu^+\mu^-$	<0.2
$e^+e^-\tau^+\tau^-$	<0.05
$Z^0 \to e^+e^-$	0.5
$Z^0 \to \mu^+\mu^-$	0.5
$Z^0 \to q\bar{q}$	2.0

Table 11.2: Main sources of background and corresponding contamination in the $\tau^+\tau^-$ event sample, estimated from simulated events.

Chapter 12

LUMINOSITY and NORMALIZATION

The expected number of events N in a given reaction with production cross-section σ, is related to the integrated luminosity $\int \mathcal{L}dt$ and the global detection efficiency ε, by

$$\int \mathcal{L}dt = \frac{N}{\sigma\varepsilon} \tag{12.1}$$

Given the high-accuracy aimed for the measurements in the framework of LEP physics, a high precision measurement of luminosity is required, to allow a normalization procedure with the smallest possible statistic and systematic error. In e^+e^- colliders, the method commonly used to determine with accuracy the machine luminosity is the measurement of the Bhabha ($e^+e^- \longrightarrow e^+e^-$) event rate at very low angle, with the small angle luminosity monitors. These detectors are placed at very small angle, close to the beam line, covering angular regions extending from a few dozens of mrad (constrained by geometrical reasons), up to a few hundreds of mrad. The reason for this is that Bhabha scattering cross-section at very small angle is well estimated at LEP energies (and below) by the computation of the pure QED Feynman diagrams, with negligible contributions from the terms due to $\gamma - Z$ interference and pure Z^0 diagrams. Also, the strictly weak radiative corrections are very small in the low angle region.

The pure QED Bhabha scattering cross-section coming from the diagrams of figure 12.1 can be written in lowest order as

$$\left(\frac{d\sigma}{d\Omega}\right)_{QED} = \frac{\alpha^2}{4s} \left[(1 + c^2) + 2\frac{(1 + c)^2 + 4}{(1 - c)^2} - 2\frac{(1 + c)^2}{(1 - c)} \right] \tag{12.2}$$
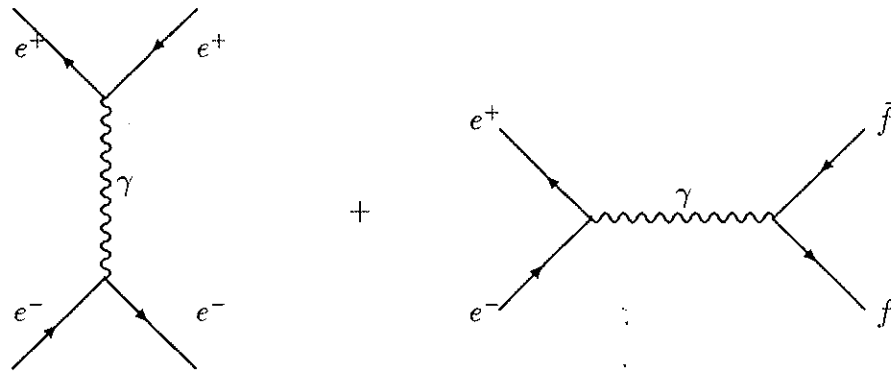
Figure 12.1: The QED diagrams (t-channel left, s-channel right) contributing to Bhabha scattering $e^+e^- \rightarrow e^+e^-$

where $s = 4E_{beam}^2$ is the center of mass energy, $c = \cos\theta$ with θ the scattering angle of the electron and α is the QED coupling constant.

The three expected contributions,annihilation(s-channel),exchange(t-channel) and interference (s-t) are clearly shown corresponding to each of the three terms in brackets.

This expression can be condensated to take the form

$$\left(\frac{d\sigma}{d\Omega}\right)_{QED} = \frac{\alpha^2}{4s}\left(\frac{3+c^2}{1-c}\right)^2 \tag{12.3}$$

and at very small angle ($\theta \ll 1$)

$$\left(\frac{d\sigma}{d\Omega}\right)_{QED} \simeq \frac{4\alpha^2}{s}\frac{1}{\theta^4} \tag{12.4}$$

At the Z^0 resonance, the terms including the Z^0 propagator have of course to be included, and the differential cross-section can be written

$$\frac{d\sigma}{d\Omega} \simeq \left(\frac{d\sigma}{d\Omega}\right)_{QED}(1+\delta_W) \tag{12.5}$$

where the correction δ_W includes all electroweak contributions (weak corrections to the vertex and to the propagator). Due to the pole in the exchange (t-channel) graph

at small angles ($\theta \ll 1$), the region of interest for luminosity monitoring, the QED approximation to the total cross-section is usually enough. In addition, in the range of the Z^0 resonance, the interference between Z^0 and γ diagrams is very small and the correction is indeed negligible.

12.1 Luminosity Measurement

SAT[1], Small Angle Tagger, is the DELPHI luminosity detector. It consists of 2 arms equally spaced in Z from the interaction point, each containing 3 layers of silicon detector (_tracker_) followed by a lead-scintillating fiber electromagnetic calorimeter. The tracker allows the reconstruction of the track trajectory of the e^+ and e^- from Bhabha scattering, and the calorimeter with good energy resolution ($\frac{11}{\sqrt{E}}\%$),reconstructs the energy of the scattered electrons(positrons). The calorimeter consists of 2 half-discs joining in the vertical plane (dead zone of a few mm). This detector covers the angular region $53 < \theta < 138$ mrad. The phi coverage is almost 2π in azimuth, taking into account the dead zone between the 2 discs.

12.1.1 The lead mask

Due to the absence of the silicon tracking detectors during the 1989 phase of data taking (only calorimeters were operational), a lead ring (mask) of 10 radiation lenghts was installed in front of the calorimeter in one of the SAT arms, to allow the accurate determination of the inner radius of acceptance, defining the fiducial region considered in the analysis.

The accurate knowledge of the inner radius is a critical issue, due to the very steep dependence of the cross-section at small angles. During the initial period (one third of the data taken by DELPHI in 1989), a 12 cm radius lead mask was installed, being later replaced by a 13 cm mask. With the 12 cm mask, covering only partially the inner SAT ring, the systematic uncertainty in the background subtraction constituted the major contribution to the total systematic error. The 13 cm mask, fully covering the first SAT ring, led to a reduction by a factor of 3 in the uncertainty on the background subtraction.

The longitudinal view of the SAT arm with the coupled lead mask (13 cm) is shown in figure 12.2. The different systematic errors in the luminosity measurement with each mask are considered in our analysis.

---

[1]see The SAT detector is described in Chapter 7
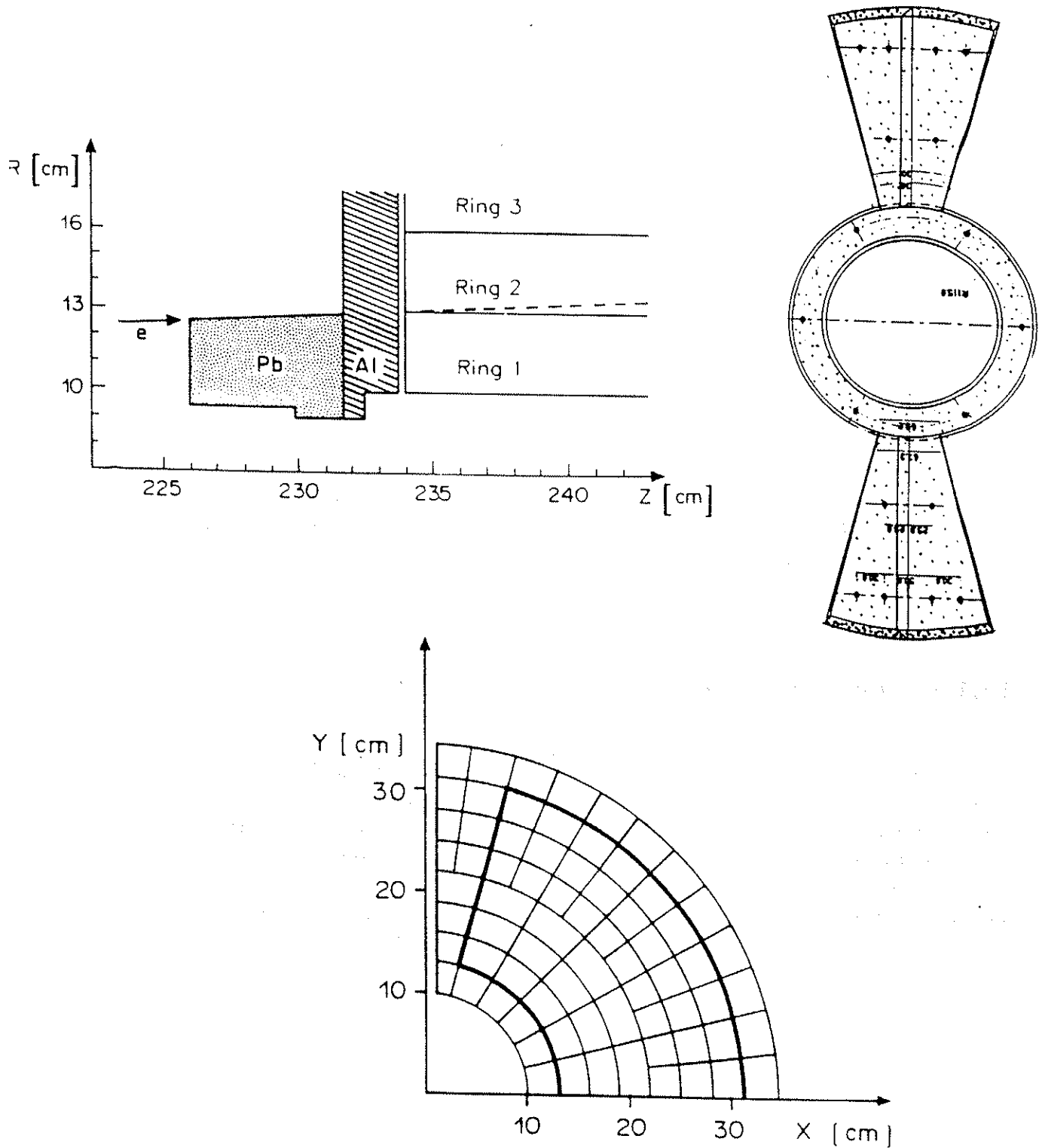
Figure 12.2: (a) Longitudinal (partial) view of the SAT calorimeter and the 13 cm lead mask in front of it, covering completely the first ring. (b) Front view of the "butterfly" wings and lead mask (c) One quadrant of the SAT calorimeter with the thick line delimiting the acceptance region.

12.1.2 The "butterfly" wings

The accurate definition of the fiducial region used in the analysis is limited by the uncertainty on the detector geometry near the vertical dead zones separating the 2 half hemispheres of the calorimeter. During the 1989 data taking period, a Φ cut was applied, removing from the geometrical acceptance the circular sector of $\pm 15°$ around the $\Phi = 90°$ axis. For the 1990 data taking period, in order to lower the systematic uncertainty due to that cut, the so-called "butterfly" wings were added to the lead mask described above. Covering the vertical dead zones, they allowed the definition with better accuracy of the fiducial region close to such zones with a consequent reduction by a factor 2 of the associated systematic uncertainty. In figure 12.2, the geometry of the wings is shown.
The 13 cm mask was also used during the whole 1990 data taking period.

12.1.3 Cross-Section and Expected Rates

The lowest order integrated QED cross-section, written as

$$\sigma_{QED} \simeq \frac{4\pi\alpha^2}{s} \left(\frac{1}{\theta_{min}^2} - \frac{1}{\theta_{max}^2} \right) \tag{12.6}$$

where $\theta_{min}, \theta_{max}$ define the angular region of acceptance for the detector. Integrated over the SAT angular region ($53 < \theta < 138$ mrad), the cross-section is

$$\sigma_{QED} \simeq 31.5 \ nb \tag{12.7}$$

(using the full electroweak correction one gets 31.8 nb)

Assuming a luminosity value (L) of

$$L = 10^{31} \ cm^{-2}s^{-1} \tag{12.8}$$

the expected event counting rate is

$$\frac{dN}{dt} = .315 \ Hz \Leftrightarrow 1130 \ h^{-1} \tag{12.9}$$

The integrated luminosity measured by the SAT, $\mathcal{L}_{SAT}$, is then

$$\mathcal{L}_{SAT} = \frac{N_{Bhabha}}{\varepsilon_{SAT} \int_{\Omega_{SAT}} \left(\frac{d\sigma}{d\Omega} d\Omega \right)} \tag{12.10}$$

with ε_{SAT} the total SAT efficiency (trigger and reconstruction), taking into account all systematics in Bhabha detection, σ is the theoretical Bhabha cross-section and Ω_{SAT} is the solid angle subtended by the SAT fiducial region.

12.1.4   Errors In Luminosity Measurement

The Bhabha event rate turns out in practice to be smaller than the one quoted above due to the need to define in the analysis a fiducial region that is smaller than the full angular region of the SAT, with the corresponding reduction in the cross-section. Assuming an "effective" event rate $\frac{dN}{dt} = 900 \ h^{-1}$ ($\sigma \simeq 25 \ nb$), the statistical error on the luminosity measurement in the SAT is:

$$\left(\frac{\delta\mathcal{L}}{\mathcal{L}} \right)_{stat} = \frac{1}{30\sqrt{t}} \quad , \quad [\,t\,] = hours \tag{12.11}$$

With N_i the number of Bhabha events in the i-th run and σ_i the effective Bhabha cross-section integrated over the detector acceptance for the same run, the absolute luminosity error can be evaluated [1] from 12.10

$$\frac{\Delta\mathcal{L}_i}{\mathcal{L}_i} = \frac{1}{\sqrt{N_i}} \oplus \frac{\Delta\sigma_i}{\sigma_i} \oplus \frac{\Delta\varepsilon}{\varepsilon} = \sqrt{\frac{1}{N_i} + \left(\frac{\Delta\sigma_i}{\sigma_i} \right)^2 + \left(\frac{\Delta\varepsilon}{\varepsilon} \right)^2} \tag{12.12}$$

Just to illustrate, for n runs, with the same luminosity ($\mathcal{L}_i = \mathcal{L}$), and the same number of counts per run (N_i=N), then

$$\frac{\delta\mathcal{L}}{\mathcal{L}} = \sqrt{\frac{1}{n} \left(\frac{1}{N} + \left(\frac{\Delta\sigma_i}{\sigma_i} \right)^2 \right) + \left(\frac{d\varepsilon}{\varepsilon} \right)^2} \tag{12.13}$$

The uncertainty in the absolute luminosity determination is dominated by the systematic errors in the global detection efficiency $d\varepsilon/\varepsilon$. The main sources of systematic errors, displayed in Table 12.1, are:

---

[1]$a \oplus b \oplus c$ means the sum in quadrature $\sqrt{a^2 + b^2 + c^2}$

• *Trigger efficiency*

The SAT trigger for Bhabha events required: i) coplanar coincidence of energy deposi-tions in the 2 endcaps, each of energy greater than 15 GeV, OR ii) energy depositions above 35 GeV in both endcaps wihtout coplanarity requirements. The efficiency of the luminosity trigger was evaluated by running the Single Arm trigger (SAAR, re-quiring energy depositions in only one endcap) together with the normal trigger in special runs.

• *Definition of the fiducial region*

The lead ring in front of the calorimeter allows the establishment within a few hun-dred microns of the inner radius of the SAT fiducial region. The uncertainty in the knowledge of the dead zone between the 2 half cylinders in each calorimeter is re-flected in the evaluation of the acceptance region, contributing to total systematic error as uncertainties in the knowledge of the internal geometry.

• *Background subtraction*

The main source of background for the acceptance of Bhabha events are random coincidences of off-momentum beam particles crossing the fiducial regions in both endcaps.

• *Interaction Point Position*

Due to the very quick variation of the cross-section at small angles the knowledge of the inner and outer radii defining the acceptance region for Bhabha events counting is of crucial importance. The counting rate of Bhabha events in SAT, related to the acceptance region of the detector is [60]

$$\frac{\delta\sigma}{\sigma} \simeq 2\,\frac{\delta\theta_{min}}{\theta_{min}} \approx 2\,\frac{\delta r_{min}}{r_{min}} \tag{12.14}$$

with r_{min} the inner radius of the acceptance region defined for the detector. As a numerical example extracted from ref.[60],

$$\frac{\frac{\delta\sigma}{\sigma}}{\delta r_{min}} \simeq 2\%/mm \tag{12.15}$$

• *Monte Carlo modelling and statistics*

The uncertainty in the the detector simulation (lead mask and calorimeter) and the number of MC events available in the comparative studies with real data contribute to uncertainties in the luminosity determination.

• *Theoretical uncertainty*

Available Monte Carlo generators for Bhabha scattering include radiative corrections computed up to order α. The absence of higher order radiative corrections in the MC reflects in the uncertainty to reproduce real data distributions. With the reduction of the experimental errors in the period of 1990, the theoretical uncertainty became the major contribution to the total systematic error in the determination of the luminosity.

SOURCE OF UNCERTAINTY	1989 (%)	1990 (%)
Trigger efficiency	0.6	0.1
Φ cuts (dead zones)	1.0	0.3
Edge effects	-	0.2
Energy cut (reconstruction)	1.0	0.6
Interaction point position	0.5	0.2
Background subtraction		
12 cm lead mask	1.5	-
13 cm lead mask	0.5	0.1
MC modelling	1.0	-
MC statistics	0.6	0.3
Miscellaneous	-	0.4
TOTAL (experimental)		
12 cm lead mask (weight 1/3)	2.5	-
13 cm lead mask (weight 2/3)	2.1	-
13 cm lead mask + butterfly	-	0.9
Theory (radiative corrections)	1.0	1.0
TOTAL	2.4	1.3

Table 12.1: Sources of uncertainty contributing to the total systematic error in the luminosity determination for each of the 1989 and 1990 data taking periods. The uncertainty of 0.4% quoted to miscellaneous sources (1990 only) include the corrections due to dead channels, reconstruction uncertainties, etc.

12.2 Normalization

As the Bhabha scattering cross-section is well estimated analitically from the QED theory at small angles, and assuming that all systematic uncertainties are controlled at a few percent level, the measured integrated luminosity ($\mathcal{L}$) in the luminosity monitors (SAT) can be used to normalize the counting rates of other physis channels.

The measured cross-section σ_i for a given channel i, where N_i events where detected with global efficiency ε_i is obtained from the measured number of Bhabha events in the SAT, N_{Bhabha}, and corresponding cross-section σ_{Bhabha}, by

$$\sigma_i = \frac{N_i}{\varepsilon_i \, N_{Bhabha}} \, \sigma_{Bhabha} \qquad (12.16)$$

or equivalently, with $\mathcal{L}_{SAT}$ the integrated luminosity measured by the SAT

$$\sigma_i = \frac{N_i}{\varepsilon_i \, \mathcal{L}_{SAT}} \qquad (12.17)$$

This expression shows why a good measurement of the Bhabha event rate with well understood and controlled systematic and statistical errors in the low angle luminosity detectors is essencial in $e^+ e^-$ collider Physics. The error in the cross-section measurement for the process being studied comes [2]

$$\frac{\Delta \sigma_i}{\sigma_i} = \frac{\Delta N_i}{N_i} \oplus \frac{\Delta \varepsilon}{\varepsilon} \oplus \frac{\Delta \mathcal{L}_{SAT}}{\mathcal{L}_{SAT}} \qquad (12.18)$$

From the interplay between the three contributions to the overall error in the cross-section it is visible that for some physics channels (high statistics and small uncertainty in the efficiency) the systematic error in the luminosity measurement can represent the biggest contribution to the global measurement error and the major constrain in the accuracy of the measurements.

---

[2] $a \oplus b \oplus c$ means the sum in quadrature $\sqrt{a^2 + b^2 + c^2}$
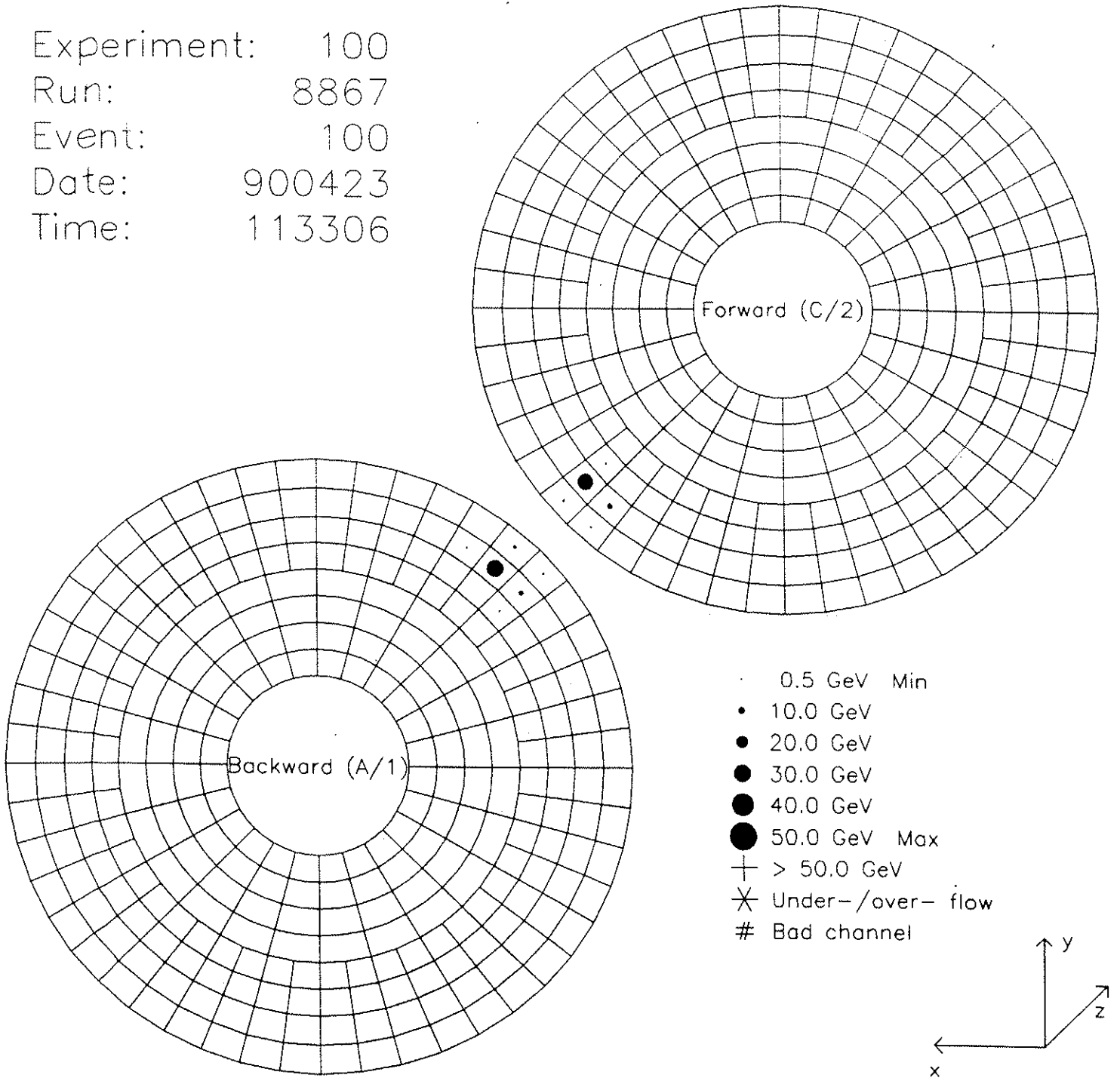
Figure 12.4: Bhabha event registered in the SAT , with one high energy shower per endcap calorimeter and the typical acoplanar behaviour of the two showers .

Part IV

Results and Discussion

In the period from October to December 1989, an energy scan around the Z^0 resonance was made. Beams were setup to collide at ten different values of the centre of mass energy E_{CM}: 88.28, 89.28, 90.28, 91.03, 91.28, 91.54, 92.28, 93.28, 94.28, 95.04 GeV. During this period, about 11000 hadronic events from Z^0 decays were collected and analysed in DELPHI and a first accurate measurement of the Z^0 resonance parameters was made, as described in reference [83].

During the data taking period extending from March to June 1990, a new energy scan was made, this time at seven different values of the centre of mass energy E_{CM}, around the resonance peak: 88.22, 89.22, 90.22, 91.22, 92.22, 93.22, 94.22 GeV. With the upgrade in the luminosity delivered by the LEP machine during this period relative to the 1989 period and the experience gained by running the DELPHI detector, a new sample of about 58000 hadronic events was collected and analysed, allowing a determination with better accuracy of the resonance parameters [85].

From the point of view of data analysis and physics results, the 2 periods are different in what concerns:

● The size of the event sample (Z^0 hadronic and leptonic decays) recorded in the detector in each period, reflecting in the statistical errors of the analysis.

● The different compreension of the systematics associated to the detector (data taking and trigger efficiencies) and to the offline software (alignment, calibrations, track and energy reconstruction efficiencies, momentum and energy resolutions).

The second period, that in the sequence will be referred as _Period II_ beneficted from the experience gained during the first phase of operation of the detector, that will be mentioned as _Period I_. This is reflected in the statistical and systematic errors quoted for the luminosity,efficiencies,fits,etc. and generally to all physics results obtained. In the sequence, all the measured quantities and computed results using the data taken during Period I or Period II will be affected respectively by the index I or II .

Chapter 13

Z^0 Resonance Parameters

The parameters characterizing the Z^0 resonance are its mass (M_Z), width (Γ_Z), peak cross-section (σ^{pole}), leptonic partial width (Γ_{ll}), hadronic partial width (Γ_h) and invisible width (Γ_{inv}). These parameters can be extracted by fitting[1] the cross-sections values measured at different centre of mass energies for each individual channel (1 hadronic and 3 leptonic) or by performing fits combining the hadronic and the three leptonic cross-section measurements. The combined fits usually assume the lepton universality hypothesis in order to reduce to four the number of free parameters, for example, M_Z,Γ_Z,Γ_{ll} and Γ_h. This assumption can be validated by performing 1-parameter fits to the individual leptonic lineshapes, using as input the values extracted from the combined fit, to determine the leptonic partial widths.

The expression connecting all the parameters above is the lowest order Breit Wigner expression for a $f\bar{f}$ final state

$$\sigma^{pole}_{f\bar{f}} = \frac{12\pi}{M_Z^2} \frac{\Gamma_{ee}\Gamma_{f\bar{f}}}{\Gamma_Z^2} \tag{13.1}$$

13.1 Combined fit of the leptonic and hadronic cross-section

Two main fits, formally equivalent and differing in the set of fitted parameters and on the assumptions made upon the extraction of the parameters are described in the sequence. In both fits, lepton universality is assumed ($\Gamma_{ee} = \Gamma_{\mu\mu} = \Gamma_{\tau\tau} = \Gamma_{ll}$) and the fitted value for Γ_{ll}, making use of the full statistics of leptonic events, has smaller statistical and systematic errors than fits performed to each individual channel.

---

[1] Several model independent parametrizations of the Z^0 line shape are discussed in refs.[79,80,81,82]

13.1.1   Fit to M_Z , Γ_Z , Γ_{ll} , R

The fit parameters are the mass (M_Z) and width (Γ_Z) of the Z^0, the leptonic partial width (Γ_{ll}) and the ratio of hadronic to leptonic partial widths (R). The parameter Γ_{ee} in equation 13.1 becomes Γ_{ll}.

From the fitted values of Γ_{ll} and R, the hadronic partial width (Γ_h) and the invisible width (Γ_{inv}) are computed as:

$$\Gamma_h \;=\; R^{fit}\, \Gamma_{ll}^{fit} \tag{13.2}$$

$$\Gamma_{inv} \;=\; \Gamma_Z^{fit} \;-\; (3 + R^{fit})\, \Gamma_{ll}^{fit} \tag{13.3}$$

13.1.2   Fit to M_Z , Γ_h , Γ_{ll} , Γ_{inv}

The fitted Z^0 parameters are the mass (M_Z), the hadronic partial width (Γ_h), the leptonic partial width (Γ_{ll}) and the invisible width (Γ_{inv}).

The number of light neutrinos N_ν is computed using the SM assumption about the Z^0 partial width into each neutrino family, $\Gamma_{\nu\nu}^{SM} \simeq 166.3\ MeV$, as follows:

$$\Gamma_{inv}^{fit} \;=\; N_\nu\, \Gamma_{\nu\nu}^{SM} \tag{13.4}$$

The total width Γ_Z of the Z^0 boson, is evaluated through

$$\Gamma_Z \;=\; \Gamma_h^{fit} + 3\Gamma_{ll}^{fit} + \Gamma_{inv}^{fit} \tag{13.5}$$

The following replacement is made in the parametrization of the cross-section:

$$\frac{1}{\Gamma_Z^2} \;\longrightarrow\; \frac{1}{(\Gamma_h \;+\; 3\Gamma_{ll} \;+\; N_\nu\, \Gamma_{\nu\nu}^{SM})^2} \tag{13.6}$$

The sensitivity of the pole cross-section to the number of neutrinos is given by

$$\frac{\delta\sigma_h^{pole}}{\sigma_h^{pole}} \;=\; 2\,\frac{\delta\Gamma_Z}{\Gamma_Z} \tag{13.7}$$

which implies that an additional $Z^0 \to \nu\bar{\nu}$ decay channel, would represent[2]

$$\frac{\delta\Gamma_Z}{\Gamma_Z} \;\simeq\; 6.6\ \% \;\longrightarrow\; \frac{\delta\sigma_h^{pole}}{\sigma_h^{pole}} \;\simeq\; 13.2\ \% \tag{13.8}$$

---

[2]Accordingly to a computation in the framework of the SM

13.2 Fit to the hadronic cross-section

Several fits can be performed to the measured hadronic cross-section values, in order to extract the resonance parameters.

13.2.1 Fit to M_Z , Γ_Z , $\Gamma_{ll}\Gamma_h$

This is a 3-parameter fit to the mass (M_Z), width (Γ_Z) and to the product of the partial widths $(\Gamma_{ll}\Gamma_h)$. As such, it is independent of the Standard Model. The Born cross-section at the pole is extracted from 13.1.

13.2.2 Fit to M_Z , Γ_Z

This is a 2-parameter fit to the mass (M_Z), width (Γ_Z), fixing the value of $\Gamma_{ll}\Gamma_h$ to the value predicted by the SM. Using the SM prediction for the fermionic partial widths the invisible width is obtained, and thus the corresponding number of light neutrino species:

$$\Gamma_Z^{fit} = \Gamma_h^{SM} + \Gamma_{ee}^{SM} + \Gamma_{\mu\mu}^{SM} + \Gamma_{\tau\tau}^{SM} + N_\nu \Gamma_{\nu\nu}^{SM} \tag{13.9}$$

13.2.3 Fit to M_Z , N_ν

This is a 2-parameter fit to the mass (M_Z) and to the number of light neutrinos N_ν (or equivalently the invisible width Γ_{inv}), making use of the SM prediction for the fermionic partial widths. The fit parameter is N_ν, entering in the expression 13.1 as:

$$\Gamma_Z = \Gamma_h^{SM} + \Gamma_{ee}^{SM} + \Gamma_{\mu\mu}^{SM} + \Gamma_{\tau\tau}^{SM} + N_\nu^{fit} \Gamma_{\nu\nu}^{SM} \tag{13.10}$$

13.3 Fit of the leptonic cross-sections

Two different fits to the cross-section values for each individual channel can be performed, differing in the fitted parameter and in the determination of its error. The mass M_Z and total width Γ_Z are fixed to the values determined from the fit to the hadronic cross-section values or from the combined fit.

13.3.1   Fit to Γ_{ff} assuming universality

The fitted parameter is the normalization of the cross-section ($\mathcal{N}$), proportional to $\Gamma_{ee}\Gamma_{ff}$. Assuming universality, and using as input the value of Γ_{ee} predicted by the SM, one has

$$\Gamma_{ff} \equiv (\Gamma_{ee}\Gamma_{ff})^{1/2} = \sqrt{\mathcal{N}^{fit}}\ \Gamma_{ee}^{SM} \tag{13.11}$$

$$\frac{\Delta(\Gamma_{ee}\Gamma_{ff})^{1/2}}{(\Gamma_{ee}\Gamma_{ff})^{1/2}} = \frac{1}{2}\ \frac{\Delta\mathcal{N}}{\mathcal{N}} \tag{13.12}$$

The systematic error in the normalization of the cross-section, is due to the uncertainties common to all channels, in the measurements of the luminosity ($\Delta\mathcal{L}$) and the Z total width ($\Delta\Gamma_Z$) as well as to the systematic uncertainties in the number of events of each channel (N_{ff}), that are related to the evaluation of the trigger efficiency, the event selection efficiency, the background or t-channel subtraction, etc. Defining ΔN_{ff} as the sum in quadrature of these errors, the relative error in the normalization is

$$\frac{\Delta\mathcal{N}}{\mathcal{N}} = \left(2\ \frac{\Delta M_Z}{M_Z}\right)\oplus\left(2\ \frac{\Delta\Gamma_Z}{\Gamma_Z}\right)\oplus\frac{\Delta\mathcal{L}}{\mathcal{L}}\oplus\frac{\Delta N_{ff}}{N_{ff}} \tag{13.13}$$

The statistical and systematic errors on Γ_{ff} determined this way are reduced by a factor of 2 relative to the errors quoted on the normalization of the fitted curve:

$$\left(\frac{\Delta(\Gamma_{ee}\Gamma_{ff})^{1/2}}{(\Gamma_{ee}\Gamma_{ff})^{1/2}}\right)_{stat} \simeq \frac{1}{2}\ \frac{1}{\sqrt{N_{ff}}} \tag{13.14}$$

$$\left(\frac{\Delta(\Gamma_{ee}\Gamma_{ff})^{1/2}}{(\Gamma_{ee}\Gamma_{ff})^{1/2}}\right)_{syst} = \frac{1}{2}\left[\left(2\ \frac{\Delta M_Z}{M_Z}\right)\oplus\left(2\ \frac{\Delta\Gamma_Z}{\Gamma_Z}\right)\oplus\frac{\Delta\mathcal{L}}{\mathcal{L}}\oplus\frac{\Delta N_{ff}}{N_{ff}}\right] \tag{13.15}$$

with N_{ff} the total number of events.

13.3.2   Fit to Γ_{ff} without assuming universality

The determination of the individual leptonic widths is obtained from fits to the individual cross-sections, using as input the values of M_Z , Γ_Z (from the combined fit) and extracting Γ_{ee} , $\Gamma_{\mu\mu}$, $\Gamma_{\tau\tau}$ as:

$$\Gamma_{ee} = \sqrt{(\Gamma_{ee}\Gamma_{ee})^{fit}} \tag{13.16}$$

$$\Gamma_{\mu\mu} = \frac{(\Gamma_{ee}\Gamma_{\mu\mu})^{fit}}{\Gamma_{ee}} \tag{13.17}$$

$$\Gamma_{\tau\tau} = \frac{(\Gamma_{ee}\Gamma_{\tau\tau})^{fit}}{\Gamma_{ee}} \tag{13.18}$$

The estimation of the errors associated to the fitted values of the leptonic widths using this method is done following closely the ideas of ref. [86]. The systematic errors common to the three leptonic channels (e.g. from uncertatinties on the measurement of luminosity and total width, respectively $\Delta\mathcal{L}$ and $\Delta\Gamma_Z$) must not be accounted twice in the computation of the total systematic uncertatinty on $\Gamma_{\mu\mu}$ and $\Gamma_{\tau\tau}$ using the ratios above, but instead they are propagated when the systematic error on the fitted value of Γ_{ee} is considered in the "unfolding" expressions.

In the sequence, ΔN_{ee} and ΔN_{ff} (f=μ,τ) are the systematic errors in the measurement of the number of $Z^0 \to e^+e^-$, $Z^0 \to \mu^+\mu^-$ or $Z^0 \to \tau^+\tau^-$ events including all the sources of systematic uncertatinties (trigger, event selection, backgrounds, etc.) added in quadrature and excluding the common systematic errors mentioned above. Starting from the expressions

$$N_{ee} \sim \mathcal{L}\,\frac{1}{M_Z^2}\,\frac{\Gamma_{ee}\Gamma_{ee}}{\Gamma_Z^2} \qquad N_{\mu\mu} \sim \mathcal{L}\,\frac{1}{M_Z^2}\,\frac{\Gamma_{ee}\Gamma_{\mu\mu}}{\Gamma_Z^2} \qquad N_{\tau\tau} \sim \mathcal{L}\,\frac{1}{M_Z^2}\,\frac{\Gamma_{ee}\Gamma_{\tau\tau}}{\Gamma_Z^2} \quad (13.19)$$

we write the partial width Γ_{ee} as:

$$\Gamma_{ee} \sim M_Z\,\Gamma_Z\,\sqrt{\frac{N_{ee}}{\mathcal{L}}} \qquad\qquad (13.20)$$

and its relative error is

$$\left(\frac{\Delta\Gamma_{ee}}{\Gamma_{ee}}\right)_{syst} = \frac{\Delta M_Z}{M_Z} \oplus \frac{\Delta\Gamma_Z}{\Gamma_Z} \oplus \left(\frac{1}{2}\,\frac{\Delta\mathcal{L}}{\mathcal{L}}\right) \oplus \left(\frac{1}{2}\,\frac{\Delta N_{ee}}{N_{ee}}\right) \qquad (13.21)$$

The partial width Γ_{ff} (f=μ,τ) is given by:

$$\Gamma_{ff} \sim M_Z\,\Gamma_Z\,\frac{N_{ff}}{\sqrt{N_{ee}}\,\sqrt{\mathcal{L}}} \qquad\qquad (13.22)$$

and its relative error becomes

$$\left(\frac{\Delta\Gamma_{ff}}{\Gamma_{ff}}\right)_{syst} = \underbrace{\frac{\Delta M_Z}{M_Z} \oplus \frac{\Delta\Gamma_Z}{\Gamma_Z} \oplus \left(\frac{1}{2}\,\frac{\Delta\mathcal{L}}{\mathcal{L}}\right) \oplus \left(\frac{1}{2}\,\frac{\Delta N_{ee}}{N_{ee}}\right)}_{\Delta\Gamma_{ee}/\Gamma_{ee}} \oplus \frac{\Delta N_{ff}}{N_{ff}} \qquad (13.23)$$

In this fit the total systematic error assigned to the electron partial width is the sum in quadrature of all systematic uncertainties in the cross-section measurement for the electron channel (including luminosity and partial width), divided by 2. The systematic error assigned to the measurement of the partial width for each of the other 2 channels is the sum in quadrature of the systematic errors specific to that channel (excluding common systematic errors) and the total systematic error in the measurement of the electron partial width. The errors in the measurement of $\Gamma_{\mu\mu}$ and $\Gamma_{\tau\tau}$ are accordingly bigger.

With N the total number of events, the statistical error quoted on Γ_{ff} determination is

$$\left(\frac{\Delta\Gamma_{ff}}{\Gamma_{ff}}\right)_{stat} \simeq \frac{1}{\sqrt{N_{ff}}} \oplus \left(\frac{1}{2}\,\frac{1}{\sqrt{N_{ee}}}\right) \qquad (13.24)$$

13.3.3   Comparison of the errors

From the expressions on the statistical and systematic errors in the determination of the $Z^0 \to \mu^+\mu^-$ and $Z^0 \to \tau^+\tau^-$ partial widths, it is seen that the price to pay by not making a priori the assumption on universality is:

• Doubling of the quoted errors specific to each channel, affecting the number of events of that channel.
• The addition (in quadrature) to $\Gamma_{\mu\mu}$ and $\Gamma_{\tau\tau}$ of half of the errors on the number of e^+e^- events, N_{ee}.

In the next table we summarize, for both fits, the weight of the relative uncertainties from each individual source contributing to the total systematic error.

Source	Universality	No-Universality
$\Delta M_Z/M_Z$	1	1
$\Delta \Gamma_Z/\Gamma_Z$	1	1
$\Delta \mathcal{L}/\mathcal{L}$	1/2	1/2
$\Delta N_{ff}/N_{ff}$	1/2	1
$\Delta N_{ee}/N_{ee}$	0	1/2

13.4 Values of the Z^0 parameters

The Z^0 resonance parameters, used in our $\tau^+\tau^+$ analysis as input parameters, were obtained from the study of the total sample of hadronic and leptonic Z^0 events collected in DELPHI (68000 hadronic events and 4000 leptonic events)[85]. Figure 13.1 shows the measured cross section for the process $e^+e^- \rightarrow hadrons$, together with the result from the fit.

In the sequence the values for the mass (M_Z), width (Γ_Z), hadronic width (Γ_h), pole cross-section (σ_h^{pole}) and invisible width (Γ_{inv}) are listed:

Mass

$$M_Z = \begin{cases} 91.171 \pm 0.030(stat) \pm 0.030(syst)\ GeV & (1989\ data) \\ 91.188 \pm 0.013(stat) \pm 0.030(syst)\ GeV & (1989+1990\ data) \end{cases}$$
(13.25)

Total width

$$\Gamma_Z = \begin{cases} 2.511 \pm 0.065(stat) \pm 0.022(syst)\ GeV & (1989\ data) \\ 2.476 \pm 0.026(stat) \pm 0.022(syst)\ GeV & (1989+1990\ data) \end{cases}$$
(13.26)

Hadronic width

$$\Gamma_h = \begin{cases} 1741 \pm 61\ MeV & (1989\ data) \\ 1756 \pm 23(stat) \pm 22(syst)\ MeV & (1989+1990\ data) \end{cases}$$
(13.27)

Hadronic pole cross section

$$\sigma_h^{pole} = \begin{cases} 41.6 \pm 0.7\ (stat) \pm 1.1\ (syst)\ nb & (1989\ data) \\ 42.38 \pm 0.30(stat) \pm 0.97(syst)\ nb & (1989+1990\ data) \end{cases}$$
(13.28)

Invisible width

$$\Gamma_{inv} = \begin{cases} 515 \pm 54\ MeV & (1989\ data) \\ 469 \pm 19(stat) \pm 22(syst)\ MeV & (1989+1990\ data) \end{cases}$$
(13.29)

A few remarks about the systematic errors assigned to these parameters:

• The systematic error of 30 MeV in the determination of M_Z is due to the intrinsic uncertainty on the energy calibration of the LEP machine

• With the assumption that the systematic error on the luminosity is the same at all energy points, the measurement of Γ_Z is independent of the normalization. A 10 MeV systematic uncertainty was assigned to the Γ_Z measurement due to a possible 0.3% point to point variation in the normalization of the cross-section.

• The systematic error on the σ_h^{pole} and Γ_h measurements is dominated by the systematic uncertainty on the luminosity measurement.

• The theoretical uncertainty on the computation of the Bhabha scattering cross-section within the SAT acceptance accounts for a 1% component in the overall systematic error in the luminosity measurement (see Chapter 12).
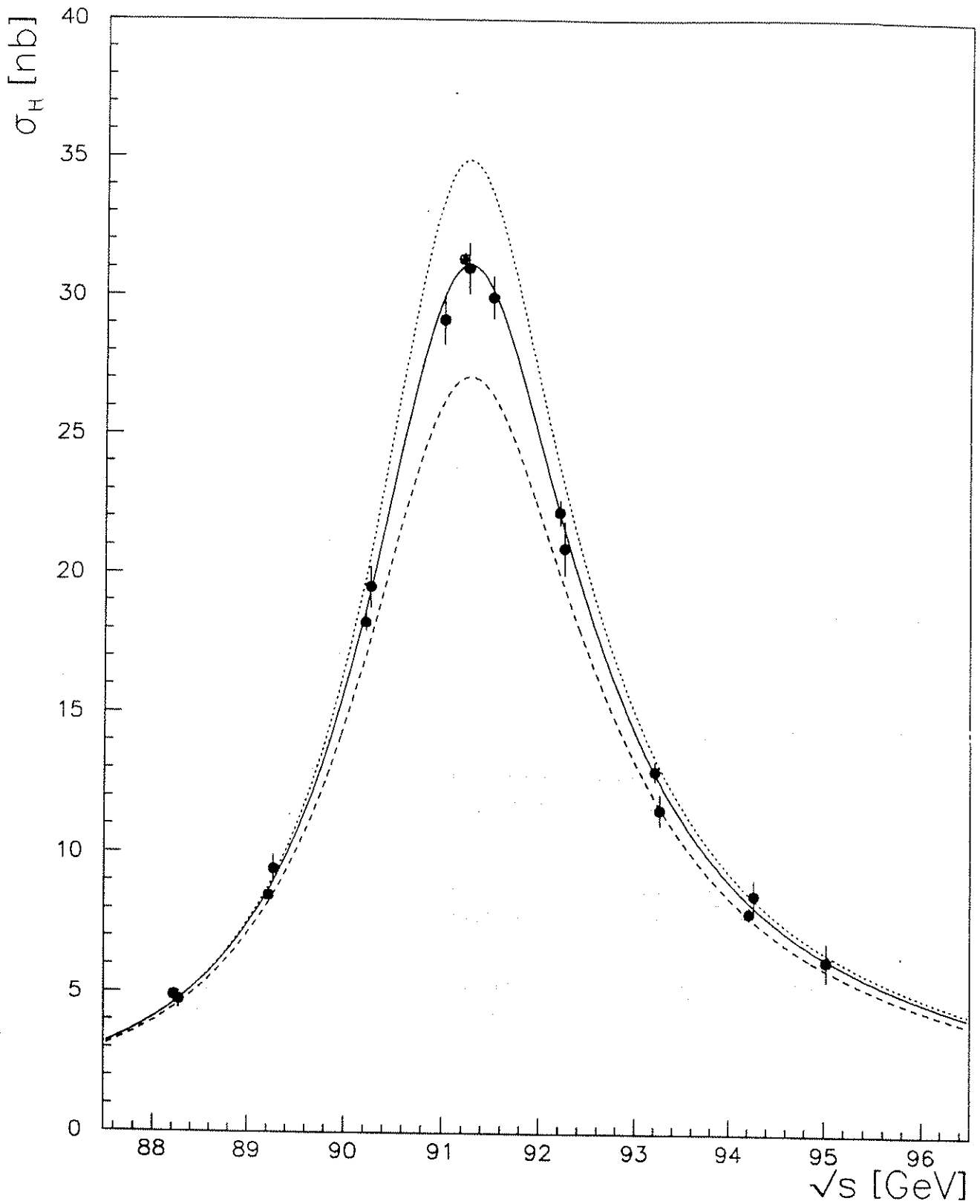
Figure 13.1: Fitted curve to the measured cross section values for the process $e^+e^- \rightarrow$ *hadrons*. Superimposed are the curves corresponding to the SM predictions for the cross section assuming two (dotted line) and four (dashed line) massless neutrino species.

Chapter 14

Measurement of $\tau^+\tau^-$ Pairs

In this chapter, after summarizing the experimental conditions related to our analysis, we present the results of the measurement of the total and differential cross-sections for $\tau^+\tau^-$ production in e^+e^- annihilation at Z^0 energies and related quantities.

The ratio $R_{\tau\tau}$ between the cross-section for $\tau^+\tau^-$ production and the cross-section for $q\bar{q}$ production (all flavours) in e^+e^- annihilation,

$$R_{\tau\tau}(E_i) = \frac{\sigma\left(e^+e^- \xrightarrow{\gamma,Z^0} \tau^+\tau^-\right)}{\sigma\left(e^+e^- \xrightarrow{\gamma,Z^0} hadrons\right)}(E_i) \tag{14.1}$$

is determined directly by the ratio, measured at each energy point E_i, between the number of $\tau\tau$ events and the number of hadronic events, corrected by the global detection efficiencies and normalized to the same geometrical acceptance.

The ratio, at each energy point, between the partial width of the Z^0 into $\tau^+\tau^-$ pairs and the partial width of the Z^0 into hadrons,

$$\frac{\Gamma_{\tau\tau}}{\Gamma_h}(E_i) = \frac{\sigma_i\left(e^+e^- \to Z^0 \to \tau^+\tau^-\right)}{\sigma_i\left(e^+e^- \to Z^0 \to hadrons\right)} \tag{14.2}$$

is obtained after subtracting to both cross-sections measured in 14.1 the contribution from γ exchange and $\gamma - Z^0$ interference, computed at each energy point. Then, recomputing the values of the ratios at each value of the centre of mass energy, the ratio $\Gamma_{\tau\tau}/\Gamma_h$ is fitted.

The importance of this measurement is twofold: it does not depend on the luminosity determination, and it is almost free of radiative corrections, namely those depending in the top quark mass that cancel out in the ratio.

The partial width $\Gamma_{\tau\tau}$ is obtained from a fit to the total production cross-section $\sigma_{\tau\tau}$ measured at different values of the centre of mass energy scattered within the resonance range. The excitation curve $\sigma_{\tau\tau}(s)$ ($s = E_{CM}^2$) can be parametrized to a good approximation by

$$\sigma_{\tau\tau}(s) = \sigma_{\tau\tau}^{peak} \frac{s\Gamma_Z^2}{\left(s - M_Z^2\right)^2 + \frac{s^2}{M_Z^2}\Gamma_Z^2} \left(1 + \delta_{RC}\right) \tag{14.3}$$

with

$$\sigma_{\tau\tau}^{peak} = \sigma_{\tau\tau}^{pole} \left(\frac{\Gamma_Z}{M_Z}\right)^\beta \quad , \quad \beta \approx \frac{2\alpha}{\pi} \left(\ln\frac{M_Z^2}{m_e^2} - 1\right) \tag{14.4}$$

$$\sigma_{\tau\tau}^{pole} = \frac{12\pi}{M_Z^2} \frac{\Gamma_{ee}\Gamma_{\tau\tau}}{\Gamma_Z^2} \tag{14.5}$$

This parametrization takes into account the electroweak radiative corrections, reflected in the modified Breit-Wigner with s-dependent width and the effect of initial state radiation, included in the factor $(\Gamma_Z/M_Z)^\beta$, which lowers the peak cross-section by approximately 30%. Other virtual photonic corrections are absorbed in the term δ_{RC}. The partial width $\Gamma_{\tau\tau}$ is directly obtained from the normalization defined by 14.5. The values of the mass and total width of the Z^0 are used as input parameters in this determination.

14.1 Experimental Conditions

In this section we summarize the experimental conditions related to our analysis. The reference values of the geometrical acceptance and of the global detection efficiency are recalled and a summary of the data sample used, as well as the corresponding luminosity is presented. Whenever necessary, reference is made to Part III.

14.1.1 Geometrical Acceptance

Two different regions of the DELPHI barrel region were considered in the two analysis: $50° < \theta < 130°$ for Period I and $43° < \theta < 137°$ for Period II. The acceptance (A_G), defined as the fraction of the full solid angle (4π) used in the analysis, due to the polar angle cuts is:

$$50° \ < \theta \ < 130° \quad \Rightarrow \quad A_G^I = .550 \tag{14.6}$$
$$43° \ < \theta \ < 137° \quad \Rightarrow \quad A_G^{II} = .645 \tag{14.7}$$
$$\tag{14.8}$$

These values are obtained by integration of $d\sigma/d\Omega$, the lowest order differential cross-section described in Chapter 2, over the symmetric interval of acceptance. The odd term in $\cos\theta$ vanishes in the integration and the term in $1 + \cos^2\theta$ determines the value of the acceptance.

14.1.2 Global detection efficiency

The global detection efficiency for τ pairs is the product of the trigger efficiency times the efficiency of the cuts used in the analysis:

$$\varepsilon_{\tau\tau} = \varepsilon_{trig} \, \varepsilon_{cuts} \tag{14.9}$$

The efficiency of the kinematical and topological cuts used to select the $\tau^+\tau^-$ events was discussed in Chapter 11. For each one of the data taking periods, this efficiency is the following:

$$\varepsilon_{cuts}^I = (64.5 \pm 3.5) \ \% \tag{14.10}$$
$$\varepsilon_{cuts}^{II} = (64.5 \pm 1.5) \ \% \tag{14.11}$$

The triggers used in the two data taking periods were the following:

• *Period I*

Track trigger - coincidences of signals from OD octants (back to back in Φ) and ID (trigger).
Scintillator trigger - coincidence of signals from TOF octants, HPC octants, TOF-HPC octants.

• *Period II*

Track trigger - In addition to the back to back ID-OD trigger (as in Period I), a single track trigger consisting of coincidence of signals from the TOF and OD octants was operational.
Scintillator trigger - as during Period I.

The use of independent and redundant triggers allowed the evaluation of the global trigger efficiency, using the information from the trigger bits recorded for each event. The measured values are the following (see Chapter 10 for more details):

$$\varepsilon^I_{trig} = (97 \pm 2)\% \tag{14.12}$$
$$\varepsilon^{II}_{trig} = (97 \pm 1)\% \tag{14.13}$$

14.1.3   Data sample

The number of τ pairs per energy point, shown in tables 14.1 and 14.2, was obtained by counting the number of events in the topologies 1-1, 1-2, 1-N, satisfying the selection criteria of Chapter 11, in all "good" runs at the given energy. The quality of a run is defined for both periods, by requiring that the detector is operated in stable [1] trigger and data taking conditions with at least:

• Stable trigger conditions for ID, OD, HPC, TOF.
• Stable data taking conditions for TPC, HPC, MUB.
• Non zero integrated luminosity information (from SAT).

Only events belonging to runs in which all these requirements were fulfilled are included in the final sample used in the analysis.

---

[1]For detectors participating in the trigger, data taking performance could be sometimes different and decoupled from their trigger performance

14.1.4 Luminosity per energy point

The integrated luminosity per run was measured by the Small Angle Tagger (SAT). The Bhabha trigger required 2 back-to-back clusters of energy bigger than 10 GeV in the 2 arms of the SAT, with an acoplanarity angle smaller than 10°. The efficiency of this trigger during Period I was estimated from the study of the single arm Bhabha trigger to be bigger than 0.994 at the 95% CL (Confidence Level). For Period II, its efficiency was higher than 99.9%. The total systematic error on the luminosity measurement was estimated to be

$$\left(\frac{\Delta\mathcal{L}}{\mathcal{L}}\right)_I = \sqrt{2.7^2\ f + 2.3^2\ (1-f)}\ \% \ \simeq 2.4\ \%\ [2.2\%(expt.)\pm 1.0\%(theory)] \quad (14.14)$$

$$\left(\frac{\Delta\mathcal{L}}{\mathcal{L}}\right)_{II} \simeq 1.3\ \%\ [0.9\%(expt.)\pm 1.0\%(theory)] \quad (14.15)$$

with f the fraction of data taken with a magnetic field of 0.7 Tesla ($f \approx \frac{1}{3}$ of the 1989 data). The improvement in the systematic uncertainty from the luminosity determination, during the 1990 running period, was due (see Chapter 12) to a better understanding and accuracy of the device used to determine the inner radius of the SAT acceptance region where the Bhabha events were detected.

The total integrated luminosity per energy point, shown in tables 14.5 and 14.6, was obtained adding the measured integrated luminosity for the individual runs belonging to LEP fills at the corresponding centre of mass energy, requiring that for each run the detector was operated in stable conditions previously defined.

14.1.5 Detection efficiency for hadronic events

For Period I, the number of detected $Z^0 \rightarrow hadrons$ events at each energy point after run selection is shown in table 14.1. The global detection efficiency for hadronic events ε_h is[83]

$$\varepsilon_h^I \approx (93.5 \pm 1.0)\ \% \quad (14.16)$$

For Period II, with harder cuts applied in the event selection and analysis, the number of detected hadronic Z^0 decays at each energy point after run selection is shown in table 14.2. The global detection efficiency for hadronic events is[85]

$$\varepsilon_h^{II} \approx (93.7 \pm 1.0)\ \% \quad (14.17)$$

In both cases, the value ε_h absorbs the correction for the geometrical acceptance of hadronic events.

$\sqrt{s}$(GeV)	$N_{\tau\tau}$	N_h	$R_{\tau\tau}(\%)$
88.28	7	188	9.92±3.75
89.28	5	194	6.87±3.07
90.28	12	808	3.96±1.14
91.03	34	1693	5.35±0.92
91.28	34	2470	3.67±0.63
91.53	47	2280	5.49±0.80
92.28	12	656	4.88±1.41
93.28	3	431	1.86±1.07
94.28	2	92	5.79±4.10
95.04	2	101	5.28±3.73

Table 14.1: 1989 data (Period I): Number of detected tau pairs ($N_{\tau\tau}$), number of detected hadronic events (N_h) and ratio $R_{\tau\tau}$ measured at each energy point after correction for the detection efficiencies.

$\sqrt{s}$(GeV)	$N_{\tau\tau}$	N_h	$R_{\tau\tau}(\%)$
88.22	9	468	4.46±1.49
89.22	27	1289	4.86±0.93
90.22	99	4074	5.64±0.57
91.22	725	34656	4.85±0.18
92.22	55	2453	5.20±0.70
93.22	41	1809	5.26±0.82
94.22	23	1043	5.11±1.07

Table 14.2: 1990 data (Period II): Number of detected tau pairs ($N_{\tau\tau}$), number of detected hadronic events (N_h) and ratio $R_{\tau\tau}$ measured at each energy point after correction for the detection efficiencies.

14.2   Measurement of $R_{\tau\tau}$ and $\Gamma_{\tau\tau}/\Gamma_h$

The measurement of $R_{\tau\tau}$ requires the knowledge of the number of hadronic Z^0 events and of the number of Z^0 decaying into $\tau^+\tau^-$ pairs per energy point, as well as the global detection efficiencies for hadronic and τ pair events.

With $N^i_{\tau\tau}, N^i_h$ being respectively the number of $\tau^+\tau^-$ events and the number of hadronic events measured at each energy point, and $\varepsilon_{\tau\tau}, \varepsilon_h$ the global detection efficiencies for $\tau\tau$ and hadronic events, the determination of $R_{\tau\tau}$ at each energy point E_i, displayed in tables 14.1 and 14.2, is given by

$$R_{\tau\tau}(E_i) = \frac{N^i_{\tau\tau}}{A_G \; \varepsilon_{\tau\tau}} \; \frac{\varepsilon_h}{N^i_h} \tag{14.18}$$

with A_G the geometrical acceptance. In the neighbourhood of the Z^0 resonance, the contribution to the total cross-section from the pure QED annihilation process (γ in s-channel) is small and in the energy range 88-95 GeV shows little variation. In table 14.4, the theoretically computed cross-section for hadron and $\tau^+\tau^-$ production is displayed at ten different energy points in the resonance region, for the 2 situations: i) Full cross-section corresponding to $\gamma + Z^0$ exchange including interference and ii) Cross section due to pure Z^0 exchange. Once this contribution is subtracted from the total number of measured $\tau^+\tau^-$ pairs and the total number of hadronic events, one is left with the ratio between the partial width of the Z^0 into $\tau^+\tau^-$ pairs and the partial width of the Z^0 into hadrons. In order to set a global value, a maximum likelihood fit was performed to the ratio between the number of corrected $\tau^+\tau^-$ and hadronic events, assuming Poissonian statistics for the number of $\tau^+\tau^-$ events observed at each energy point. The fit to the 17 data points yielded:

$$\frac{\Gamma_{\tau\tau}}{\Gamma_h} = (4.95 \pm 0.15(stat) \pm 0.11(syst)) \; \%$$

The result of the fit, superimposed to the experimental data, is shown in figure 14.1. The statistical error is compatible with the gaussian $1/\sqrt{N^{total}_{\tau\tau}}$ error, with $N^{total}_{\tau\tau}$ the total number of measured $\tau\tau$ pairs (all energy points). For the assigned systematic error, several contributions were taken into account as discriminated in table 14.3. Given the reduced number of $\tau^+\tau^-$ events at some energy points for Period I data, possible distortions introduced by the 1989 data points on the fitted result were investigated. Using only the 1990 data points, the fitted value changed by about 0.4%. This was interpreted an additional source of uncertainty and added to the total systematic error, computed as the sum in quadrature of the several uncertainties in the analysis of Period II data. Its contribution is neverthless negligible.

Source	Systematic error (%) Period I	Systematic error (%) Period II
Trigger efficiency	2.0	0.7
Selection procedure	5.5	1.8
Hadronic background	2.0	0.8
Hadronic detection	1.0	1.0

Table 14.3: Assigned systematic errors to the measurement of $\frac{\Gamma_{\tau\tau}}{\Gamma_h}$ and their origin, for both 1989 and 1990 data taking periods.

$\sqrt{s}$(GeV)	$\sigma_h^{\gamma+Z}$(nb)	σ_h^Z(nb)	$\sigma_{\tau\tau}^{\gamma+Z}$(nb)	$\sigma_{\tau\tau}^Z$(nb)
88.28	4.74	4.69	0.25	0.23
89.28	9.00	8.96	0.45	0.43
90.28	19.47	19.44	0.95	0.94
91.03	29.73	29.69	1.45	1.43
91.28	30.58	30.52	1.49	1.47
91.53	29.44	29.38	1.43	1.41
92.28	20.75	20.67	1.01	0.99
93.28	12.07	11.99	0.60	0.58
94.28	7.85	7.76	0.39	0.37
95.04	6.05	5.97	0.31	0.29

Table 14.4: Theoretical cross-section for hadron and $\tau^+\tau^-$ production in the resonance range, computed by the ZFITTER program. Displayed are the total cross-section (pure γ, pure Z^0, and γZ interference) and the cross-section for pure Z exchange.
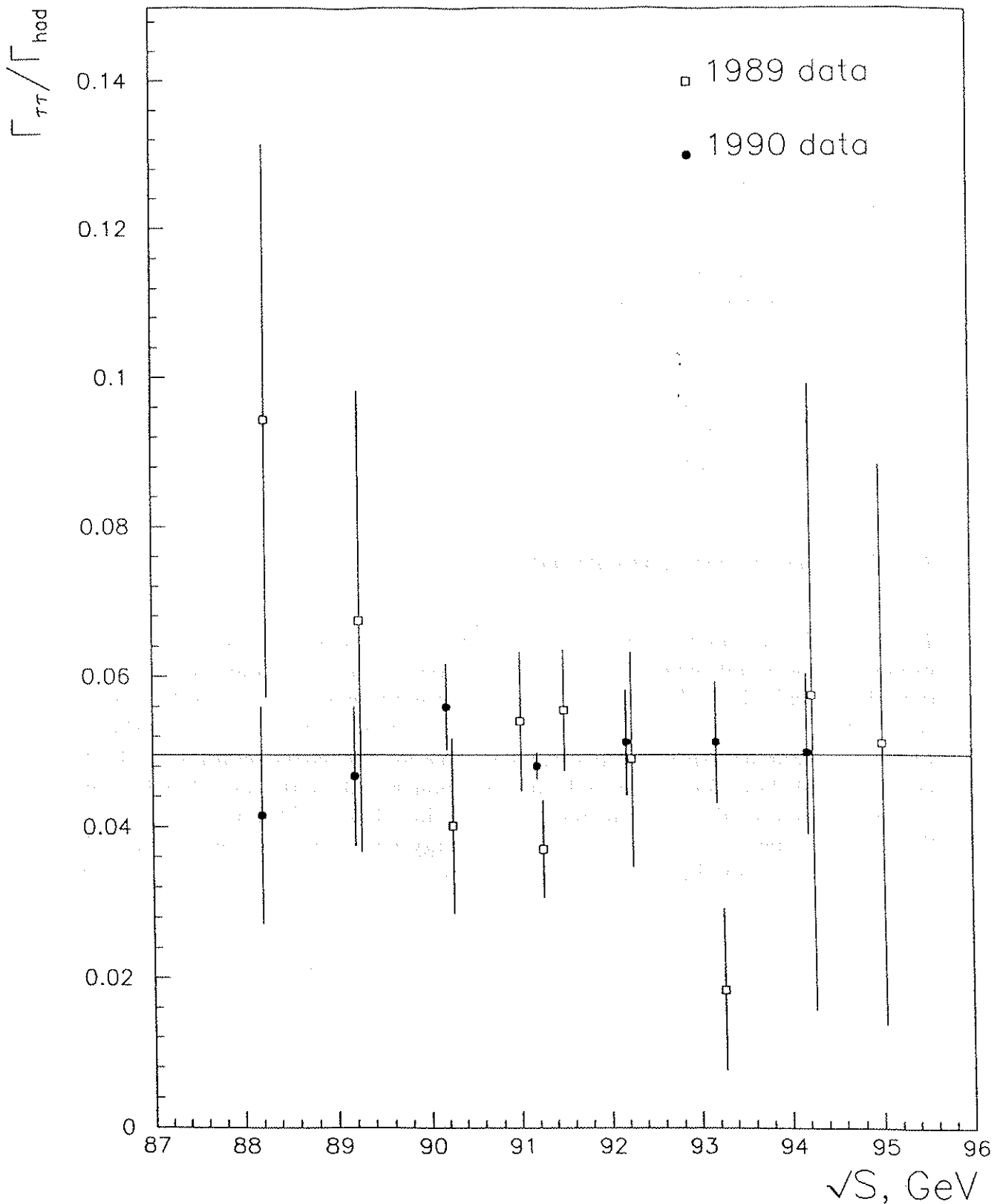
Figure 14.1: Ratio between the partial widths for $Z^0 \to \tau^+\tau^-$ and $Z^0 \to hadrons$ decays at 17 values of the center of mass energy across the Z^0 resonance. The fitted value is superimposed.

14.3   Total cross-section $\sigma_{\tau^+\tau^-}$

The determination of the total $\tau^+\tau^-$ cross-section at each energy point is done using the following expression:

$$\sigma_{\tau\tau}(E_i) = \frac{1}{\varepsilon_{\tau\tau}} \frac{N^i_{\tau\tau}}{\mathcal{L}_i} \tag{14.19}$$

where $N^{\tau\tau}_i, \mathcal{L}_i$ are respectively the number of measured $\tau^+\tau^-$ pairs and the integrated luminosity measured by the SAT at each energy point, and $\varepsilon_{\tau\tau}$ is the global efficiency for the detection of $\tau^+\tau^-$ pairs. The total cross-section in the full solid angle is obtained as:

$$\sigma^{4\pi}_{\tau\tau}(E_i) = \frac{\sigma_{\tau\tau}}{A_G} \tag{14.20}$$

with A_G the geometrical acceptance previously defined. The measured cross-section values are displayed in tables 14.5 and 14.6 for both 1989 and 1990 Periods.

14.4   Determination of $\Gamma_{\tau\tau}$

The determination of $\Gamma_{\tau\tau}$ results from an overall fit to the measured cross-section values using as input parameters the values of the Z^0 mass and width given in equations 13.25 and 13.26. The only free parameter is the normalization of the curve or equivalently the numerator of the expression defining the pole cross-section (formula 14.5). Assuming universality, the extracted value for the partial width is $(\Gamma_{ee}\Gamma_{\tau\tau})^{\frac{1}{2}}$. For the 1989 data (Period I), a fitting function based in the model independent parametrization of the Z^0 resonance proposed in reference [80], was used. Due to the small number of $\tau^+\tau^-$ events at some energy points, a maximum likelihood fit was performed, assuming a Poissonian distribution for the number of events at each point. The fit to the cross-sections measured at ten different values of the centre of mass energy yielded[84]

$$(\Gamma_{ee}\Gamma_{\tau\tau})^{\frac{1}{2}} = (82.6 \pm 3.3(stat) \pm 3.2(syst))\ MeV \qquad (1989\ data)$$

The systematic errors assigned in the analysis are displayed in table 14.7. The event sample consisted of 158 $\tau^+\tau^-$ events.

$\sqrt{s}$(GeV)	$\mathcal{L}(nb^{-1})$	$N_{\tau\tau}$	$\sigma_{\tau\tau}(nb)$	$\sigma_{\tau\tau}^{4\pi}(nb)$
88.28	41.87	7	0.27±0.10	0.49±0.19
89.28	22.32	5	0.36±0.16	0.66±0.30
90.28	46.66	12	0.41±0.12	0.75±0.22
91.03	63.99	34	0.85±0.15	1.55±0.27
91.28	87.81	34	0.62±0.11	1.13±0.19
91.53	80.42	47	0.93±0.14	1.69±0.25
92.28	40.81	12	0.47±0.14	0.86±0.25
93.28	40.16	3	0.12±0.07	0.22±0.13
94.28	12.83	2	0.25±0.18	0.46±0.32
95.04	17.41	2	0.18±0.13	0.33±0.23

Table 14.5: 1989 data (Period I): Integrated luminosity, number of measured $\tau^+\tau^-$ pairs and cross-section for tau pair production, measured in the region $50° < \theta < 130°$ and corrected to the full solid angle. The errors in the cross-section are only statistical (gaussian).

$\sqrt{s}$(GeV)	$\mathcal{L}(nb^{-1})$	$N_{\tau\tau}$	$\sigma_{\tau\tau}(nb)$	$\sigma_{\tau\tau}^{4\pi}(nb)$
88.22	181.83	18	0.16±0.037	0.25±0.058
89.22	420.12	85	0.32±0.035	0.50±0.053
90.22	374.17	154	0.66±0.053	1.02±0.082
91.22	2693.09	1670	0.99±0.024	1.53±0.038
92.22	355.51	137	0.62±0.053	0.95±0.081
93.22	390.61	93	0.38±0.039	0.59±0.061
94.22	449.68	61	0.22±0.028	0.34±0.043

Table 14.6: 1990 data (Period II): Integrated luminosity, number of measured $\tau^+\tau^-$ pairs and cross-section for tau pair production, measured in the region $43° < \theta < 137°$ and corrected to the full solid angle. The errors in the cross-section are only statistical (gaussian).

For the 1990 data (Period II), the analysed sample consisted of about 2500 $\tau^+\tau^-$ events. The measured cross-sections at the seven energy points across the resonance and the corresponding values corrected to the full solid angle are shown in tables 14.5 and 14.6 together with the number of measured events (after run selection) and the corresponding integrated luminosity. The program ZFITTER[81] was used to perform a least squares fit to the cross-section values. The fitted curve superimposed to the measured points is shown in figure 14.2. The fitted value is

$$(\Gamma_{ee}\Gamma_{\tau\tau})^{\frac{1}{2}} = (84.27 \pm 0.90(stat) \pm 1.10(syst)) \; MeV \qquad (1990 \; data)$$

$$\chi^2/d.o.f. = 9.3/(7-1)$$

The systematic errors assigned in the analysis are displayed in table 14.7. To check the consistency of the results obtained using the 2 data sets, a similar fit was performed combining the 17 cross-section values (10 in 1989 and 7 in 1990): the extracted value for the partial width changed by 0.5 MeV (0.6%) when the 10 additional points were included in the fit. To check for possible biases in the extracted result, introduced by the parametrization used as fitting function, the 1990 data was fitted with the same program used to fit the 1989 data set: the discrepancies between the results from the 2 fits were at the level of 0.3 MeV, clearly not important given the level of precision set by the other souces of systematic uncertainties.

Source	Systematic error (%) Period I	Systematic error (%) Period II
Trigger efficiency	2.0	0.7
Selection procedure	5.5	1.8
Hadronic background	2.0	0.8
Luminosity	2.4	1.3
Γ_Z uncertainty	2.5	0.9

Table 14.7: Assigned systematic errors in the measurement of the partial width $\Gamma_{\tau\tau}$ and their origin, for both the analysis of the 1989 (Period I) and 1990 (Period II) data

The last result, obtained using the selected sample of $\tau^+\tau^-$ events corresponding to the full period of 1990, is in good agreement with the measurements of the partial widths for the processes $Z^0 \rightarrow e^+e^-$, $Z^0 \rightarrow \mu^+\mu^-$ and $Z^0 \rightarrow \tau^+\tau^-$ published earlier by DELPHI[85]. There, performing combined fits to the hadronic and leptonic cross-sections measured using the partial sample of events mentioned in Chapter 13, the leptonic width was obtained assuming universality:

$$\Gamma_{ll} \;=\; (83.7 \;\pm\; 1.0(stat) \;\pm\; 1.1(syst)) \; MeV \qquad (14.21)$$

Fitting separately the cross-sections values measured for each leptonic channel, the last value was used[2] to extract the individual partial widths:

$$\Gamma_{ee} \;=\; (82.0 \pm 1.4(stat) \pm 1.3(syst)) \; MeV \qquad (14.22)$$
$$\Gamma_{\mu\mu} \;=\; (87.2 \pm 2.7(stat) \pm 2.2(syst)) \; MeV \qquad (14.23)$$
$$\Gamma_{\tau\tau} \;=\; (86.0 \pm 3.1(stat) \pm 2.7(syst)) \; MeV \qquad (14.24)$$

The analysis of both sets of results shows that, within the present accuracy, the universality hypothesis is confirmed.

---

[2] see Chapter 13 for the details of the fitting procedures

14.4.1   Error Analysis

The check on the consistency of the obtained errors can be done by relating the errors in the determination of $(\Gamma_{ee}\Gamma_{\tau\tau})^{\frac{1}{2}}$ with the errors of other "independent" measurements. Using the expressions

$$\sigma_h^{pole} = \frac{12\pi}{M_Z^2} \frac{\Gamma_{ee}\Gamma_h}{\Gamma_Z^2} \tag{14.25}$$

$$R_{\tau\tau} \approx \frac{\Gamma_{\tau\tau}}{\Gamma_h} \tag{14.26}$$

and neglecting correlations between the pole cross-section and the width, the magnitude on the relative error on the determination of $(\Gamma_{ee}\Gamma_{\tau\tau})^{\frac{1}{2}}$, is given by

$$\frac{\Delta(\Gamma_{ee}\Gamma_{\tau\tau})^{\frac{1}{2}}}{(\Gamma_{ee}\Gamma_{\tau\tau})^{\frac{1}{2}}} = \frac{\Delta M_Z}{M_Z} \oplus \underbrace{\frac{\Delta\Gamma_Z}{\Gamma_Z}}_{\simeq 0.9\%} \oplus \left(\frac{1}{2} \underbrace{\frac{\Delta R_{\tau\tau}}{R_{\tau\tau}}}_{\simeq 2.2\%} \right) \oplus \left(\frac{1}{2} \underbrace{\frac{\Delta\sigma_h^{pole}}{\sigma_h^{pole}}}_{\simeq 1.7\%} \right) \tag{14.27}$$

where the $\oplus$ symbol means sum in quadrature of the individual relative error contributions. The relative errors in the hadronic cross-section at the pole, the mass and width of the Z^0 are taken from [83]: the error in the hadronic cross-section at the pole is mainly dominated by the systematic error in the luminosity measurement (in the meantime reduced to 1.3%) and the error in Γ_Z dominated by the statistical uncertainty from the fit to the hadronic cross-section while the relative error in M_Z is negligible, when compared with the others. The relative systematic error of 1.3% in the determination of $(\Gamma_{ee}\Gamma_{\tau\tau})^{1/2}$, obtained from table 14.7, is in good agreement with the above estimation of 1.7%, where the correlations have been neglected.

14.4.2   Branching ratio $Z^0 \rightarrow \tau^+\tau^-$

The branching ratio for the decay process $Z^0 \rightarrow \tau^+\tau^-$ can be determined using the DELPHI measurements of the partial width into tau pairs and of the Z^0 total width (Γ_Z):

$$BR\,(Z^0 \rightarrow \tau^+\tau^-) = \frac{\Gamma_{\tau\tau}}{\Gamma_Z} = (\,3.41\,\pm\,0.08\,)\,\% \tag{14.28}$$

$$e^+e^- \longrightarrow \tau^+\tau^-$$

$$M_Z = 91.188 \text{ GeV (fixed)}$$

$$\Gamma_Z = 2.476 \text{ GeV (fixed)}$$

$$(\Gamma_{ee}\Gamma_{\tau\tau})^{1/2} = (84.27 \pm 0.90_{stat} \pm 1.10_{syst}) \text{ MeV}$$

$$\chi^2/\text{Ndf} = 9.1/6$$

Figure 14.2: 1990 data (Period II): Measured $\tau^+\tau^-$ cross-section per point with gaussian errors and fitted curve superimposed.

14.5 A_{FB}^{f}, Forward-Backward Asymmetry

The Forward-Backward Asymmetry[3] is related to the difference of cross-sections for fermion production in the forward ($\cos\theta > 0$) and backward ($\cos\theta < 0$) hemispheres. This can be translated into the measurement of the asymmetry of charge in each hemisphere. Writing $d\sigma_f(\theta), d\sigma_{\bar{f}}(\theta)$ respectively the differential cross-section for fermion and anti-fermion production at polar angle θ in the process $Z^0 \rightarrow f\bar{f}$ and recalling that $d\sigma_f(\pi - \theta) \equiv d\sigma_{\bar{f}}(\theta)$ one has:

$$A_{FB}^{f}(\theta) = \frac{[d\sigma_f/d\cos\theta](\theta) - [d\sigma_f/d\cos\theta](\pi - \theta)}{[d\sigma_f/d\cos\theta](\theta) + [d\sigma_f/d\cos\theta](\pi - \theta)} = \frac{[d\sigma_f/d\cos\theta] - [d\sigma_{\bar{f}}/d\cos\theta]}{[d\sigma_f/d\cos\theta] + [d\sigma_{\bar{f}}/d\cos\theta]} \tag{14.29}$$

From the last expression, after integration of the differential cross-section, the difference between the cross-section for producing fermions in the Forward and in the Backward hemisphere is equivalent to the imbalance between the number of fermions and anti-fermions, respectively N_f and $N_{\bar{f}}$, (or equivalently between the number of negative and positive charged particles, N_- and N_+) produced in each hemisphere, giving the *charge asymmetry*:

$$A_{FB}^{f} = \frac{N_f(\cos\theta > 0) - N_f(\cos\theta < 0)}{N_f(\cos\theta > 0) + N_f(\cos\theta < 0)} \equiv \frac{N_-(\cos\theta > 0) - N_+(\cos\theta > 0)}{N_-(\cos\theta > 0) + N_+(\cos\theta > 0)} = A_{CH}^{f} \tag{14.30}$$

The differential cross-section for s-channel exchange can be written as

$$\frac{d\sigma^f}{d\Omega} = \sigma_0 \left[(1 + \cos^2\theta) + \frac{8}{3} A_{FB}^{f} \cos\theta \right] \tag{14.31}$$

The forward-backward asymmetry, deduced from this expression when integrated over the full angular domain $0 < \theta < \pi$, is A_{FB}^{f}. The angular dependence of $A_{FB}(\theta)$ relative to the asymmetry $A_{FB}(\theta = 0)$, is:

$$A_{FB}^{f}(\theta) = A_{FB}^{f}(0) \frac{2\cos\theta}{1 + \cos^2\theta} \tag{14.32}$$

---

[3]See Chapter 3 about asymmetries

14.5.1 Statistical Error on the measurement of A_{FB}^τ

The forward-backward asymmetry A_{FB}^τ is defined as

$$A_{FB}^\tau = \frac{N_F - N_B}{N_F + N_B} \tag{14.33}$$

with N_F (N_B) the number of events with the τ^- produced in the Forward (Backward) hemisphere and $N_{\tau\tau} = N_F + N_B$ is the total number of $\tau^+\tau^-$ events. For a given value of the asymmetry, the number of τ^- in the forward and backward hemisphere are:

$$N_F = \frac{N_{\tau\tau}}{2} \left(1 + A_{FB}^\tau\right) \qquad N_B = \frac{N_{\tau\tau}}{2} \left(1 - A_{FB}^\tau\right) \tag{14.34}$$

N_F^τ follows a binomial distribution of parameter $p = (1 + A_{FB}^\tau)/2$:

$$Pr(N = N_F) = \binom{N_{\tau\tau}}{N_F} p^{N_F} (1 - p)^{N_{\tau\tau} - N_F} \tag{14.35}$$

The standard deviation of the distribution of the number of observed τ in the forward hemisphere is given by

$$\sigma_{N_F} = \sqrt{N_{\tau\tau}\, p\, (1 - p)} = \sqrt{N_{\tau\tau}}\, \frac{\sqrt{1 - \left(A_{FB}^\tau\right)^2}}{2} \tag{14.36}$$

and the statistical error on the asymmetry becomes

$$\Delta(A_{FB}^\tau)_{stat} = \frac{2}{N_{\tau\tau}}\, \sigma_{N_F} = \sqrt{\frac{1 - \left(A_{FB}^\tau\right)^2}{N_{\tau\tau}}} \tag{14.37}$$

14.5.2   Systematic Error on the measurement of A^τ_{FB}

The main source of systematic error in the determination of the forward-backward asymmetry is the *Charge Misidentification*.

Let us define $p = Probability\ (+ \to -) \simeq Probability\ (- \to +)$ as the probability of wrong charge reconstruction. The systematic error in the asymmetry measurement, coming from the category $1-1$ of $\tau^+\tau^-$ events and due to wrong charge reconstruction, is of order p^2, if total charge zero is required for the event. For the categories 1-2 and 1-N, the systematic error in the asymmetry measurement comes from the wrong charge reconstruction of the isolated track. The measured number of negative charged tracks in the forward and backward hemispheres, respectively N_F and N_B, can be written as as function of the "true" number of negative tracks in the forward hemisphere, N^t_F, the "true" number of negative tracks in the backward hemisphere, N^t_B and p, as[87]:

$$N_F = N^t_F - p\,N^t_F + p\,N^t_B = N^t_F - p\,(\,N^t_F - N^t_B\,) \qquad (14.38)$$

$$N_B = N^t_B - p\,N^t_B + p\,N^t_F = N^t_B + p\,(\,N^t_F - N^t_B\,) \qquad (14.39)$$

If $p \ll 1$, N^t_F and N^t_B can be written to a good approximation as:

$$N^t_F \simeq N_F + p\,(\,N_F - N_B\,) \qquad (14.40)$$

$$N^t_B \simeq N_B - p\,(\,N_F - N_B\,) \qquad (14.41)$$

The true value of the asymmetry, A^t_{FB}, is:

$$A^{true}_{FB} = \frac{N^t_F - N^t_B}{N^t_F + N^t_B} \simeq \frac{N_F - N_B + 2\,p\,(\,N_F - N_B\,)}{N_F + N_B} = A^{meas}_{FB}\,(1 + 2\,p\,) \qquad (14.42)$$

with $A^{meas}_{FB} = (N_F - N_B)/(N_F + N_B)$. The relative systematic error is obtained from:

$$\left(\frac{\Delta A^\tau_{FB}}{A^\tau_{FB}}\right)_{syst} = \frac{A^{true}_{FB} - A^{meas}_{FB}}{A^{meas}_{FB}} \simeq 2\,p \qquad (14.43)$$

The fraction of events with like sign $+\,+$ and $-\,-$ tracks passing all the selection cuts for 1-1 category except the cut requiring total charge zero is shown in table 14.8, together with the fraction e^-e^- and $\mu^+\mu^-$ events with of like sign tracks. The probabilities $P(+ \to -)$ and $P(- \to +)$, of wrong charge reconstruction, can be extracted from the table.

Like-sign	e^+e^-	$\mu^+\mu^-$	$\tau^+\tau^-$
$+\ +$	3.6	0.6	0.9
$-\ -$	2.8	0.4	1.1

Table 14.8: Fraction (%) of reconstructed like sign pairs of tracks for each family of leptons, relative to the reconstructed opposite charge pairs.

For $\tau^+\tau^-$ events, $p \simeq 1\%$ and the contribution to the total systematic error from the terms of order p^2 can be neglected. Having in mind that about 60% of the events fall in the category 1-1, the systematic error due to charge misidentification can be estimated, as:

$$\left(\frac{\Delta A_{FB}^\tau}{A_{FB}^\tau} \right)_{syst} = 0.4 \cdot (2\,p) \sim 0.8\ \% \qquad (14.44)$$

14.5.3 A_{FB}^τ measurement at the Z^0 resonance

The determination of the forward-backward asymmetry is done in a symmetric interval defined by $|\cos\theta| < \cos\theta_{min}$, imposed by the detector acceptance or the cuts in the analysis. The value obtained in this case is smaller than the one expected by integration over the full solid angle, but can be corrected using the known $\cos\theta$ dependence of the asymmetry (formula 14.32).

For the determination of the forward-backward asymmetry using $\tau^+\tau^-$ events, tracks belonging to events in the 3 topologies (1-1,1-2,1-N) were considered. For the events falling in the categories 1-2,1-N, only the isolated track was analysed, while for events falling in the category 1-1, both tracks were analysed. The τ is taken to be in the forward (backward) hemisphere if the measured polar angle of corresponding charged track satisfies the $\cos\theta > 0$ ($\cos\theta < 0$) condition. The measured differential cross section $(d\sigma/d\cos\theta)$ at $\sqrt{s} = 91.22\ GeV$ for all negative charged tracks in $\tau^+\tau^-$ events is shown in figure 14.3. In figure 14.4 the forward-backward asymmetry A_{FB}^f in the interval $|\cos\theta| < .73$, is plotted at the seven energy points at which data was collected in the 1990 scan of the Z^0 resonance. Superimposed is the parametrization from the program ZFITTER of Bardin et. al., taking into account QED+electroweak radiative corrections to the asymmetry. The expected change of sign and trend of the asymmetry across the resonance (crossing point close to $\sqrt{s} = M_Z$) are well reproduced by the data. The values of the asymmetry at each energy and corresponding errors are shown in table 14.9.

$\sqrt{s}(\text{GeV})$	$N_{\tau\tau}$	$A_{FB}^\tau(\%)$
88.22	29	-44.83±16.60
89.22	88	-13.64±10.56
90.22	154	-14.29± 7.98
91.22	1649	+1.52± 2.46
92.22	137	+3.65± 8.54
93.22	93	-3.23±10.36
94.22	61	-4.92±12.79

Table 14.9: Number of $\tau^+\tau^-$ events and Forward-Backward asymmetry, measured in the angular interval $|\cos\theta| < .73$, at the seven energy points covering the Z^0 resonance. Errors are statistical.
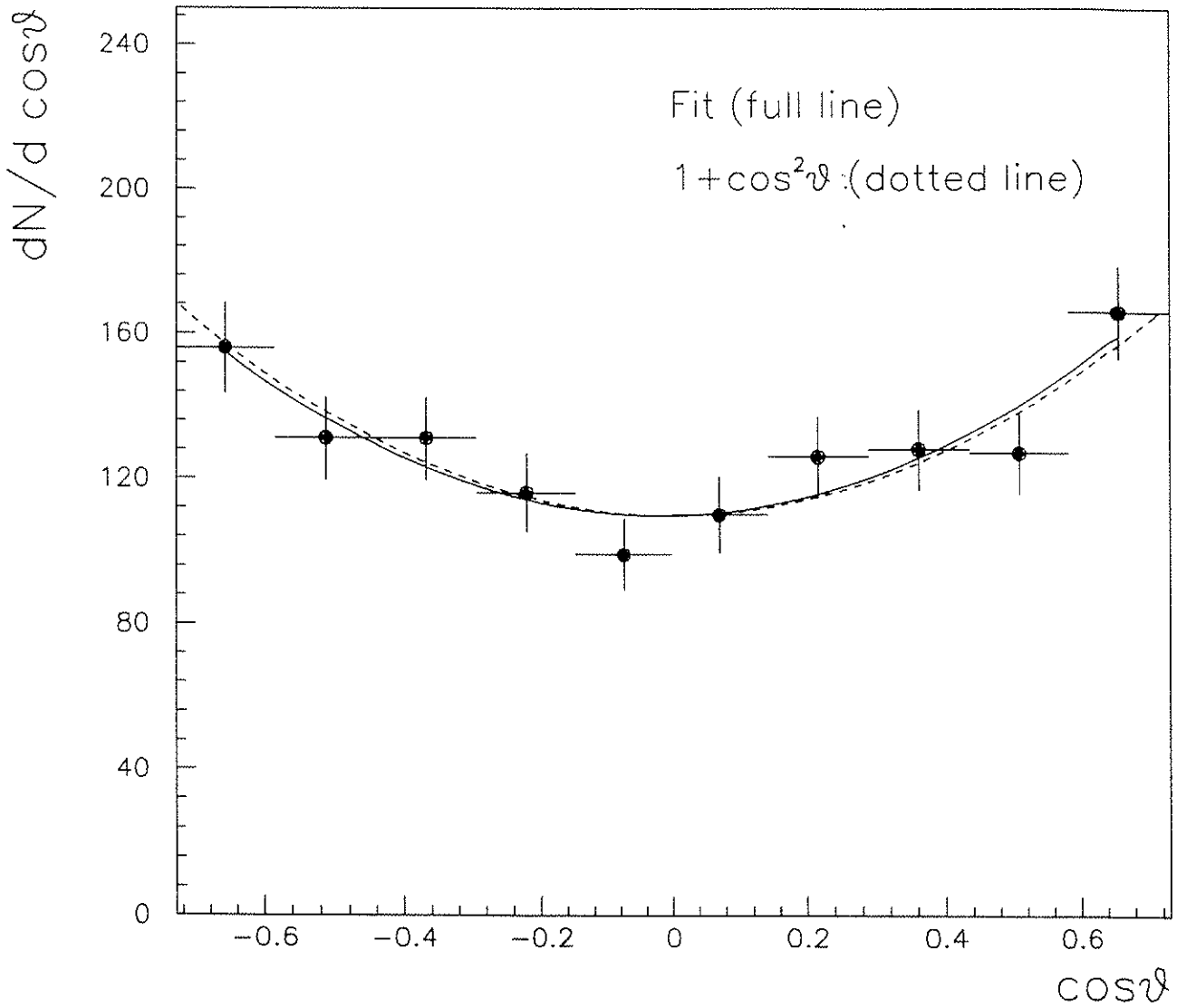
Figure 14.3: Angular distribution of the negative charged tracks isolated in one hemisphere and belonging to selected $\tau^+\tau^-$ events measured at 91.22 GeV (peak).
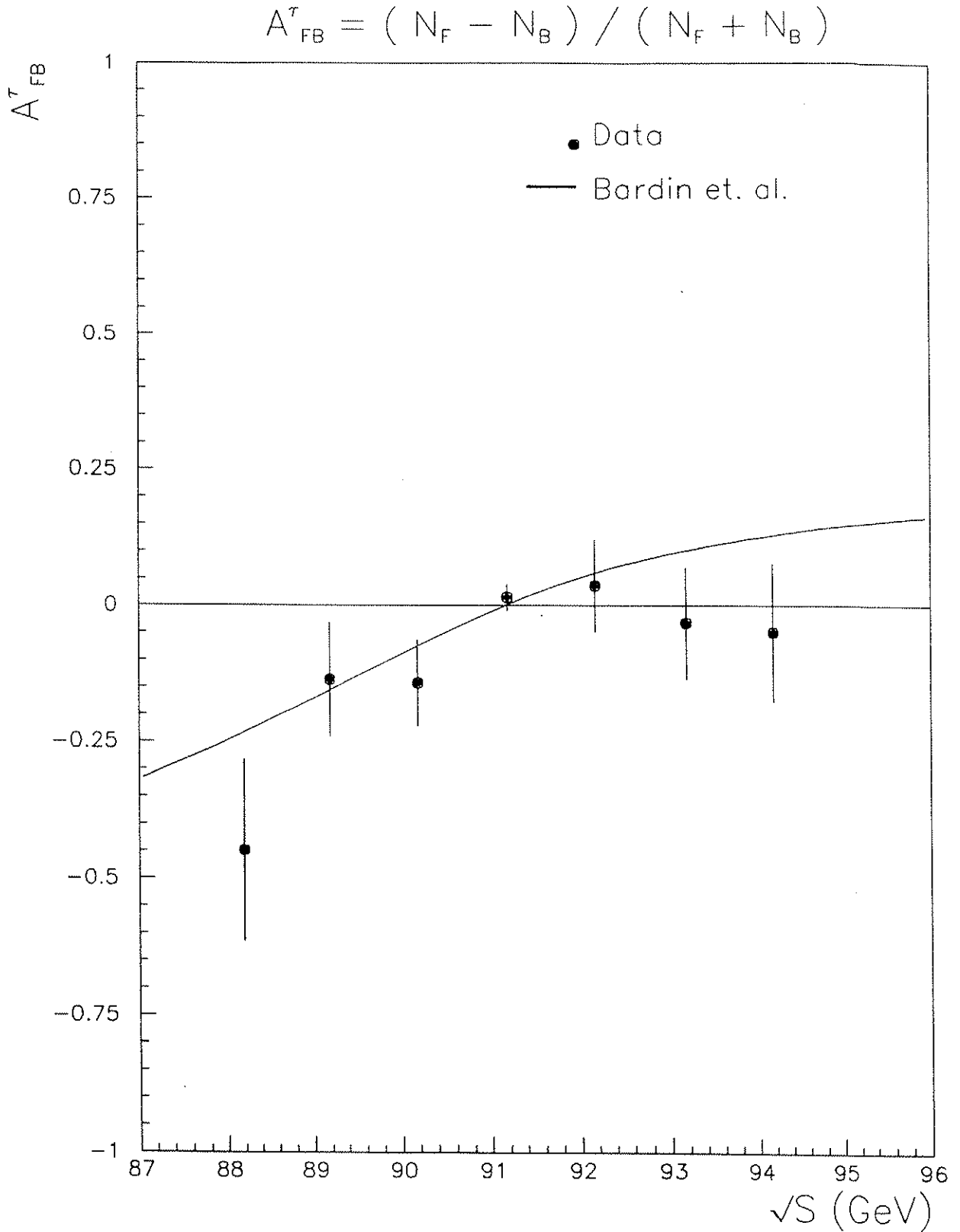
Figure 14.4: Charge asymmetry and errors, measured in DELPHI, in the angular interval $|\cos\theta| < .73$, using $\tau^+\tau^-$ events for the seven energy points covering the Z^0 resonance range. Superimposed is the theoretical curve computed by the program ZFITTER of Bardin et. al.

Chapter 15

The τ polarization

For the measurement of the τ polarization[1] A^τ_{POL}, identification of the final states in τ decay is needed. The polarization is due to the helicity asymmetry, constraining the energy spectra of the final state leptons and hadrons. The energy spectrum of the final state leptons ($l = e, \mu$) can be written in lowest order as[16,94]

$$\frac{dN_l}{dX_l} \simeq \left(\frac{5}{3} - 3X_l^2 + \frac{4}{3}X_l^3 \right) \mp A^{\tau^\pm}_{POL} \left(\frac{1}{3} - 3X_l^2 + \frac{8}{3}X_l^3 \right) \qquad (15.1)$$

where $X_l = \frac{2E_l}{E_{cm}}$ and E_l, E_{cm} are respectively the energy of the final state lepton and the centre of mass energy. The energy spectrum of the final state hadrons (h=π, ρ) is in lowest order given by[15]

$$\frac{dN_h}{dX_h} \simeq 1 \mp \alpha_h A^{\tau^\pm}_{POL} (2X_h - 1) \qquad (15.2)$$

with $\alpha_h = \frac{M_\tau^2 - 2m_h^2}{M_\tau^2 + 2m_h^2}$ and as above, $X_h = \frac{2E_h}{E_{cm}}$ and E_h, E_{cm} are respectively the energy of the final state hadron and the centre of mass energy.

Comparing the energy spectra of both hadronic final states it is clear that the sensitivity of the π spectrum to the polarization value is about twice the sensitivity of the ρ spectrum. Also, higher systematic errors are expected to affect the measurement of the ρ energy spectrum from its decay products (π, π^0): the identification of the charged π and the reconstruction of the two photons from the π^0 must be performed. Neverthless, the branching ratio for $\tau \rightarrow \rho\nu$ decays, approximately 2.3 times bigger than the branching ratio for $\tau \rightarrow \pi\nu$ decays, can play an important factor in the statistical and systematic errors from the two measurements.

---

[1]See chapter 3 and references therein

The higher order polynomial dependence of the leptonic spectra induces more systematic effects than the simple straight line dependence of the hadronic spectra. Once again, the relative branching ratios and the detection efficiencies condition any a priori comparative statement on the systematic and statistical errors.

The percentage of contamination from the other leptonic channels into the $\tau^+\tau^-$ sample is kept at the level of 0.7%. Thus, as discussed in the sequence, the main sources of backgrounds and uncertainties in the selection of each individual final state in τ decays arise from the competing decay modes.

In the sequence, some results on the identification of the e, μ, π final states from τ decays are shown, and a low-statistics measurement of the τ polarization, extracted from the fit to the energy spectrum of muons and pions is presented. The measurement of the *sign* of the v/a ratio between the vector and axial couplings of the τ lepton is derived from the polarization measurement. A value of $\sin^2\theta_w$ can also be extracted but the uncertainty in its determination is clearly not competitive with previous results obtained in this analysis.

The acceptance region is restricted to:

$$43° \ < \ \theta \ < \ 137° \tag{15.3}$$

and only tracks isolated in their hemisphere, (both tracks in 1-1 category, and the isolated track in the categories 1-2 and 1-N) are analysed.

15.1   QED radiative corrections in τ decays

Final state bremsstrahlung is the most important correction to take into account in the measured energy spectra of τ decay products[17]. Radiation from the produced taus and from their final state particles causes significant deviations in the measured spectra relative to the lowest order predictions of eqs. 15.1,15.2. The corrections to the lowest order predictions are described in [17].
The parametrizations used to fit the measured dN/dX spectra of the leptonic and hadronic τ decay products are taken from the program CALASY [95] and include the above QED corrections. Such parametrizations are well suited for the present level of accuracy in the measured spectra. The comparison between the dN/dX spectrum obtained using the CALASY parametrization and the lowest order parametrization previously presented is shown in figure 15.1, for muons and pions.
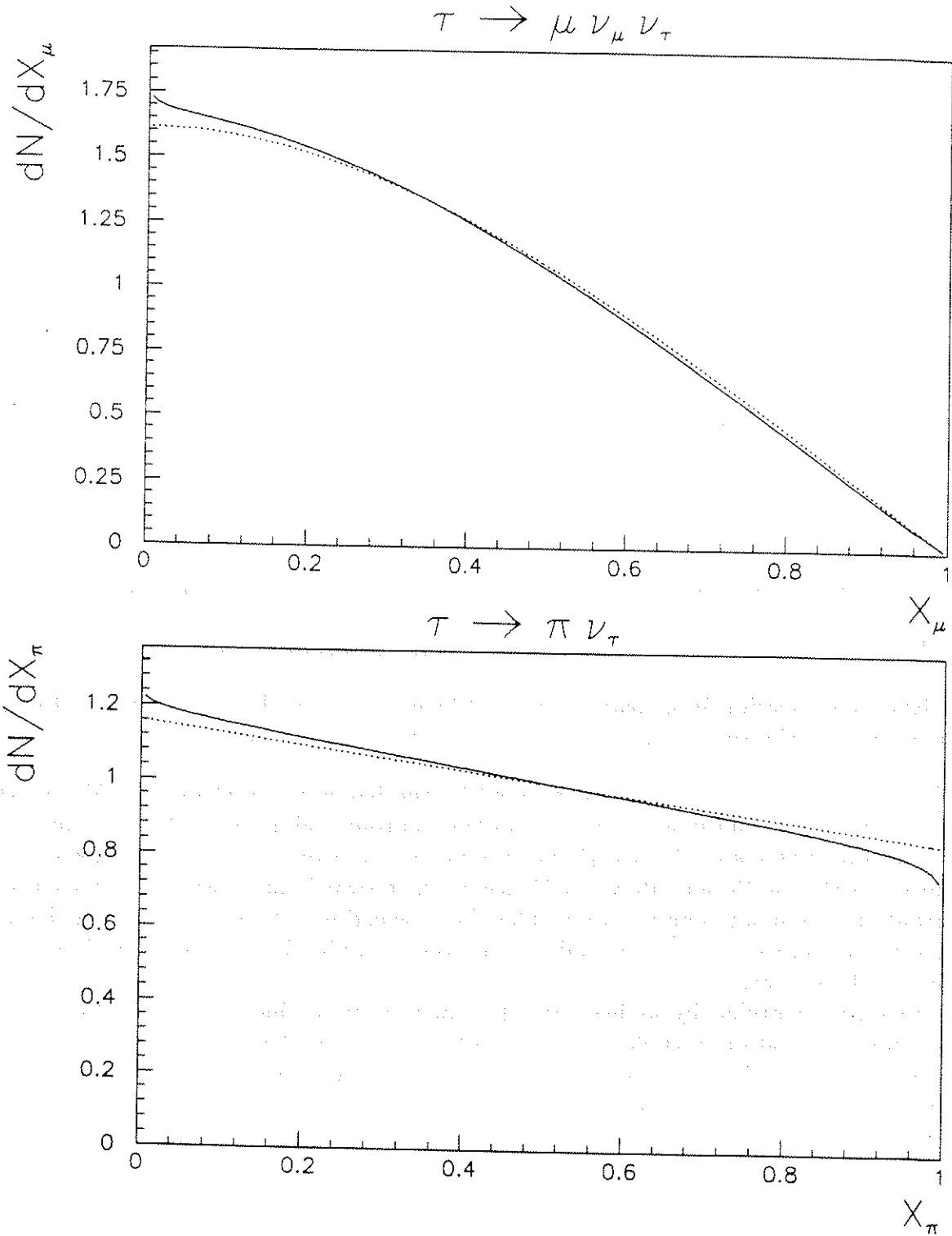
Figure 15.1: dN/dX spectrum obtained using the parametrization from CALASY, superimposed to the lowest order dN/dX spectrum, for muons and pions from tau decays. The deviations to the lowest order spectra are mainly caused by the final state bremssthralung from the tau and its decay products.

15.2   Measurement of the $\tau \to \mu \bar{\nu}_\mu \nu_\tau$ final state

15.2.1   Selection of muons

The muon chambers information is used to identify the muons. In addition to the selection cuts for the $\tau^+ \tau^-$ events presented in Chapter 11, the following selection criteria are applied to each isolated track [2]:

- $P_{track} > 3\ GeV$

- $43° < \theta_{track} < 137°$

These criteria are complemented by the or of the following conditions:

- At least 2 hits in the Barrel Muon Chambers matching the track

$$OR \tag{15.4}$$

- $E_{em} < 1.\ GeV$, electromagnetic energy associated to the track

- No neutral showers in a cone of 30° half-opening angle around the track.

- $E_{had} < 7.5\ GeV$, for the total hadronic energy associated to the track.

- Energy deposition in at least 2 of the 4 layers of the hadron calorimeter. Energy deposition in the third or fourth layers (or both) is mandatory.

The region $50° < \theta < 130°$ is covered by the barrel muon chambers (MUB), the electromagnetic calorimeter (HPC) and the hadronic calorimeter (HAC). The complementary regions of the acceptance are not covered by muon chambers, except at the edges (below 45° and above 135°), where the forward muon chambers (MUF) contribute to the muon identification. The above selection cuts exploit the independent information of the three types of detectors to get a redundant and efficient identification of the muons.
A muon is identified by at least two hits in the muon chambers or by the typical minimum ionization particle signal in both the HPC and HAC. In the last case, it is further required that no other electromagnetic shower exists around the track and that the topology of the signal in the hadronic calorimeter be such that no containment in the first two layers exists (typical of pion showers). The efficiency of the cuts above is

$$\varepsilon_\mu = 60\ \% \tag{15.5}$$

---

[2] A minimum momentum of about 2 GeV (angle dependent) is required for a muon to cross the iron of the hadron calorimeter and reach the muon chambers

15.2.2 Background to the sample of $\tau \rightarrow \mu$ events

$\pi \rightarrow \mu$ Misidentification

The main contamination into the $\tau \rightarrow \mu$ event sample is mainly coming from the pions from $\tau \rightarrow \pi \; n\pi^0$ ($n \geq 0$) decays. Punch-through pions, crossing the hadron calorimeter and producing hits in the muon chambers or hadronic showers reaching the muon chambers, contaminate the muon sample. This contamination increases with the energy of the pions and affects the high-x_μ bins of the dN/dX_μ distributions. Also, pions showering until the third or fourth layers of the calorimeters without reaching the muon chambers survive the cuts. To reduce the contamination from the decays with π^0's in the final state, the cut on the electromagnetic energy associated to the track and on the number of neutral showers surrounding the track is applied.

$K \rightarrow \mu$ Misidentification

The iron of the hadronic calorimeter amounts to 3 interaction lenghts for the charged kaons produced in tau decays. The probability that charged kaons do not interact inside the calorimeter is of the order of $e^{-3} \simeq 5\%$. Neverthless, given the small branching ratio for producing kaons in tau decays ($< 2\%$), the total contamination is at the level of few per mil. As above, for the modes with π^0's in the final state, the cut on the electromagnetic energy associated to the track and on the number of neutral showers surrounding the track is applied.

$Z^0 \rightarrow \mu^+ \mu^-$ Contamination

The selection cuts for the 1-1 category explicitely require that events with both tracks matched by muon hits or with total electromagnetic energy below a threshold set quite above $2E_{mip}$ are rejected. This last requirement rejects those events in which, due to inefficiencies or dead zones in the muon chambers, only one track is matched by hits. The contamination from $Z^0 \rightarrow \mu^+ \mu^-$ events in the total $\tau^+\tau^-$ sample is estimated (see Chapter 11) to be 0.5% mainly in the 1-1 category, after the cuts in acolinearity, acoplanarity and visible momentum are applied.

Using simulated events, the estimated contamination from the other final states from τ decays is shown in table15.1.

Background type	Contamination (%)
$\tau \to \pi\nu$	7.6
$\tau \to \pi\pi^0\nu$	7.1
$\tau \to \pi\pi^0\pi^0\nu$	4.9
$\tau \to hadron\ X\ \nu$ (incl.)	21.3

Table 15.1: Main sources of background and corresponding contamination (estimated from simulated events) in the $\tau \to \mu$ event sample.

15.2.3   Determination of A_{POL}^{τ}

The corrected dN/dX spectrum, shown in figure 15.2, is obtained from the raw dN/dX spectrum (containing all the events passing the selection cuts) after background subtraction and correction for the acceptance are performed at each bin. The corrected dN/dX spectrum is then fitted using as fitting function the CALASY parametrization for dN/dX_{μ}[17]. The extracted value for the polarization obtained from the $\tau \to \mu$ channel is

$$A_{POL}^{\tau} = -0.165 \pm 0.170(stat)$$

The statistical error is the dominant uncertainty in this measurement.

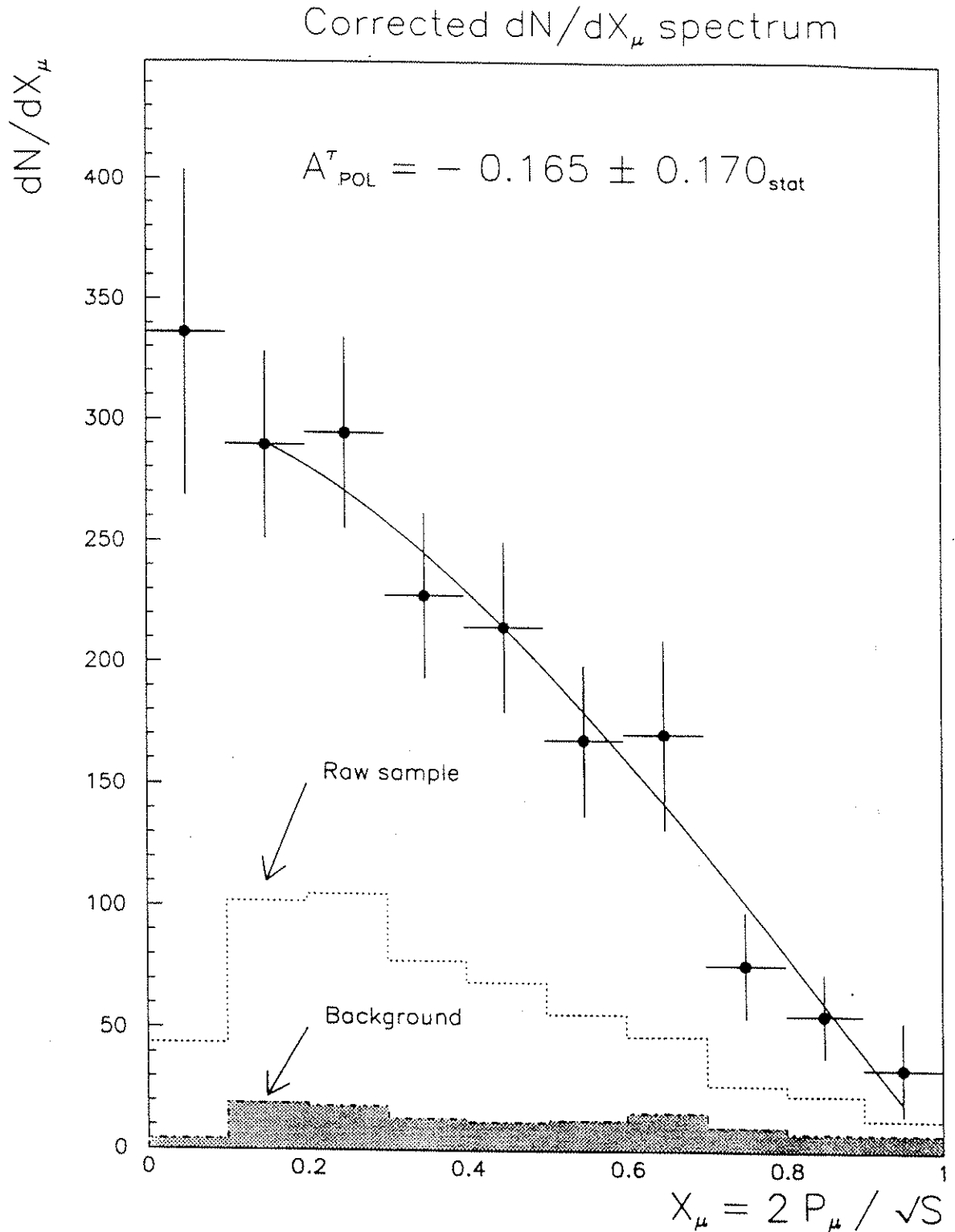Figure 15.2: dN/dX spectrum after background subtraction and acceptance correction at each bin, of the identified muons from $\tau \to \mu\bar{\nu}_\mu\nu_\tau$ decays. Superimposed is the raw spectrum of the selected muons candidates and the dN/dX spectrum of the background estimated from simulated events.

15.3   Measurement of the $\tau \rightarrow \pi \nu_\tau$ final state

15.3.1   Selection of pions

To select the $\tau^+ \tau^-$ events, the values of the cuts in the visible momentum and electromagnetic energy of the event were slightly modified [3]:

- $P_{vis} < 70$ GeV (instead of 60 GeV).

- $E_{EM}^{total} < 50$ GeV (instead of 30 GeV per track or per hemisphere).

The following cuts are applied to the isolated track of the events falling in the category 1-N and to both tracks of the events belonging to the category 1-1:

- $P_{track} > 5$ GeV

- $50° < \theta_{track} < 130°$

- $E_{em} < 1.0$ GeV and a single shower associated to the track.

These criteria are complemented by:

- $E_{HC} > 10$ Gev

$$OR \tag{15.6}$$

- $E_{HC} > 5$ GeV

- No hits matching the track extrapolated to the muon chambers.

- $(E_4 + E_3)/(E_2 + E_1) < 0.5$, ratio between the energy in the 4 layers of the hadronic calorimeter.

The final state pions from the decays $\tau \rightarrow \pi \, n\pi^0$ ($n \geq 1$) are vetoed requiring the track to be matched by one shower of less than 1 GeV in the electromagnetic calorimeter and that no other neutral showers exist in a wide cone around the particle. Muons from $\tau \rightarrow \mu$ decays are vetoed requiring an energy bigger than 10 GeV associated to the track in the hadron calorimeter (muon signal is contained below 7.5 GeV) or that no hits are associated to the track in the muon chambers and the pattern of energy deposition in the 4 layers of the hadron calorimeter is such that the sum of the energy in the first and second layer is more than twice the sum of the energy in the third and fourth layers. The efficiency of the cuts above is

$$\varepsilon_\pi = 50 \% \tag{15.7}$$

---

[3]The selection cuts for $\tau^+ \tau^-$ events are discussed in Chapter 11

15.3.2 Background to the sample of $\tau \to \pi$ events

$\tau \to \rho \nu_\tau$

This is the main source of background. The sample of pions from $\tau \to \pi\nu_\tau$ decays is contaminated by those pions from the decay $\rho \to \pi\pi^0$, when both photons from the process $\pi^0 \to \gamma\gamma$ are not detected. The main causes for the the photon losses are:

- Photon in "40° hole" regions. This happens when its polar angle θ_γ is:

$$35.5° < \theta_\gamma < 41.5° \quad \underline{OR} \quad 138.5° < \theta_\gamma < 144.5° \quad (15.8)$$

Restriction of the pion tracks to the angular domain $50° < \theta_{track} < 130°$ is made to avoid the pion contamination from the $\tau \to \rho, A_1$ final states produced at the edges of the acceptance region, when photons are lost in this dead region.

- Photon in Φ cracks of HPC

- $E_\gamma < E_{thr}$, photon energy below calorimeter threshold

This contamination happens mainly at small values of E_π, and the measured spectrum dN/dX_π, is distorted from its predicted linear dependence on x_π.

$\tau \to A_1 \nu_\tau$

This background is analogous (but smaller) to the background from $\tau \to \rho$ decays. The final state pions from the decay $A_1 \to \pi\pi^0\pi^0$, when for the same reasons stated above all photons are lost, contaminate the measured dN/dX_π spectrum. As before, the contamination occurs mainly at small values of x_π.

$\mu \to \pi$ Misidentification

The differentiation between muons and pions is not very efficient in the hadron calorimeter below 7.5 GeV, because the μ signal in the hadron calorimeter is of the same order of magnitude than the energy of showers developped by low energy pions.

$Z^0 \to \mu^+\mu^-$ Before releasing the visible momentum cut, the contamination from these events in the total $\tau^+\tau^-$ sample is estimated (see Chapter 11) to be 0.5% mainly in the 1-1 category. The selection cuts for $\tau^+\tau^-$ events in the 1-1 category act redundantly in the rejection of the $Z^0 \to \mu^+\mu^-$ background: removing the visible momentum cut, the acolinearity and acoplanarity cuts are complemented by the cuts in the total electromagnetic energy of the event or by the cut requiring that at least one of the two tracks is not matched by hits in muon chambers.

A study of the major background sources contributing to the measured X_π-spectrum must be made and only after background subtraction is made, bin per bin, the slope of the corrected spectrum can be fitted to extract the polarization.
Using simulated events, the estimated contamination from the other final states from τ decays is shown in table15.2.

Background type	Contamination (%)
$\tau \rightarrow \pi\pi^0\nu$	10.
$\tau \rightarrow \pi\pi^0\pi^0\nu$	7.1
$\tau \rightarrow \mu\bar{\nu}_\mu\nu_\tau$	4.3
$Z^0 \rightarrow \mu^+\mu^-$	1.0

Table 15.2: Main sources of background and corresponding contamination (estimated from simulated events) in the $\tau \rightarrow \pi$ event sample.

In figure 15.3, using simulated $\tau^+\tau^-$ events, the dN/dX spectrum (before background subtraction) for the tracks passing the pion cuts is shown. The distortion of the linear spectrum from $\tau \rightarrow \pi\nu_\tau$ due to the contamination of each background channel is also shown.

15.3.3   Determination of A^τ_{POL}

The corrected dN/dX spectrum, shown in figure 15.4, is obtained from the raw dN/dX spectrum (containing all the events passing the selection cuts) after background subtraction and correction for the acceptance are performed at each bin. The corrected dN/dX spectrum is then fitted using as fitting function the CALASY parametrization for dN/dX_π[17]. The extracted value for the tau polarization is

$$A^\tau_{POL} = -0.222 \pm 0.186(stat)$$
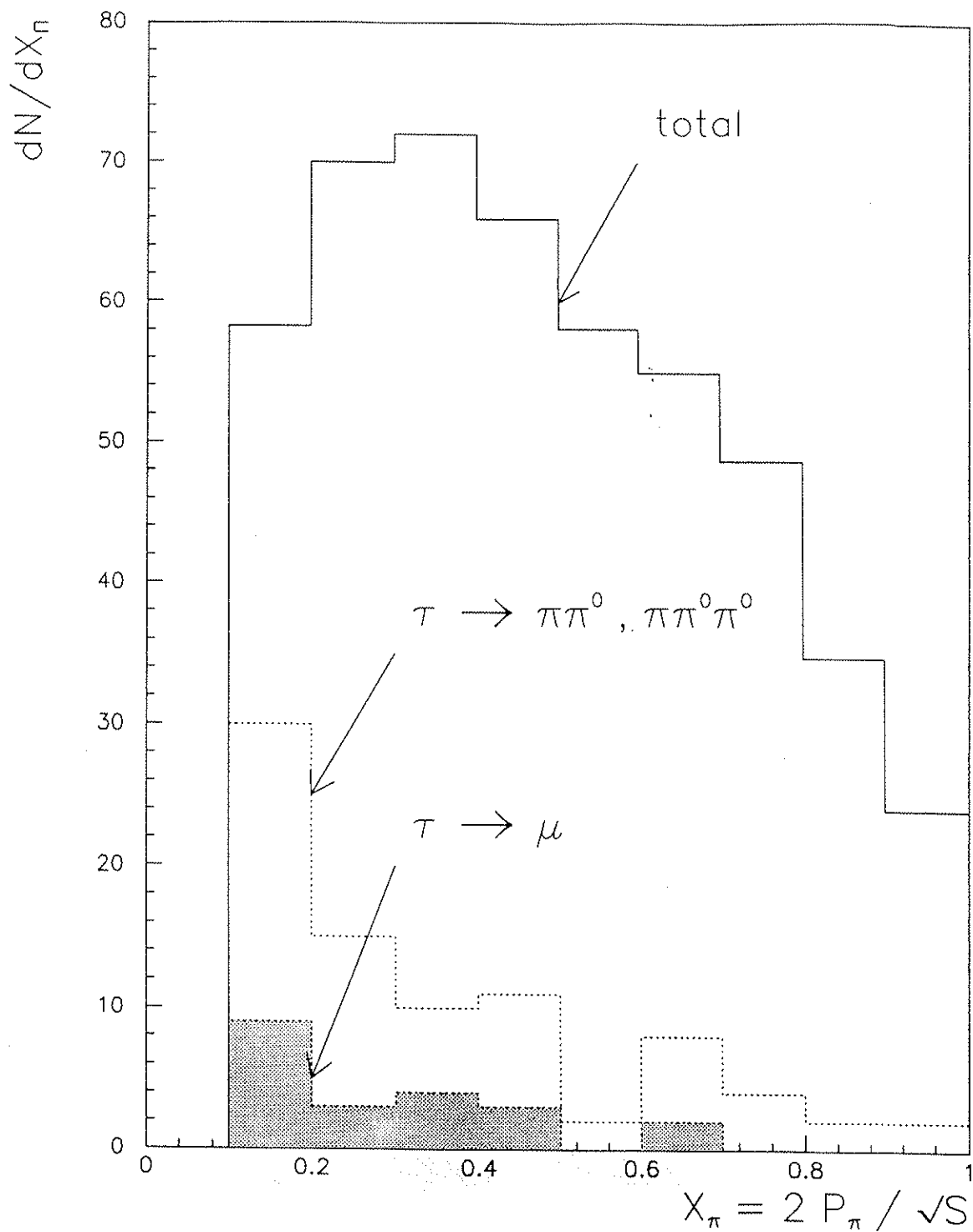
Figure 15.3: dN/dX spectrum of all the particles surviving the selection cuts for pions from $\tau \to \pi\nu_\tau$ decays in simulated $\tau^+\tau^-$ events. The several components of the spectrum due to the different background channels are shown.
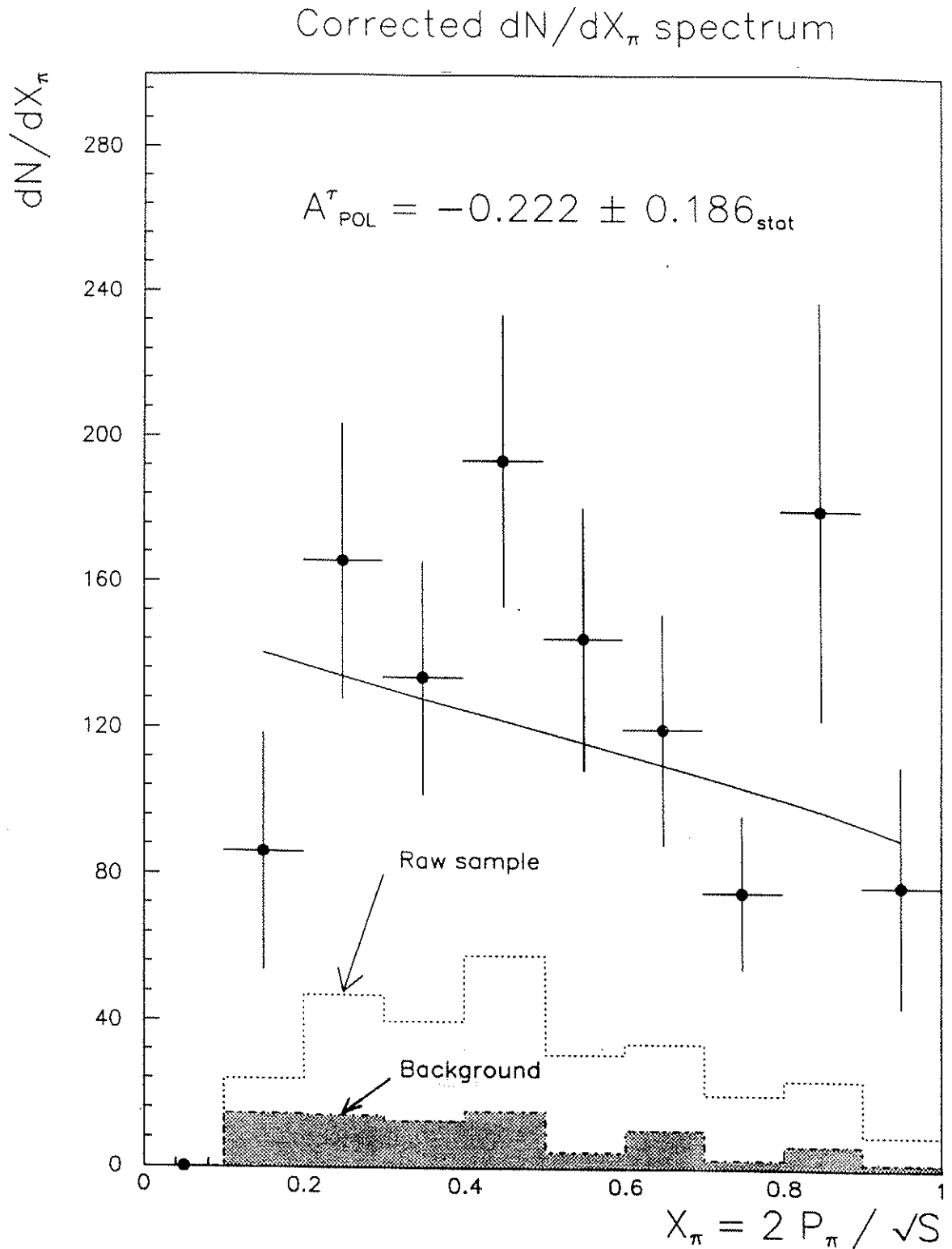
Figure 15.4: dN/dX spectrum after background subtraction and acceptance correction at each bin, of the identified pions from $\tau \rightarrow \pi\nu_\tau$ decays. Superimposed is the raw spectrum of the selected pion candidates and the dN/dX spectrum of the background estimated from simulated events.

15.4 Measurement of the $\tau \to \pi X \nu_\tau$ final state

As seen in the last section, the main backgrounds to the measurement of the exclusive pions from the decay $\tau \to \pi \nu_\tau$ come from the competing decay modes $\tau \to \pi \pi^0$ and $\tau \to \pi \pi^0 \pi^0$. The branching ratio for the decays $\tau \to hadron + \geq 0$ *neutrals* is $(50.3 \pm 0.6)\%$ and the final state hadron is predominantly a pion. Compared to the exclusive measurement, the inclusive measurement of the single charged pion final states has the following advantages:

• It is free of the uncertainties associated to the cuts used to reduce the contamination from the other tau decay modes into pions. Then, is less sensitive to the systematics of the selection criteria, has higher efficiency and smaller biases.

• The size of the event sample after the selection cuts is considerably bigger than in the case of exclusive measurement (smaller statistical errors).

15.4.1 Selection of inclusive pions

In a similar way as was done for the measurement of the exclusive pions, the selection criteria for $\tau^+ \tau^-$ events were slightly modified in what concerns the values of the cuts in the visible momentum and electromagnetic energy of the event. These cuts are set to:

• $P_{vis} < 70$ GeV (instead of 60 GeV).

• $E_{EM}^{total} < 65$ GeV (instead of 30 GeV per track or per hemisphere).

For those events surviving the $\tau^+ \tau^-$ selection cuts, the following set of cuts is applied to the isolated track of the events falling in the category 1-N and to both tracks of the events belonging to the category 1-1:

• $E_{HC} > 10$ GeV

$$OR \qquad (15.9)$$

• $P_{track} > 5$ GeV

• $E_{HC} > 5$ GeV

• No hits matching the track extrapolated to the muon chambers.

• $(E_4 + E_3)/(E_2 + E_1) < 0.5$, ratio between the energy in the 4 layers of the hadronic calorimeter.

$$OR \qquad (15.10)$$

- $P_{track} > 2$ GeV

- $E_{HC} > 1$ GeV

- $E_{em} > 1$ GeV

- $E_{em}/P_{track} < 0.7$ *or* $E_{em}/P_{track} > 1.3$

These cuts require in the interval $50° < \theta < 130°$:

• One track with associated energy deposition in the hadronic calorimeter bigger than 10 GeV (muon signal is contained below 7.5 GeV).

• One track with momentum and associated hadronic energy bigger than 5 GeV. Muons are vetoed by requiring in addition that the track extrapolated to the muon chambers is not matched by hits and that the pattern of energy deposition in the 4 layers of the hadron calorimeter is such that the sum of the energy in the first and second layer is more than twice the sum of the energy in the third and fourth layers.

• One track with momentum bigger than 2 GeV and associated hadronic energy bigger than 1 GeV. Muons are vetoed by requiring more than 1 Gev associated to the track in the electromagnetic calorimeter (typical muon signal is 200 MeV) and electrons with showers leaking the electromagnetic calorimeter are vetoed by requiring that the E_{em}/P_{track} ratio falls outside the interval 0.7–1.3.

15.4.2   Background to the sample of $\tau \to \pi X$ events

The main sources of background to the selected sample of inclusive pions come from the leptonic tau decay modes:

$\tau \to e\bar{\nu}_e\nu_\tau$

Electrons with showers leaking into the hadron calorimeter can fake a $\pi\pi^0$ final state in case of wrong energy reconstruction (due to the holes in the electromagnetic calorimeter) or wrong momentum reconstruction (due to the dead zones of TPC or due to bremsstrahlung) distorting the measured E_{em}/P_{track} ratio.

$\tau \to \mu\bar{\nu}_\mu\nu_\tau$

Muon tracks not matched by hits in the muon chambers (due to inefficiencies or dead zones) can fake a pion signal in the hadron calorimeter in the low-X region of the spectrum.

In table 15.3 the percentage of contamination in the selected event sample is displayed for each background channel. In figure 15.5, the correction factor per bin due to the background is shown, estimated from simulated events. Finally, in figure 15.6, the corrected dN/dX distribution is shown, after background subtraction and correction for the acceptance at each bin.
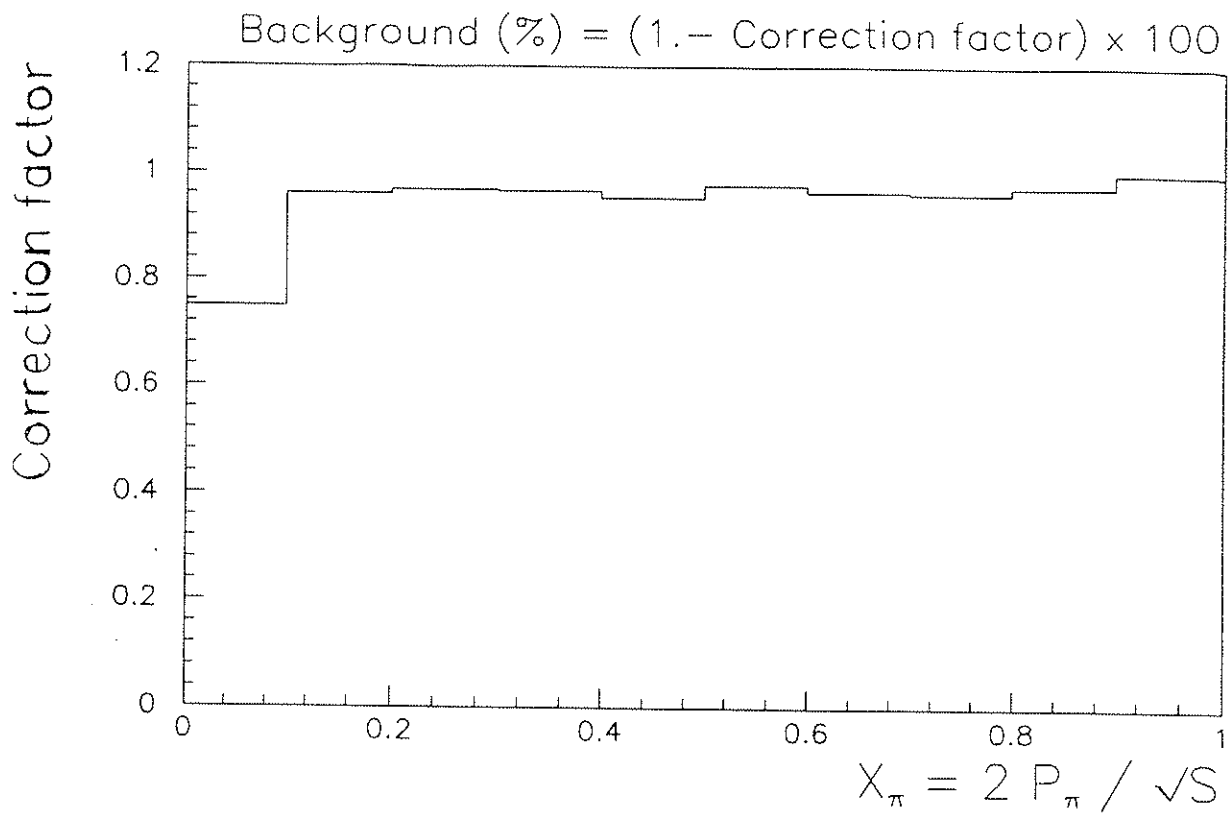
Figure 15.5: Correction factor at each bin, due to the background in the sample of inclusive pions.

Background type	Contamination (%)
$\tau \to e \bar{\nu}_e \nu_\tau$	1.3
$\tau \to \mu \bar{\nu}_\mu \nu_\tau$	2.6

Table 15.3: Main sources of background and corresponding contamination (estimated from simulated events) in the $\tau \to \pi X$ event sample.
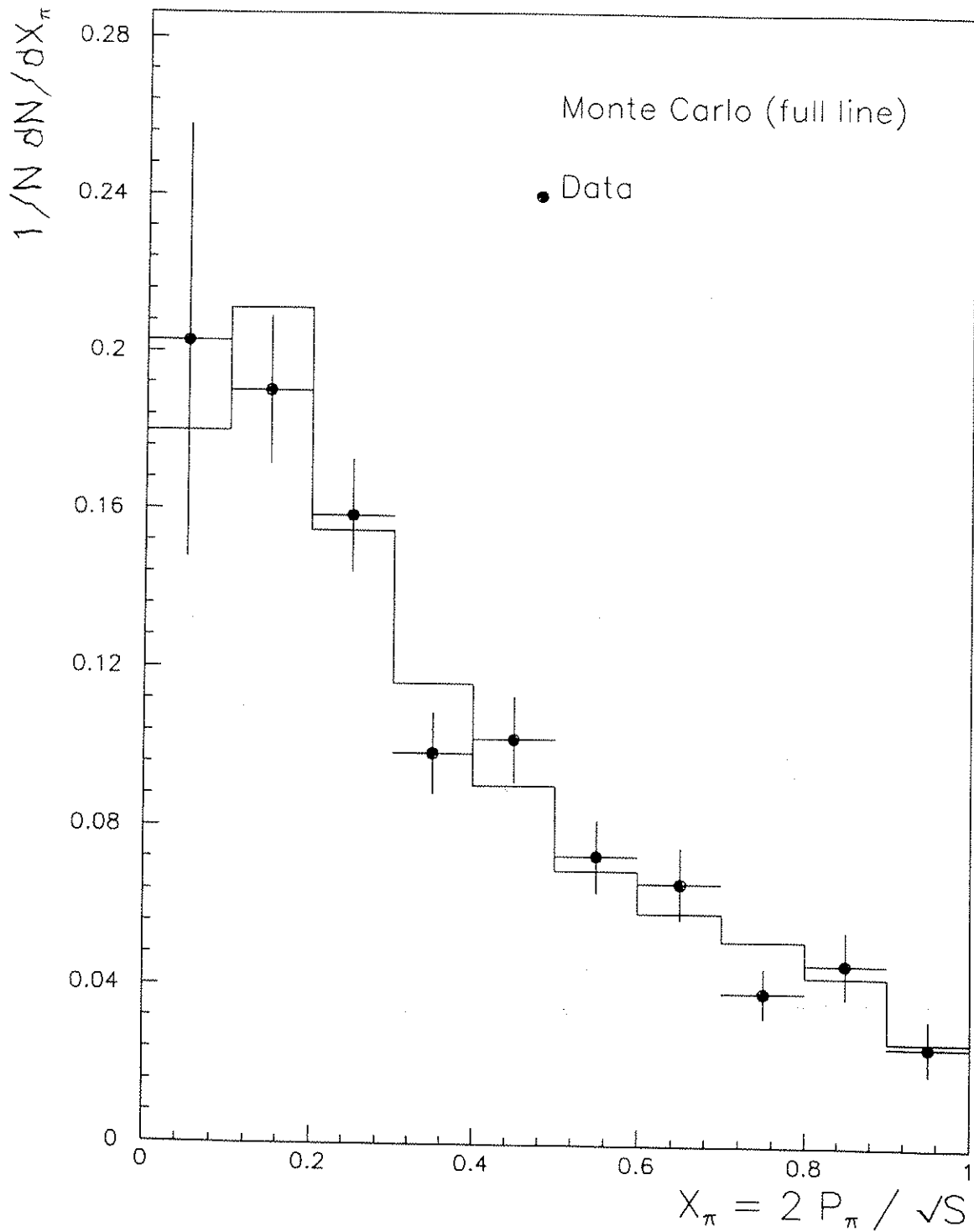
Figure 15.6: Normalized dN/dX spectrum after background subtraction and acceptance correction at each bin, of the inclusive pions from $\tau \rightarrow \pi X$ decays. Superimposed is the equivalent spectrum as obtained from KORALZ generated events.

15.4.3 Determination of A^τ_{POL} and $\sin^2 \theta_w$

Using $\tau^+ \tau^-$ events generated with KORALZ, the dN/dX spectrum of the inclusive pions (mainly from the decays $\tau \to \pi \nu_\tau$, $\pi \pi^0 \nu_\tau$, $\pi \pi^0 \pi^0 \nu_\tau$) is obtained, for two different values of $\sin^2 \theta_w$ (0.22 and 0.24) as shown in figure 15.7. The following ratio is taken for both spectra:

$$R = \frac{N_\pi(0. < X_\pi < 0.5)}{N_\pi(0.5 < X_\pi < 1.)} \tag{15.11}$$

In Table 15.4, the obtained values of R for the two values of $\sin^2 \theta_w$ are shown.

$\sin^2 \theta_w$	R (Monte Carlo)
0.22	3.1354
0.24	2.9311

Table 15.4: Ratio between number of inclusive pions with $0. < X_\pi < 0.5$ and number of pions with $0.5 < X_\pi < 1.$, from KORALZ generated events.

From the data, the number of events in each X interval before the acceptance correction (after background subtraction) is

$$N_\pi(0. < X_\pi < 0.5) = 664 \tag{15.12}$$
$$N_\pi(0.5 < X_\pi < 1.) = 310 \tag{15.13}$$
$$\tag{15.14}$$

which leads to a relative statistical error in the determination of R of about 6.9%. After background subtraction and correction for the acceptance at each bin, we get from the spectrum plotted in figure 15.6:

$$R_{data} = 3.0273 \pm 0.2082(stat) \tag{15.15}$$

Using the values of R extracted from the Monte Carlo generated events at the two values of $\sin^2 \theta_w$ we write, to a good approximation, the statistical error in $\sin^2 \theta_2$ as:

$$(\Delta \sin^2 \theta_w)^{data}_{stat} \simeq \left(\frac{\delta \sin^2 \theta_w}{\delta R} \right)_{MC} (\Delta R)^{data}_{stat} = 0.0199 \tag{15.16}$$

with

$$\delta \sin^2 \theta_w = 0.02 \tag{15.17}$$

$$\delta R = R_{MC}(\sin^2 \theta_w = 0.24) - R_{MC}(\sin^2 \theta_w = 0.22) = -0.2043 \tag{15.18}$$

Using the determined value of R_{data}, the corresponding value of $\sin^2 \theta_w$ is obtained by interpolation, using the values from Table 15.4. We get:

$$\overline{\sin^2 \theta_w} = 0.2308 \pm 0.0199(stat)$$

or, equivalently,

$$A_{POL}^\tau = -0.154 \pm 0.159(stat)$$

The statistical error is the most important contribution to the uncertainties affecting this measurement.
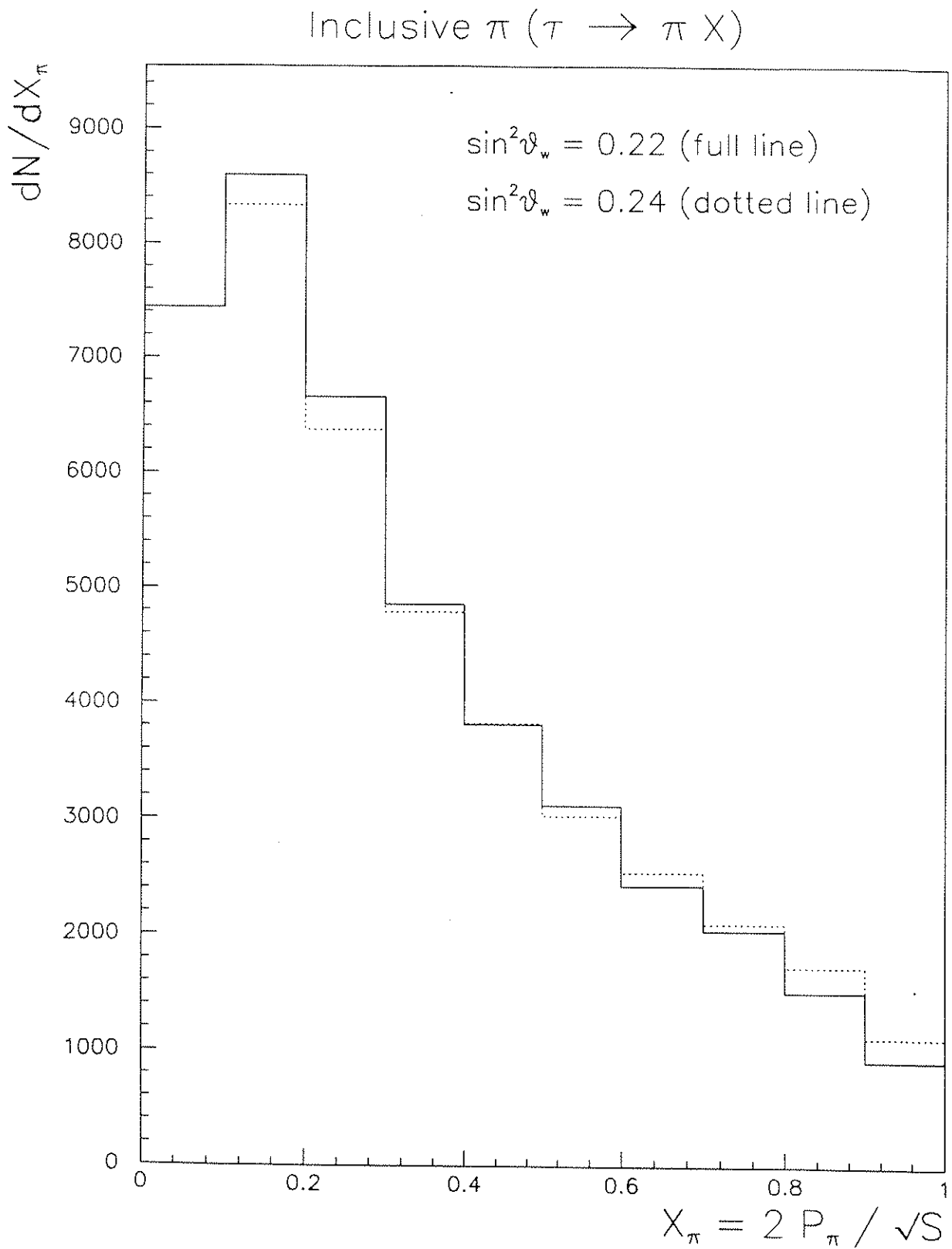
Figure 15.7: KORALZ generated dN/dX spectrum of the pions from $\tau \rightarrow \pi X \nu_\tau$ (inclusive) decays, for $\sin^2 \theta_w = 0.22$ (full line) and $\sin^2 \theta_w = 0.24$ (dotted line).

Chapter 16

Parameters of the Standard Model

In this chapter, the physical properties of the measured $\tau^+\tau^-$ pairs produced in Z^0 decays are analysed in the framework of the Standard Model, in order to extract some of its parameters and to check its consistency and agreement with the data.

The measurement of $\Gamma_{\tau\tau}/\Gamma_h$, combined with the DELPHI determination of M_Z and σ_h^{pole}, is used to get an estimation of the number of neutrino species. This determination must be considered simply as a check to the consistency of the $\tau^+\tau^-$ data with the measurement of N_ν obtained from the combined fit, using the complete statistics on leptonic events.

It is followed by a "model independent" determination of the vector and axial couplings of the Z^0 to lepton pairs. The measurement uses the $\tau^+\tau^-$ data but assumes lepton universality. The same data is used to get a measurement of the Standard Model parameters ρ and $\sin^2 \theta_w$.

An independent measurement of $\sin^2 \theta_w$, done in the framework of the minimal Standard Model, tests the consistency of the model within the present experimental accuracy. Further consistency checks are performed comparing the theoretical predictions with the measurements of $\Gamma_{\tau\tau}$, $\Gamma_h/\Gamma_{\tau\tau}$ and A_{FB}^τ.

16.1 Number of neutrino species

After the measurement of the total width (Γ_Z), the partial decay width into hadrons (Γ_h), and the leptonic partial widths (respectively $\Gamma_{ee}, \Gamma_{\mu\mu}, \Gamma_{\tau\tau}$), the total invisible width (Γ_{inv}) can be obtained from

$$\Gamma_{inv} = \Gamma_Z - \Gamma_h - \Gamma_{ee} - \Gamma_{\mu\mu} - \Gamma_{\tau\tau} \tag{16.1}$$

In this way, the total error on the determination of the invisible width is (neglecting correlations) the sum of the errors in each individual width measurement. Another way to determine the partial width with smaller errors is to combine the measured widths of each leptonic channel, to obtain the leptonic width (Γ_{ll}). Assuming universality (the validity of this assumption is supported by the results of the individual partial widhts measurements presented in Chapter 13), the following expression holds

$$\frac{\Gamma_{inv}}{\Gamma_{ll}} = \frac{\Gamma_Z}{\Gamma_{ll}} - \frac{\Gamma_h}{\Gamma_{ll}} - 3 \tag{16.2}$$

In the framework of the Standard Model, the number of neutrino species is

$$N_\nu = \frac{\Gamma_{inv}}{\Gamma_{\nu\nu}} \tag{16.3}$$

where $\Gamma_{\nu\nu}$ is the partial width of the Z^0 into each neutrino family. We get

$$N_\nu = \frac{\Gamma_{ll}}{\Gamma_{\nu\nu}} \left[\frac{\Gamma_Z}{\Gamma_{ll}} - \frac{\Gamma_h}{\Gamma_{ll}} - 3 \right] \tag{16.4}$$

and using the expression 14.5 for the pole cross-section of hadronic events, we have

$$N_\nu = \frac{\Gamma_{ll}}{\Gamma_{\nu\nu}} \left[\sqrt{\frac{12\pi}{M_Z^2} \frac{1}{\sigma_h^{pole}} \frac{\Gamma_h}{\Gamma_{ll}}} - \frac{\Gamma_h}{\Gamma_{ll}} - 3 \right] \tag{16.5}$$

Using the Standard Model prediction for $\Gamma_{ll}/\Gamma_{\nu\nu} = 0.5010 \pm 0.0005$, the M_Z and σ_h^{pole} measurements of Chapter 13 and our measurement of $\Gamma_h/\Gamma_{\tau\tau}$ one finds [1]

$$\boxed{N_\nu = 2.80 \pm 0.38(stat) \pm 0.33(syst)}$$

---

[1]This measurement does not intend to be at the same precision level as the similar measurement with the full leptonic statistics and combined leptonic partial widths, as published by the DELPHI Collaboration

16.2 Determination of the vector and axial couplings

16.2.1 $(\Gamma_{\tau\tau}\ ,\ A_{FB}^{\tau}) \to (v_{\tau}\ ,\ a_{\tau})$

Defining θ as the angle between the outgoing fermion and the incoming e^-, the angular differential cross-section for the process $e^+e^- \to f\bar{f}$ can be written in the Born approximation as

$$\frac{d\sigma}{d\Omega} = \frac{\pi\alpha^2}{2s} R_{ff} \left[(1 + \cos^2\theta) + \frac{8}{3} A_{ff} \cos\theta \right] \tag{16.6}$$

with

$$R_{ff} = 1 + 2v_e v_f \, \mathcal{R}(\chi) + (v_e^2 + a_e^2)(v_f^2 + a_f^2)|\chi|^2 \tag{16.7}$$

$$A_{ff} = \frac{\frac{3}{2}a_e a_f \, \mathcal{R}(\chi) + 3v_e v_f a_e a_f \, |\chi|^2}{R_{ff}} \tag{16.8}$$

The axial and vector couplings of the electron (e) and final state fermion (f) to the Z^0 are respectively a_e, a_f, v_e, v_f being χ the resonance amplitude, s the square of the centre of mass energy and α the QED coupling constant.
An equivalent way of writing the differential cross-section exhibits clearly the factorization of the different contributions: the pure QED contribution related only to the symmetric part of the differential cross-section (through coefficient $C_{\gamma\gamma}$), while the contributions from the pure Z^0 annihilation or from the γZ interference result in both symmetric and anti-symmetric terms in the differential cross-section (respectively through coefficients $C_{ZZ}^{(1)}, C_{ZZ}^{(2)}, C_{\gamma Z}^{(1)}, C_{\gamma Z}^{(2)}$):

$$\frac{2s}{\pi\alpha^2} \frac{d\sigma}{d\cos\theta} = C_{\gamma\gamma} (1 + \cos^2\theta) + \tag{16.9}$$

$$\mathcal{R}(\chi) \left[C_{\gamma Z}^{(1)} (1 + \cos^2\theta) + C_{\gamma Z}^{(2)} \cos\theta \right] + \tag{16.10}$$

$$|\chi|^2 \left[C_{ZZ}^{(1)} (1 + \cos^2\theta) + C_{ZZ}^{(2)} \cos\theta \right] \tag{16.11}$$

with the coefficients $C_{\gamma\gamma}, C_{\gamma Z}^{(1)}, C_{\gamma Z}^{(2)}, C_{ZZ}^{(1)}, C_{ZZ}^{(2)}$ easily determined by comparison with equation 16.6. Close to the Z^0 peak the cross-section is dominated by the term in equation 16.11. The leptonic partial width Γ_{ll}, derived from the peak cross-section is related to $C_{ZZ}^{(1)}$ by:

$$C_{ZZ}^{(1)} = \left(\frac{24\pi\sqrt{2}}{G_\mu M_Z^3}\,\Gamma_{ll}\right)^2 \tag{16.12}$$

and the forward-backward asymmetry at the peak is determined by the ratio $C_{ZZ}^{(2)}/C_{ZZ}^{(1)}$. Thus, the two observables Γ_{ll} and A_{FB}^l are related to the vector and axial couplings through the expressions:

$$\Gamma_{ll} \sim (v_l^2 + a_l^2)^2 \tag{16.13}$$

$$A_{FB}^l \sim \frac{v_e a_e v_l a_l}{(v_e^2 + a_e^2)(v_l^2 + a_l^2)} = \frac{v_l^2 a_l^2}{(v_l^2 + a_l^2)^2} \tag{16.14}$$

assuming leptonic universality in the last expression.

When the electroweak radiative corrections are considered, the previous relations remain valid provided that the bare vector and axial couplings are replaced by effective couplings. In fact, as shown for instance in refs. [88],[91],[92], the effects of the weak corrections (propagator corrections, vertex corrections, box corrections) are taken into account in a good approximation replacing in the "tree-level" relations the vector (v_f) and axial (a_f) couplings by their values "dressed" by the radiative corrections, respectively $\bar{v}_f$ and $\bar{a}_f$, and taking the resonance factor χ with an s-dependent width as discussed in Chapter 4. The photonic effects are correctly taken into account if in addition to the corrections to the peak cross-section already discussed, the QED running coupling constant is defined as $\alpha(M_Z) = \alpha(0)/(1 - \Delta\alpha)$. This is the so-called "improved Born approximation". The effective couplings are calculated in the framework of a particular renormalization scheme and are function of the set of physical input parameters used. Normally, the chosen parameters are experimentally measured quantities, namely the QED coupling constant α, the Fermi constant G_μ and the Z^0 mass M_Z. Moreover, they are also function of yet unknown mass parameters, the top quark mass m_t and the Higgs mass M_H.

16.2.1.1   Fit of $(\overline{a}_\tau, \overline{v}_\tau)$

In order to get the effective vector and axial couplings of $\tau^+\tau^-$ to the Z^0, a simultaneous fit of the measured total cross-section and asymmetry values at each energy point was performed. The theoretical values are given by the program ZFITTER[81], which implements the ideas introduced before.

It should be noted that the determination of $\overline{v}_\tau$ and $\overline{a}_\tau$ is independent of the Standard Model, in particular of the structure of the Higgs sector. This is true in the limit of the improved Born approximation, which is precise enough for the present level of accuracy.

The value of $\overline{a}_\tau$ is determined mainly by the cross-section measurements while the value for $\overline{v}_\tau$ is mainly determined by the asymmetry measurements. Using these considerations, the systematic errors are determined as:

$$\Gamma_{\tau\tau} \sim \overline{a}_\tau^2 \longrightarrow \left(\frac{\Delta \overline{a}_\tau}{\overline{a}_\tau}\right)_{syst} \simeq \frac{1}{2}\left(\frac{\Delta\Gamma_{\tau\tau}}{\Gamma_{\tau\tau}}\right)_{syst} \tag{16.15}$$

$$A_{FB}^\tau \sim \overline{v}_\tau^2\,\overline{a}_\tau^2 \longrightarrow \left(\frac{\Delta \overline{v}_\tau}{\overline{v}_\tau}\right)_{syst} \simeq \left(\frac{\Delta \overline{a}_\tau}{\overline{a}_\tau}\right)_{syst} \oplus \frac{1}{2}\left(\frac{\Delta A_{FB}}{A_{FB}}\right)_{syst} \tag{16.16}$$

It is not possible to determine the sign of $\overline{v}_\tau$ and $\overline{a}_\tau$ using the cross-section and asymmetry data alone. Using as input to the fit the values of the Z^0 mass and width measured in DELPHI (see Chapter 13), we get for the value of the effective vector and axial couplings:

$$\overline{v}_\tau = -0.028\ ^{+\ 0.126}_{-\ 0.070}(stat)$$

$$\overline{a}_\tau = -1.0073\ ^{+0.0070}_{-0.0057}(stat)\ \pm\ 0.0066(syst)$$

$$\chi^2/d.o.f. = 15.5/(14-2)$$

The systematic error in the determination of $\overline{v}_\tau$, much smaller than the statistical error, has been neglected. The ratio $\overline{v}_\tau/\overline{a}_\tau$ results

$$\overline{v}_\tau/\overline{a}_\tau = 0.028\ ^{+\ 0.126}_{-\ 0.070}(stat)\ \pm\ 0.007(syst)$$

16.2.2 $A_{POL}^\tau \rightarrow v_\tau/a_\tau$

The measurement of the τ polarization allows a unique determination of the sign of the ratio v_τ/a_τ between the vector and axial couplings of the tau. In previous determinations of v_τ and a_τ using the partial width and forward-backward asymmetry measurements, the sign of the couplings is taken to be negative for the sake of consistency with previous results from neutrino experiments.

As seen in Chapter 3, the τ polarization is expressed in terms of the vector (v_τ) and axial (a_τ) couplings of the τ by the following relation derived in Chapter 3:

$$A_{POL}^\tau = -\frac{2v_\tau a_\tau}{v_\tau^2 + a_\tau^2} = -\frac{2\frac{v_\tau}{a_\tau}}{1 + \frac{v_\tau^2}{a_\tau^2}} \qquad (16.17)$$

Averaging the 2 values for the polarization extracted from the fit to the dN/dX_μ and inclusive dN/dX_π spectra, we get

$$\boxed{(A_{POL}^\tau)_{average} = -0.159 \pm 0.116 \longrightarrow \bar{v}_\tau/\bar{a}_\tau = 0.080 \pm 0.058}$$

16.2.3 Combined Determination of $\bar{a}_\tau$ and $\bar{v}_\tau$

The one (68%) and two (95%) standard deviation confidence level contours in the plane $\bar{v}_\tau$ vs $\bar{a}_\tau$, obtained from the measurement of the $\tau^- \tau^-$ cross-section and asymmetry values, are shown in figure 16.1. Superimposed are the 2 lines defining the one standard deviation confidence level band obtained from the measurement of the τ polarization. The three measurements are combined performing a fit to $\bar{v}_\tau$ and $\bar{a}_\tau$ imposing the constrain on the ratio between the couplings, obtained by the measurement of the τ polarization. The result of the global fit is

$$\bar{v}_\tau = -0.070 \; {}^{+\, 0.039}_{-\, 0.033}(stat)$$

$$\bar{a}_\tau = -1.0052 \; {}^{+\, 0.0061}_{-\, 0.0059}(stat) \pm 0.0066(syst)$$

The one (68%) and two (95%) standard deviation confidence level contours in the plane $\bar{v}_\tau$ vs $\bar{a}_\tau$, obtained from the combined fit are shown in figure 16.2.

Figure 16.1: 68% and 95 % confidence level contours in the plane v_τ vs a_τ, obtained from the fit to the measured $\tau^+\tau^-$ cross-sections and asymmetries. The fitted pair of parameters is superimposed. The 68% confidence level band obtained from the measurements of the τ polarization is also shown.
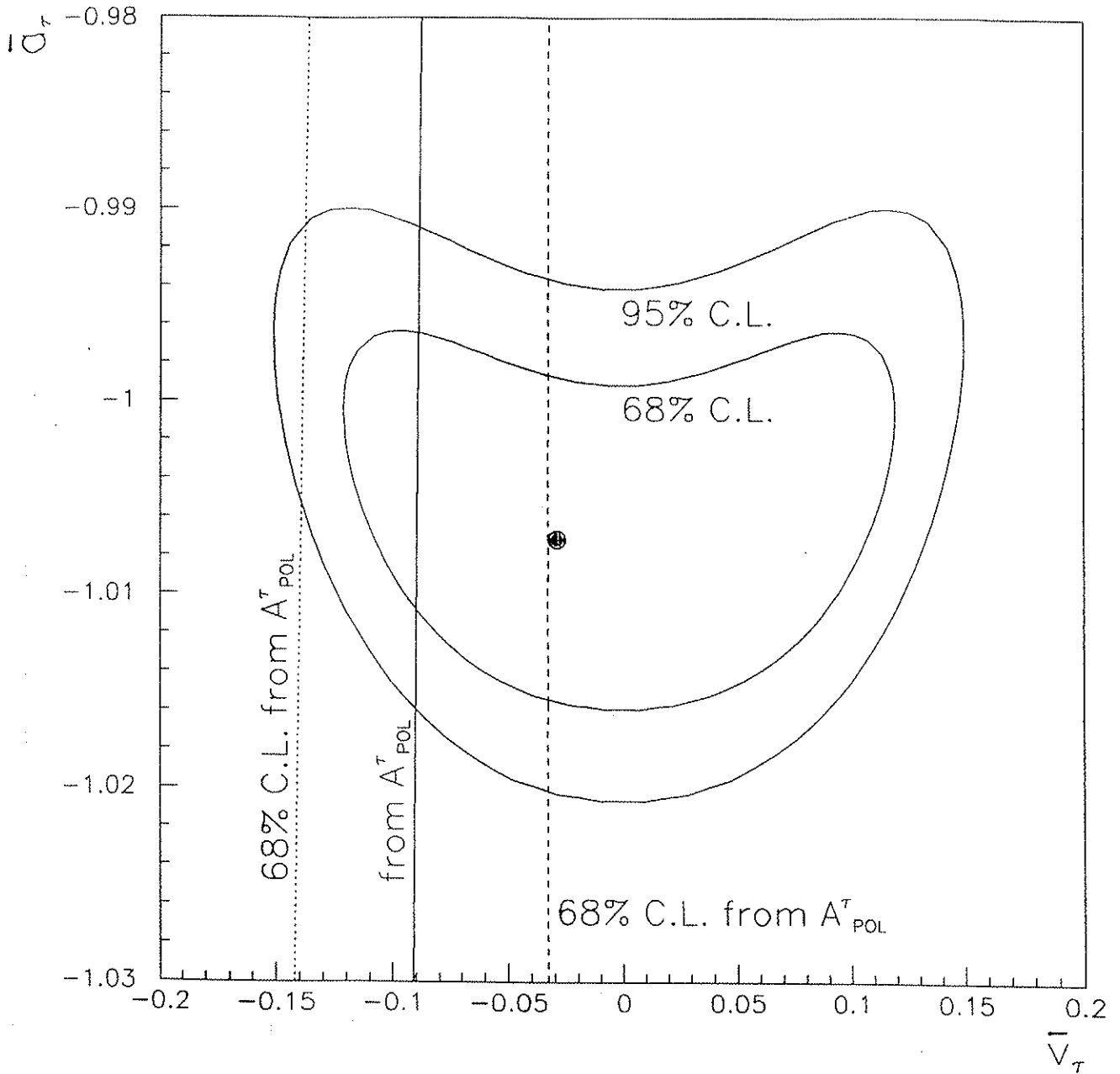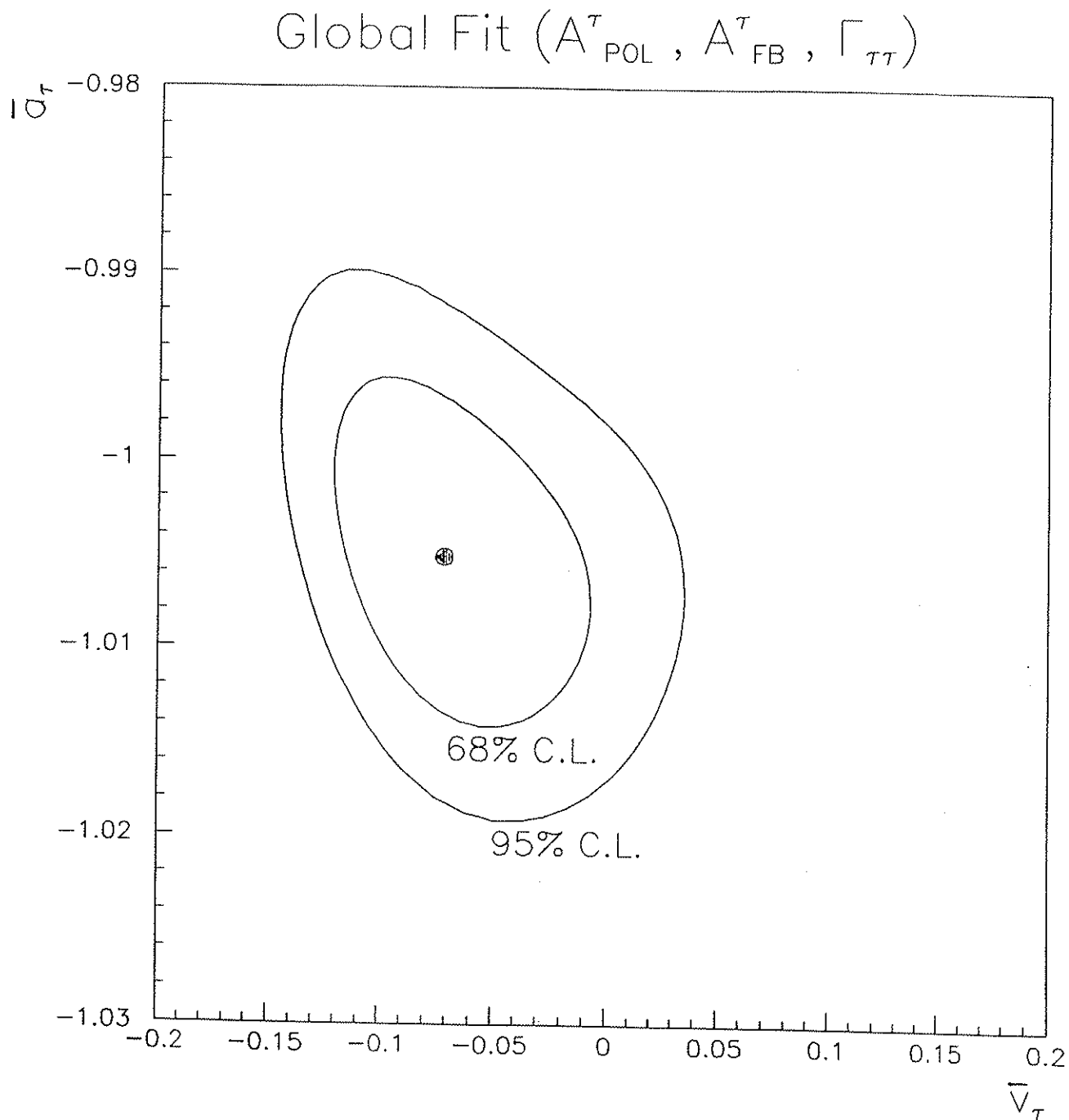
Figure 16.2: 68% and 95 % confidence level contours in the plane v_τ vs a_τ, obtained from the fit to the measured $\tau^+\tau^-$ cross-sections and asymmetries, with the constrain on the ratio v/a obtained from the measurement of the τ polarization.

16.3 Determination of $\sin^2 \theta_w$

16.3.1 $(\Gamma_{\tau\tau}, A_{FB}^\tau) \to (\rho_\tau, \overline{\sin^2 \theta_w})$

The differential cross-section in the improved Born approximation can be written in terms of the neutral current strength parameter ρ and of the effective mixing angle $\sin^2 \theta_w$. In this approximation, the effective vector and axial couplings are related to the SU(2)xU(1) quantum numbers and effective mixing angle by the tree level relations

$$\overline{v}_f = 2I_3^f - 4|Q_f|\,\overline{\sin^2 \theta_w} \tag{16.18}$$

$$\overline{a}_f = 2I_3^f \tag{16.19}$$

In particular, the leptonic partial width is given by

$$\Gamma_{ll} = \frac{G_\mu M_Z^3}{24\pi\sqrt{2}}\,\rho\,\left[1 + (1 - 4\,\overline{\sin^2 \theta_w})^2 \right] \tag{16.20}$$

and the forward backward asymmetry at the peak is

$$A_{FB}^l(s \simeq M_Z^2) = \frac{3(1 - 4\,\overline{\sin^2 \theta_w})^2}{\left[1 + (1 - 4\,\overline{\sin^2 \theta_w})^2 \right]^2} \tag{16.21}$$

In the framework of the Standard Model, ρ and $\overline{\sin^2 \theta_w}$ are computed in terms of the input parameters (α, G_μ, M_Z) and of the unknown masses of the top quark and the Higgs boson, m_t and M_H. The theoretical predictions can be approximated by the following expressions [3]:

$$\rho = \frac{1}{1 - \Delta\rho} \quad , \quad \Delta\rho \simeq \frac{3G_\mu}{8\pi^2\sqrt{2}}\,m_t^2 \tag{16.22}$$

$$\overline{\sin^2 \theta_w} = \frac{1}{2}\left(1 - \sqrt{1 - \frac{4\pi\alpha(M_Z^2)}{\sqrt{2}\,G_\mu\,\rho\,M_Z^2}} \right) \tag{16.23}$$

$$\alpha(M_Z^2) = \frac{\alpha(0)}{1 - \Delta\alpha} \quad , \quad \Delta\alpha \simeq 0.06 \tag{16.24}$$

---

[3] In writing $\Delta\rho$ Higgs mass contribution and logarithmic terms in m_t are neglected

16.3.1.1   Fit of $(\rho_\tau, \overline{\sin^2 \theta_w})$

The value of ρ is determined mainly by the cross-section measurements, while $\overline{\sin^2 \theta_w}$ is mainly determined by the asymmetry measurements as can be deduced from the inspection of the expressions above. The systematic errors are evaluated as

$$A^\tau_{FB} \sim \overline{v}_\tau{}^2 \simeq \left(1 - 4\,\overline{\sin^2 \theta_w} \right)^2 \longrightarrow \left(\Delta\overline{\sin^2 \theta_w} \right)_{syst} \simeq \frac{(\Delta A_{FB})_{syst}}{24\,(1 - 4\,\overline{\sin^2 \theta_w})} \tag{16.25}$$

$$\Gamma_{\tau\tau} \sim \rho_\tau \longrightarrow \left(\frac{\Delta\rho_\tau}{\rho_\tau} \right)_{syst} \simeq \left(\frac{\Delta\Gamma_{\tau\tau}}{\Gamma_{\tau\tau}} \right)_{syst} \tag{16.26}$$

The values of ρ and $\overline{\sin^2 \theta_w}$ obtained from the fit of the $\tau^+\tau^-$ data are:

$$\rho_\tau = 1.0146 \; {}^{+\,0.0140}_{-\,0.0116}(stat) \; \pm \; 0.0132(syst)$$

$$\overline{\sin^2 \theta_w} = 0.2430 \; {}^{+\,0.0315}_{-\,0.0175}(stat) \; \pm \; 0.0002(syst))$$

$$\chi^2/d.o.f. = 15.3/(14 - 2)$$

In figure 16.3 we show the 68% (1 standard deviation) and 99% (2 standard deviations) confidence level contours in the ρ vs $\overline{v}_\tau = 1 - 4\sin^2 \theta_w$ plane. Due to the fact that $\overline{v}_\tau$ enters quadratically in the above expressions, the confidence level contours are symmetric about the axis $\overline{v}_\tau = 0$ $\left(\sin^2 \theta_w = 0.25 \right)$. A value $\overline{v}_\tau < 0$ $\left(\sin^2 \theta_w < 0.25 \right)$ has been chosen by comparison with the neutrino scattering data.
The predictions of the SM are compared with the data in figure 16.3. They are compatible provided $m_t < 250$ GeV, irrespective of the Higgs mass.

16.3.2 $\Gamma_{\tau\tau} \longrightarrow \overline{\sin^2 \theta_w}$

An independent way to extract the value of $\overline{\sin^2 \theta_w}$ is based on the $\tau^+\tau^-$ partial width, $\Gamma_{\tau\tau}$. Notice that the determination obtained in the last section was mainly based on the measured asymmetry A^τ_{FB}. We start from the expression already introduced for the leptonic partial width:

$$\Gamma_{ll} = \frac{G_\mu\, M_Z^3}{24\,\pi\,\sqrt{2}}\, \rho \left[1 + (1 - 4\,\overline{\sin^2 \theta_w})^2 \right] \tag{16.27}$$
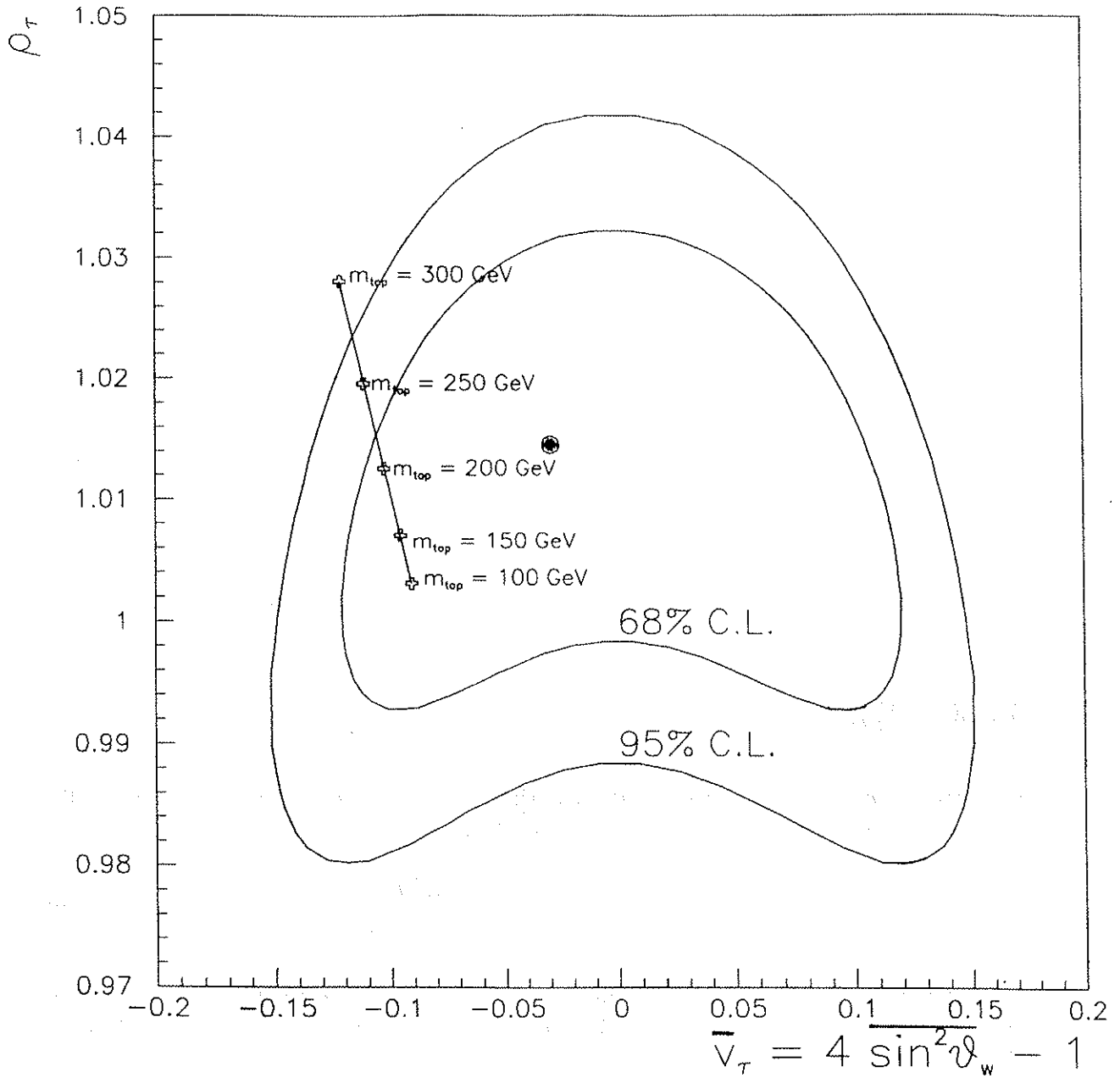
Figure 16.3: 68% and 99% confidence level contours for ρ_τ and $\bar{v}_\tau$. The fitted pair of parameters is superimposed and the allowed excursion, parametrized as a function of the top quark mass is shown.

to which we apply the approximated SM expression relating the Z^0 mass and the effective electroweak mixing angle:

$$M_Z^2 \; = \; \frac{\pi \; \alpha(M_Z^2)}{\sqrt{2} \; G_\mu \; \rho \; \overline{\sin^2 \theta_w} \; (1 - \overline{\sin^2 \theta_w})} \tag{16.28}$$

Equation 16.27 can then be rewritten as

$$\Gamma_{ll} \; = \; \frac{\alpha(M_Z^2) \; M_Z \; (1 + (1 - 4 \; |Q_l| \; \overline{\sin^2 \theta_w} \;)^2 \;)}{48 \; \overline{\sin^2 \theta_w} \; (1 - \overline{\sin^2 \theta_w} \;)} \tag{16.29}$$

Figure 16.4 shows $\Gamma_{\tau\tau}$ vs $\sin^2 \theta_w$, according to the last equation. From the allowed excursion of $\Gamma_{\tau\tau}$ within the $\pm 1\sigma$ bands we get

$$\boxed{\overline{\sin^2 \theta_w} \; = \; 0.2303^{+0.0047}_{-0.0046}}$$

This value is compatible with the determination from the previous section.

16.3.3 $A_{POL}^\tau \to \overline{\sin^2 \theta_w}$

The ratio v_τ/a_τ is related to $\sin^2 \theta_w$ via the relation $\bar{v}_\tau/\bar{a}_\tau = 1 - 4 \; \overline{\sin^2 \theta_w}$. The polarization measurement allows a determination of the weak mixing angle via

$$A_{POL}^\tau \; = \; -2 \; \frac{1 - 4 \; \overline{\sin^2 \theta_w}}{1 + (1 - 4 \; \overline{\sin^2 \theta_w} \;)^2} \tag{16.30}$$

The uncertainty in the determination of $\sin^2 \theta_w$ is in good approximation related to the error in the determination of A_{POL}^τ by the expression $\Delta \sin^2 \theta_w \simeq \Delta A_{POL}^\tau/8$. Taking the averaged value of A_{POL}^τ, we finally get

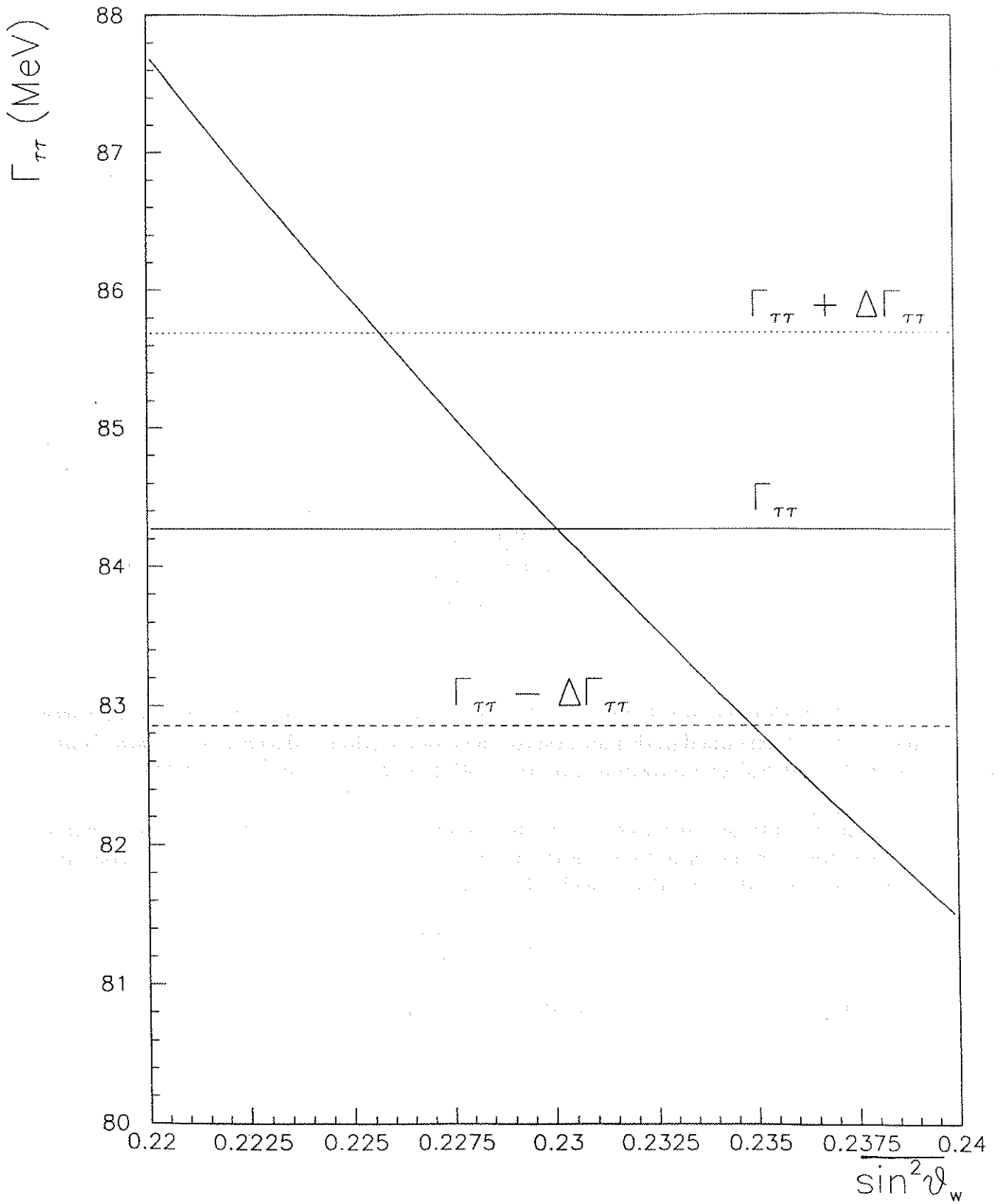$$\boxed{\overline{\sin^2 \theta_w} \; = \; 0.2301 \pm 0.0145}$$

Figure 16.4: Γ_{ll} vs $\overline{\sin^2 \theta_w}$. Superimposed is the measured value of the partial width, $\Gamma_{\tau\tau} = 84.27 \pm 0.90(stat) \pm 1.10(syst)$.

16.4   Consistency of the Standard Model

The quantities measured so far with the $\tau^+\tau^-$ data are in good agreement with the Standard Model predictions assuming three families of leptons and quarks. A comparison of the most relevant measurements and the theoretical predictions is given in table 16.1.

Observable	Experimental Measurement	SM prediction
$\Gamma_{\tau\tau}/\Gamma_h(\%)$	4.88 ± 0.19	4.80
$\Gamma_{\tau\tau}(MeV)$	84.27 ± 1.42	83.9
$A^\tau_{FB}(\%)$	1.52 ± 2.46	0.13
A^τ_{POL}	-0.159 ± 0.116	-0.16
$\bar{v}_\tau$	$-0.070\ {}^{+\ 0.039}_{-\ 0.033}$	-0.08
$\bar{a}_\tau$	$-1.0052\ {}^{+\ 0.0090}_{-\ 0.0088}$	1
N_ν	2.80 ± 0.50	3

Table 16.1: Comparison between SM predictions and experimental values for some parameters determined in this analysis of the cross-section and asymmetry data. Input values for the SM computations are $M_Z = 91.188\ GeV$ and $\sin^2\theta_w = 0.230$

The $\overline{\sin^2\theta_w}$ obtained from equation 16.29 corresponds to the effective weak mixing angle defined as the ratio between the QED coupling constant and the weak coupling constants, both defined at the scale $Q^2 \sim M_Z^2$:

$$\overline{\sin^2\theta_w} = \frac{e^2(M_Z^2)}{g^2(M_Z^2)} \tag{16.31}$$

In the framework of the Standard Model it is given by

$$\overline{\sin^2\theta_w} = 1 - \frac{M_W^2}{\rho M_Z^2} \tag{16.32}$$

This relation can be used to obtain an estimation of the W boson mass, M_W. Using the measured values of ρ and $\sin^2\theta_w$ we get

$$M_W = (80.9 \pm 1.0)\ GeV \tag{16.33}$$

This determination is compatible with the measurement of reference [93], $M_W = (79.91 \pm 0.39)$ GeV.

Summary and Conclusions

Using a sample of 2376 $Z^0 \rightarrow \tau^+\tau^-$ events produced at seventeen centre of mass energy points across the Z^0 resonance, corresponding to an integrated luminosity of $5319.29 \; nb^{-1}$ and to an equivalent number of 125000 hadronic Z^0 decays, the following measurements were performed:

- The cross-section, $\sigma_{\tau\tau}$.

- The ratios $R_{\tau\tau}$ and $\Gamma_{\tau\tau}/\Gamma_h$.

- The partial width, $\Gamma_{\tau\tau}$.

- The branching ratio, $\Gamma_{\tau\tau}/\Gamma_Z$.

- The Forward-Backward Asymmetry, A^τ_{FB} .

- The τ Polarization, A^τ_{POL} .

Using the measurements of the cross-section, the forward-backward asymmetry and the polarization, the vector (v_τ) and axial (a_τ) couplings of the τ lepton to the Z^0 were determined at $Q^2 = M_Z^2$ and the value of the Standard Model parameter $\sin^2\theta_w$ was obtained at the same energy scale.

At the present level of accuracy and with the used sample of events, the uncertainty in the measurements of the partial width and of the cross-section for $\tau^+\tau^-$ production are already dominated by the systematic errors while the uncertainty in the measurement of the forward-backward asymmetry and the polarization are still dominated by the statistical errors. The accuracy in the determination of a_τ is mainly dictated by the systematic error attributed to the measurement of the partial width while the accuracy in the determination of v_τ depends strongly on the statistical error in the measurement of the forward-backward asymmetry. Concerning the effective weak mixing angle, $\sin^2\theta_w$, the most precise value is derived from the measurement of the partial width and the accuracy in its determination is constrained by the systematic errors in the determination of $\Gamma_{\tau\tau}$.

The results are summarized as follows:

$$\Gamma_{\tau\tau}/\Gamma_h = (4.95 \pm 0.15(stat) \pm 0.11(syst)) \%$$

$$\Gamma_{\tau\tau} = (84.27 \pm 0.90(stat) \pm 1.10(syst)) \, MeV$$

$$A_{FB}^{\tau} \, (peak) = (1.52 \pm 2.46) \%$$

$$A_{POL}^{\tau} = -0.159 \pm 0.116$$

$$\bar{v}_{\tau} = -0.070 \, {}^{+ \, 0.039}_{- \, 0.033}(stat)$$

$$\bar{a}_{\tau} = -1.0052 \, {}^{+0.0061}_{-0.0059}(stat) \pm 0.0066(syst)$$

$$\overline{\sin^2 \theta_w} = 0.2303^{+0.0047}_{-0.0046}$$

The measurements of A_{FB}^{l} and A_{POL}^{τ}, foreseen to be the observables allowing the most precise determination of $\sin^2 \theta_w$ at LEP, were expected to be obtained with at least a factor ten more luminosity than the one accumulated during the run periods of 1989 and 1990. An increase in statistics and a reduction of the systematic uncertainties in the determination of the observables are required in order to achieve the aimed level of accuracy of $\Delta \sin^2 \theta_w < 0.002$.

Bibliography

[1] M.Perl et. al. (MARKI/SPEAR), *Phys. Rev. Lett. 35 (1975) 1489.*

[2] Y.S.Tsai, *Phys. Rev. D4 (1971) 2821.*

[3] H.B.Thacker,J.J.Sakurai, *Phys.Lett. 36B (1971) 103.*

[4] M.Bernardini et. al., *Nuovo Cimento 17 (1973) 383.*

[5] S.Orito et. al., *Phys. Lett. B48 (1974) 165.*

[6] M.Perl et. al. (MARKI/SPEAR), *Phys. Lett. B63 (1976) 466.*

[7] M.Perl, *Ann. Rev. Nucl. Part. Sci. 30 (1980) 299.*

[8] J.Burmester et. al. (PLUTO), *Phys. Lett. B68 (1977) 297.*

[9] J.Burmester et. al. (PLUTO), *Phys. Lett. B68 (1977) 301.*

[10] R.Brandelik et. al. (DASP), *Phys. Lett. B73 (1978) 109.*

[11] W.Bacino et. al. (DELCO), *Phys. Rev. Lett. 41 (1978) 13.*

[12] M.Aguilar-Benitez et al., *Review of Particle Properties, Phys. Lett. B204, 1988*

[13] D.Treille, *in Workshop on Polarization in LEP, CERN report (1987) p.. 20.*

[14] R.Marshall, *RAL-88-051, December 1988*

[15] J.E.Augustin, *in Proceedings of LEP Summer Study, CERN 79-01, Vol. 2, p. 499*

[16] G.Goggi, *in Proceedings of LEP Summer Study, CERN 79-01, Vol. 2, p. 483*

[17] S.Jadach,Z.Was, *in "Z Physics at LEP I", CERN 89-08, Vol. 1 p. 235*

[18] S.Orteu, *Ph.D. thesis , UAB-LFAE 89-04.*

[19] R.Cahn, *Phys. Rev. D36 (1987) 2666.*

[20] F.Block,A.Nordsieck, *Phys. Rev. 52 (1937) 54.*

[21] J.Haissinski, *LAL 87-19 and LAL 89-50*

[22] W.Hollik, *DESY 88-188 and in Proceedings of Workshop at Ringberg Castle , ed. Springer-Verlag*

[23] J.Alexander et. al., *SLAC PUB-4376, (1987).*

[24] M.Veltman, *Nucl. Phys. B123 (1977) 89.*

[25] W.J.Marciano and A.Sirlin, *Phys. Rev. Lett. 46 (1981) 163.*

[26] W.J.Marciano and A.Sirlin, *Phys. Rev. D22 (1980) 2695.*

[27] W.J.Marciano and A.Sirlin, *Phys. Rev. D29 (1984) 75.*

[28] W.J.Marciano and A.Sirlin, *Phys. Rev. D22 (1984) 945.*

[29] D.C.Kennedy, *Nucl. Phys. B321 (1989) 83.*

[30] G.Burgers et. al., *in "Z Physics at LEP I", CERN 89-08 , Vol. 1, p. 55*

[31] W.Hollik, *preprint DESY 88-188 (1988).*

[32] M.Consoli et. al., *"Z Physics at LEP I", CERN 89-08, Vol. 1 p. 7*

[33] G.Altarelli, *CERN-TH.5590/89*

[34] R.D.Peccei, *UCLA/90/TEP/11*

[35] A.Blondel, *CERN-EP/90-10.*

[36] W.J.Marciano and A.Sirlin, *Phys. Rev. Lett. 61 (1988) 1815.*

[37] L.B.Okun, *"Leptons and Quarks", North-Holland Pub.*

[38] F.Gilman and S.H.Rhie, *Phys. Rev. D31 (1985) 1066 .*

[39] B.C.Barish and R.Stroynowski, *CALT-68-1425 and Phys. Reports 157 (1988) 1.*

[40] C.Kiesling, *in "High Energy Electron-Positron Physics", p. 177 , eds. A.Ali and P.Soding , World Scientific Pub. (1988).*

[41] A.Pich, *FTUV/89-21 and IFIC/89-10.*

[42] E.Berger and H.Lypkin, *Phys. Rev. Lett. 59 (1987) 1394.*

[43] E.Berger and H.Lypkin, *Phys. Lett. B189 (1987) 226.*

[44] M.Derrick et al., *Phys. Lett. B189 (1987) 260.*

[45] C.K.Zachos and Y.Meurice, *Mod. Phys. Lett. A2 (1987) 247.*

[46] G.V.Holtey, *CERN/LEP-BI/88-52*

[47] G.V.Holtey and D.Ritson *DELPHI 88-70 GEN-83*

[48] P.Roudeau, *MIG note Sept. 87 and DELPHI 90-8 GEN-105*

[49] The DELPHI detector, *CERNL/LEPC/83-3 and DELPHI 83-66/1*

[50] The DELPHI detector, *CERNL/LEPC/84-16 and DELPHI 84-60 GEN-11*

[51] The DELPHI detector at LEP, *CERN-PPE/90-128, submitted to NIM.*

[52] P.Antilogus, *Ph.D. thesis , LAL 88-19*

[53] F.Navarria, *NIM A257 (1987) 499.*

[54] P.Checchia et. al., *NIM A275(1989) 49.*

[55] M.Burns et. al., *CERN-EP/88-82*

[56] A.Amery et. al., *NIM A283 (1989) 502.*

[57] Ph. Gavillet, *NIM A235 (1985) 363.*

[58] Ph. Charpentier, *Lecture Series, 1989-1990 Academic Training at CERN*

[59] D.Treille, *DELPHI internal note (unpublished).*

[60] L.Bugge and M.Dam, *DELPHI 87-81 PHYS-21*

[61] S.Jadach and Z.Was, *Comp. Phys. Commun. 36 (1985) 191*

[62] S.Jadach and Z.Was, *in "Z Physics at LEP I", CERN 89-08, Vol. 1, p. 235*

[63] Yennie et. al. *Ann. Phys. 13 (1961) 379*

[64] S.Jadach, H.Kuhn and Z.Was, *description of TAUOLA library, CERN-TH 5856/90*

[65] DELSIM, *DELPHI 89-67 (users guide) and DELPHI 89-68 (reference manual)*

[66] DELANA, *users guide DELPHI 89-44*

[67] *DELPHI 86-56 PROG-51*

[68] *DELPHI 87-35 PROG-77*

[69] R.L.Gluckstern, *NIM 24 (1963) 381.*

[70] K.Kleinknecht, *Detectors for particle radiation, Cambridge University Press*

[71] TANAGRA User's Guide, *DELPHI 87-95 PROG-98*

[72] Event Viewing Software, *DELPHI 89-6 PROG-126*

[73] R.Brun et. al., *Physics Analysis Workstation, CERN Program Library Q121*

[74] J.Marco, *Ph.D thesis , University of Santander ,1989*

[75] H.-U.Martyn, *DESY 89-121*

[76] F.A.Brends,P.H.Daverveldt and R.Kleiss, Comp. Phys. Comm. 40 (1986) 285.

[77] F.A.Berends,P.H.Daverveldt and R.Kleiss, *Phys. Lett. B148 (1984) 489.*

[78] Kleiss et.al. *in "Z Physics at LEP I", CERN 89-08, Vol. 3, p. 98*

[79] F.A.Berends et. al. *in "Z Physics at LEP I", CERN 89-08, Vol. 1, p. 89*

[80] A.Borrelli,M.Consoli,L.Maiani,R.Sisto, *prep. CERN-TH 5441/89 (1989)*

[81] D.Bardin et. al., *description of ZFITTER program, under preparation*

[82] M.Martinez et. al., *prep. CERN-PPE/90-109 (1990)*

[83] DELPHI Collaboration, *A Precise Meaurement of the Z resonance Parameters Through Its Hadronic Decays, CERN-EP/90-32*

[84] DELPHI Collaboration *Study Of The Leptonic Decays Of the Z^0 Boson CERN-EP/90-31*

[85] DELPHI Collaboration, *DELPHI Results on the Z Resonance Parameters trough its Hadronic and Leptonic Decay Modes, presented at Singapore Conf. CERN-PPE/90-119*

[86] A.Olshevsk, *private communication.*

[87] L.Pape, *private communication.*

[88] D.Bardin et. al., *Z. Phys. C44 (1989), 493*

[89] D.Bardin et. al., *JINR preprint E2-89-792, Dubna(1989)*

[90] G.Feldman, *SLAC MKII Note 2-24 (1987)*

[91] M.Bohm et. al. *in "Z Physics at LEP I", CERN 89-08, Vol. 1, p. 203*

[92] M.Bilenky and M.Sachwitz, *Berlin-Zeuthen prep. PHE 89-10 (1989)*

[93] CDF Collaboration, *1990 results from CDF, submitted for publication*

[94] J.Chauveau, *in "Physics at LEP", CERN 86-02, Vol. 1, p. 177.*

[95] S.Jadach and Z.Was, *CALASY (Calculator of Asymmetries) program (1989)*

Acknowledgements

This thesis wouldn't have been possible without the advise, guidance and patience of Daniel Treille. I thank him for his ideas, fruitful discussions and for all the physics I learnt from him over the last three and half years.

José Mariano Gago showed me the way to High Energy Physics and followed my first steps in this field. From him I always received wisdom and encouragement, that helped me to solve difficult problems.

I thank João Varela for his guidance in the pre-DELPHI period of my formation and for helpful criticism and sugestions about the contents of this thesis.

At CERN, I could count on the enormous help and friendship of Maria Elena Pol. Without her criticism this thesis would have been unreadable and the number of uncorrect sentences and misplaced commas would have been at least one order of magnitude bigger. With her help, life was much easier.

A part of activity in DELPHI was in the Offline Software Group. Under the guidance of Luc Pape I gained a lot of experience in software development and in data analysis. I thank him for very useful discussions.

From Sasha Olshevsk I got a lot of insight into the fitting procedures and in the extraction of the Z^0 resonance parameters. With him I had a lot of very fruitful discussions.

I acknowledge Ugo Amaldi for correcting my careless treatment of the systematic errors discussed in this thesis.

I thank all my DELPHI colleagues who contributed to the achievement of the results presented in this thesis.

Last but certainly not the least, I thank my parents for their continuous encouragement and help, and to Fátima for keeping my soul alive during the years of my stay at CERN.

1) Vannucci
2) Ballor. gabin
3) Linear colliders
4) de Rujula

Oleshowski

blind

$\Gamma: 84.1 \pm 0.42 \pm 0.22 \pm 0.7 \pm 0.7$
$\quad\quad\quad\quad s_{tr} \quad L \quad \Delta\Gamma$

$v = 0.05 \pm 0.05$
$a = 1.007 \pm 0.003$

Rnd
$83.0 \pm 0.9 \pm 0.8$
$A = (0.72 \pm 2.6)\%$
$v = 0.01 \pm^{0.02}_{0.01} \pm 0.004$
$a = 1 \pm^{0.006}_{0.008} \pm 0.004_{sysr}$

$\Delta\Lambda = -2 \Delta v$
$\quad\quad = -8 \Delta \sin^2\theta$

$\Delta\sin^2\theta = \dfrac{\Delta A}{8} \quad\quad \underline{0.014}$ \quad\quad interaction point

O Variation of corr with $\sqrt{s}$

O Comparison with polar

O where do we go with P_τ \quad\quad leptonic stream
ideal detector \quad\quad identification
Delphi t_{rms}, E_{min}
other values of $\Delta\sin^2\theta$ \quad $b\bar{b}$

O The τ in itself \quad\quad\quad O machine
τ charm factory \quad\quad\quad beam beam effect

O No man's land \quad\quad\quad O τ lifetime

O $\tau \rho / \tau e$ \quad\quad\quad O use of Delphi
\quad\quad\quad\quad\quad\quad\quad specificity for τ
\quad\quad\quad\quad\quad\quad\quad physics
o Cabibbo angle \quad $0.66 \pm 0.2\%$

\quad\quad\quad\quad\quad\quad\quad O correlation between
o p 86 " background \quad\quad decay products
\quad\quad it is commonly \quad\quad approximation
\quad\quad accepted " \quad\quad $\rightarrow$ τ \quad TN
\quad\quad\quad\quad\quad\quad\quad spin correl.
o Delsim \quad nuclear absorption

o read HPC p132 \quad\quad O evolution error sept $A_{(H)}$ p222

o Selection of leptonic events

o normalization p190